Ex libris
universitatis
albertaensis

Digitized by the Internet Archive
in 2019 with funding from
University of Alberta Libraries

https://archive.org/details/Rawluk1994

UNIVERSITY OF ALBERTA

RELEASE FORM

NAME OF AUTHOR: **Leslie John Rawluk**

TITLE OF THESIS: **Experimental and Calculational Study of Hydrogen Fluoride + Argon Differential Scattering**

DEGREE: **Doctor of Philosophy**

YEAR THIS DEGREE GRANTED: **Spring 1994**

Permission is hereby granted to the University of Alberta Library to reproduce single copies of this thesis and to lend or sell such copies for private, scholarly or scientific research purposes only.

The author reserves all other publication and other rights in association with the copyright in the thesis, and except as hereinbefore provided neither the thesis nor any substantial portion thereof may be printed or otherwise reproduced in any material form whatever without the author's prior written permission.

UNIVERSITY OF ALBERTA

Experimental and Calculational Study of Hydrogen Fluoride + Argon Differential Scattering

by

Leslie John Rawluk

©

A thesis submitted to the Faculty of Graduate Studies and Research in partial fulfillment of the requirements for the degree of **Doctor of Philosophy**

DEPARTMENT OF CHEMISTRY

EDMONTON, ALBERTA

Spring, 1994

UNIVERSITY OF ALBERTA

FACULTY OF GRADUATE STUDIES AND RESEARCH

The undersigned certify that they have read, and recommend to the Faculty of Graduate Studies and Research for acceptance, a thesis entitled **Experimental and Calculational Study of Hydrogen Fluoride + Argon Differential Scattering** submitted by Leslie John Rawluk in partial fulfillment of the requirements for the degree of Doctor of Philosophy.

To Louise

ABSTRACT

This thesis presents an in-depth study into the experimental and calculational results of the angular dependence of the scattering of hydrogen fluoride by argon. The experimental results contain the effects of rotationally elastic and inelastic scattering, where the initial rotational state of the HF molecules is unspecified, and the final rotational state population is measured with an HF laser + bolometer detection system. The calculational effort is centered upon a comparison of four recent intermolecular potential functional forms with varying abilities to reproduce the measured results.

The development of the HF continuous wave chemical laser is an essential component of these experiments. The cavity length is kept short (26 cm) to allow only one longitudinal mode to oscillate. An intracavity iris stoppered down to $\sim$ 4 mm in diameter allows only one transverse mode to oscillate. This is confirmed by a spatial scan of the laser power density. Line tunability is provided by a diffraction grating used as one of two surfaces in the optical cavity. R-branch transitions ($R_1(0)$, $R_1(1)$, and $R_1(2)$) allow for probing of the $j = 0$ population, and for comparison of rotor populations determined via R-branch *vs.* P-branch transitions.

HF and Ar supersonic beams are constructed to provide optimum intensity and a well-collimated velocity distribution. The resulting collision energy is 120 meV. A differential cross section (DCS) for each rotational state after the collision (j') is measured as a function of laboratory scattering angle. The most interesting features are an unexpected shoulder in the 30° angular range for the $j' = 0$ DCS, and a resurgence of signal at large scattering angles for the $j' = 4$ and 5 DCS's. This latter feature is believed to be caused by rotational rainbow scattering.

The most recently proposed potential energy (PE) surface by Hutson (*J. Chem. Phys* **96**, 6752 (1992)) has the greatest success at reproducing the experimental results, and so is used for further investigative work. The origin of the

$j' = 0$ shoulder is determined to be due to a complex interplay between attractive and repulsive forces, coupled with the degree of anisotropy in the PE surface. It is found that this feature cannot be characterized classically, and that it appears to be a novel interference effect. As well, it is proposed that a greater extent of anisotropy in the repulsive wall of this PE surface would improve the agreement between measured and calculated rotationally inelastic DCS's for HF+Ar scattering.

ACKNOWLEDGEMENTS

I cannot help but feel that a most gracious thank-you must be passed on to the many people that have helped to make this thesis a reality. Foremost, I want to thank my wife Louise, who has been a constant source of encouragement and support throughout my entire education. I have been able to complete this project because of her patience and understanding during my time as a graduate student. In respect of her love, I dedicate this thesis to her.

I would also especially like to thank Dr. Mark Keil for his unrelenting support, leadership, and dedication as my supervisor. I do not believe that anybody else could have shown me more clearly what hard work and effort can accomplish. I will be forever grateful for his patience and friendship that has been my guidance for so many years, and my pride and satisfaction at how well we worked together will be an eternal inspiration. My words at one of our meetings come to mind, "I may have given you five years of work, but you have given me a career. Thank-you."

Several people need to be thanked for their efforts in the laboratory: Dr. Laurie Danielson for his original construction of the molecular beams apparatus; Dr. YiBing Fan for solving a particularily difficult problem with the active stabilization of the laser; Mr. Yoram Apelblat, who joined the group when I was half way through and spent many long hours collecting data and "babysitting the machine"; Mr. Rick Eng for his efforts in automating the rotating flange positioning, and being an audience to my hunting stories.

To the individuals that have been co-authors on my publications, it is my pleasure to say thank-you for your efforts. In particular, Dr. YiBing Fan and Mr. Yoram Apelblat, who helped collect data and write the papers containing the experimental data; Dr. Howard Mayne and Mr. James Barrett for their classical trajectory work; Dr. Millard Alexander for the kind distribution of his close-coupling program, and the patience to teach me how to use it; and finally Dr. Tom Dingle

for his SCF work on He-CO_2 and He-OCS to which I was able to contribute with some line-broadening calculations.

I must also say thank-you to the support staff at the University of Alberta. Without the help of Hubert, Stan, Ernie, Randy, Dieter, Roman, Theo, Frank, Ed, Henry, Al and Kim, many of the little stumbling blocks that I came across would have turned into insurmountable technical obstacles. Also, my thanks must go out to Bob M^{c}Donald and Steve Thornton for their help with my computer troubles.

To all of my family, and especially my parents, I would like to express a heartfelt thank-you for the love and support that they have given throughout my schooling. It is with their encouragement that I was able to face the challenge of post-graduate work. I am only sorry that my dearly departed father will not be able to see the completion of this thesis, but I know in my heart that he is extremely proud of his son.

Finally, I express my thanks to the University of Alberta and to NSERC for the funding they have provided through the years.

TABLE OF CONTENTS

Chapter Page

1. Introduction 1

1.1 General 1

1.2 HF+Ar 5

1.3 Theoretical Background 9

1.3.A Classical Mechanics of Scattering 10

1.3.B Quantum Mechanics of Scattering 16

1.4 Quantum Mechanics of Atom+Diatom Scattering 21

1.4.A Close-coupling 22

1.4.B Infinite-Order-Sudden-Approximation 25

1.5 Validity 28

References 30

2. Use of A Chemical Laser for Molecular Beam Scattering Experiments 35

2.1 Introduction 35

2.2 Apparatus 37

2.3 Results 41

2.3.A R–branch 41

2.3.B Spectral Overlap 43

2.3.C Inelastic Differential Cross Sections 48

2.4 Summary 51

References 52

Chapter Page

3. **Effect of Velocity on Saturation Behavior For HF Molecular Beams** 54

3.1 Introduction 54

3.2 Experimental 57

3.3 Rate Equation Theory 63

3.4 Results and Discussion 68

3.4.A Saturation Behavior 68

3.4.B Rotational Distributions 73

3.4.C Detection Sensitivity 77

3.5 Summary and Conclusions 78

References 79

4. **Differential Cross Sections for Rotationally State-Resolved Inelastic Scattering of HF by Argon** 82

4.1 Introduction 82

4.2 Apparatus 86

4.2.A Beam Sources and Detector 86

4.2.B Laser Stabilization 92

4.2.C Alignment and Background Suppression 94

4.3 Data Aquisition and Analysis 97

4.3.A Measurement Technique 97

4.3.B Conversion to Population 100

4.3.C Polarization Considerations 102

Chapter Page

4.4 Results and Discussion 104
4.4.A Experimental Results 104
4.4.B Kinematic Transformations 109
4.4.C Comparison to Previous Results 113
4.4.D Rainbow Scattering 115
4.4.D.1 The DCS for $j' = 0$ 117
4.4.D.2 The DCS for $j' \geq 4$ 119
4.5 Summary and Conclusions 121
References 124

5. **Quantum Effects in the Inelastic Scattering of HF and DF by Argon** 128
5.1 Introduction 128
5.2 Apparatus and Calculations 130
5.3 Results and Discussion 134
5.3.A Laboratory Frame 134
5.3.A.1 Conclusion from Laboratory Frame Results 154
5.3.B Center-of-Mass Frame 155
5.4 Isotope Effect 161
5.5 Sensitivity to Features of the PE Surface 167
5.5.A $j = 0 \rightarrow j' = 0$ DCS 177
5.5.B $j = 0 \rightarrow j' = 1$ DCS 179
5.6 Conclusion 181
References 182

TABLE OF CONTENTS (continued)

Chapter Page

6. **General Discussion** 184

References 192

Appendix A: **Experimental Details** 194

A.1 Continuous Wave HF Chemical Laser 194

A.2 Molecular Beams Apparatus 204

A.2.A Molecular Beam Angular Resolution 207

A.2.B Molecular Beam Formation and Characterization 212

A.2.C Laser–HF Molecular Beam Interaction 220

A.3 HF+Ar Scattering 228

References 230

Appendix B: **Calculational Details** 231

B.1 Experimental Input 231

B.2 Calculational Aspects 235

References 244

Appendix C: **Unpublished Experimental Data** 245

Appendix D: **Additional Publication** 252

D.1 Introduction 252

D.2 Potential Energy Surfaces 254

D.2.A Hartree-Fock Calculations 254

D.2.B Analytical Fitting 267

Chapter Page

D.3 Pressure Broadening 276

D.4 Summary 280

References 281

LIST OF TABLES

Table Page

3.1 HF Molecular Beam Conditions 62

3.2 HF Rotational Distribution 74

4.1 Molecular Beam Operating Conditions 89

4.2 HF Molecular Beam Rotational Distribution 90

4.3 Experimentally Measured DCS's 105

5.1 PE Surface Predictive Quality 135

5.2 Ratio of $j = 1 \rightarrow j' = 0 : j = 0 \rightarrow j' = 1$ DCS's at 135 meV 157

5.3 PE Surface Modifications 168

A.1 HF Chemical Laser Output Frequencies 198

A.2 Periscope Alignment During Bolometer Rotation 226

B.1 Scattering Program Input 232

B.2 Newton Diagram Setup 236

B.3 Center-of-Mass to Laboratory Transformation Summary 243

C.1 Molecular Beam Operating Conditions 247

C.2 Seeded HF Rotational Distribution 248

C.3 High Energy DCS's 251

D.1 Hartree-Fock Calculations and Fitting for $HeCO_2$ 258

D.2 Hartree-Fock Calculations and Fitting for HeOCS 260

D.3 Parameters Fitted to $HeCO_2$ Hartree-Fock Calculations 269

D.4 Parameters Fitted to HeOCS Hartree-Fock Calculations 272

LIST OF FIGURES

Figure Page

1.1 Reduction of the Two-body Problem 10

1.2 Classical Deflection Function 13

1.3 3-dimensional Scattering Event 14

1.4 Phase Shift Curve 19

1.5 HF+Ar Coordinate System 21

2.1 HF Laser with Crossed Molecular Beams Apparatus 38

2.2 Multi-mode Laser Power 42

2.3 Longitudinal Mode Scan 44

2.4 Multi-mode Laser–Bolometer Interaction 47

2.5 Preliminary Inelastice DCS's for $j' = 1$, 2, and 3 49

3.1 Schematic Diagram of HF Laser/Crossed Molecular Beams Apparatus .. 58

3.2 Isolated Three-level System for Rotational State Detection 64

3.3 Saturation Curves 70

3.4 Boltzmann Plots for Rotational Distributions 75

4.1 Schematic Diagram of HF Laser/Crossed Molecular Beams Apparatus .. 87

4.2 Laser-based Bolometric Detection Scheme 98

4.3 Measured DCS's for $j' \leq 4$ 106

4.4 Incident and Scattered Rotational State Populations 108

4.5 Inelastic Newton Diagram 110

4.6 Experimental DCS Transformed to the Center-of-Mass 112

4.7 Comparison of Total DCS's 116

5.1 Four PE Surfaces in the Calculational Study 131

5.2a H6 Close-coupling DCS's 136

5.2b M5 Close-coupling DCS's 137

LIST OF FIGURES (continued)

Figure Page

5.2c RKR Close-coupling DCS's 138

5.2d HFD Close-coupling DCS's 139

5.3 H6 $\nu = 0$ *vs.* $\nu = 1$ DCS Comparison 141

5.4a H6 Infinite-Order-Sudden DCS's 143

5.4b M5 Infinite-Order-Sudden DCS's 144

5.4c RKR Infinite-Order-Sudden DCS's 145

5.4d HFD Infinite-Order-Sudden DCS's 146

5.5 State-to-state Laboratory Frame DCS's 148

5.6 Experimental Total DCS 151

5.7 Close-coupling Total DCS's 152

5.8 Infinite-Order-Sudden Total DCS's 153

5.9 Comparison of Close-coupling, Infinite-Order-Sudden, and Classical Trajectory DCS's 158

5.10 Variation of the Close-coupled DCS with Collision Energy 160

5.11a HF Reduced Mass on HF+Ar and DF+Ar PE Surfaces 164

5.11b DF Reduced Mass on HF+Ar and DF+Ar PE Surfaces 165

5.12 Comparison of the HF+Ar PE Surface to the DF+Ar PE Surface 166

5.13a Unmodified H6 PE Surface DCS's 169

5.13b Modification #1 on H6 PE Surface DCS's 170

5.13c Modification #2 on H6 PE Surface DCS's 171

5.13d Modification #3 on H6 PE Surface DCS's 172

5.13e Modification #4a on H6 PE Surface DCS's 173

5.13f Modification #4b on H6 PE Surface DCS's 174

5.13g Modification #5 on H6 PE Surface DCS's 175

LIST OF FIGURES (continued)

Figure Page

5.13h Modification #6 on H6 PE Surface DCS's 176

A.1 Scan of Spatial Distribution of Laser Power 200

A.2 Collimating Apertures on Crossed Molecular Beams Apparatus 208

A.3a Angular Divergence of HF Molecular Beam 209

A.3b Angular Divergence of Ar Atomic Beam 210

A.4 HF and Ar Nozzle-Skimmer Scans 214

A.5 Ar Time-of-Flight Measurement 215

A.6 Intensity of the HF Molecular Beam as a function of Nozzle Pressure .. 216

A.7 Intensity of the HF Molecular Beam as a function of Nozzle Temperature 219

A.8 Background Suppression with Cooled Aluminum Sponge 223

B.1a Sample Newton Diagrams for Elastic or Slightly Inelastic Transitions .. 240

B.1b Sample Newton Diagrams for Highly Inelastic Transitions 241

C.1 Published *vs.* Unpublished Low Energy DCS's 249

C.2 Unpublished High Energy DCS's 250

D.1 Coordinate System for HeOCS 255

D.2 Hartree-Fock Calculations for $HeCO_2$ 262

D.3 Hartree-Fock Calculations for HeOCS 263

D.4 Contour Plot for $HeCO_2$ 273

D.5 Contour Plot for HeOCS 274

D.6 Pressure Broadening Coefficients for $HeCO_2$ and HeOCS 278

CHAPTER 1

INTRODUCTION

1.1 GENERAL

The study of intermolecular forces as they apply to physical and chemical processes has had a long and varied history.[1-7] The motivation for such studies originates from the knowledge that when two particles approach, their relative motion is dictated by the force they feel for each other. Current technology allows for intermolecular forces to be studied via bulk property measurements[6] and/or molecular beam methods[8-10] which include some forms of spectroscopy.[11] This thesis is a detailed study of the gas phase interaction between hydrogen fluoride and argon. For the most part, it discusses the experimental results obtained from interfacing a crossed molecular beams apparatus with a chemical laser (Chapters 2–3). The central experimental measurements are of rotational energy transfer collisions and their angular dependence (Chapter 4). Procedural details are provided in Appendix A. A physical understanding of the experimental results, and their relation to the intermolecular forces between hydrogen fluoride and argon is also included in a theoretical discussion (Chapter 5).

Understanding the interparticle forces present during any two-particle collision is of fundamental importance to the scientific community. Limiting the discussion to closed-shell atoms, it has long been understood that the electrostatic interaction force is a function of only the internuclear separation.[4,6] However, it is necessary to also consider interactions which include non-spherical polyatomic molecules since these interactions will depend upon the relative orientation of one particle to the other (specified by one or more angles depending on the number of atoms involved), as well as the separation between the molecules. Considering the

general two-dimensional case of an atom plus a linear molecule, and remembering that force is the gradient of the potential energy,[12]

$$F(r,\gamma) = -\nabla V(r,\gamma) \qquad (1-1)$$

we see that it is actually the intermolecular potential energy (PE) (often called the PE surface because of its dependence on the two variables r and γ defined in Figure 1.5) that one is probing when considering a two particle collision. The value of knowing the intermolecular potential is that one is able to calculate experimentally observable gas phase features of a system. The corollary to this statement is that through experimental measurements one is able to extract an intermolecular potential for the system being considered. Thus, the intermolecular potential is pivotal to understanding gas phase dynamics.

Several physical properties can be directly related to the intermolecular potential. They include virial coefficients and the transport properties (viscosity, thermal conductivity, diffusion, and thermal diffusion).[6] Also, spectroscopy of the van der Waals molecle in the radio frequency, microwave, infrared, and far infrared regions can give data on pressure broadening, rotational constants and low frequency bending vibrations.[11,13,14]

The interest to this laboratory is that the "size" of the interaction of two particles can be measured via the integral or differential cross section. The correlation of the experimentally measured differential cross section (DCS) to the intermolecular potential energy,[6,15] and an understanding of the energy transfer which takes place during the collision, are the points emphasized in this research.

In simple terms, the DCS is the outcome of measuring the angular pattern which results from the scattering of one molecular beam by another. The initial direction and energy of each participant is known, whereas the final direction and relative magnitude of flux of the scattering partners is determined. There are three

broad classes of DCS's which can be determined: elastic, inelastic, and reactive. In elastic scattering,[16] the internal energy and center-of-mass speed of the colliding partners is unchanged, and only the post-collision angular distribution of the participants need be measured:

$$\mathrm{A}(\mathrm{v}, \mathrm{E_{int}}, \theta_\mathrm{A}) + \mathrm{B}(\mathrm{v}, \mathrm{E_{int}}, \theta_\mathrm{B}) \xrightarrow{\text{scattering}} \mathrm{A}(\mathrm{v}, \mathrm{E_{int}}, \theta'_\mathrm{A}) + \mathrm{B}(\mathrm{v}, \mathrm{E_{int}}, \theta'_\mathrm{B}) \quad (1-2)$$

where the prime ($'$) denotes parameters specified after the collision, θ is the angle of approach relative to some specified axis, v is the speed of the particle, and $\mathrm{E_{int}}$ is the internal energy. These were the first type of experiments carried out in this laboratory.[17]

Another type of DCS experiment is one where a chemical reaction occurs.[18-20] In this case, the products differ from the reactants.

$$\mathrm{A}(\mathrm{v}, \mathrm{E_{int}}, \theta_\mathrm{A}) + \mathrm{B}(\mathrm{v}, \mathrm{E_{int}}, \theta_\mathrm{B}) \xrightarrow{\text{scattering/rxn}} \mathrm{C}(\mathrm{v}', \mathrm{E'_{int}}, \theta'_\mathrm{C}) + \mathrm{D}(\mathrm{v}', \mathrm{E'_{int}}, \theta'_\mathrm{D}) \quad (1-3)$$

Inelastic scattering is the last type of DCS considered. The internal energy and speed of each scattering partner can change as a result of the collision. In general, one would write

$$\mathrm{A}(\mathrm{v}, \mathrm{E_{int}}, \theta_\mathrm{A}) + \mathrm{B}(\mathrm{v}, \mathrm{E_{int}}, \theta_\mathrm{B}) \xrightarrow{\text{scattering}} \mathrm{A}(\mathrm{v}', \mathrm{E'_{int}}, \theta'_\mathrm{A}) + \mathrm{B}(\mathrm{v}', \mathrm{E'_{int}}, \theta'_\mathrm{B}) \quad (1-4)$$

but specific to atom + diatom scattering this is represented as

$$\mathrm{AB}(\mathrm{v}, \nu, j, \theta_\mathrm{AB}) + \mathrm{C}(\mathrm{v}, \theta_\mathrm{C}) \xrightarrow{\text{scattering}} \mathrm{AB}(\mathrm{v}', \nu', j', \theta'_\mathrm{AB}) + \mathrm{C}(\mathrm{v}', \theta'_\mathrm{C}) \quad (1-5)$$

where ν, ν', j, and j' are the initial and final vibrational and rotational states of the diatom. This thesis is a study of DCS's for elastic and rotationally inelastic collisions, where $\nu' = \nu$ and both cases of $j' = j$ or $j' \neq j$ are investigated.

Atom + molecule scattering has been an interesting topic of study for many years.[8,21,22] Early studies, *e.g.*, Ref. 23, were able to measure differential cross

sections which did not contain any information about the internal energy distribution of the molecule (known as total differential cross sections). As experimental technology progressed, rotational state-specific scattering with diatomic molecules was conducted for weakly attractive, weakly anisotropic systems.[24,25]

A specific subset of atom + molecule scattering is the rare gas-hydrogen halide (Rg•HX) interaction. Much effort has been put into understanding systems such as these, including all combinations of (He, Ne, Ar, Kr, Xe) with (HF, HCℓ). Techniques include radio frequency and microwave spectroscopy,[13,26-32] and infrared spectroscopy[33-36] on the Rg•HX van der Waals molecule. Differential cross sections have been restricted to total cross sections[37-42] with no internal energy (*i.e.*, rotational state) selectivity reported previous to that which is included in this thesis.[43]

1.2 HF+Ar

The HF+Ar system is well suited to the methods of study mentioned in Section 1.1. The van der Waals molecule, bound by ~27 meV,[44] has a collinear equilibrium geometry with the Ar nearest to the H atom. Comparing this to the bond energy of the HF molecule (6.4 eV)[45], one would be inclined to say that the structure is not very stable. However, a molecular beam environment is collision free or "cold", and this binding energy is sufficient to make the Ar•HF van der Waals molecule relatively easy to prepare and quite stable. This strong attractive potential energy (~22% of the HF+Ar incident kinetic energy when doing the scattering experiments described in this thesis) is also beneficial in molecular beam scattering studies because it gives rise to richer scattering patterns.[10]

The development of the HF+Ar interaction potential has proceded in two directions. One way is through analysis of experiments which involve spectroscopic studies of bound states of the van der Waals molecule. The second method is through theoretical work on this interaction. Given below is the motivation for the development of the four most recent HF+Ar interaction potentials available in the literature. These potentials are further analyzed in Chapter 5 in terms of their ability to reproduce molecular beam scattering data presented in Chapter 4. It is noted that scattering studies have not yet been directly involved in determining the PE surface, and have had only a minor role in critically analyzing the available interaction potentials.

The first reports on the Ar•HF van der Waals complex were in 1963 by Vodar and Vu.[46] These infrared studies on bulk gas mixtures were of insufficient resolution to extract an interaction potential. More detailed microwave spectra on Ar•HF and Ar•DF[26,28] were obtained from molecular beam electric resonance (MBER) spectroscopy. Fourier transform microwave spectroscopy[29] added to the current knowledge of this system. This information was used by Hutson and

Howard[47] to construct a potential energy surface for Ar interacting with HF($\nu = 0$) reliable in the vicinity of the minimum energy position only. They did not have any information regarding the repulsive part of the potential or the "backside" (*i.e.*, Ar — F-H) region of the attractive well. This PE surface is the first of four investigated in Chapter 5.

The publication of Hutson and Howard's PE surface[47] inspired further spectroscopic studies on the van der Waals molecule. Rotationally resolved infrared spectra of Ar•HF were first obtained by Lovejoy *et al.*[35] using frequency difference laser spectroscopy on a supersonic expansion. Reported nearly coincidentally were high resolution infrared spectra in a gas cell again using frequency difference laser spectroscopy.[34] The authors of reference 34 were able to extract an interaction potential from their data, but this potential only varied with Ar–HF separation and did not contain any dependence on the interaction angle γ. For this reason it was not included in the analysis of available PE surfaces. Optothermal molecular beam spectroscopy reported at this time was also able to determine vibrational predissociation lifetimes.[48] The experiments of reference 35 were subsequently expanded[49] to include many different bending and stretching frequencies. Using Hutson and Howard's PE surface[47] to theoretically reproduce the results of these experiments resulted in only limited success. Consequently, Nesbitt *et al.* developed a new HF+Ar PE surface from high-resolution infrared rotational spectra[50]. In this study the HF molecules were in the $\nu = 1$ vibrational state. This PE surface is also extensively tested in Chapter 5.

Still further spectroscopic studies on the Ar•HF molecule have been undertaken.[51,52] The two above mentioned potentials[47,50] are unable to adequately predict these measurements, as well as the other experimental measurements mentioned above except for the data from which they were determined. This has led to the most recently developed HF+Ar PE surface[44] which takes into account the data

from references 28, 29, 34, 48, 49, 51, 52 and 53 to produce an Ar – HF (Ar – DF) PE surface (for HF in $\nu = 0, 1, 2$ and DF in $\nu = 0, 1$). Due to the extensive set of data from which this potential is derived, it is expected to be the most accurate of the three spectroscopic based potentials, and is also included in discussions in Chapter 5.

In parallel with the Ar•HF spectroscopic work, studies have also been completed on Ar–HF collisions. Barnes *et al.*[54] measured integral cross sections for Ar colliding with HF($\nu = 1$) which involve rotational transitions in the HF. Rotational relaxation,[55] pressure broadening of the infrared spectrum,[56,57] and collisional narrowing effects[57] have also been measured. Differential cross section measurements are those which have been mentioned earlier.[37,43]

Theoretical investigation on the Ar–HF interaction has been pursued as well. Self-consistent-field (SCF) calculations[37,58] attempt to accurately reproduce the repulsive forces at short range, while the long-range attraction is determined through HF electrical properties.[59,60] These pieces of information have been assembled to produce a semiempirical potential[61], the last one used for calculational studies in Chapter 5. Only a small amount of additional theoretical work has been carried out[62–64] since the development of this potential.[61]

Chapters 2, 3, and 4 provide experimental results and details pertinent to the measurement of final rotational state resolved differential cross sections for the scattering of HF by Ar. This information directly probes the repulsive potential energy between these two scattering partners, as well as being sensitive to their attraction. The majority of previous experimental work on this system has been restricted to the spectroscopic studies of the weakly-bound van der Waals molecule, which is a direct probe of the attractive potential energy of this system. Chapter 5 attempts to theoretically critique the four most recent intermolecular PE surfaces introduced in the literature, and to use the information in the differential cross sections to suggest improvements to the reliability of the repulsive region

of the intermolecular PE surface. Simultaneously, the suggested improvement of the PE surface results in a better understanding of the energy transfer between translational and rotational degrees of freedom.

1.3. THEORETICAL BACKGROUND

In order to understand how to discriminate between the four potential energy surfaces[44,50,47,61] used for study in this thesis, the theoretical connection between intermolecular potential and experimentally measured DCS's must be made. Realizing that the literature has many thorough renditions of this complicated solution,[3,6,8,10] the following discussion is intended to provide the reader with an introduction to the equations used to solve the scattering problem.

A fundamental step in solving the scattering problem is to separate the center of mass motion from the relative motion of the two partners. This modifies the two-body laboratory frame problem into a one-body problem in the center of mass frame with a reduced mass $\mu = \frac{m_1 m_2}{m_1+m_2}$.[10] This separation is essentially the same procedure as that used for the solution of the hydrogen atom.[65]

The simplest case to consider (*i.e.*, without any internal degrees of freedom) is the scattering of two structureless particles (*i.e.*, atoms). This allows the development of the scattering theory, but ignores the complication arising from the rotational and vibrational degrees of freedom in a molecule. Section 1.3.A shows this theory development using classical mechanics, and Section 1.3.B shows a parallel development done with quantum mechanics. It is noted that these developments are not only sufficient to deal with elastic scattering, but also form the basis for many useful approximation schemes relevant to atom + molecule scattering. Inclusion of the molecule's internal degrees of freedom (rotation only) will only be treated in the quantum mechanical development of atom + diatom scattering, and is presented in Section 1.4.

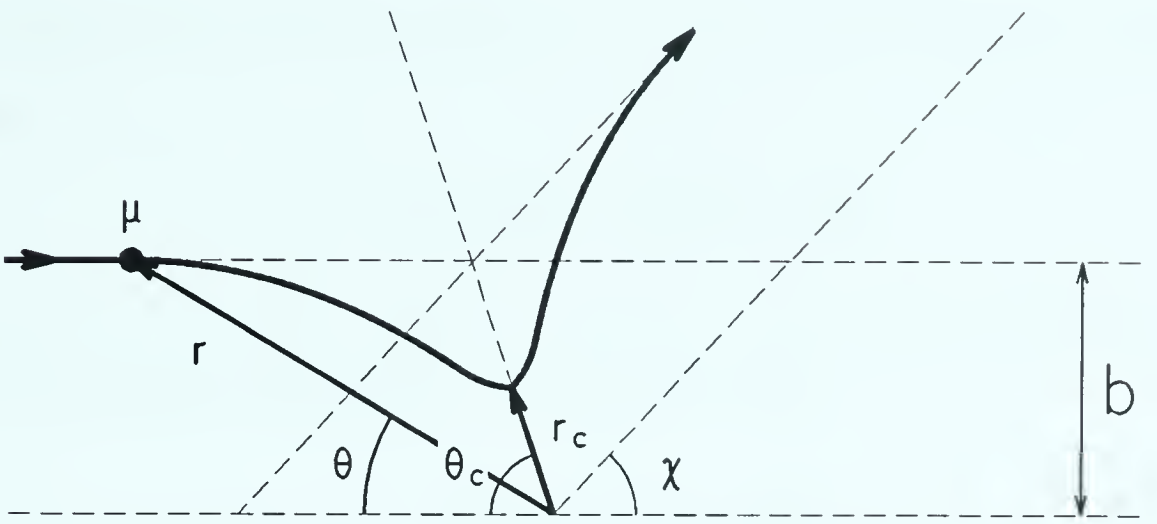

Figure 1.1 Reduction of the two body problem to a one body problem in the center of mass frame with a central force. The particle has reduced mass μ; b is the impact parameter; r_c is the distance of closest approach (classical turning point); θ_c is the angle corresponding to the distance of closest approach; χ is the scattering angle.

When the constant center-of-mass motion is separated from the relative planar motion of the particles, and polar coordinates are used in the resulting one-body problem, the total energy (kinetic + potential) of the system[66] is given by

$$E = \frac{1}{2}\mu(\dot{r}^2 + r^2\dot{\theta}^2) + V(r) \qquad (1-6)$$

and the angular momentum[66] is expressed as

$$L = \mu r^2 \dot{\theta} \ . \qquad (1-7)$$

The asymptotic speed v (relative speed of the particles) and the impact parameter b (distance of closest approach in the absence of the potential) are related to the total energy and the angular momentum by

$$E = \frac{1}{2}\mu v^2 \qquad (1-8)$$

and

$$L = \mu v b \ . \qquad (1-9)$$

The elimination of $\dot{\theta}$ from equations 1–6 and 1–7 leads to the equation for radial motion

$$E = \frac{1}{2}\mu \dot{r}^2 + \frac{L^2}{2\mu r^2} + V(r) \ . \qquad (1-10)$$

Equation 1–10 describes the one-dimensional radial motion of a single particle with mass μ and total energy E in an effective potential

$$U_L(r) = V(r) + \frac{L^2}{2\mu r^2} \ . \qquad (1-11)$$

The second term in equation 1–11 is the centrifugal potential energy.

Equations 1–7 and 1–10 can be rearranged to give the two differential equations

$$\frac{d\theta}{dt} = \frac{L}{\mu r^2} \qquad (1-12)$$

and

$$\frac{dr}{dt} = \pm\left[\frac{2}{\mu}\left(E - V(r) - \frac{L^2}{2\mu r^2}\right)\right]^{\frac{1}{2}} \ . \qquad (1-13)$$

These two equations can be combined to give the rate of change of orientation angle θ with respect to separation distance r

$$\frac{d\theta}{dr} = \pm\frac{L}{\mu r^2}\left[\frac{2}{\mu}\left(E - V(r) - \frac{L^2}{2\mu r^2}\right)\right]^{-\frac{1}{2}} \ . \qquad (1-14)$$

The ultimate goal of this presentation is to calculate the scattering angle χ as a function of impact parameter b. In Figure 1.1, χ is related to θ by

$$2\theta_c + \chi = \pi \qquad (1-15)$$

where θ_c is the angle of closest approach. Thus, the observable χ is given as

$$\chi = \pi - 2\int_{r_c}^{\infty} \frac{L}{\mu r^2}\left[\frac{2}{\mu}\left(E - V(r) - \frac{L^2}{2\mu r^2}\right)\right]^{-\frac{1}{2}} dr.$$

Substitution of the asymptotic kinetic energy and angular momentum gives

$$\chi = \pi - 2b \int_{r_c}^{\infty} \frac{dr}{r^2(1 - b^2/r^2 - V(r)/E)^{\frac{1}{2}}} \cdot \qquad (1-16)$$

The sign of χ is not experimentally discernible, but the relation between the measured quantity $|\chi|$ and the intermolecular potential energy which controls the scattering pattern is clearly shown. Note that from this point onward, the experimentally measured scattering angle θ can be used interchangeably with χ, and that $\theta = |\chi|$.

Equation 1–16 which describes χ as a function of b is called the classical deflection function (see Figure 1.2). For small b, the repulsive part of the intermolecular potential is sampled, and a large χ value results. As b increases, the deflection angle decreases until there is no net deflection due to a balance in repulsive and attractive forces. Larger b gives rise to negative deflection angle, whose magnitude goes through a maximum when the attractive forces are at a maximum (known as the rainbow angle). Still larger b has decreasing χ due to the intermolecular potential being weak and having little influence upon the trajectory.

Laboratory scattering experiments cannot control the impact parameter and then measure the scattering angle for a single interaction. Rather, narrowly collimated beams of atoms and/or molecules are made to intersect, and the resulting range of impact parameters on the molecular scale is virtually infinite. With reference to Figure 1.3, all particles which enter annular area A_1 are scattered through angle χ into annular area A_2 (recall from Figure 1.2 that for each impact parameter b there is a unique value of scattering angle χ).

The differential cross section which describes this scattering event is defined as

$$\text{DCS} = \sigma(\chi, E) = \frac{\text{Number of scattered particles/time/solid angle}}{\text{Number of incident particles/time/area}} \qquad (1-17a)$$

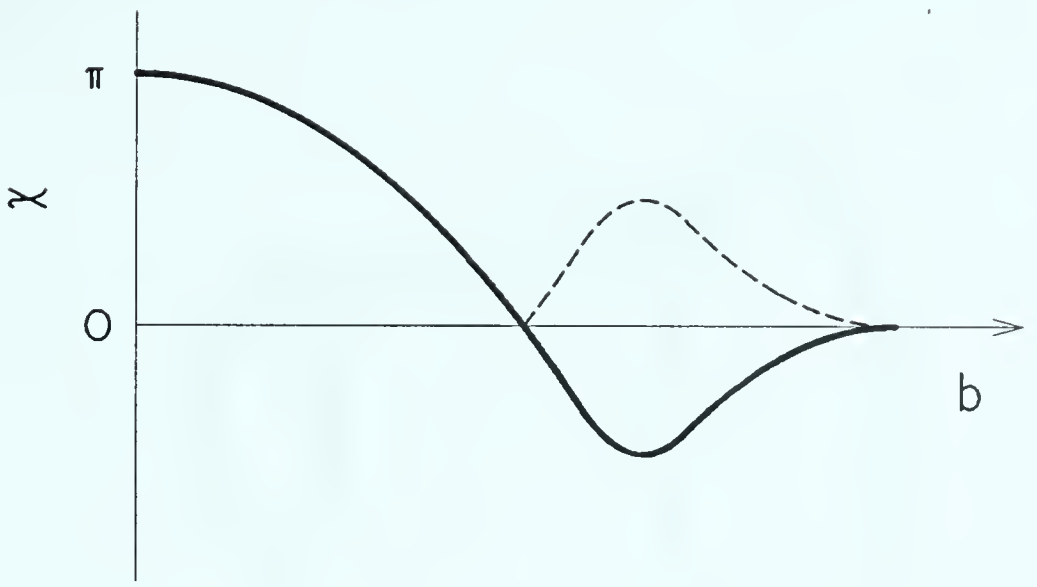

Figure 1.2 The classical deflection function χ as a function of the impact parameter b. For a "head–on" collision (*i.e.*, b = 0) the particle back onto its incoming trajectory. As the impact parameter increases in magnitude, the collision becomes less impulsive such that the attractive forces predominate and χ becomes negative. This is usually called being a soft collision. At large impact parameter the attractive force is negligible, and the particles trajectory is undeflected.

By reorganizing this equation in a slightly different manner, it is possible to easily obtain a mathematical equation representing the definition.

$$\sigma(\chi, \mathrm{E}) = \frac{\text{Number of scattered particles/time}\times\text{area}}{\text{Number of incident particles/time}\times\text{solid angle}} \qquad (1-17\mathrm{b})$$

First of all, the incident flux or number of incident particles per unit time per unit area is simply I_0. The number of scattered particles per unit time in the area A_1 is given by the input flux (assumed to be constant over the entire cross section of the molecular beam) multiplied by the area of the annulus ($\mathrm{I}_0 \times 2\pi \mathrm{b}\ \mathrm{db}$). The solid angle into which the particles have been scattered is given by $2\pi \sin\chi\ \mathrm{d}\chi$ after integration over the azimuthal angle. Substituting into equation 1–17b gives

$$\sigma(\chi, \mathrm{E}) = \left| \frac{\mathrm{I}_0 \times 2\pi\ \ \mathrm{b}\ \mathrm{db}}{\mathrm{I}_0 \times 2\pi\ \ \sin\chi\ \mathrm{d}\chi} \right|$$

$$\sigma(\chi, \mathrm{E}) = \frac{\mathrm{b}}{\sin\chi \left| \frac{\mathrm{d}\chi}{\mathrm{db}} \right|} \qquad (1-18)$$

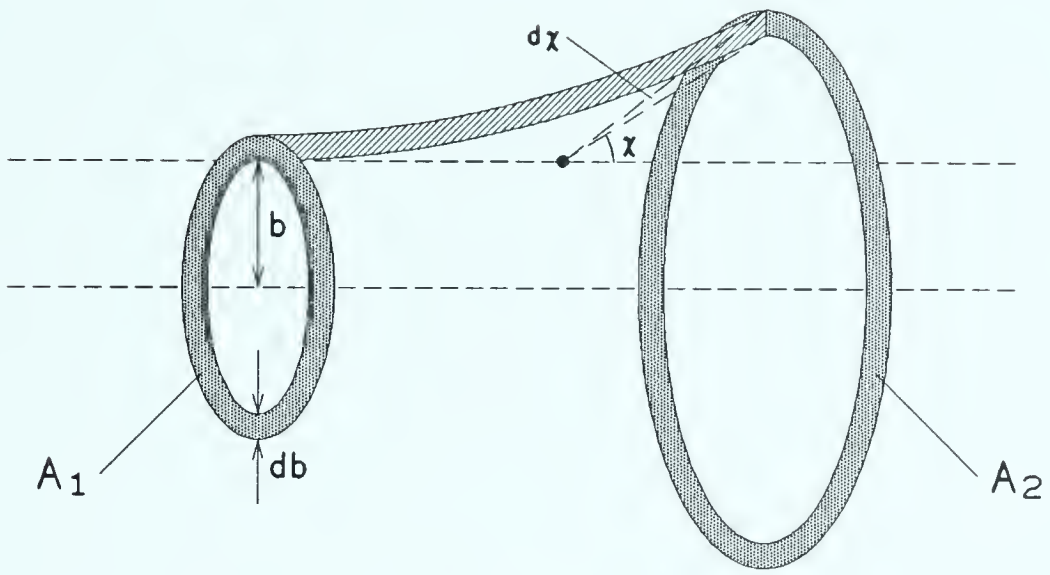

Figure 1.3 Three dimensional depiction of the scattering event: incident particles within the annular area A_1 are scattered through angle χ into annular area A_2.

There is now a clear connection between the experimentally measured DCS and the intermolecular potential energy function that describes the classical dynamics of the interaction. As a rule, the shape of the DCS is well reproduced for systems that have a large reduced mass. However, singularities in the DCS can occur in two particular instances:

i. $\sin\chi \rightarrow 0$ called the glory effect[6,10,67]

ii. $\left| \frac{d\chi}{db} \right| = 0$ called the rainbow effect[6,10,67]

Experimentally, one does not observe discontinuities in the DCS. The glory effect, corresponding to scattering at 0°, is usually not at all visible under the strong forward scattering[67], and often only a broad "bump" is seen in the DCS due to the rainbow effect.[6,10,67] Hence, the strongest reason for studying a system via classical mechanics is to obtain a good estimate of the order of magnitude and position of

rainbow features in the DCS. More quantitative reproduction of DCS features now requires one to turn to a quantum mechanical description of the scattering event.

1.3.B. Quantum Mechanics of Scattering

We now turn to quantum mechanics to provide an accurate description of the differential cross section. For simplicity during the development of the necessary equations, we will again assume the case of atom–atom scattering which necessitates a spherically symmetric potential energy function.

The quantum treatment of atom-atom scattering describes the system in terms of a wave function $\Psi(\overrightarrow{r})$ which depends only on the relative position $\overrightarrow{r}$ of a particle moving in a central force field.[6] The Schrödinger equation is given by

$$\left(-\frac{\hbar^2}{2\mu}\nabla^2 + V(r)\right)\Psi(\overrightarrow{r}) = E\Psi(\overrightarrow{r}) \qquad (1-19)$$

where $\nabla^2 = \frac{1}{r^2}\frac{\partial}{\partial r}\left(r^2\frac{\partial}{\partial r}\right) - \frac{\hat{L}^2}{r^2\hbar^2}$, with $\hat{L}^2$ the angular momentum operator. The required boundary conditions of $\Psi(\overrightarrow{r})$ are

$$\Psi(\overrightarrow{r}) = 0 \text{ (or any finite value)} , \quad r \to 0 , \qquad (1-20)$$

and

$$\Psi(\overrightarrow{r}) = \Psi^0(\overrightarrow{r}) + \frac{f(\chi)e^{ikr}}{r} , \qquad r \to \infty \qquad (1-21)$$

where $\Psi^0(\overrightarrow{r})$ is the wavefunction if $V(r) = 0$ everywhere, $f(\chi)$ is the scattering amplitude, and $\overrightarrow{k}$ is the wavevector whose magnitude corresponds to the particle momentum,

$$k = \frac{(2\mu E)^{1/2}}{\hbar} . \qquad (1-22)$$

The intensity of a wave with eigenfunction Ψ is Ψ^2 and the flux is $\Psi^2\overrightarrow{v}$, where $\overrightarrow{v}$ is the wave velocity given by $\frac{k\hbar}{\mu}$. The incident flux magnitude is therefore just $\overrightarrow{v}$ since $|\Psi^0(\overrightarrow{r})|^2 = 1$, *i.e.*, $\Psi^0(\overrightarrow{r})$ is normalized. Similarly, the scattered flux is given by $\left|\frac{f(\chi)}{r}\right|^2\overrightarrow{v}$. The area of the annular region (A_2 in Figure 1.3) resulting from the scattering is $2\pi r^2 \sin\chi \, d\chi$, which corresponds to particles being scattered

into a solid angle of $2\pi\sin\chi\ d\chi$. Thus, the scattered flux per unit solid angle into this area is given by

$$\begin{aligned} \text{Flux} &= \left|\frac{f(\chi)}{r}\right|^2 \overrightarrow{v} \times \frac{2\pi\, r^2\, \sin\chi\, d\chi}{2\pi\, \sin\chi\, d\chi} \\ &= \left|f(\chi)\right|^2 \overrightarrow{v} \end{aligned} \qquad (1-23)$$

Recalling that the differential cross section is defined as the amount of scattered flux relative to the input flux, we now get for the quantal differential cross-section

$$\begin{aligned} \sigma(\chi, E) &= \frac{|f^k(\chi)|^2 \times \overrightarrow{v}}{\overrightarrow{v}} \\ &= |f^k(\chi)|^2 \ . \end{aligned} \qquad (1-24)$$

The entire objective of the quantum mechanical treatment of scattering is therefore to determine $|f^k(\theta)|$, just as in the classical description it was to find the deflection function $\chi(b)$. In other words, the Schrödinger equation must be solved for $\Psi(\overrightarrow{r})$.[6]

Multiplying the wave equation (Equation 1–19) by $\frac{2\mu}{\hbar^2}$ gives

$$(\nabla^2 + k^2 - u(r))\Psi(\overrightarrow{r}) = 0 \ . \qquad (1-25)$$

where $u(r) = V(r)\frac{2\mu}{\hbar^2}$. Expanding the wave equation in terms of partial waves, each of which corresponds to a particular angular momentum state of the system gives

$$\Psi(\overrightarrow{r}) = \frac{1}{r}\sum_{\ell=0}^{\infty} C_\ell\, \psi_\ell(r) P_\ell(\cos\theta) \qquad (1-26)$$

where C_ℓ are the amplitudes of the partial waves $\psi_\ell(r)$, $P_\ell(\cos\theta)$ are the Legendre polynomials, and ℓ is the angular momentum quantum number.[6] Substituting Equation 1–26 into Equation 1–25 gives the set of equations

$$\left(\frac{d^2}{dr^2} + k^2 - u_\ell(r)\right)\psi_\ell(r) = 0 \qquad (1-27)$$

where $u_\ell(r) = u(r) + \frac{\ell(\ell+1)}{r^2}$ is called the effective potential. It is made up of the regular potential summed with the centrifugal potential energy.

Equation 1–27 is called the partial wave equation and can be solved as follows. Providing[3] $ru(r) \to 0$ as $r \to \infty$ the solution of the partial wave equation for each partial wave is given by[6]

$$\psi_\ell(r) \cong \sin(kr + \delta_\ell) \qquad (1-28)$$

where δ_ℓ is the relative phase of the incoming and outgoing parts of $\psi_\ell(r)$. If $u(r) = 0$, then the partial wave equation has the following solution[6]

$$\psi_\ell^0(r) \cong \sin(kr - \ell\pi/2) \qquad (1-29)$$

where $-\ell\pi/2$ is δ_ℓ^0, the phase term due solely to the centrifugal contribution $\frac{\ell(\ell+1)}{r^2}$. The phase shift caused by the potential is therefore

$$\eta_\ell = \delta_\ell - \delta_\ell^0 = \delta_\ell + \ell\pi/2\ . \qquad (1-30)$$

Asymptotically then,

$$\psi_\ell(r) \cong \sin(kr + \eta_\ell - \ell\pi/2)\ . \qquad (1-31)$$

The coefficients C_ℓ in Equation 1–26 may be determined from the normalization condition for $\Psi(\vec{r})$, $\int \Psi^* \Psi dr = 1$, and from the orthogonality of the Legendre polynomials. This leads to

$$f^k(\theta) = \frac{1}{2ik} \sum_{\ell=0}^{\infty} (2\ell+1)\ \left(e^{2i\eta_\ell} - 1\right)\ P_\ell(\cos\theta)\ . \qquad (1-32)$$

The phase shift, η_ℓ, is essential to calculating the quantum differential cross section, and in turn the interaction potential is the physical property which determines the phase shift. Thus, experimentally measuring the DCS is one way of probing the interaction potential.

Visualization of the phase shift is best done by considering the wave function which satisfies Equation 1–27. When r is large enough so that $V(r) \sim 0$, $u_\ell(r)$ will behave as sin(kr), thus meaning that a comparison of $u_\ell(r)$ with the same wavefunction obtained when $V(r) = 0$ (Equation 1–29) will give the phase shift in $\psi_\ell(r)$ due to the presence of the interaction potential. The qualitative shape of the phase shift versus ℓ curve is given in Figure 1.4. At small ℓ the phase shift is large and negative due to the potential being large (*i.e.*, sampling the repulsive wall). As ℓ increases, the phase shift goes through zero, reaches a maximum positive value, and then assymptotically goes to zero as the effective potential has very little contribution from the true potential.[6] Analytical and numerical techniques for solution of η_ℓ are well developed in the literature[10] and not discussed in any further detail.

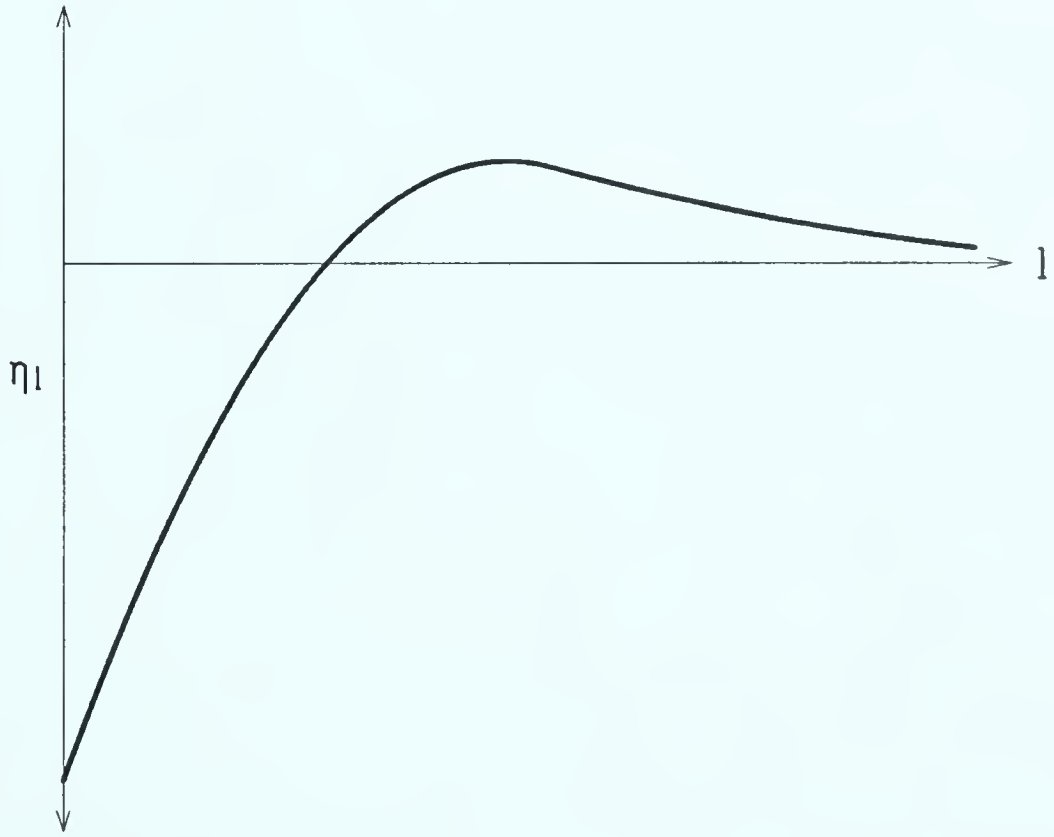

Figure 1.4 Generic relation between the phase shift η_ℓ and the orbital angular momentum quantum number ℓ for an interaction potential with both repulsive and attractive parts.

The connection is made between the experimentally observable feature (*i.e.*, the DCS), to the calculationally important phase shift, and finally to the

desired intermolecular potential. In practice however, due to the complicated equations relating the potential to the DCS, this calculation is carried out in the forward sense by first assuming a potential form, and then calculate a DCS from this assumed potential. Comparison to the experimental DCS implies the possibility of iteration to improve the potential form to agree with experiment.

1.4 QUANTUM MECHANICS FOR ATOM + DIATOM SCATTERING

The above equations are essential in understanding the connection between the intermolecular PE surface and the measured DCS. However, the HF+Ar system studied in this thesis is more complicated than the atom-atom case because of its non-spherical PE surface. The two coordinates used to describe the PE surface are the distance "r" between the HF center of mass and the Ar atom, and the angle "γ" between the vector passing through the HF molecular axis and the vector from the HF center of mass and the Ar atom (see Figure 1.5).

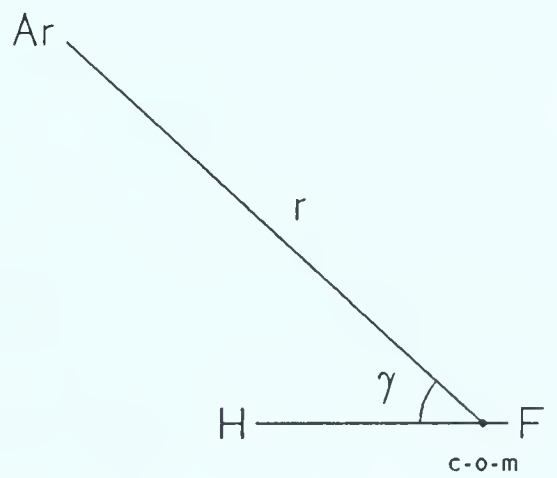

Figure 1.5 Coordinate system for the interaction between Ar and the HF rigid rotor.

The calculation of the DCS is handled via two different methods: the first method is called the Close-Coupling (CC) technique, and is an exact quantum mechanical formulation subject to the condition that the angular dependence of the intermolecular potential can be approximated by an infinite Legendre series.[68] The second method is called the Infinite-Order-Sudden-Approximation (IOSA). It involves two distinct approximations which greatly simplify the coupled differential equations.

1.4.A Close-coupling‡

It is easiest to start the calculational process by taking advantage of the fact that in the molecular beam environment the HF molecule will be in its ground vibrational state, and that the vibrational quantum for HF is ~500 meV. Since the collision energy is only ~120 meV (see Chapter 4 for complete details), then all vibrational transitions are energetically closed. This allows the useful approximation of treating the HF molecule as a rigid rotor to remove all dependences upon the HF bond length and the vibrational state.

The Schrödinger equation for this calculation is very similar to Equation 1–19, except that now we include the kinetic energy operator for an HF rigid rotor

$$\left(-\frac{\hbar^2}{2\mu}\nabla^2 + \frac{\hat{\mathrm{J}}^2}{2\mu_{\mathrm{HF}}\mathrm{d}^2} + \mathrm{V}(\mathrm{r},\gamma)\right)\Psi(\vec{\mathrm{r}}) = \mathrm{E}\Psi(\vec{\mathrm{r}})\ . \qquad (1-33)$$

Note that there are two angular momentum operators in this equation, namely $\hat{\mathrm{J}}^2$ which is the angular momentum for the rotating HF molecule, and $\hat{\mathrm{L}}^2$ inside the ∇^2 operator which is the orbital angular momentum between the HF and Ar as they approach each other.

Now to solve the Schrödinger equation (Equation 1–33) exactly via the technique called "close-coupling" originally developed by Arthurs and Dalgarno.[68] Briefly, the method is as follows: the eigenfunctions of the rigid rotor are spherical harmonics ($\mathrm{Y}_{j\ m_j}$) with rotational energy $\frac{\hbar^2}{2\mathrm{I}}j(j+1)$. The total energy when the

‡ It is noted that while the development of the close-coupling equations is shown in the following section, they were not actually programmed by the author. A working program solving the close-coupling equations was obtained from Professor Millard H. Alexander at the University of Maryland in College Park, Maryland. Through help from Prof. Alexander, operation of the HIBRIDON code as specifically set up for the Ar + HF problem was mastered over a period of several months. Computer code developed at the University of Alberta includes transformation of center-of-mass frame DCS's to the laboratory frame, followed by subsequent averaging over experimental conditions to allow direct comparison to measured DCS's. No further programming or deconvolution of the close-coupling code was attempted.

rotor is in a specific quantum state[68] j is

$$\mathrm{E}_j = \mathrm{E} + \frac{\hbar^2}{2\mathrm{I}} j(j+1) \ . \qquad (1-34)$$

where E is the incident kinetic energy.

Recognizing that the orbital angular momentum **l** will couple with the rotational angular momentum **j** to give the total angular momentum **J**, a new function is defined as

$$\mathrm{Y}^{\mathrm{M}}_{\mathrm{J}jl} = \sum_{m_l=-l}^{l} \sum_{m_j=-j}^{j} (jlm_j m_l \,|\, jl\mathrm{JM})\ \mathrm{Y}_{lm_l} \mathrm{Y}_{jm_j} \qquad (1-35)$$

where $(jlm_j m_l \,|\, jl\mathrm{JM})$ is a vector-coupling or Clebsch-Gordon coefficient[69]. This new function describes the total angular dependence of the diatomic and the incident particle plus target.

The Schrödinger equation is now written as

$$\mathrm{H}\Psi^{\mathrm{JM}}_{jl} = \mathrm{E}_j \Psi^{\mathrm{JM}}_{jl} \ . \qquad (1-36)$$

Expanding this wavefunction according to

$$\Psi^{\mathrm{JM}}_{jl} = \sum_{j'} \sum_{l'} \mathrm{r}^{-1} u^{\mathrm{J}jl}_{j'l'}(\mathrm{r})\ \mathrm{Y}^{\mathrm{M}}_{\mathrm{J}j'l'} \ , \qquad (1-37)$$

substituting into Equation 1–25 (which is actually a shorthand version of Equation 1–19), multiplying from the left by $\mathrm{Y}^{\mathrm{M}}_{\mathrm{J}j'l'}{}^{*}$, and integrating over angular variables yields a set of coupled differential equations,

$$\left[\frac{\mathrm{d}^2}{\mathrm{dr}^2} + \mathrm{k}^2_{j'} - \frac{l(l+1)}{\mathrm{r}^2}\right] u^{\mathrm{J}jl}_{j'l'}(\mathrm{r}) = \frac{2\mu}{\hbar^2} \sum_{j''} \sum_{l''} \langle j''l''; \mathrm{J} \,|\, \mathrm{V} \,|\, j'l'; \mathrm{J} \rangle\ u^{\mathrm{J}jl}_{j''l''}(\mathrm{r}) \ , \quad (1-38)$$

where

$$\mathrm{k}^2_{j'} = \frac{2\mu}{\hbar^2} \left[\mathrm{E}_j - \frac{\hbar^2}{2\mathrm{I}} j'(j'+1)\right] \qquad (1-39)$$

and

$$\langle j''l''; \mathrm{J} \,|\, \mathrm{V} \,|\, j'l'; \mathrm{J} \rangle = \iint \mathrm{Y}^{\mathrm{M}}_{\mathrm{J}j''l''}{}^{*} \mathrm{V}\, \mathrm{Y}^{\mathrm{M}}_{\mathrm{J}j'l'}\, \mathrm{d}\Omega \ . \qquad (1-40)$$

At large r, $u^{\mathrm{J}jl}_{j'l'}(\mathrm{r})$ may be written as

$$u^{\mathrm{J}jl}_{j'l'}(\mathrm{r}) \sim \delta_{j'j}\delta_{l'l} \exp\left[-i(\mathrm{k}_j \mathrm{r} - \frac{1}{2} l\pi)\right]$$
$$- \left(\frac{\mathrm{k}_j}{\mathrm{k}_{j'}}\right)^{\frac{1}{2}} \mathrm{S}^{\mathrm{J}}(j'l', jl) \exp\left[i(\mathrm{k}_{j'}\mathrm{r} - \frac{1}{2} l'\pi)\right] \ . \qquad (1-41)$$

This defines the S matrix which gives rise to the scattering amplitudes $\mathrm{f}(j'm_{j'}, jm_j)$. The differential cross section I is then given as

$$\mathrm{I} = \mathrm{k}_j^{-2} \,|\, \mathrm{f}\,(j'm_{j'}, jm_j)\,|^2 \qquad (1-42)$$

and

$$\mathrm{f}\,(j'm_{j'}, jm_j) = \sum_{\mathrm{J}=0}^{\infty} \sum_{\mathrm{M}=-\mathrm{J}}^{\mathrm{J}} \sum_{l=|\mathrm{J}-j|}^{\mathrm{J}+j} \sum_{l'=|\mathrm{J}-j'|}^{\mathrm{J}+j'} \sum_{m_{l'}=-l}^{l'} i^{l-l'} \pi^{\frac{1}{2}}$$
$$\times (2l+1)^{\frac{1}{2}} (jlm_j 0 \,|\, jl\mathrm{JM})\, (j'l'm_{j'}m_{l'} \,|\, j'l'\mathrm{JM}) \left(\delta_{jj'}\delta_{ll'} - \mathrm{S}^{\mathrm{J}}(jl; j'l')\right) \mathrm{Y}_{l'm_{l'}} \ . \qquad (1-43)$$

1.4.B Infinite-Order-Sudden-Approximation

Solution of the close-coupled equations is a daunting task, and it is a reasonable expectation that there exist many approximations which will decrease the calculational effort. The most common approximation techniques are mentioned in reference 6, from which an in depth reference listing can be obtained. The infinite-order-sudden (IOS) approximation used in this thesis was chosen for two main reasons: one is that the resulting differential equations are uncoupled (*i.e.*, one dimensional only), and thus relatively straight-forward to solve. The second reason is that the IOS approximation was familiar to this laboratory when doing calculations on a different set of atom-molecule scattering (selected papers in reference 17), and a transition to HF+Ar scattering calculations was hoped to be relatively straightforward.

There are many descriptions of the IOS method in the literature,[70–72] but for the purpose of actually doing the calculations the best direction is given by Parker and Pack.[73]

The Schrödinger equation for this calculation is identical to Equation 1–33 which includes the kinetic energy operator for an HF rigid rotor

$$\left(-\frac{\hbar^2}{2\mu}\nabla^2 + \frac{\hat{\mathrm{J}}^2}{2\mu_{\mathrm{HF}}\mathrm{d}^2} + \mathrm{V}(\mathrm{r},\gamma)\right)\Psi(\overrightarrow{\mathrm{r}}) = \mathrm{E}\Psi(\overrightarrow{\mathrm{r}})\ . \qquad (1-44)$$

Again note the presence of the two different angular momentum operators, $\hat{\mathrm{J}}^2$ and $\hat{\mathrm{L}}^2$ inside the ∇^2 term, which couple the HF rotational motion with the angular momentum of the system. Replacing these operators with their eigenvalue forms

$$\hat{\mathrm{L}}^2 \approx \bar{l}(\bar{l}+1)\,\hbar^2 \qquad (1-45)$$

and

$$\hat{\mathrm{J}}^2 \approx \bar{j}(\bar{j}+1)\,\hbar^2 \qquad (1-46)$$

removes all angular dependence except for that which is present in the potential term. Equation 1–45 is the centrifugal sudden "CS" approximation, which decouples the orbital angular momentum from the rotational angular momentum. Since the orbital angular momentum is now independent of all other terms in the Schrodinger equation, it can be chosen to be one constant value with no consequence to any other quantum numbers, and so the centrifugal potential term becomes degenerate in energy throughout the entire interaction. Parallel to the CS approximation is the energy sudden "ES" approximation (Equation 1–46), which has the effect of making all rotational energy levels degenerate. When these two approximations are taken together, they form the IOS approximation.[6]

The angular dependence of the potential is now treated in a parametric fashion, leaving an uncoupled second-order differential equation to solve in a manner which is parallel to that shown in Section 1.3.B. Slight changes in some of the equations occur along with an extension in computation to include the averaging over the interaction angle.

The simplifications of Equations 1–45 and 1–46 give

$$\left[\frac{\mathrm{d}^2}{\mathrm{dr}^2} + \bar{\mathrm{k}}^2 - \frac{\bar{l}(\bar{l}+1)}{\mathrm{r}^2} + \frac{2\mu}{\hbar^2}\,\mathrm{V}(\mathrm{r},\gamma)\right]\, g^{\bar{\mathrm{k}}\,\bar{l}}(\mathrm{r};\gamma) = 0\ , \qquad (1-47)$$

where V(r,γ) is the intermolecular potential itself and

$$\bar{\mathrm{k}}^2 = \frac{2\mu}{\hbar^2}\,\left[\mathrm{E} - \bar{j}(\bar{j}+1)\hbar^2/2\mathrm{I}\right]\ . \qquad (1-48)$$

I is the moment of inertia of the diatomic (HF). Equation 1–47 is very similar to Equation 1–25, and is solved in the same manner to give the phase shifts as a function of ℓ for the given parametric angle. The scattering amplitude is

$$\mathrm{f}^{\bar{\mathrm{k}}}(\gamma\,|\,\theta) = \frac{1}{2\mathrm{i}\bar{\mathrm{k}}}\sum_{\ell=0}^{\infty}(2\ell+1)\left(\mathrm{e}^{2\mathrm{i}\eta_\ell^{\bar{\mathrm{k}}}} - 1\right)\mathrm{P}_\ell(\cos\theta)\ . \qquad (1-49)$$

Expansion of $f^{\bar{k}}(\gamma \,|\, \theta)$ in Legendre polynomials in γ

$$f^{\bar{k}}(\gamma \,|\, \theta) = \sum_{L=0}^{\infty} F_L^{\bar{k}}(\theta)\, P_L(\cos\gamma) \;, \qquad (1-50)$$

leads to

$$I(j' \leftarrow j \;|\theta) = \frac{k_0^2}{k_j^2} \sum_{j''=|\,j-j'\,|}^{j+j'} C^2(j, j'', j'; 000) I(j'' \leftarrow 0) \qquad (1-51)$$

where $C^2(j, j'', j'; 000)$ are Clebsch-Gordon coefficients and

$$I(j'' \leftarrow 0) = \left(\frac{\bar{k}^2}{k_0^2}\right) \,|\, F_{j''}^{\bar{k}}(\theta) \,|^2 \;. \qquad (1-52)$$

Thus, we get all of the cross sections from only a few integrals, and have averaged over the interaction angle in Equation 1–50.

1.5 VALIDITY

The close-coupling calculation is the exact solution of the Schrödinger equation, and hence is the most accurate calculation available. However, this technique suffers from being a very difficult computational problem, with cumbersome equations for programming, vast computer storage requirements, as well as large amounts of central processing unit time required. Nevertheless, it remains the method of choice because the results are, to the best of the scientific community's knowledge, the most accurate.

One can reduce computer requirements by employing various approximations to help solve the complicated equations. This has been done with the infinite order sudden approximation. It is expected to be valid[6] whenever the relative kinetic energy is large compared to (i) the change in rotational energy for a given collision (the ES approximation), and (ii) the difference in the adjacent centrifugal potentials (the CS approximation). Expressed differently, this same validity criteria requires the relative collision energy to be much larger than the well depth.[6]

For the Ar + HF system studied, point (ii) is valid since $E_{rel} \approx 5\epsilon$, where $\epsilon \sim 27$ meV is the potential well depth. Moreover, in the vicinity of the attractive well minimum (r$\sim$ 3.4Å) the centrifugal potential varies from one value of ℓ to the next as $\sim \ell \times 0.01$ meV. When doing summations over ℓ as described in Section 1.4, ℓ was never allowed beyond 400, and so the change in adjacent centrifugal potentials is always much less than the relative collision energy.

More difficulty arises from point (i). The rotational constant for HF is 2.55 meV (20.56 cm^{-1}) which is quite large in comparison to other diatomics (*e.g.*, $B_e \sim 6.55\,cm^{-1}, 1.7\,cm^{-1}$ for HI, N_2 respectively).[45] Following the criteria in reference 6 shows that only for elastic ($\Delta j = 0$) and slightly rotationally inelastic transitions ($\Delta j = 1$) should the IOSA be valid. However, transitions with $\Delta j \geq +2$ also contribute a significant amount to the DCS ($\sim$ 50% at wide angles as

shown in Chapter 5). This leads one to be suspicious about the validity of the ES approximation in studying the HF+Ar system.

Another way to view the ES approximation is to say that the molecule does not rotate for the duration of the collision (*i.e.*, pick a γ and integrate the one-dimensional Schrödinger equation). As explained in Chapter 5, an HF molecule in $j = 1$ will execute ~ 1.7 rotations during the collision, and this clearly does not conform to IOSA requirements. Thus, the IOSA is not expected to be quantitatively accurate for the Ar + HF system. On the other hand, it is relatively simple to program and is expected to provide qualitative insight into the scattering phenomenon.

REFERENCES:

1. S. Chapman and T. G. Cowling, *The Mathematical Theory of Non-Uniform Gases* (Cambridge University Press, Cambridge, 1939).

2. S. Glasstone, K. J. Laidler, and E. H. Erying, *Theory of Rate Processes* (McGraw-Hill, New York, 1941).

3. N. F. Mott and H. S. W. Massey, *The Theory of Atomic Collisions* (Oxford University Press, Oxford, 1949).

4. J.O. Hirschfelder, G.F. Curtiss, and R.B. Bird, *Molecular Theory of Gases and Liquids* (Wiley, New York, 1954).

5. *Adv. Chem. Phys.* **12**, *Intermolecular Forces* ed. by J.O. Hirschfelder (Interscience, New York, 1967).

6. G.C. Maitland, M. Rigby, E.B. Smith, and W.A. Wakeham, *Intermolecular Forces: Their Origin and Determination* (Clarendon, Oxford, 1981).

7. R.A. Aziz, *Inert Gases: Springer Series in Chemical Physics*, ed. by M. Klein (Springer, Berlin, 1984); Vol. **34**.

8. (a) *Atom-Molecule Collision Theory: A Guide for the Experimentalist*, ed. by R.B. Bernstein (Plenum, New York, 1979); (b) R.B. Bernstein, *Chemical Dynamics via Molecular Beam and Laser Techniques* (Clarendon, Oxford, 1982).

9. *Adv. Chem. Phys.* **10**, *Molecular Beams*, ed. by J. Ross (Interscience, New York, 1966), particularly chapters 2, 3, 8 and 9.

10. M. A. D. Fluendy and K. P. Lawley, *Chemical Applications of Molecular Beam Scattering* (Chapman and Hall, London, 1973).

11. J. M. Hutson, *Annu. Rev. Phys. Chem.* **41**, 123 (1990); A. D. Buckingham, P. W. Fowler and J. M. Hutson, *Chem. Rev.* **88**, 963 (1988); A. C. Legon and D. J. Millen, *Chem. Rev.* **86**, 635 (1986); D. J. Nesbitt, *Chem. Rev.* **88**, 843 (1988); R. J. Saykally, *Acc. Chem. Res.* **22**, 295 (1989); A. Weber, *Structure and Dynamics of Weakly Bound Complexes*, ed. by D. Reidel (NATO ASI Series C.) **212**.

12. D. Halliday and R. Resnick, *Fundamentals of Physics – Second Edition* (John Wiley and Sons, New York, 1981). Chapter 8.

13. A. C. Legon, *Annu. Rev. Phys. Chem.* **34** 275 (1983).

14. T. R. Dyke, B. J. Howard, and W. Klemperer, *J. Chem. Phys.* **56**, 2442 (1972); E. W. Kaiser, *J. Chem. Phys.* **53**, 1686 (1970); S. E. Novick, P. Davies, S. J. Harris, and W. Klemperer, *J. Chem. Phys.* **59**, 2273 (1973); S. E. Novick, K. C. Janda, S. L. Holmgren, M. Waldman, and W. Klemperer, *J. Chem. Phys.* **65**, 1114 (1976); S. J. Harris, S. E. Novick, W. Klemperer, and W. E. Falconer *J. Chem. Phys.* **61**, 193 (1974); S. E. Novick, K. C. Janda, and W. Klemperer, *J. Chem. Phys.* **65**, 5115 (1976); S. L. Holmgren, M. Waldman, and W. Klemperer, *J. Chem. Phys.* **67**, 4414 (1977); S. L. Holmgren, M. Waldman, and W. Klemperer, *J. Chem. Phys.* **69**, 1661 (1978);

15. J. E. G. Farina, *Quantum Theory of Scattering Processes* (Pergamon Press, Oxford, 1973).

16. U. Buck, *Atomic and Molecular Beam Methods – Volume 1.*, ed. by G. Scoles. (Oxford University Press, 1988). Chapter 20 and references within.

17. M. Keil, L. J. Danielson, U. Buck, J. Schleusener, F. Huisken, and T. W. Dingle, *J. Chem. Phys.* **89** 2866 (1988); L. J. Danielson and M. Keil, *J. Chem. Phys.* **88**, 851 (1988); L. J. Danielson, *Ph.D. Thesis* University of Alberta, 1989.

18. Y. T. Lee, *Atomic and Molecular Beam Methods – Volume 1.*, ed. by G. Scoles. (Oxford University Press, 1988). Chapter 22 and references within.

19. P. J. Dagdigian, *Atomic and Molecular Beam Methods – Volume 1.*, ed. by G. Scoles. (Oxford University Press, 1988). Chapter 24 and references within.

20. R. D. Levine and R. B. Bernstein, *Molecular Reaction Dynamics and Chemical Reactivity* (Oxford University Press, New York, 1987).

21. U. Buck, *Atomic and Molecular Beam Methods – Volume 1.*, ed. by G. Scoles. (Oxford University Press, 1988). Chapter 21 and references within.

22. P. J. Dagdigian, *Atomic and Molecular Beam Methods – Volume 1.*, ed. by G. Scoles. (Oxford University Press, 1988). Chapter 23 and references within.

23. M. Keil, G. A. Parker, and A. Kuppermann, *Chem. Phys. Lett.* **59**, 443 (1978).

24. P. L. Jones, U. Hefter, A. Mattheus, J. Witt, K. Bergmann, W. Müller, W. Meyer, and R. Schinke, *Phys. Rev. B* **26**, 1283 (1982); P. L. Jones, E. Gottwald, U. Hefter, and K. Bergmann, *J. Chem. Phys.* **78**, 3838 (1983), and references therein.

25. U. Buck, H. Meyer, and R. J. LeRoy, *J. Chem. Phys.* **80**, 5589 (1984).

26. S. J. Harris, S. E. Novick and W. Klemperer, *J. Chem. Phys.* **60**, 3208 (1974).

27. T. J. Ball, E. J. Campbell, M. R. Keenan, and W. H. Flygare, *J. Chem. Phys* **71**, 2723 (1979); T. J. Ball, E. J. Campbell, M. R. Keenan, and W. H. Flygare, *J. Chem. Phys* **72**, 922 (1980).

28. T. A. Dixon, C. H. Joyner, F. A. Baiocchi, and W. Klemperer, *J. Chem. Phys.* **74**, 6539 (1981).

29. M. R. Keenan, L. W. Buxton, E. J. Campbell, A. C. Legon and W. H. Flygare, *J. Chem. Phys* **74**, 2133 (1981).

30. T. R. Dyke, *Top. Curr. Chem* **120**, 85 (1984).

31. M. D. Marshall, A. Charo, H. O. Leung, and W. Klemperer, *J. Chem. Phys.* **83**, 4924 (1985)

32. B. L. Cousins, S. O'Brien and J. M. Lisy, *J. Phys. Chem.* **88**, 5142 (1984).

33. B .J. Howard and A. S. Pine, *Chem. Phys. Lett* **122**, 1 (1985).

34. G. T. Fraser and A. S. Pine, *J. Chem. Phys* **85**, 2502 (1986).

35. C. M. Lovejoy, M. D. Schuder and D. J. Nesbitt, *J. Chem. Phys* **85**, 4890 (1986).

36. D. Ray, R. L. Robinson, D. Gwo, and R. J. Saykally, *J. Chem. Phys* **84**, 1171 (1986); R. L. Robinson, D. Gwo, D. Ray, and R. J. Saykally, *J. Chem. Phys* **86**, 5211 (1987).

37. P. F. Vohralik, R. E. Miller, and R. O. Watts, *J. Chem. Phys.* **90**, 2182 (1989).

38. W. D. Held, E. Piper, G. Ringer, and J. P. Toennies, *Chem. Phys. Lett.* **75**, 260 (1980).

39. C. V. Boughton, R. E. Miller, P. F. Vohralik, and R. O. Watts, *Mol. Phys.* **58**, 827 (1986).

40. J. M. Farrar and Y. T. Lee, *Chem. Phys. Lett.* **26**, 428 (1974).

41. U. Buck and P. McGuire, *Chem. Phys.* **16**, 101 (1976); U. Buck and J. Schleusener, *J. Chem. Phys.* **75**, 481 (1981).

42. C. H. Becker, P. W. Tiedemann, J. J. Valentini, Y. T. Lee, and R. B. Walker, *J. Chem. Phys.* **71**, 481 (1979).

43. L. J. Rawluk, Y. B. Fan, Y. Apelblat, and M. Keil, *J. Chem. Phys.* **94**, 4205 (1991).

44. J. M. Hutson, *J. Chem. Phys.* **96**, 6752 (1992).

45. G. Herzberg, *Spectra of Diatomic Molecules* (Van Nostrand Reinhold Company, New York, 1950), pp. 536 - 537.

46. B. Vodar and H. Vu, *J. Quant. Spectrosc. Rad. Trans.* **3**, 397 (1963).

47. J. M. Hutson and B. J. Howard, *Mol. Phys.* **45**, 791 (1982).

48. Z. S. Huang, K. W. Jucks and R. E. Miller, *J. Chem. Phys.* **85**, 6905 (1986).

49. C. M. Lovejoy, and D. J. Nesbitt, *J. Chem. Phys.* **91**, 2790 (1989).

50. D. J. Nesbitt, M. S. Child, and D. C. Clary, *J. Chem. Phys.* **90**, 4855 (1989).

51. M. A. Dvorak, S. W. Reeve, W. A. Burns, A. Grushow, and K. R. Leopold, *Chem. Phys. Lett.* **185**, 399 (1991).

52. J. T. Farrell, Jr., O. Sneh, A. E. W. Knight, and D. J. Nesbitt, (unpublished).

53. C. M. Lovejoy, T. G. Lindeman and D. J. Nesbitt, (unpublished).

54. J. A. Barnes, M. Keil, R. E. Kutina and J. C. Polanyi, *J. Chem. Phys.* **76**, 913 (1982).

55. C. A. Taatjes, and S. R. Leone, *J. Chem. Phys.* **89**, 302 (1988); *J. Chem. Phys.* **95**, 5870 (1991)

56. T. A. Wiggins, N. C. Griffen, E. M. Arlin and D. L. Kersteffer, *J. Mol. Spectrosc.* **36**, 77 (1970).

57. A. S. Pine, *J. Mol. Spectrosc.* **82**, 435 (1980).

58. W. Kolos, G. Corongiu and E. Clementi, *Int. J. Quantum Chem.* **17**, 775 (1980).

59. H.-J. Werner and W. Meyer, *Mol. Phys.* **31**, 855 (1976).

60. R. D. Amos, *Chem. Phys. Lett.* **88**, 89 (1982).

61. C. Douketis, J. M. Hutson, B. J. Orr, and G. Scoles, *Mol. Phys.* **52**, 763 (1984).

62. S.-Y. Liu and C. E. Dykstra, *J. Chem. Phys.* **90**, 3097 (1986).

63. A. Kumar and W. Meath, *Mol. Phys.* **54**, 823 (1985).

64. A. Kumar and W. Meath, *Can. J. Chem.* **63**, 1616 (1985).

65. I. N. Levine, *Quantum Chemistry* (Allyn and Bacon, Inc., Toronto, Ontario, 1983), Chapter 6.

66. R. N. Zare, *Angular Momentum* (John Wiley and Sons, Toronto, Ontario, 1988), pp. 23-41.

67. R. D. Levine and R. B. Bernstein, *Molecular Reaction Dynamics* (Oxford University Press, New York, 1974).

68. A. M. Arthurs and A. Dalgarno, *Proc. Roy. Soc. (London Series)* **A256**, 540 (1960).

69. Note the different notation for the Clebsch-Gordon coefficients used in reference 68 versus that in reference 73.

70. R. Schinke and J. M. Bowman, *Molecular Collision Dynamics*, ed. by J. M. Bowman (Springer-Verlag, Berlin, 1982), Chapter 4.

71. D. Secrest, *J. Chem. Phys* **62**, 710 (1975).

72. L. W. Hunter, *J. Chem. Phys* **62**, 2855 (1975).

73. G. A. Parker and R. T Pack, *J. Chem. Phys.* **68**, 1585 (1978).

74. D. Secrest, *Atom-Molecule Collision Theory: A Guide for the Experimentalist*, ed. by R.B. Bernstein (Plenum, New York, 1979), Chapter 8.

CHAPTER 2

USE OF A CHEMICAL LASER FOR MOLECULAR BEAM SCATTERING EXPERIMENTS†

2.1 INTRODUCTION

Lasers have become ubiquitous in their marriage with molecular beam techniques as applied to spectroscopic studies and internal quantum state-specific scattering.[1] Studies involving the ground electronic state exclusively have used optical pumping,[2–4] F-center[5,6] and frequency difference lasers,[7] all of which are continuously tunable. Line tunable molecular lasers have also been applied to scattering studies. Despite their inflexibility, these lasers naturally overlap spectrally with the scattering partner to be studied and are often quite powerful. In particular, the HF chemical laser has been used for studying enhanced chemical reactivity due to vibrational excitation[8] and to rotation and reactant orientation,[9] as well as rotationally inelastic scattering.[10] These experiments have been restricted to exciting HF gas clouds or poorly collimated beams. However, measuring rotationally inelastic differential cross sections (DCS) requires highly collimated molecular beams[2,3,11,12] and hence better spectral overlap due to sub-Doppler absorption profiles. Our interest in measuring scattering intensity as a function of scattering angle and rotational state is to help determine intermolecular potential energy functions, especially for systems exhibiting substantial attractive wells.[13]

This paper describes application of a cw HF chemical laser for preliminary DCS measurements in rotationally inelastic HF+Ar scattering. The laser is described, with special attention devoted to the achievement of single-line operation

† A version of this chapter has been published.
L.J.Rawluk and M. Keil *J. Opt. Soc. Am. B* **6**, 1278 (1989).

for some R-branch transitions useful in these studies. Signal intensities and spectral linewidths for single-mode and multi-mode laser interactions with the molecular beam are compared. We also discuss locking the laser output to the intra-cavity Lamb dip, thus closely matching the molecular beam absorption peak. Finally, we present some preliminary inelastic scattering measurements as an example showing the laser's utility for rotationally inelastic DCS experiments.

2.2 APPARATUS

The laser used in this study is similar in many respects to other subsonic cw chemical lasers described in the literature.[14–17] Figure 2.1 depicts the laser and molecular beams system. Fluorine atoms are produced in a 2450 MHz microwave discharge by flowing SF_6 and He (15 and 600 atm-cm^3/sec respectively) through an air-cooled alumina tube. The magnetron (Hitachi M57D11) delivers 1200 W of microwave energy from a highly regulated 4 kV power supply. Hydrogen (300 atm-cm^3/sec) is injected perpendicular to the flow through a row of 62 0.5 mm diameter holes drilled along the top and bottom of the flow channel, which is 4 mm high by 115 mm wide. With all gases flowing, the pressure in the mixing region is 5.5 Torr, maintained by a 165 ℓ/sec Roots pump backed by a 60 ℓ/sec mechanical pump (Leybold-Heraeus WAU500 and S160C, respectively). Brewster-angle CaF_2 windows are mounted 5 mm downstream of the H_2 injection flow. A He purge flow (20 atm-cm^3/sec) is used to sweep out any deactivated HF trapped behind these windows. Without this flow, $\nu = 1 \rightarrow 0$ laser transitions are completely absent for $j \leq 5$.

The optical cavity consists of a plane diffraction grating mounted in the first-order Littrow configuration, and a ZnSe output coupler with a 3 m radius of curvature. The grating (Bausch and Lomb) has 300 lines/mm with a blaze angle of 22.2°, and is gold-coated. The output coupler (Two-Six) is coated for 90% reflectance at 2.7 μm, dropping to 87% at 2.43 and 2.91 μm. These optics are held by adjustable mirror mounts (Newport 600A-3), separated by three invar rods mounted to a pneumatic table (Newport GS-34). The table also holds all the extra-cavity optics, but it does not touch the laser mixing channel, mechanical pumps, or microwave generator. The cavity length is kept as short as possible (26 cm) to prevent multiple longitudinal modes from lasing. The cavity length may be adjusted by a piezo-electric translator (PZT) which can also provide active stabilization (Lansing

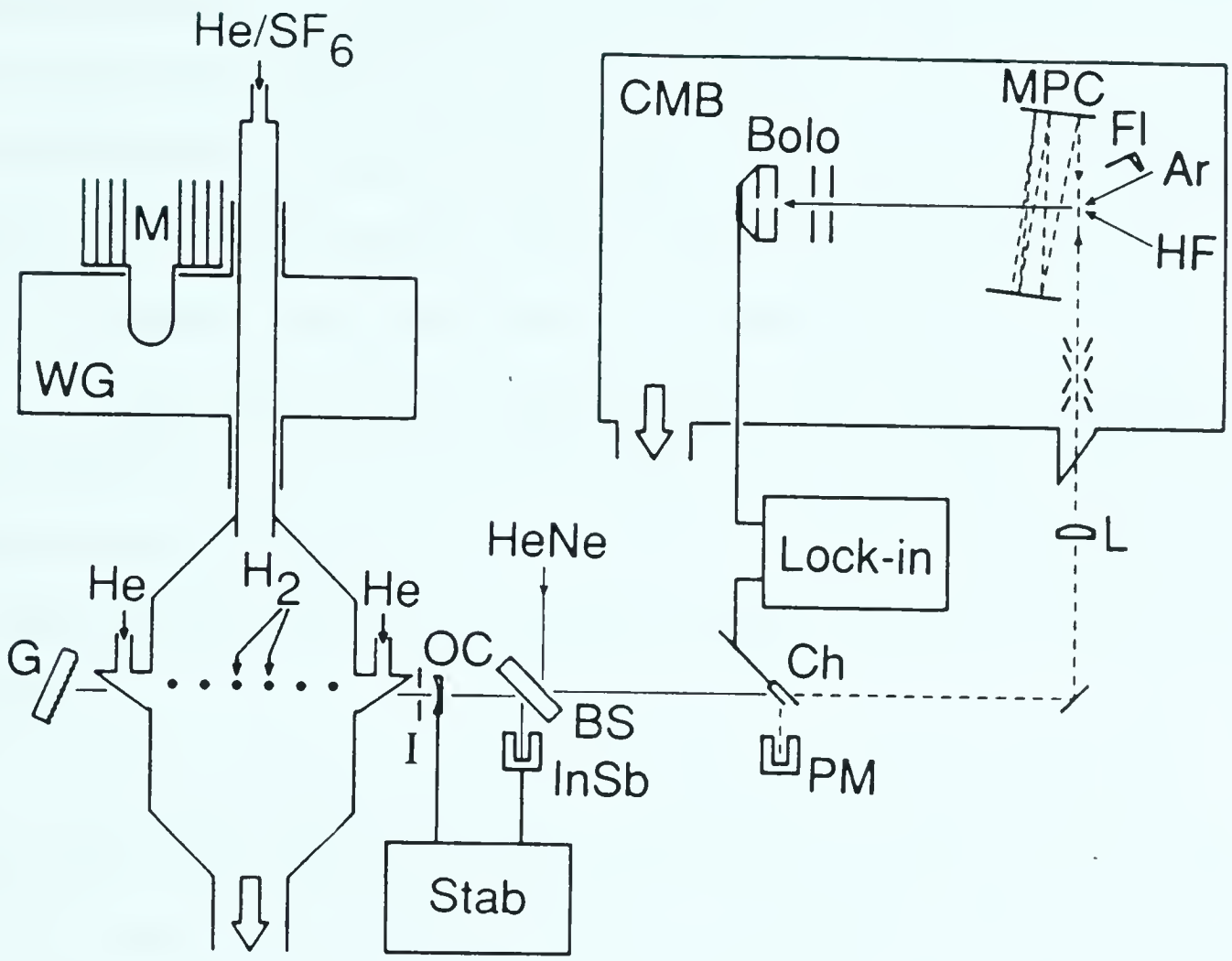

Figure 2.1: Schematic diagram of the cw HF chemical laser and crossed molecular beams apparatus (not to scale). The microwave energy generated by magnetron M is coupled into the He/SF_6 mixture via waveguide WG. The optical cavity is provided by grating G and output coupler OC mounted on a PZT driven by the stabilizer Stab. Transverse mode structure is controlled by intra-cavity iris I. The laser output is combined with a tracer beam at BS, which also provides stabilizer feedback via detector InSb. The beam is chopped at Ch for synchronous lock-in detection. Laser power is monitored by reflection from the chopper at power meter PM and is collimated at lens L before entering the crossed molecular beams (CMB) apparatus. The top mirror of the rotatable multiple-pass cell (MPC) may be adjusted externally for 12 passes (shown), or for direct reflection of the laser perpendicular to the plane formed by the supersonic HF and Ar molecular beams. The Ar beam is flagged at Fl to correct for background HF and scattered laser light contributions. Vibrational excitation induced by the laser is detected as heat by the bolometer, Bolo. Rotational state specific DCS's are measured by line-tuning G to the desired j' while rotating Bolo and MPC to a selected scattering angle θ.

80-214). The laser output is collimated by a 1 m focal length CaF_2 plano-convex lens located 1.05 m from the output coupler. Laser power reflected from a 40 Hz tuning fork chopper is measured by a thermopile (Ophir); faster response is achieved by an InSb detector at 77 K (Infrared Associates). The chopped laser is directed into a crossed molecular beams apparatus, using a CaF_2 Brewster-angle window and conical baffles to suppress scattered light. The entire path from the output coupler to the evacuated molecular beams chamber can be purged with dry N_2 to prevent attenuation of some laser lines due to water absorption.

The crossed molecular beams apparatus, which has been described elsewhere in elastic scattering experiments[18] consists of two independent, differentially pumped supersonic beam sources for HF and Ar. The HF beam is operated neat at a nozzle pressure of 300 Torr. The nozzle is heated to 580 K to suppress dimer formation.

The translational distribution of the HF beam is characterized by a velocity FWHM of 22%, although the nozzle conditions are not fully optimized. Rotational state populations are estimated from measurements with the laser operating multi-mode. Higher-gain laser lines attain higher power, but contain higher-order modes within a laser beam that is then physically larger. The power density is thus roughly similar, and corrections have not been made to the measured signals. Likewise, we have not yet attempted to correct our measured signals for possible saturation effects. The measured $j = 1 : 2 : 3 = 1.00 : 0.25 : 0.12$ distribution for the incident molecular beam should therefore be regarded only as an approximation of the initial rotational state distribution. The scattering measurements are unaffected by these approximations however, since we do not attempt comparisons between different scattered rotational states.

The Ar beam is optimized for intensity and narrow velocity distribution.[18] Both beams are angularly collimated to 4° FWHM and intersect at a point

on the rotation axis of a bolometer detector (Infrared Laboratories). The bolometer is a thermal detector with a specified noise-equivalent power of $10^{-14}\,\mathrm{W}/\sqrt{\mathrm{Hz}}$ and a time constant of $\sim$ 15 msec. Scattered and background HF in one specific (ν, j) state absorb the modulated laser beam and impinge upon the bolometer to produce a synchronous signal.[19] Scattered laser light contributes coincidentally to the bolometer signal. The scattered light and background HF signals are subtracted by periodically flagging the Ar beam. By rotating the bolometer and tuning the diffraction grating, we measure rotational state-specific DCS's for scattering of HF by Ar.

2.3 RESULTS

2.3.A R-Branch Lasing

Due to the high pressure present in most cw chemical lasers, the vib-rotational population inversion attained is incomplete, and only P-branch emission is observed.[14–17] This implies that scattered HF in $j' = 0$ would be undetectable; indeed most cw HF lasers have little usable output even for $j' = 1$.[20] R-branch lasing has been observed in a study using specially coated mirrors, but without line-selectivity.[21] Figure 2.2 displays our measured single-line power output as the diffraction grating is tuned across the HF laser emission. We have observed strong $R_1(0)$ and $R_1(1)$ lasing, with weaker $j = 2, 3$ lines. Though not evident from Figure 2.2, weak R_2 lines for $j = 0 - 3$ can also be seen when overlapping P_1 lines are eliminated by turning off the He window purge. This demonstration of R-branch lasing shows directly the presence of a "complete" inversion in our laser.[21,22]

Since our pumping speed is not dramatically higher than other laboratory cw lasers, it is possible that most of these devices actually do achieve complete population inversion. We have noticed however, that these R-branch lines are very sensitive to gas flows, and the R_1 lines are easily lost if the optics become too transmissive for wavelengths less than 2.5 μm. We note that the R_1 lines occur at wavelengths unaffected by water absorption.

The present chemical laser has output powers sufficient to probe $j' = 0$ through to $j' = 7$. The $j' = 1, 2$ states may be probed both by P- and R-branch emissions. This may make it possible for the laser to probe non-statistical m_j distributions produced by rotationally inelastic scattering,[23,24] since the plane-polarized laser output implies a spectral selection rule of $\Delta m_j = 0$.

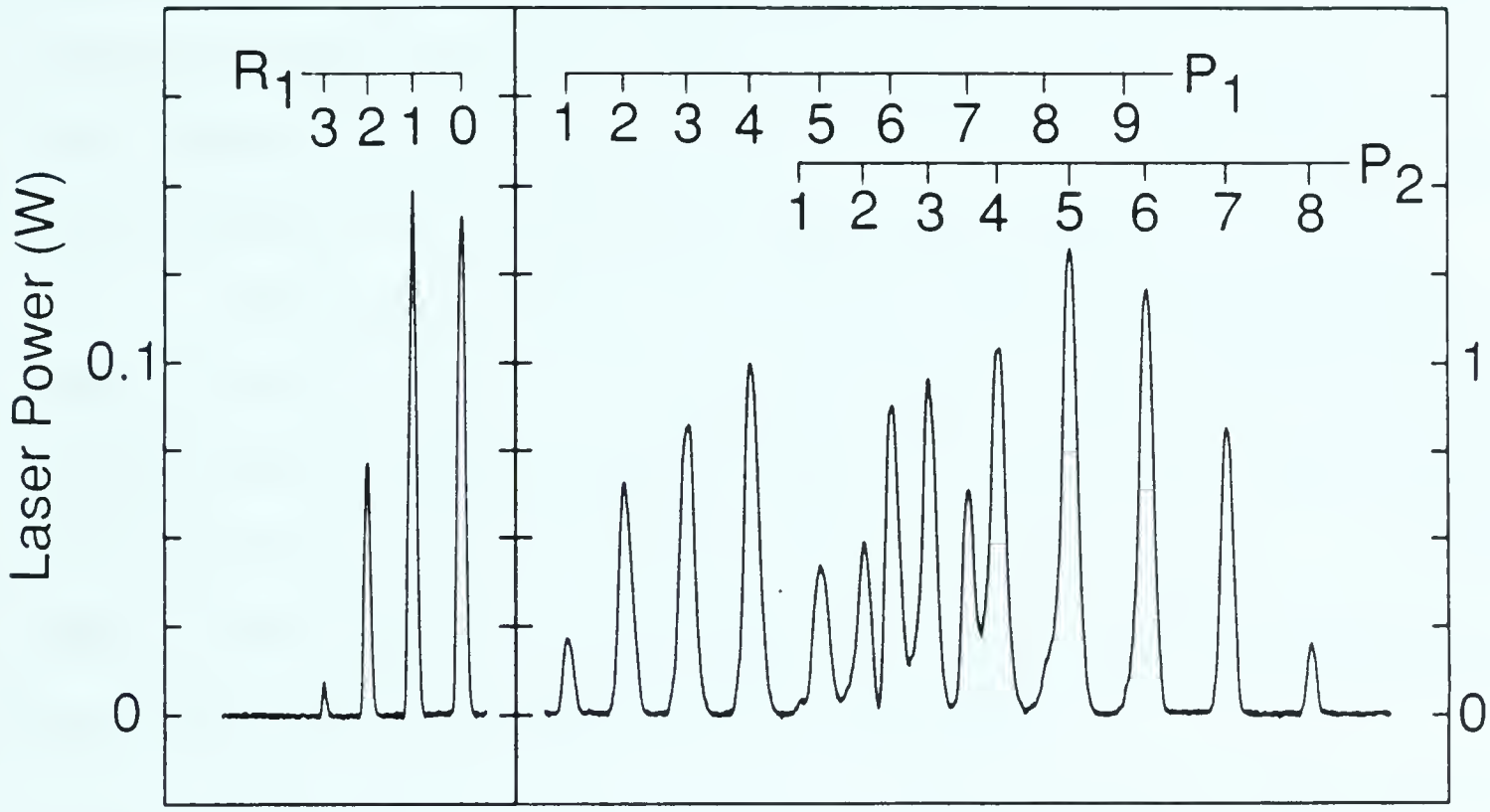

Figure 2.2: Multi-mode laser power obtained as the intra-cavity grating is rotated while the output coupler PZT is scanned rapidly. Note the vertical scale change between the R_1 and P_1 branches. The $P_1(8)$ and $P_1(9)$ transitions appear only as weak shoulders and are not usable with the present diffraction grating resolution.

2.3.B Spectral Overlap

Spectroscopic requirements for high resolution are often incompatible with scattering requirements for high signal intensity and stabilty. Our current focus is on the latter requirements and we make no attempt to match some very high resolution HF lasers.[17] Moderately high resolution can easily be attained by adjusting the intra-cavity iris for TEM_{00} operation (confirmed by guassian spatial scans). Figure 2.3 shows the consequent appearance of a strong and stable Lamb dip, coinciding with the molecular beam absorption maximum.

The measured absorption width from Figure 2.3(c) is ~30 MHz, resulting at least partially from the bolometer's slow response relative to the PZT scan rate. Slower scans yield measured widths of ~15 MHz. This is slightly broader than the sub-Doppler molecular beam absorption breadth of 10 MHz, calculated for single-pass MPC alignment and HF originating from the nozzle. The unstabilized laser therefore has a single-mode linewidth of $\widetilde{<}$15 MHz.

The presence of a strong Lamb dip (Figure 2.3) should permit active stabilization of the laser to the molecular beam absorption maximum. This has been achieved for the relatively weak $R_1(0)$ and $P_1(1)$ lines for various periods ranging up to 1 hr. Such long stabilization periods are necessary for the scattering experiments, which require long signal integration times (~20 min).

Unfortunately, higher-gain laser lines tend to oscillate on higher-order transverse modes. Repression of these higher-order modes by stopping down the intra-cavity iris results in severe diffraction losses for the TEM_{00} mode, and only ~20 mW of single-mode power can be obtained for the high-gain $P_1(4)$ line. This results in a weak and unstable Lamb dip, prohibiting long-term measurements for the molecular beam absorption. Lowering the microwave discharge current reduces the laser gain, and we are able thereby to recover strong Lamb dips and ~100 mW of single-mode power even for the $P_1(4)$ line. This is not completely satisfactory

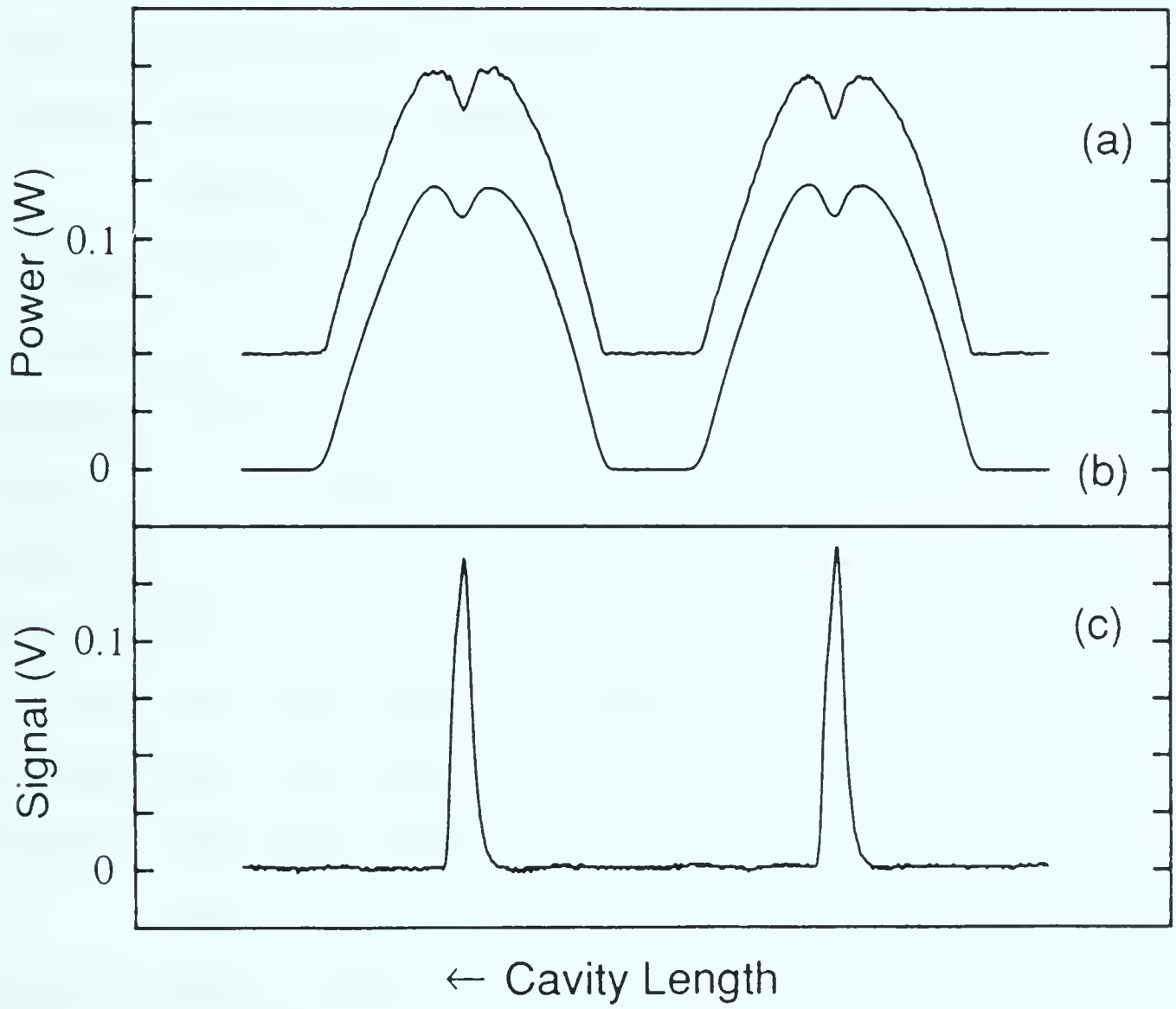

Figure 2.3: The top traces show single-mode laser power for the $R_1(0)$ line obtained as the PZT is scanned through two successive longitudinal modes. These two modes correspond to a measured PZT displacement of 1.22 μm, compared to the empty-cavity movement of $\lambda/2 = 1.25\mu$m (free spectral range = 580 MHz). The output shown in (a) is a single sweep displaced upwards by 50 mW. Trace (b) shows an average of 20 sweeps taken over 15 sec and shows good stability of the intra-cavity Lamb dip. Trace (c) shows the bolometer signal corresponding to the molecular beam absorption.

however, because the microwave discharge loses stability and we still cannot achieve long-term locking to the Lamb dip.

Active stabilization to the Lamb dip for selected spectral lines with moderate powers (~100 mW) yields strong molecular beam signals, but for periods too short for the scattering experiments. On the other hand, passive stabilization results in laser frequency drift sufficient to render signal intensities highly unstable. At the present time, we have therefore had to degrade the laser resolution in order to achieve acceptable signal stability.

Optimum use of the present laser for scattering experiments relies on maximum possible excitation (ideally saturation) of as large a spatial fraction of the scattered molecular beam as possible. Since resolvable DCS structure for HF+Ar scattering will likely be limited to rainbow features,[25,26] the desired angular resolution need not be better than ~5°. Under these low resolution conditions, the Doppler width of *ca* 35 MHz (for HF originating from the scattering centre) is broader than the unstabilized laser linewidth determined above. The high-resolution laser then cannot excite molecules diverging more than 1° or so above or below the scattering plane. The signal obtained would be lower than if all the scattered molecules could interact with the laser.

More intense signals can be achieved by allowing several different laser frequencies to oscillate simultaneously, each exciting distinct Doppler-shifted "sheets" of molecules lying above or below the scattering plane. An even larger spatial fraction of the molecular beam can be excited by adjusting the MPC for 12 reflections through the scattered molecular beam. Ten of these crossings are non-orthogonal, by up to 6° (Figure 2.1).

Higher-order transverse modes achieve oscillation by opening up the intra-cavity iris. Their appearance can be seen by tuning the laser wavelength across the molecular beam absorption using a single-pass MPC alignment. Up to

6 transverse modes can be seen in Figure 2.4(c) even for the relatively low-gain $R_1(0)$ line. The observed spacing of ~ 50 MHz agrees well with the 55 MHz spacing calculated for our optical cavity. The presence of these higher-order modes washes out the much narrower Lamb dip [Figure 2.4(a)], prohibiting active stabilization at the molecular beam absorption maximum.

Using the MPC with 12 passes further congests the multi-mode absorption lines with 10 discrete Doppler shifts up to ± 70 MHz. The results presented in Figure 2.4 show an almost continuous series of absorption lines. Since the lines are so closely spaced, the PZT may be scanned more rapidly than the bolometer time constant. The resulting integrated signal has about the same intensity as that achieved with the stabilized laser, with the advantage of being stable over an indefinite period.

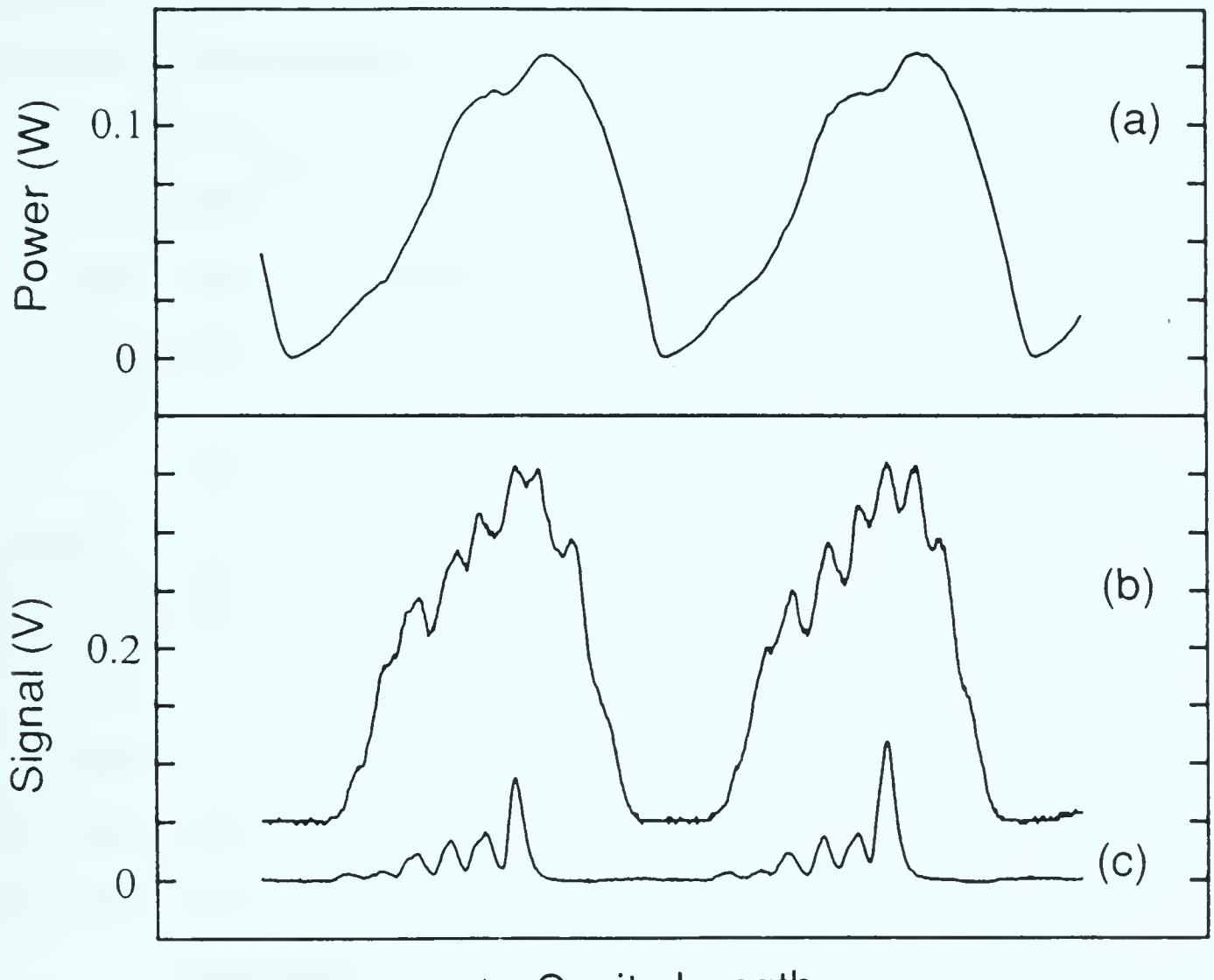

Figure 2.4: Trace (a) shows multi-mode laser power for the $R_1(0)$ line, as in Figure 2.3(b). The bolometer signal shown in (b) is obtained when the MPC is adjusted for 12 crossings, while (c) shows the bolometer signal for a single (orthogonal) laser/beam crossing. Trace (b) is displaced upwards by 50 mV.

2.3.C Inelastic Differential Cross Sections

Choosing between the two modes of operation presented in Figures 2.3 and 2.4 depends on resolution and signal-to-noise considerations. Thus far, it has been difficult for us to stabilize the high-gain laser lines [$P_1(3)$ to $P_1(6)$] for the long signal integration times required (~20 min). Furthermore, we do not yet need the angular resolution afforded by the high-resolution laser. The preliminary scattering data therefore were taken with the laser operated multi-mode, and with 12 passes through the MPC. Unfortunately, the low-resolution laser results in larger scattered light signals due to the physically larger multi-mode laser beam and scattering from the MPC mirrors. A second disadvantage is that each laser line has a different mode structure and size, complicating comparisons amongst rotational states.

The preliminary DCS data presented in Figure 2.5 for each scattered rotational state are normalized independently at 10°. The scattering data shows excellent reproducibility, especially for $j' = 2$ where the DCS was measured in 3 independent runs. Uncertainty in laser mode structure and its corresponding wavelength distribution have no effect on the scattering measurements as presented, since the measurements are normalized only for angular distributions and not between laser lines. The same is true of saturation effects.

Typical differential scattering patterns for light systems (e.g., involving He) exhibit quantum "diffraction" oscillations,[18] while semi-classical "rainbow" oscillations dominate DCS's for heavier systems (e.g., Ar+Kr, Ar+Xe).[27] Both types of oscillations can be seen for systems of intermediate reduced mass (e.g., Ne+Ar), but this requires very high angular and energy resolution and has been achieved only for atom-atom systems.[28]

The rotational state-specific results displayed in Figure 2.5 show the broad rainbow structure generally expected for systems of intermediate reduced mass and low angular and velocity resolution. These experimental results are compared to a calculated "total" DCS (i.e., unresolved elastic plus inelastic scattering)

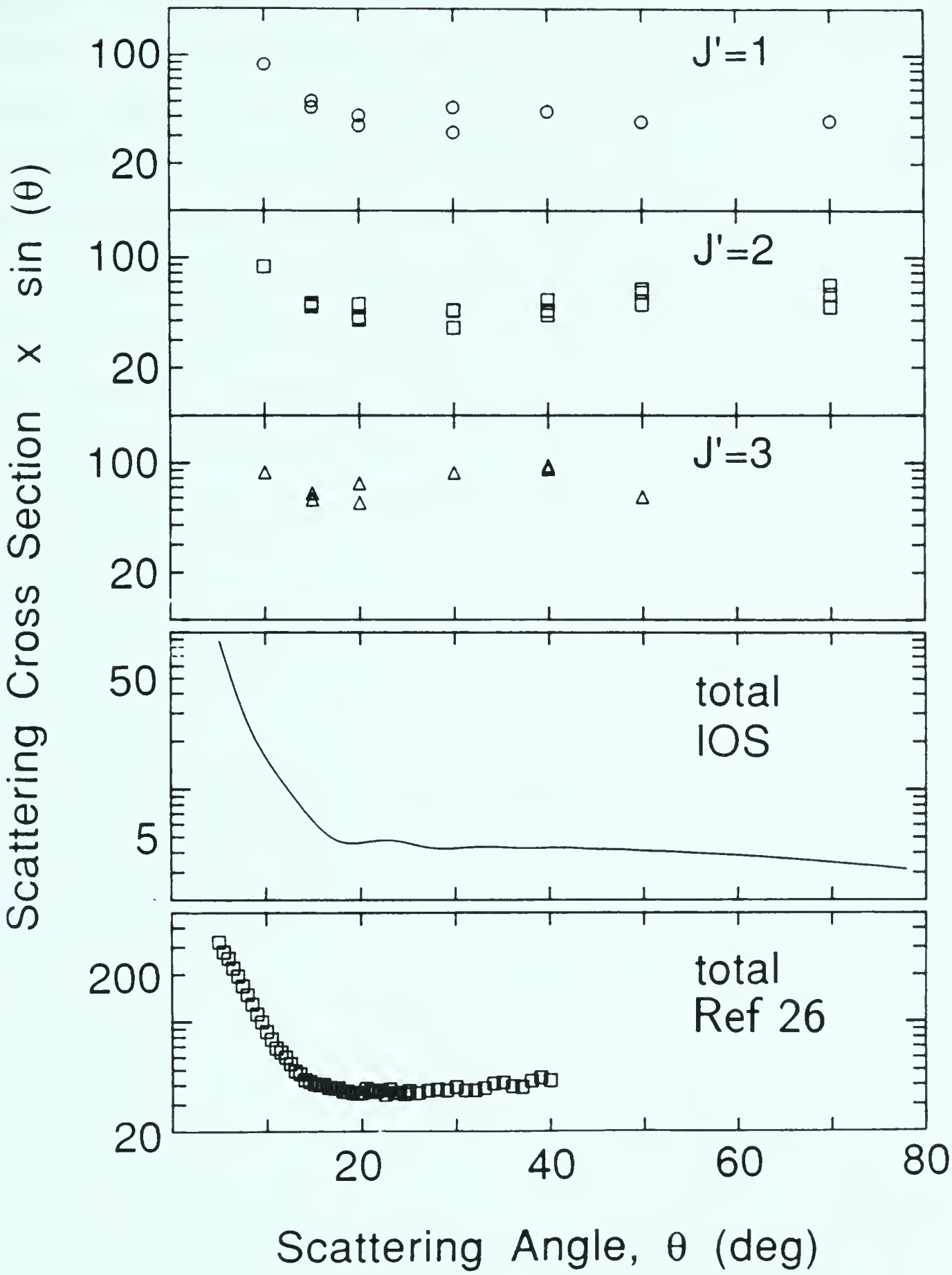

Figure 2.5: Measured inelastic DCS results for $j' = 1, 2, 3$, and the corresponding "total" DCS calculated from a fitted potential energy surface (Ref 29) and the infinite-order sudden approximation (which provides only a qualitative guide; see Ref 30). The lowest frame shows a "total" DCS measured under conditions similar to ours (Ref 26). The experimental cross sections are each normalized to 500 at θ=10°; the IOS calculation is given in units of $Å^2$/sr.

in Figure 2.5. The potential energy surface used in this calculation is most accurate for the attractive well region,[29] especially for the minimum-energy Ar···H—F orientation. Figure 2.5 also shows very recent experimental measurements of the "total" DCS rainbow structure for beam conditions similar to our own.[26] This DCS rainbow structure depends rather sensitively upon the HF+Ar attractive well.

A feature of the preliminary measurements presented in Figure 2.5, unavailable from the rotationally unresolved results, is the increasingly prominent rainbow structure as j' is increased. These results likely depend sensitively upon the shape of the repulsive wall region,[13] which is not yet well characterized for this system. Our preliminary state-resolved measurements, for a system with a reasonably strong attractive well, therefore complement detailed observations of rainbow structures for systems with very weak attractive interactions.[2,3]

Our current efforts aim to optimize the state-specific measurements and to extend them over more j' states in order to more clearly discern the rainbow behaviour. Although we do not intend to analyze the preliminary data, we believe that forthcoming results will be useful in determining the anisotropy of the attractive well and repulsive wall regions of the HF+Ar potential energy surface.

2.4 SUMMARY

We have described a laser capable of producing relatively high output powers for single-line operation in the 2.4-2.5 μm R_1 region of the HF chemical laser. These lines show strong Lamb dips, allowing long-term active frequency stabilization. High-order transverse modes present in higher-gain lines wash out the Lamb dip, and we have not yet used active stabilization for our scattering studies. Preliminary state-specific scattering measurements with excellent reproducibility are presented, showing rainbow structure that evidently becomes more pronounced for higher scattered rotational states. These data provide preliminary results for HF+Ar scattering, governed by a significantly attractive potential energy surface that may show a transition from "elastic" to "rotational" rainbows with increasing j'.[13]

Future prospects include enabling active stabilization for the higher-gain laser lines. We would then be able to dispense with the rotating MPC, much reducing scattered light. Unfortunately, this may also reduce the signal intensity. Higher collision energies and other scattering partners will be investigated, including inelastic scattering for chemically-bonded species.

REFERENCES:

1. See for example, R.D.Levine and R.B.Bernstein, *"Molecular Reaction Dynamics and Chemical Reactivity,"* Oxford University Press (1987).
2. K.Bergmann, U.Hefter, and J.Witt, *J.Chem.Phys.* **72**, 4777 (1980); E.Gottwald, A.Matthews, and K.Bergmann, *J.Chem.Phys.* **84**, 756 (1986).
3. J.A.Serri, A.Morales, W.Moskowitz, D.E.Pritchard, C.H.Becker, and J.L. Kinsey, *J.Chem.Phys.* **72**, 6304 (1980); W.P.Moskowitz, B.Stewart, R.M.Bilotta, J.L.Kinsey, and D.E.Pritchard, *J.Chem.Phys.* **80**, 5496 (1984).
4. M.Fuchs and J.P.Toennies, *J.Chem.Phys.* **85**, 7062 (1986); H.G.Rubahn and J.P.Toennies, *J.Chem.Phys.* **89**, 287 (1988).
5. Z.S.Huang, K.W.Jucks, and R.E.Miller, *J.Chem.Phys.* **85**, 3338 (1986).
6. C.-K.Man and R.C.Estler, *J.Chem.Phys.* **75**, 2779 (1981); M. Hoffmeister, R.Schleysing, and H.J.Loesch, Book of Abstracts, *1987 Conference on the Dynamics of Molecular Collisions,* page RE14.
7. C.M.Lovejoy, D.D.Nelson, and D.J.Nesbitt, *J.Chem.Phys.* **87**, 5621 (1987).
8. A.Gupta, D.S.Perry, and R.N.Zare, *J.Chem.Phys.* **72**, 6250 (1980); A.Torres-Filho and J.G.Pruett, *J.Chem.Phys.* **72**, 6736 (1980).
9. Z.Karny, R.C.Estler, and R.N.Zare, *J.Chem.Phys.* **69**, 5199 (1978).
10. J.A.Barnes, M.Keil, R.E.Kutina, and J.C.Polanyi, *J.Chem.Phys.* **76**, 913 (1982).
11. M.Faubel, K.H.Kohl, and J.P.Toennies, *Faraday Disc.Chem.Soc.* **73**, 205 (1982).
12. U.Buck, H.Meyer, M.Tolle, and R.Schinke, *Chem.Phys.* **104**, 345 (1986).
13. H.R.Mayne and M.Keil, *J.Phys.Chem.* **88**, 883 (1984).
14. R.R.Stephens and T.A.Cool, *Rev.Sci.Inst.* **42**, 1489 (1971).
15. J.J.Hinchen, *J.Appl.Phys.* **45**, 1818 (1974); J.J.Hinchen and R.J.Freiburg, *Appl.Optics*, **15**, 459 (1976).
16. A.Tönnißen, J.Wanner, K.W.Rothe, and H.Walther, *Appl.Phys.* **18**, 297 (1979).
17. J.Munch, M.A.Kolpin, and J.Levine, *IEEE J.Quantum Elec.* **QE-14**, 17 (1978).

18. L.J.Danielson, K.M.McLeod, and M.Keil, *J.Chem.Phys.* **87**, 239 (1987); L.J.Danielson and M.Keil, *J.Chem.Phys.* **88**, 851 (1988).

19. T.E.Gough, R.E.Miller, and G.Scoles, *Appl.Phys.Lett.* **30**, 338 (1977).

20. See for example, specifications for the Helios Inc. "HF/DF MiniLaser".

21. H.Injeyan and J.H.S.Wang, *Optics Lett.* **8**, 172 (1983).

22. J.C.Polanyi, *J.Chem.Phys.* **34**, 347 (1961); J.C.Polanyi, *Chemica Scripta* **27**, 229 (1987).

23. M.Keil and H.R.Mayne, *Chem.Phys.Lett.* **85**, 456 (1982).

24. A.J.McCaffery, *Gas Kinet.Energy Transfer* **4**, 47 (1980).

25. C.H.Becker, P.W.Tiedemann, J.J.Valentini, and Y.T.Lee, *J.Chem.Phys.* **71**, 481 (1979).

26. P.H.Vohralik, R.E.Miller, and R.O.Watts, *J.Chem.Phys.* **90**, 2182 (1989).

27. R.T Pack, J.J.Valentini, C.H.Becker, R.J.Buss, and Y.T.Lee, *J.Chem.Phys.* **77**, 5475 (1982).

28. L.Beneventi, P.Casavecchia, and G.G.Volpi, *J.Chem.Phys.* **84**, 4828 (1986).

29. J.M.Hutson and B.J.Howard, *Mol.Phys.* **45**, 791 (1982).

30. G.A.Parker and R.T Pack, *J.Chem.Phys.* **68**, 1585 (1978).

CHAPTER 3

EFFECT OF VELOCITY ON SATURATION BEHAVIOUR FOR HF MOLECULAR BEAMS†

3.1 INTRODUCTION

This study was motivated by our desire to measure population distributions for HF molecules after rotationally inelastic collisions. Such measurements typically use direct laser-based probes[1] such as laser-induced fluorescence or multi-photon ionization. Indirect probes, based on measurements of post-collision kinetic energy and then invoking conservation of total energy, have also been very successful.[2] The latter typically require a very high kinetic energy resolution that is often difficult to achieve. Conversely, the former techniques require well-characterized electronic transitions, which are very difficult to access for the hydrogen halides that we are studying.[3]

The choice of HF for the present study is dictated by our use of an HF chemical laser. More generally, atom–hydrogen halide systems are particularly interesting due to their strongly attractive and highly anisotropic interactions.[4] Investigations of bound states of atom–HF interactions have become very detailed, including use of radio-frequency and microwave spectroscopy,[5–7] and infrared spectroscopy.[7–11] However, there are very few detailed (*i.e.,* simultaneous angular and rotational state resolution) scattering studies available for *any* system exhibiting strong attractive forces.[12] Integral and rotational unresolved differential scattering cross sections have been measured and analyzed to test intermolecular potentials and to investigate the dynamics of rotational energy transfer.[13–17] Many

† A version of this chapter has been published.
Y. B. Fan, L. J. Rawluk, Y. Apelblat, and M. Keil, *J. Opt. Soc. Am. B* **8**, 1218 (1991).

of these studies, for example total[13,14,16] or state-selected[17] differential cross section measurements, require the accurate determination of rotational population distributions.

Besides the visible- and UV-based laser detection techniques mentioned, another successful method for rotationally state-specific measurements uses the optothermal infrared spectroscopic technique.[18,19] This method, developed by Gough, Miller and Scoles,[18] is based on thermal detection—using a windowless bolometer—of the energy deposited into a molecular beam by an infrared laser. Since bolometers typically have rather slow time constants, this technique generally requires a cw laser.

Rotational relaxation in supersonic molecular beam expansions have been reported by many groups using this technique.[20–24] Due to the scarcity of suitable cw infrared lasers, these studies rely on tunable but low-power F–centre or diode lasers, or on spectral coincidences with line-tunable molecular lasers. Within the latter category, using an HF chemical laser to detect an HF molecular beam guarantees such coincidences to within the Doppler width of a free-running laser, without external fields often used to bring the molecular beam absorption into resonance with the laser emission line.[23,25]

For the low laser power typical of F–centre and diode lasers, the absorption signals are linear or nearly so,[21,26] and equations for converting bolometer signals into populations have been given by Bassi *et al.*[20] As the laser power is increased, saturation and coherence phenomena can occur which sometimes complicate extraction of rotational populations from measured signals. Several recent studies using molecular lasers with powers high enough to observe strong non-linear effects have focussed on very elegant observations of coherent excitation processes.[25] Also, strong saturation of the absorption signal was observed in a detailed study of the rotational relaxation of CH_3F, but no attempt was made to characterize this saturation behaviour.[23]

For the scattering studies being undertaken, we naturally wish to maximize the sensitivity of the laser+bolometer technique in measuring the very weak flux encountered. Fortunately, our spectral resolution is only what is required for good overlap between the laser emission and the molecular beam absorption. Thus, we aim for a régime avoiding coherent phenomena and the appearance of Rabi oscillations, whose understanding requires solution of the optical Bloch equations.[25] At the other extreme, incoherent phenomena yielding population inversion can also occur. In this case, the Bloch equations lead to a chaotic path,[27] rendering an accurate description very difficult. Nevertheless, such a description may not be appropriate for incoherent processes in which the absorption is saturated and the populations are balanced by spontaneous and stimulated emission. Perhaps the best way to describe such incoherent absorption is to use a phenomenological method, ignoring the complicated micro-dynamic process.[28]

Our approach in this paper is to use Einstein's spontaneous and stimulated emission coefficients to describe the absorption process. This rate equation approach has also appeared elsewhere,[28,29] though not in the context of bolometric detection of infrared transitions. We apply the rate equation to the present case of thermally detecting modulated laser absorption. Various limiting cases of laser power and interaction time with the molecules are discussed. We then demonstrate that our stabilized HF chemical laser generates enough power to fully saturate a sub-Doppler molecular beam absorption. We also present rotational state distribution measurments for HF supersonic beams generated under a wide range of nozzle expansion conditions. Finally, we comment on the sensitivity for HF actually attained by the current detection system.

3.2 EXPERIMENTAL

The saturation behaviour and rotational distributions were determined using a crossed molecular beams apparatus designed for measuring the angular dependence of scattering processes at thermal collision energies. This scattering apparatus has been described in previous publications presenting elastic[30,31] or rotationally inelastic[17] scattering results. Here we describe aspects directly related to determining the saturation behaviour and rotational distributions. The basic principle is founded upon the opto-thermal laser+bolometer technique developed by Gough, Miller, and Scoles:[18] an HF molecular beam impinging on a bolometer (thermal) detector gives up its kinetic and internal energy, which is seen as a dc signal. If a modulated laser beam excites some of the HF on its way to the bolometer, selective amplification of this ac component gives a direct measure of the excited population. Attenuating the laser power with neutral density filters then allows the saturation behaviour to be characterized, while tuning the laser frequency allows the rotational population distribution to be measured.

The HF supersonic molecular beam is generated by continuous expansion through a 100 μm–diameter Pt nozzle into a chamber evacuated by an unbaffled diffusion pump having a rated speed of 8000 litre/sec. The beam emerges into a differentially-pumped chamber through a 0.73 mm–diameter Ni skimmer. The pressure in this chamber is maintained below $\sim 5 \times 10^{-7}$ torr by a combination of diffusion- and liquid N_2 cryo-pumping. The molecular beam then passes through a non-collimating aperture prior to interacting with the laser used to label the HF rotational state. Internal energy excitation produced by the laser is then detected by a liquid He–cooled bolometer detector located directly in the path of the HF molecular beam. A schematic diagram of the apparatus is shown in Fig. 3.1. A second molecular beam, required for our scattering experiments, is not utilized in the present measurements and is not shown in the figure.

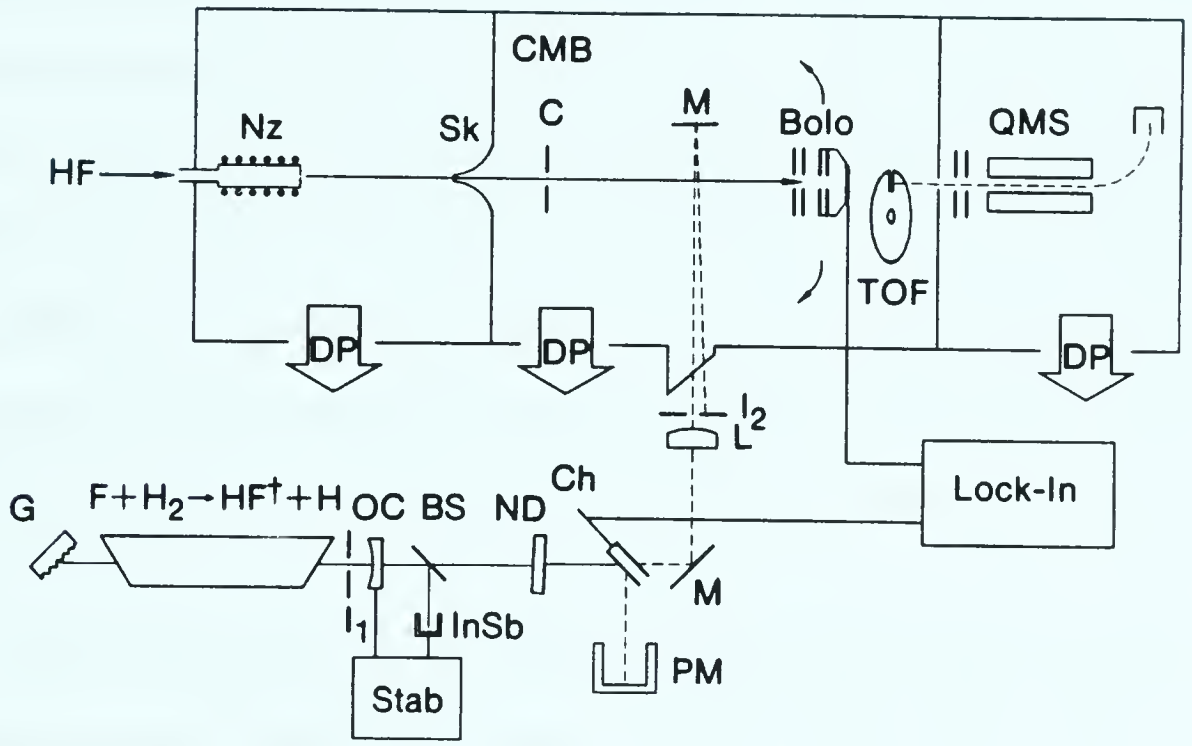

Figure 3.1: Schematic diagram of the apparatus (not to scale). Rotational state selectivity is provided by grating G, which forms an optical cavity with output coupler OC mounted on a piezo-electric translator driven by the stabilizer (Stab). Transverse mode structure is controlled by intra-cavity iris I_1. Feedback for the stabilizer is provided by beam-splitter BS and detector InSb. After attenuation by a neutral-density filter (ND), the laser is chopped at Ch for synchronous lock-in detection. Laser power is monitored by reflection from the chopper into power meter PM and is collimated by lens L. A second iris I_2 blocks optical feedback from the double-pass mirror M located within the crossed molecular beams (CMB) apparatus. The molecular beam is formed by expansion of HF through the heated nozzle Nz, skimmed at Sk, collimated at C, and detected by the bolometer Bolo. A time-of-flight chopper TOF, in conjunction with the mass spectrometer QMS, is used for beam characterizations only, for which the bolometer is rotated clear of the molecular beam.

The nozzle pressure for the HF beam is regulated by thermostatting liquid HF in a monel cylinder. For seeded beams, He is bubbled through the liquid and regulated by a mass flow controller. The nozzle is heated to 500°K to suppress HF dimer formation, though HF dimers are entirely transparent to the laser radiation. A mass spectrometer located downstream of the laser and bolometer monitors the HF beam with the bolometer rotated out of the way. The measured $\frac{m}{e} = 21 : 20$ ratio, indicative of dimer concentration, is kept below $\sim 5\%$ for all beam conditions used in these experiments, and is usually $< 3\%$. The beam velocity is measured using a time-of-flight chopper in conjunction with the mass spectrometer. A large nozzle–skimmer separation of 100 mm is used to avoid overloading the cryogenic bolometer, yielding a calculated beam angular divergence of 0.42°. Measurements with the molecular beam blocked inside the source chamber confirm that effusion of HF from the source chamber is insignificant, even for the highest rotational states examined.

The continuous-wave chemical laser used in this study has been described before in some detail.[32] It operates on the $F + H_2 \longrightarrow HF^\dagger + H$ reaction, where $HF^\dagger$ denotes vib-rotationally excited HF in the ground electronic state. Specific lasing frequencies in the $R_1(j)$– and $P_1(j)$–branches are selected by tuning an intra-cavity diffraction grating. Sub-Doppler linewidths are obtained by actively stabilizing the cavity length, whose feedback loop uses a prominent Lamb dip observed in the single-mode power dependence upon cavity length. To ensure a well-characterized interaction between the laser and molecular beams, we have removed the multiple-pass cell used in our earlier work. A single mirror now reflects the laser back upon itself for two perpendicular passes through the molecular beam. The mirror is slightly mis-aligned ($\sim 0.5°$) to eliminate optical feedback into the laser oscillator. We estimate the stabilized laser linewidth to be $\lesssim 15$ MHz,[32] which we can now maintain for the duration of an entire experiment (> 10 hr). As can

be seen from Fig. 3.1, the present stabilization scheme is considerably simpler for the line-tunable HF laser than for continuously-tunable colour-centre lasers in this wavelength region,[33] as well as providing more power. Conversely, the line tunability restricts the chemical laser to probing a severely limited number of molecules (*e.g.*, HF, DF and HCl).[34]

For most laser lines, an intra-cavity iris is essential for suppressing high-order mode structure, and for observing the Lamb dip. Besides ensuring constant power output and frequency linewidth, the Lamb-dip stabilization also ensures that the laser frequency is sufficiently close to line-centre for exciting the molecular beam. Slow scans across the laser gain profile verify that the stabilized laser frequency is optimized for interaction with the molecular beam (we do not observe double-peak profiles, thought indirectly to be due to beam clustering[22]). Spatial scans verify TEM_{00} operation of the stabilized laser. Laser powers $\gtrsim 100\,\mathrm{mW}$ invariably show multi-mode structure, and all measurements conducted here are below this limit.

The HF laser beam is interrupted mechanically at a frequency of 39.6 Hz by a tuning-fork chopper, which also provides the reference signal for a lock-in amplifier with which the modulated bolometer signal is detected. Power reflected from the chopper is used to monitor the laser intensity while simultaneously measuring the bolometer signal. After a distance of $\sim 2\,\mathrm{m}$ from the output coupler, the laser beam is admitted into the scattering chamber through a Brewster–angle window; scattered laser light is suppressed with baffles. Flushing the entire laser path with dry N_2 ensures that $\gtrsim 80\%$ of the laser power is transmitted to the intersection point of the laser and molecular beams. The laser is 1.9 mm in diameter at the intersection point ($\frac{1}{e}$ width), 160 mm downstream from the nozzle. The HF molecular beam at this point is calculated to be 1.2 mm in diameter, so that the laser intensity is roughly uniform over the full width of the molecular beam. The low divergence of the laser is accomplished by a collimating lens.

Vibrational excitation of the molecular beam from the ground state to $\nu = 1$ is detected by a cryogenic bolometer (composite Ge, Infrared Laboratories) intercepting the HF molecular beam 230 mm downstream from the nozzle. Rotational state selectivity is achieved since the laser is tuned to excite only one specific rotational state of $\nu = 0$. For the highest possible sensitivity required for our scattering experiments, we operate the bolometer at 1.5°K; for the present experiments, the on-beam flux is high enough that the bolometer may be operated at 4.2°K. The bolometer's specified noise-equivalent power is $10^{-14}\,\mathrm{W}/\sqrt{\mathrm{Hz}}$ at 1.5°K, but it is much less sensitive at 4.2°K (see also Sec. 3.4.C).

Two types of measurements are performed in this study. For examining the bolometer response as a function of laser beam intensity, we attenuate the laser with reflectance-type neutral-density filters (Melles-Griot) placed ahead of the power meter. These filters are placed after the Lamb-dip feedback loop so that the laser stabilization is not affected, but before the tuning-fork chopper so that the actual laser intensity is monitored. Beam conditions for conducting these saturation studies as a function of beam velocity are listed in Table 3.1

For measuring the HF molecular beam rotational distribution, we remove the filters and tune the diffraction grating to lase on successive $\mathrm{R}_1(j)$– and $\mathrm{P}_1(j)$–branch lines. The chemical laser has sufficient intensity only up to $j = 2$ in the R–branch,[32] though there is no such restriction for the P–branch. Since the experimental sensitivity slowly shifts due to the large HF flux impinging on the bolometer, we monitor the signal due to the $\mathrm{R}_1(0)$ laser line—with filters removed—as the reference to which the bolometer sensitivity is periodically normalized.

Table 3.1 HF Molecular Beam Conditions[a]

	Pure HF	Seeded HF
HF bath temperature (°C)	$+10.0\pm0.5$	-50 ± 1
Static HF vapour pressure (atm)	0.76	0.05
Nozzle diameter (mm)	0.10	0.10
Nozzle temperature (°K)	500 ± 10	500 ± 10
Nozzle pressure (atm)	0.74	5.7
Most probable velocity (km/sec)	1.21	2.11[b]
Velocity FWHM $\left(\frac{\Delta v}{v_{mp}}\right)$	0.21	0.10[b]
Relative intensity (arb. units)[c]	1.0	0.8

[a] Conditions selected as the best compromises—for pure and seeded beams—between intensity and velocity and rotational distributions. All measured entries are for optimized nozzle-skimmer separations.

[b] The He component has $\frac{\Delta v}{v_{mp}} = 0.13$ with no appreciable velocity slippage.

[c] Mass spectrometric signals at $\frac{m}{e} = 20$, uncorrected for HF beam velocity.

3.3 RATE EQUATION THEORY

The present experiments were designed for saturating the HF infrared absorption, rather than for very high-resolution spectral characterization of the infrared absorption process. For example, the residual Doppler width of the HF molecular beam, including the slight mis-alignmnent of the mirror used for double-passing the laser through the molecular beam, is $\sim 5 - 10\,\mathrm{MHz}$. Under these conditions, it is appropriate to use the rate equation approach[1,28] in examining the dependence of measured bolometer signals upon the laser power. We estimate that the strong-signal limit would be approached only for powers exceeding several hundred milliwatts, judging by the laser intensity required to yield Rabi oscillations for wavelengths 4× longer than ours.[25] The rate equation approach has also been applied to laser-induced fluorescence studies of electronic transitions using pulsed lasers.[29,35]

Due to the collision-free molecular-beam environment, the $\nu = 0, j \longrightarrow \nu = 1, j'$ laser pumping process can be treated as the isolated three-level system portrayed in Fig. 3.2.[29] This can be approximated as a two-level system if the $2 \longrightarrow 3$ spontaneous emission rate is much slower than the $2 \longrightarrow 1$ rate from induced and spontaneous emission. Although this assumption is not necessary for the treatment that follows, it will be validated in Sec. 3.4.A below for the long-lived infrared transitions being considered, given the short interaction time between the laser and molecular beam.

Ignoring laser polarization and molecular orientation effects,[29] the rate equation for the upper state is

$$\frac{dN_2(t)}{dt} = N_1(t)B_{12}\rho - N_2(t)(A_{21} + B_{21}\rho). \qquad (3-1)$$

Here we are using standard notation,[36] with $N_1(t)$ and $N_2(t)$ the time-dependent populations of the ground and excited states, respectively, and ρ the energy density

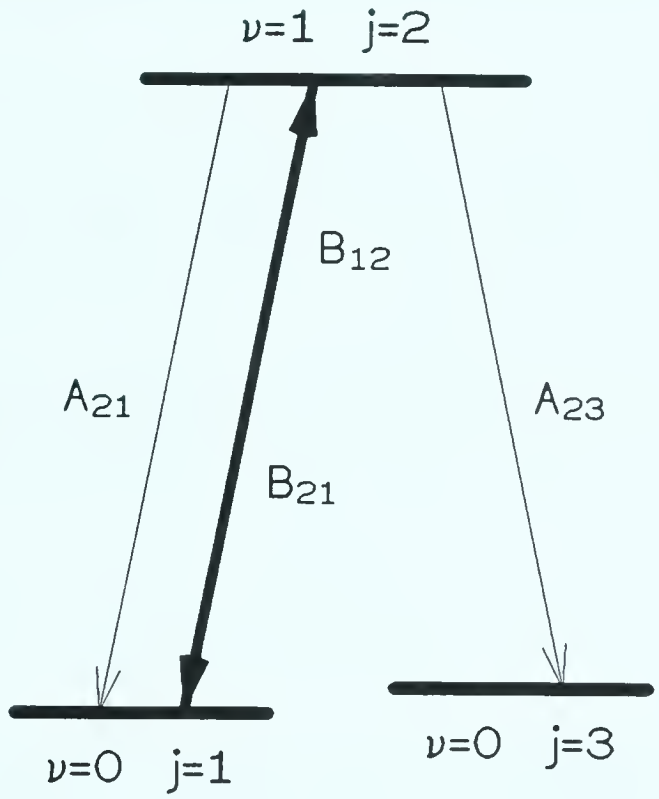

Figure 3.2: Isolated three-level system depicting laser-induced absorption, and stimulated and spontaneous emission. For convenience in labelling the states involved, the laser is tuned to the $R_1(1)$ line in this example. Under the present experimental conditions, the rate of $P_1(3)$ spontaneous emission accompanying the laser excitation is shown to be negligible (Sec. 3.4.A).

per unit frequency range of the radiation. The HF($\nu = 1, j'$) excited state is empty before interaction with the laser beam, so that $N_1(t) = N$ and $N_2(t) = 0$, where N is the total population. This yields the transient response function

$$N_2(t) = \frac{N B_{12} \rho}{A_{21} + (B_{21} + B_{12})\rho} \left[1 - e^{-[A_{21} + (B_{12} + B_{21})\rho]t}\right]. \qquad (3-2)$$

Note that the interaction time t in this treatment is the transit time of the molecular beam across the laser, while it is the laser pulse length in Altkorn and Zare's treatment.[29]

We now particularize this result for a bolometer detector, whose signal is proportional to the total energy content of the incident molecules. Modulating the laser, and assuming that all forms of the impinging molecules' energy are accomodated upon the cold bolometer surface independently of internal state, we obtain a lock-in signal proportional to the population promoted to the excited state,

$$S_{\text{bolo}} \propto N_2 \Delta E_{12}, \qquad (3-3)$$

where $\Delta E_{12} \equiv E_2 - E_1$ and E_1 and E_2 are the vib-rotational energy contents of the ground and excited states, respectively. This equation also assumes that the proportion of molecules accomodated on the bolometer surface again is independent of the internal energy state. Under such conditions, modulating the laser removes such constant terms as the kinetic energy and heats of adsorption and condensation. In the present case, the energy difference ΔE_{12} may be written approximately as

$$\Delta E_{12} \simeq \begin{cases} \omega_e - 2\omega_e x_e + 2B(j+1) & \text{(R–branch);} \\ \omega_e - 2\omega_e x_e - 2Bj & \text{(P–branch),} \end{cases} \qquad (3-4)$$

where j designates the rotational level in the ground vibrational state and we have neglected differences in the rotational constant B between the two vibrational levels.

Combining Eqns. (3–2) and (3–3), we may now write the modulated bolometer signal as a function of the energy density ρ and the interaction time t of the molecule with the laser as

$$S_{\text{bolo}} \propto \frac{N B_{12} \rho \Delta E_{12}}{A_{21} + (B_{21} + B_{12})\rho} \left[1 - e^{-[A_{21} + (B_{12} + B_{21})\rho]t}\right]. \qquad (3-5)$$

The first factor in this equation, which depends upon the laser power but not on the interaction time, is also independent of the dipole moment transition matrix element μ_{12}: the A_{21} and both B coefficients are proportional to μ_{12}. The second factor does depend upon t, and refers to attainment of equilibrium in the pumping process. For very weak energy densities, Eqn. (3–5) yields a linear dependence of S_{bolo} *vs.* ρ. At higher energy densities, a non-linear dependence develops that is qualitatively different for each of the two factors. We now discuss several limiting cases in distinguishing these differences.

For low energy density and a short interaction time,

i.e., $[A_{21} + (B_{12} + B_{21})\,\rho]\,t \ll 1$, we obtain

$$S_{\text{bolo}} \propto N B_{12} \rho t \Delta E_{12}, \qquad (3-6)$$

which gives the usual linear power dependence typically found in absorption experiments involving incoherent sources. This dependence is also used for low-power laser+bolometer experiments,[20] sometimes with corrections for minor non-linearities.[21]

For the opposite limit of high energy density and a long interaction time,

i.e., $[A_{21} + (B_{12} + B_{21})\,\rho]\,t \gg 1$, we obtain

$$S_{\text{bolo}} \propto \frac{N B_{12} \rho \Delta E_{12}}{A_{21} + (B_{12} + B_{21})\rho}. \qquad (3-7)$$

In this case, the non-linearity with power depends upon the relative magnitude of the A_{21} and B factors.

A third limiting case of Eqn. (3–5) can be distinguished that also yields a non-linear power dependence. For energy densities high enough that stimulated processes are much faster than spontaneous emission, *i.e.*, $(B_{12} + B_{21})\,\rho \gg A_{21}$, we obtain

$$S_{\text{bolo}} \propto \frac{N B_{12} \Delta E_{12}}{(B_{12} + B_{21})} \left[1 - e^{-(B_{12}+B_{21})\rho t}\right], \qquad (3-8)$$

provided that t is reasonably short. This non-linear dependence is particularly relevant for infrared transitions, since their spontaneous lifetimes are often rather long. In addition, the laser interaction time with the molecular beam may be made rather short, so that the conditions of Eqn. (3–7) are not necessarily satisfied.

The high energy density "saturated" limit of Eqns. (3–7) and (3–8) are identical, and can be simplified using the relation $g_1 B_{12} = g_2 B_{21}$ to obtain

$$S_{\text{sat}} \propto \frac{N g_2 \Delta E_{12}}{g_1 + g_2}, \qquad (3-9)$$

where g_1 and g_2 are the degeneracies of the ground and excited states, respectively. For the R(j)– and P(j)–branches, this saturated absorption signal then takes the form

$$S_{\text{sat}} \propto \begin{cases} \frac{2j+3}{4(j+1)} N \Delta E_{12} & \text{(R–branch);} \\ \frac{2j-1}{4j} N \Delta E_{12} & \text{(P–branch),} \end{cases} \qquad (3-10)$$

where ΔE_{12} is given by Eqn. (3–4). Experimental evidence to distinguish between the saturation behaviour of Eqn. (3–7) *vs.* Eqn. (3–8) appears not to be discussed extensively in the literature, and will be provided in the next section.

3.4 RESULTS and DISCUSSION

3.4.A Saturation Behaviour

In order to determine the rotational distribution accurately, we must first be able to convert the measured bolometer signal for each laser line to a population for the corresponding rotational state. This requires adequate characterization of Eqn. (3–5) in the sense of deciding, under ideal circumstances, which of the three limiting cases identified by Eqns. (3–6)–(3–8) is appropriate.

A first indication of the appropriate limiting behaviour of Eqn. (3–5) may be provided by estimating the experimental energy density and interaction time. Taking the laser beam size as $\sim 2.5\,\mathrm{mm}^2$ and the frequency width as $\widetilde{<} 15\,\mathrm{MHz}$, the energy density in the intersection zone is $\frac{\rho}{P} \widetilde{>} 9 \times 10^{-20}\,\mathrm{j-sec/cm}^3$, where P is the laser power in milliwatts. For the $\mathrm{R}_1(0)$ line of HF, Einstein's A_{21} and B_{12} factors are $61.9\,\mathrm{sec}^{-1}$ and $1.74 \times 10^{23}\,\mathrm{cm}^3\,\mathrm{j}^{-1}\,\mathrm{sec}^{-2}$ respectively.[37] For the slower of the two beams characterized in Table 3.1, the interaction time is $t \simeq 1.6\,\mu\mathrm{sec}$. Under these conditions, the laser power must be $> 30\,\mathrm{mW}$ for $[A_{21} + (B_{12} + B_{21})\,\rho]\,t$ to exceed unity, so that the limit of high energy density and long interaction time of Eqn. (3–7) is by no means assured. Conversely, $(B_{12} + B_{21})\,\rho > A_{21}$ corresponds to a laser power as low as $\sim 3\,\mu\mathrm{W}$. Even allowing for spontaneous emission to the third level shown in Fig. 3.2, this estimate would be increased to only $\sim 10\,\mu\mathrm{W}$. These estimates therefore suggest that Eqn. (3–8) should be used in preferrence to Eqn. (3–7) for describing non-linearities in the power dependence of the bolometer signals measured here.

One clear experimental difference between Eqns. (3–7) and (3–8) is that the power dependence of the latter should be affected by the interaction time, whereas the former should not be. We have measured the laser power dependence of the bolometer signal, usually known as saturation curves, for each j state. As an example, such measurements for $\mathrm{R}_1(0)$ are shown in Fig. 3.3 for the two different HF

beam velocities detailed in Table 3.1, while maintaining identical laser conditions. It is evident that these curves depend strongly upon the HF velocity. The curves in Fig. 3.3 are obtained by fitting the data to the function

$$S_{\text{bolo}} \propto \left(1 - e^{-KP}\right), \qquad (3-11)$$

as suggested by the form of Eqn. (3–8). The fitted parameter K is $0.066\,\text{mW}^{-1}$ for $v_{\text{HF}} = 1.21\,\text{km/sec}$, and $0.026\,\text{mW}^{-1}$ for $v_{\text{HF}} = 2.11\,\text{km/sec}$.

These results substantiate the inverse velocity dependence for K suggested by Eqn. (3–8). In addition, the fitted values for K agree qualitatively with those calculated from the above estimates for ρ and t, which yield $K \gtrsim 0.033\,\text{mW}^{-1}$ for the slow HF beam, and $\gtrsim 0.019\,\text{mW}^{-1}$ for the fast one. Considering our order-of-magnitude estimate for the laser frequency width, we regard this as satisfactory agreement with the fitted parameter values. Conversely, a fit to the functional form

$$S_{\text{bolo}} \propto \frac{P}{K' + P}, \qquad (3-12)$$

as suggested by Eqn. (3–7), yields fitting parameters K' several orders of magnitude different from the corresponding estimates.

Regarding transitions other than $R_1(0)$, we note from Eqn. (3–8) that the laser power required for saturation depends upon the sum of the Einstein B_{12} and B_{21} factors. For any of the transitions used here, this sum varies by no more than $\pm 25\%$.[37] Measurements confirm that saturation for all these R_1 and P_1 transitions is virtually complete for $P \gtrsim 50\,\text{mW}$.

Under the present experimental conditions, it is apparent that saturation behaviour is governed by the exponential factor of Eqn. (3–5), and that the laser–molecular beam interaction time plays an important role in this behaviour. We note that this conclusion is unlikely to be affected by power broadening or transit time considerations. Using the A and B factors given above and a power of

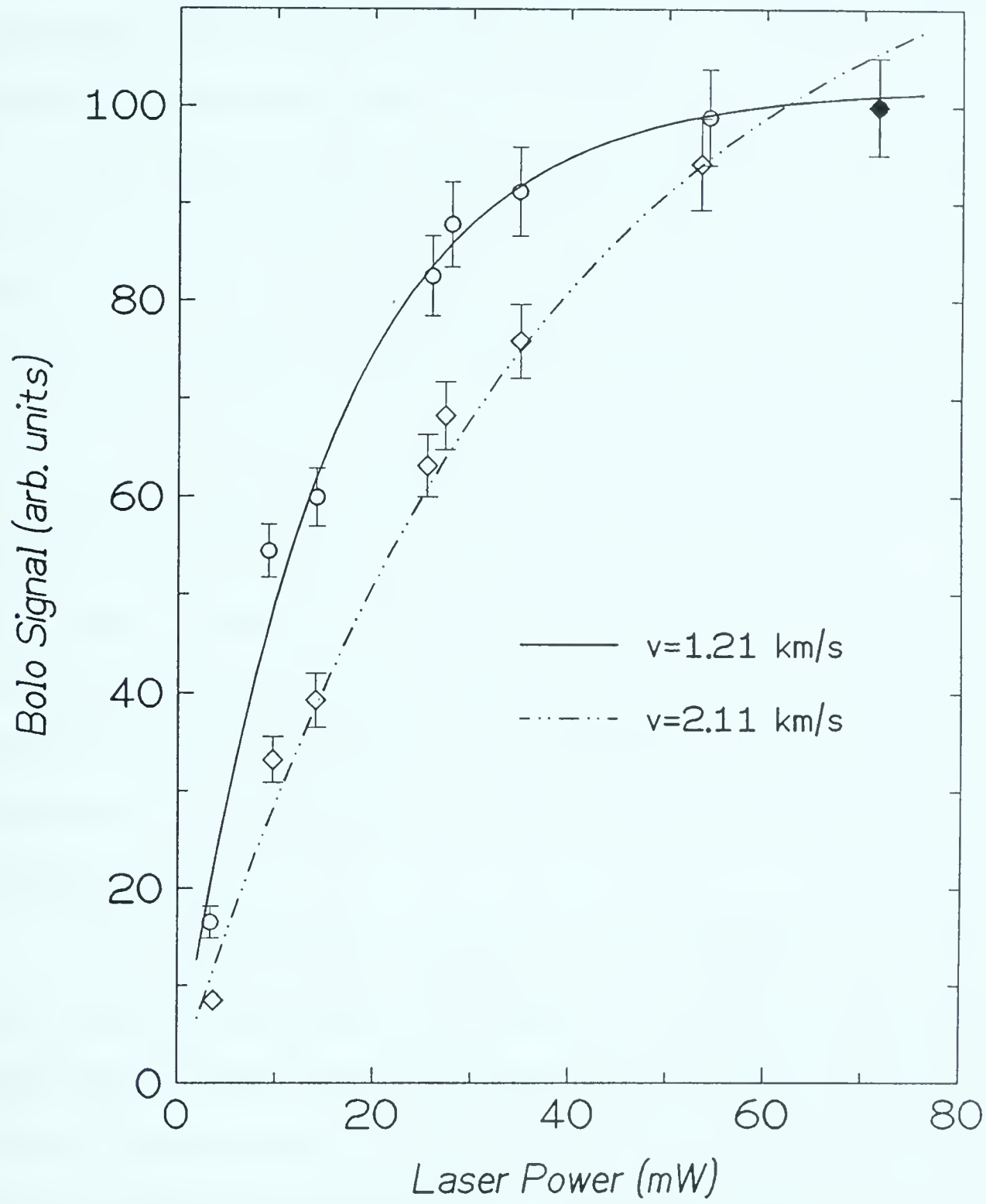

Figure 3.3: Saturation curves for two HF beam velocities using the $R_1(0)$ chemical laser line. Beam conditions are given in Table 3.1. Measured signals are normalized independently at the highest laser power shown (filled symbols). The curves correspond to best-fit results using Eqn. (3–11).

80 mW, the upper-state lifetime is estimated to be $\gtrsim 0.6\,\mu$sec, while the transit time is somewhat longer even for the fast molecular beam. These broadening mechanisms contribute $\lesssim 0.3$ MHz to the observed absorption linewidth. Considerably narrower Doppler widths than the presently achieved $\sim 5 - 10$ MHz (Sec. 3.3) are thus needed to observe such broadening.[26]

The strong saturation exhibited in Fig. 3.3 is very useful both for the present rotational state distribution measurements, and for our rotationally inelastic scattering studies.[17] Saturated transitions maximize the detection sensitivity, unless one is willing to go through the difficulties of generating Rabi oscillations or inversion effects.[25,27] Furthermore, saturated signals are essentially independent of laser power,[23] markedly improving stability in three-beam scattering experiments. It is apparent that we have achieved—at least in the mid-infrared region—the particularly convenient circumstances for molecular quantum state population measurements referred to by Altkorn and Zare as the "limit of very strong saturation".[29] Indeed as they point out, converting signals to populations becomes simpler [Eqn. (3–10)], requiring much less experimental information and eliminating the need even for the Einstein factors.

The bolometer used in conjunction with a modulated saturating laser functions essentially as a *particle flux* detector (*i.e.*, $S_{\rm sat} \propto N$) after allowing for the degeneracy and (small) rotational energy factors of Eqns. (3–10) and (3–4), respectively. This circumstance is particularly helpful for scattering studies, wherein the bolometer's sensitivity would otherwise be complicated by the scattering velocity (and hence kinetic energy) dependence upon the scattering angle, and by adsorption effects on the bolometer surface.[31]

The experimental conditions used in this study may also provide a particularly important régime for HF detection under alternative circumstances. In particular, the bolometric signal would be proportional to population *differences* if

the excited state is already populated before interacting with the laser, as might be the case in reactive scattering experiments, for example.

3.4.B Rotational Distributions

The rotational distribution data are measured for laser powers corresponding to complete saturation of all the transitions, over a wide range of HF and He diluent nozzle pressures. As an example, results for a seeded HF beam are presented in Table 3.2. Signals for R– and P–branch lines originating from common rotational states in $\nu = 0$ are near the ratios calculated from Eqn. (3–10). In particular, ten additional measurements for the $R_1(1)$ and $P_1(1)$ bolometer signal intensities yield a ratio of 2.45 ± 0.16, in satisfactory agreement with the calculated ratio of 2.58. The corresponding ratio for the $R_1(2)$ and $P_1(2)$ signals is 11% higher than calculated from Eqn. (3–10); we therefore take $\pm 10 - 15\%$ as a reasonable estimate of the error in our rotational population measurements.

Rotational distributions measured for four beam expansion conditions are displayed in Fig. 3.4. These data show significant deviations from Boltzmann behaviour that increase with nozzle pressure, such that higher rotational levels are overpopulated in comparison with a Boltzmann distribution fit to the lower j–states. This non-Boltzmann behaviour has been observed many times for many different molecules[1] including HF.[19,21] We fit the results to the function

$$N_j = (2j+1) \times \exp\left[-\frac{B_0 j(j+1)}{kT_{\rm rot} + \beta B_0 j(j+1)}\right], \qquad (3-13)$$

where $T_{\rm rot}$ is the limiting low–j rotational temperature and β provides a measure of the deviation from thermal behaviour.[24] Determining the low–j limiting rotational temperature using Eqn. (3–13) is more appropriate than using a pair temperature based on the $j = 0$ and $j = 1$ populations, since the former is determined by fitting all the observed j states. The rotational distribution parameterized by Eqn. (3–13) is seen to describe the measured populations quite well, under a wide variety of nozzle expansion conditions.

Table 3.2 HF Rotational Distribution[a]

	R–branch				P–branch			
j	Laser line	$\frac{g_2}{g_1+g_2}$	Signal[b]	N_j[c]	Laser line	$\frac{g_2}{g_1+g_2}$	Signal[b]	N_j[c]
0	$R_1(0)$	$^3/_4$	100.00	1.000	—	—	— —	—
1	$R_1(1)$	$^5/_8$	68.54	0.815	$P_1(1)$	$^1/_4$	28.57	0.875
2	$R_1(2)$	$^7/_{12}$	17.57	0.222	$P_1(2)$	$^3/_8$	9.59	0.198
3	$R_1(3)$	$^9/_{16}$	n.m.[d]	—	$P_1(3)$	$^5/_{12}$	3.30	0.062
4	$R_1(4)$	$^{11}/_{20}$	n.m.[e]	—	$P_1(4)$	$^7/_{16}$	1.05	0.019

[a] Seeded beam conditions of Table 3.1.

[b] Signals and populations arbitrarily normalized for $j = 0$.

[c] Populations determined from Eqn. (3–10).

[d] Laser line too weak for frequency stabilization.

[e] Laser line not observed.

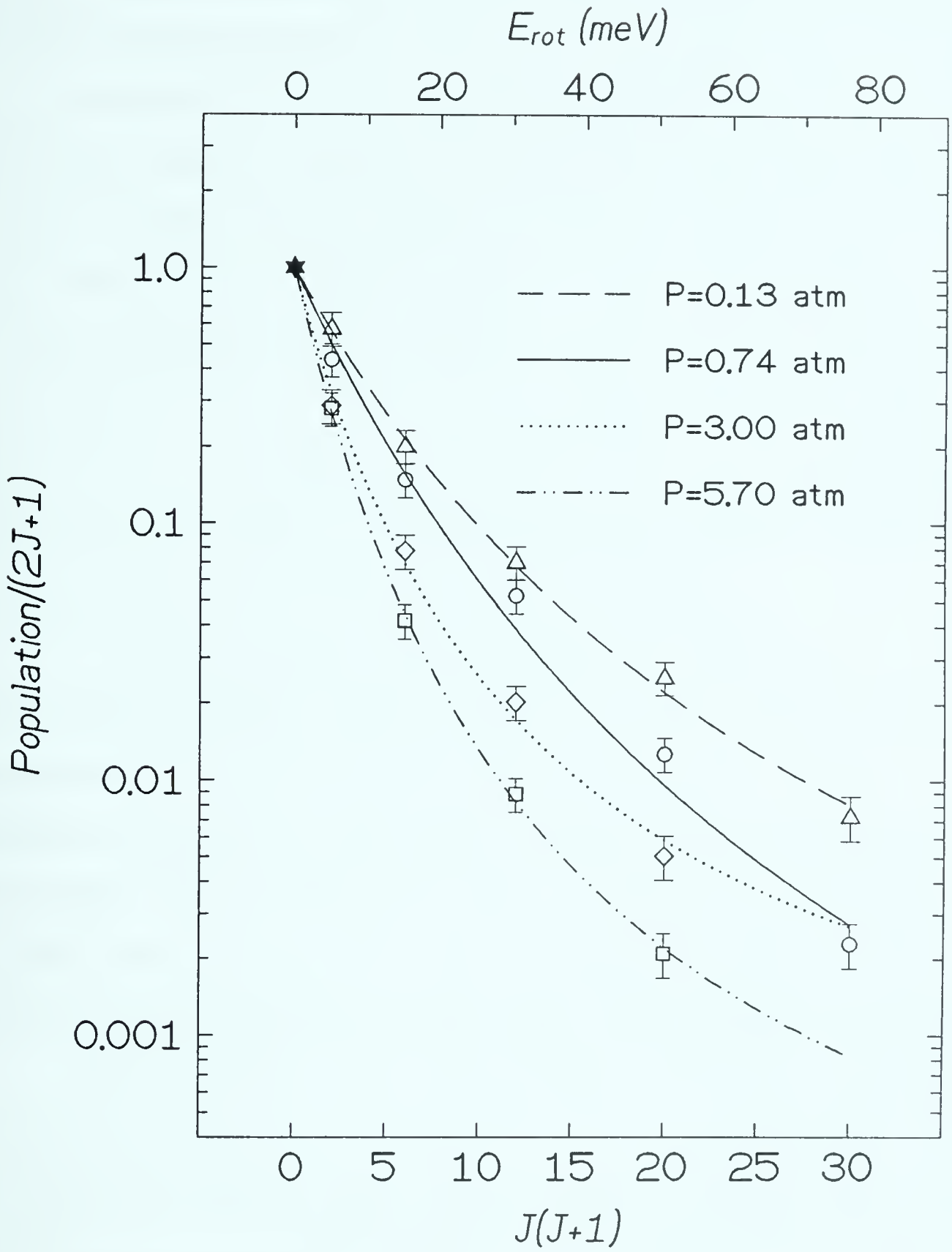

Figure 3.4: Boltzmann plots for rotational distributions measured for four different nozzle expansion conditions. The two lowest pressures correspond to expansions of pure HF and the two highest pressures to seeding in He. Bath temperatures used to regulate the HF flow are -30, $+10$, -30, and -50°C, corresponding respectively to increasing the total nozzle pressure. Measured signals are normalized independently for the $j = 0$ population (filled symbol). The curves are obtained by fitting a non-Boltzmann parameterization to the data using Eqn. (3–13). Fitted parameter values are $T_{\rm rot} = 98,\ 82,\ 46,\ 40^{\circ}$K, and $\beta = 0.097,\ 0.077,\ 0.117,\ 0.096$, respectively.

Considering our use of a heated nozzle, the present results agree nicely with those of Gough and Miller.[21] In fact, the rotational distribution shown in Table 3.2 is practically identical to one recorded by Miller.[19] Using $P_0 d$ as a measure of the nozzle expansion conditions, where P_0 is the nozzle pressure and d is its diameter, our highest-pressure expansion is about 2.5× more forceful. Despite the present relatively balmy rotational temperature (for free-jet expansions) of 40°K, the coldest distributions yield a plurality of rotors in the $j = 0$ state due to the large rotational constant for HF. For some measurements, we used a smaller nozzle diameter with correspondingly higher pressure, but we were unable to obtain significantly colder distributions. It appears that we have reached a practical limit for rotational cooling under the present expansion conditions.

Using the procedure originally proposed by Rabitz and Lam[38] and applied by Gough and Miller,[21] kinetic modelling of our HF expansions seeded in He yield substantially the same results as obtained by the latter authors. Despite the difficulty in obtaining lower temperatures experimentally, calculations show that the kinetic model predicts rotational distributions continuing to cool towards 0°K as the nozzle pressure increases. It is clear that agreement between the kinetic model and the experimental results is limited to rather modest expansion conditions.

We note that it may yet be possible to obtain lower rotational temperatures by seeding in heavier rare gases, but scattering of the lighter "seed" gas out of the beam would then reduce the HF intensity. Since our crossed molecular beams scattering experiment requires the highest possible beam intensity, we have not pursued use of different diluents.[9] On the other hand, an improved rotational state distribution might be achieved by using a second laser to pump the incident HF beam, performing the scattering in $\nu = 1$.[15]

3.4.C Detection Sensitivity

Finally, it is interesting to estimate the best laser+bolometer detection sensitivity that we can currently attain. In this case, we of course operate the bolometer at 1.5°K. For the lowest signal levels encountered in our inelastic scattering studies,[17] we use an overall integration time for each measurement of 1000 sec. Under these circumstances, our measured noise level is $\sim 4\,\mathrm{nV}$. Taking a specified bolometer responsivity of $1.45 \times 10^6\,\mathrm{V/W}$ as measured from its load curve, and the HF energy content as one vibrational quantum of $4000\,\mathrm{cm}^{-1}$, the detector has a sensitivity of $\sim 3 \times 10^4$ excited HF molecules/sec. Under our experimental conditions, this corresponds to a sensitivity of $\sim 5 \times 10^4$ molecules/sec per quantum state, since the optical transitions are saturated. Such a high sensitivity compares favourably with mass spectrometer detectors (with ionization efficiencies of $\sim 10^{-3} - 10^{-4}$), and with other laser-based detectors.

3.5 SUMMARY and CONCLUSIONS

We have used a bolometer detector to monitor the vibrational excitation induced in an HF molecular beam by a narrow linewidth chemical laser. The laser provides energy densities high enough to "saturate" the absorption. In order to characterize this saturation behaviour, we extend a rate equation treatment—based on the rates of spontaneous and induced processes—to the case of bolometric detection in the infrared. It is shown that the approach to saturated absorption consists of two factors. Under the present experimental conditions of high laser power and short interaction times, the results indicate that the observed "saturation behaviour" is caused by attainment of equilibrium in the transition being pumped. This is substantiated by altering the molecular beam velocity, thus changing the interaction time of the laser with the HF beam.

Using the laser to saturate the HF absorption greatly simplifies the conversion of measured signals to rotational state populations, while maximizing the signal levels. We have measured rotational distributions for pure and seeded HF beams under conditions yielding beams intense enough for inelastic scattering measurements. The coldest beam we could obtain for pure HF had a temperature of 82°K, while 40°K was reached for a He–seeded HF beam. These rotational temperatures correspond to peak populations in $j = 1$ and $j = 0$, respectively.

For saturated optical transitions, measured noise levels yield an estimate for the laser+bolometer detection system sensitivity. For HF, this corresponds to $\sim 5 \times 10^4$ molecules/sec per quantum state.

REFERENCES:

1. U. Hefter and K. Bergmann, "Spectroscopic Detection Methods," in *Atomic and Molecular Beam Methods Vol. 1*, edited by G. Scoles (Oxford University Press, Oxford, 1988), Chapter 9.

2. U. Buck, "Inelastic Scattering I: Energy Loss Methods," in *Atomic and Molecular Beam Methods Vol. 1*, edited by G. Scoles (Oxford University Press, Oxford, 1988), Chapter 21.

3. S. Arepalli, Y.–L. Huang, R. Callaghan, and R. J. Gordon, *AIP Conf. Proc. Phys.* **191**, 481 (1989).

4. J. M. Hutson, *J. Chem. Phys.* **91**, 4448 (1989); *J. Chem. Phys.* **89**, 4550 (1988); and references therein.

5. S. J. Harris, S. E. Novick, and W. Klemperer, *J. Chem. Phys.* **60**, 3208 (1974); T. A. Dixon, C. H. Joyner, F. A. Baiocchi, and W. Klemperer, *J. Chem. Phys.* **74**, 6539 (1981).

6. M. R. Keenan, L. W. Buxton, E. J. Campbell, A. C. Legon, and W. H. Flygare, *J. Chem. Phys.* **74**, 2133 (1981).

7. M. D. Marshall, A. Charro, H. O. Leung, and W. Klemperer, *J. Chem. Phys.* **83**, 4924 (1985).

8. G. T. Fraser and A. S. Pine, *J. Chem. Phys.* **85**, 2502 (1986).

9. Z. S. Huang, K. W. Jucks, and R. E. Miller, *J. Chem. Phys.* **85**, 6905 (1986).

10. C. M. Lovejoy, M. D. Schuder, and D. J. Nesbitt, *J. Chem. Phys.* **85**, 4890 (1986).

11. R. L. Robinson, D. Gwo, D. Ray, and R. J. Saykally, *J. Chem. Phys.* **86**, 5211 (1987).

12. U. Buck, *Comments At. Mol. Phys.* **17**, 143 (1986).

13. C. H. Becker, P. W. Tiedmann, J. J. Valentini, Y. T. Lee, and R. B. Walker, *J. Chem. Phys.* **71**, 481 (1979).

14. U. Buck and J. Schleusener, *J. Chem. Phys.* **75**, 2470 (1981).

15. J. A. Barnes, M. Keil, R. E. Kutina, and J. C. Polanyi, *J. Chem. Phys.* **72**, 6306 (1980); *J. Chem. Phys.* **76**, 913 (1982).

16. P. F. Vohralik, R. E. Miller, and R. O. Watts, *J. Chem. Phys.* **90**, 2182 (1989).

17. L. J. Rawluk, Y. B. Fan, Y. Apelblat, and M. Keil, *J. Chem. Phys.*, in press (1991).

18. T. E. Gough, R. E. Miller, and G. Scoles, *Appl. Phys. Lett.* **30**, 338 (1977).

19. R. E. Miller, *Ph.D. Thesis* (University of Waterloo, 1980).

20. D. Bassi, A. Boschetti, S. Marchetti, G. Scoles, and M. Zen, *J. Chem. Phys.* **74**, 2221 (1981).

21. T. E. Gough and R. E. Miller, *J. Chem. Phys.* **78**, 4486 (1983).

22. K. Veeken and J. Reuss, *Appl. Phys. B* **34**, 149 (1984).

23. C. Douketis, T. E. Gough, G. Scoles, and H. Wang, *J. Phys. Chem.* **88**, 4484 (1984).

24. N. Dam, C. Liedenbaum, S. Stolte, and J. Reuss, *Chem. Phys. Lett.* **136**, 73 (1987).

25. A. G. Adam, T. E. Gough, N. R. Isenor, and G. Scoles, *Phys. Rev. A* **32**, 1451 (1985).

26. A. S. Pine and G. T. Fraser *J. Chem. Phys.* **89**, 6636 (1988).

27. S. Avrillier, J.-M. Raimond, Ch. J. Borde, D. Bassi and G. Scoles, *Opt. Commun.* **39**, 311 (1981).

28. A. E. Siegman, *Lasers* (University Science, Mill Valley, California, 1986), Chapter 4.

29. R. Altkorn and R. N. Zare, *Ann. Rev. Phys. Chem.* **35**, 265 (1984).

30. L. J. Danielson, K. M. McLeod, and M. Keil, *J. Chem. Phys.* **87**, 239 (1987).

31. L. J. Danielson and M. Keil, *J. Chem. Phys.* **88**, 851 (1988).

32. L. J. Rawluk and M. Keil, *J. Opt. Soc. Am. B* **6**, 1278 (1989).

33. Z. S. Huang, K. W. Jucks, and R. E. Miller, *J. Chem. Phys.* **85**, 3338 (1986).

34. O. Svelto, *Principles of Lasers* (Plenum, New York, 1982), pp. 247 – 250.

35. J. A. Silver, W. L. Dimpfl, J. H. Brophy, and J. L. Kinsey, *J. Chem. Phys.* **65**, 1811 (1976); J. F. Córdova, C. T. Rettner, and J. L. Kinsey, *J. Chem. Phys.* **75**, 2742 (1981).

36. L. Pauling and E. B. Wilson, *Introduction to Quantum Mechanics* (Mc-Graw Hill, New York, 1935).

37. K. Tamagake and D. W. Setser *J. Phys. Chem.* **83**, 1000 (1979).

38. H. Rabitz, S.-H. Lam, *J. Chem. Phys.* **63**, 3532 (1975).

CHAPTER 4

DIFFERENTIAL CROSS SECTIONS FOR ROTATIONALLY STATE–RESOLVED INELASTIC SCATTERING OF HF BY ARGON[†]

4.1 INTRODUCTION

Investigations of angular scattering distributions for rotational energy transfer caused by atom+diatom collisions in crossed molecular beams have been proceeding along three general trends since their inception.[1] State-to-state resolution has been achieved by time-of-flight techniques for scattering measurements of H_2 and its isotopic analogues by rare gas atoms,[2,3] and of He by various molecules.[4] Optical pumping and laser-induced fluorescence measurements have been applied to the scattering of Na_2 and other alkali molecules by atomic beams.[5,6] Both sets of techniques have focussed on systems whose interactions are almost exclusively repulsive[7,8] and have thereby elucidated such elegant structures as rotational rainbow scattering.[9,10]

Interactions governed by more attractive potential energy (PE) surfaces have also been studied, though not with the same high degree of precision, nor (typically) with resolution of state-to-state rotational inelasticities. Among recent examples, these studies include incompletely resolved angular scattering of O_2 by Ar[11] and of CO_2 by He[12] and Xe.[13] Such interactions are expected to exhibit features typical both of attractive systems, *e.g.*, the impact parameter rainbows familiar from atom+atom scattering, and of repulsive systems, *e.g.*, the rotational rainbows mentioned earlier.[14] Studies of such mixed systems are then particularly important[15] in elucidating the balance between attractive and repulsive forces during collisions that induce energy transfer.[16,17]

[†] A version of this chapter has been published.
L. J. Rawluk, Y. B. Fan, Y. Apelblat, and M. Keil, *J. Chem. Phys.* **94**, 4205 (1991).

The hydrogen halide+rare gas (HX+Rg) interactions have served as workhorses for investigations of anisotropic PE surfaces.[18] With their large dipole moments, HX molecules exhibit strongly directional binding to the Rg partner.[19,20] This binding has been studied by very precise and extensive spectroscopic techniques over the last 18 years.[21] Testifying to their elegance, these techniques continue to provide ever deeper insights.[19,20,22–24] Taking advantage of the large HX vibrational excitation energies and transition probabilities, infrared spectroscopy has also been used to study details of the photodissociation of HX•Rg van der Waals molecules.[25,26] A recent article by Vohralik, Miller, and Watts[27] provides an extensive bibliography for much of the recent work done on HX+Rg interactions.

In this paper we focus on the HF+Ar interaction. Combining infrared excitation with bolometric detection,[28] we are able to measure the differential cross section (DCS) for HF scattered into specific final rotational states. The choice of HF is dictated by the availability of a laser bright enough for optical saturation, thus maximizing our signal and simultaneously simplifying its interpretation.[29] We choose Ar as a scattering partner because of reasonably large inelastic cross sections. For example, the $j = 0 \longrightarrow j' = 1$ integral cross section is expected to be $\sim 21\,\text{Å}^2$ for HF+Ar,[27] but only $\sim 3.4\,\text{Å}^2$ for HF+He.[30] Also, a lighter partner would compress the HF into a small angular range in the laboratory scattering frame, thereby prohibiting good angular resolution for the DCS. In addition, the HF+Ar system in particular has been subjected to very extensive and varied studies, both experimental[22,25,27,31–35] and theoretical.[27,36–38]

Microwave[31–33] and infrared[22,25,34,35] spectroscopy have provided very detailed data for the HF•Ar van der Waals molecule. These data have been exploited in developing reliable PE surfaces in the vicinity of the PE surface's absolute minimum. In addition, the full angular dependence of the attractive minimum has recently been determined for some favourable HX•Rg cases.[19,20] Theoretical and

semi-empirical efforts have led to construction of Hartree-Fock plus damped dispersion (HFD) types of PE surfaces that include reasonable representations for the repulsive wall.[27,36] The repulsive regions are not probed spectroscopically, except indirectly by HF•Ar photodissociation experiments.[25]

On the other hand, scattering experiments conducted at collision energies considerably in excess of the attractive well are sensitive to repulsive interactions. Such experiments therefore complement the spectroscopic probes, and also serve to examine the balance between attractive and repulsive regions of the PE surface.

The most sensitive scattering probe for anisotropic PE surfaces is provided by state-to-state DCS measurements. To date however, the only state-to-state HX+Rg cross sections available are integrated over scattering angles, and are not very sensitive to details of the PE surface.[39] DCS measurements for these systems have not yet attained state-to-state resolution even for the experimentally most favourable of systems. Nevertheless, even "total" DCS (*i.e.*, unresolved elastic+inelastic) measurements are quite sensitive to the PE surface at various levels of detail.[27,40–42] In most cases, the total DCS can be used to generate an effective spherical potential.[30,40,41,43] In particularly favourable circumstances, it may even be possible to add anisotropic components to a spherical potential,[40] further improving its reliability.[44] At the very least, the total DCS provides a powerful constraint on the acceptability of a given PE surface.

It should be noted that much of the sensitivity to the PE surface exhibited by scattering probes is contained in diffraction or rainbow structure of the DCS. For the lightest systems (*i.e.*, Rg = He), well-resolved diffraction oscillations are easily measured.[30,43] Unfortunately, these systems exhibit only weak rotational inelasticities.[30] For Rg = Ne, diffraction oscillations become so closely spaced that they can be observed only with extremely high velocity and angular resolution.[45,46]

For the three heaviest Rg scattering partners, semi-classical rainbow oscillations become more prominent than the quantum mechanical diffraction effects, and have been observed in studies of the HCl+Ar,[40,42] HF+Xe,[41], and HF+Ar[27] systems.

In the present paper, determination of the HF rotational state subsequent to the scattering event is intended to improve the sensitivity with which the HF+Ar PE surface is probed. While these experiments are not fully state-to-state because of a distribution over rotational states before the collision, we find features that have not been observed in earlier, total DCS scattering studies for any HX+Rg system. In Sec. 4.2 of this paper, we provide detailed descriptions of the changes made to our crossed molecular beams apparatus[47,48] that allow determination of the HF rotational state after scattering. These changes focus upon our use of a stabilized HF chemical laser.[49] The data acquisition and analysis procedure is described in Sec. 4.3, where we pay particular attention to the extraction of the DCS from measured bolometer signals.[29] Our results are presented in Sec. 4.4. Here we also show that the observed features are independent of kinematic transformations, and we compare our data to the total DCS for the same system, as measured of Vohralik *et al.*[27] The observed features are discussed in terms of possible types of rainbow scattering. Finally, we summarize our findings in Sec. 4.5 and outline possible progress for conducting and interpreting these types of experiments.

4.2 APPARATUS

The scattering apparatus has been described in previous publications presenting elastic[47,48] or preliminary inelastic[49] differential cross section (DCS) scattering results. Here we describe aspects directly related to determining the HF+Ar rotationally state-resolved DCS, as measured using a crossed molecular beams apparatus. A schematic diagram of the apparatus is presented in Fig. 4.1. The principal modification from the elastic scattering measurements involves determining the rotational state of the scattered HF; here we use a cw HF chemical laser operating in conjunction with a rotatable bolometer (thermal) detector. The basic principle is founded upon the opto-thermal laser+bolometer technique developed by Gough, Miller, and Scoles:[28] an HF molecular beam impinging on a cryogenic bolometer gives up its kinetic and internal energy, which is seen as a dc signal. If a modulated laser beam excites some of the HF on its way to the bolometer, selective amplification of this ac component gives a direct measure of the excited population. Rotating the bolometer—while maintaining the laser wavelength fixed to excite just one specific vib-rotational transition of HF—allows measurement of the DCS into that specific state. Figure 4.2 portrays this detection scheme, as applied herein for rotationally inelastic scattering.

4.2.A Beam Sources and Detector

Briefly, the apparatus consists of two supersonic molecular beam sources, each pumped independently by unbaffled diffusion pumps (Varian) having rated speeds of 8000 litre/sec. The beams are generated by continuous expansions through circular Pt nozzles (Pelco), followed by home-made Ni skimmers that sample the expansion and collimate the beams. Emerging into the scattering chamber at right angles to one another, each horizontally directed molecular beam passes through a circular collimator placed 22 mm before the collision zone. During scattering experiments, the pressure is maintained below $\sim 4 \times 10^{-6}$ Torr. Nearly all of

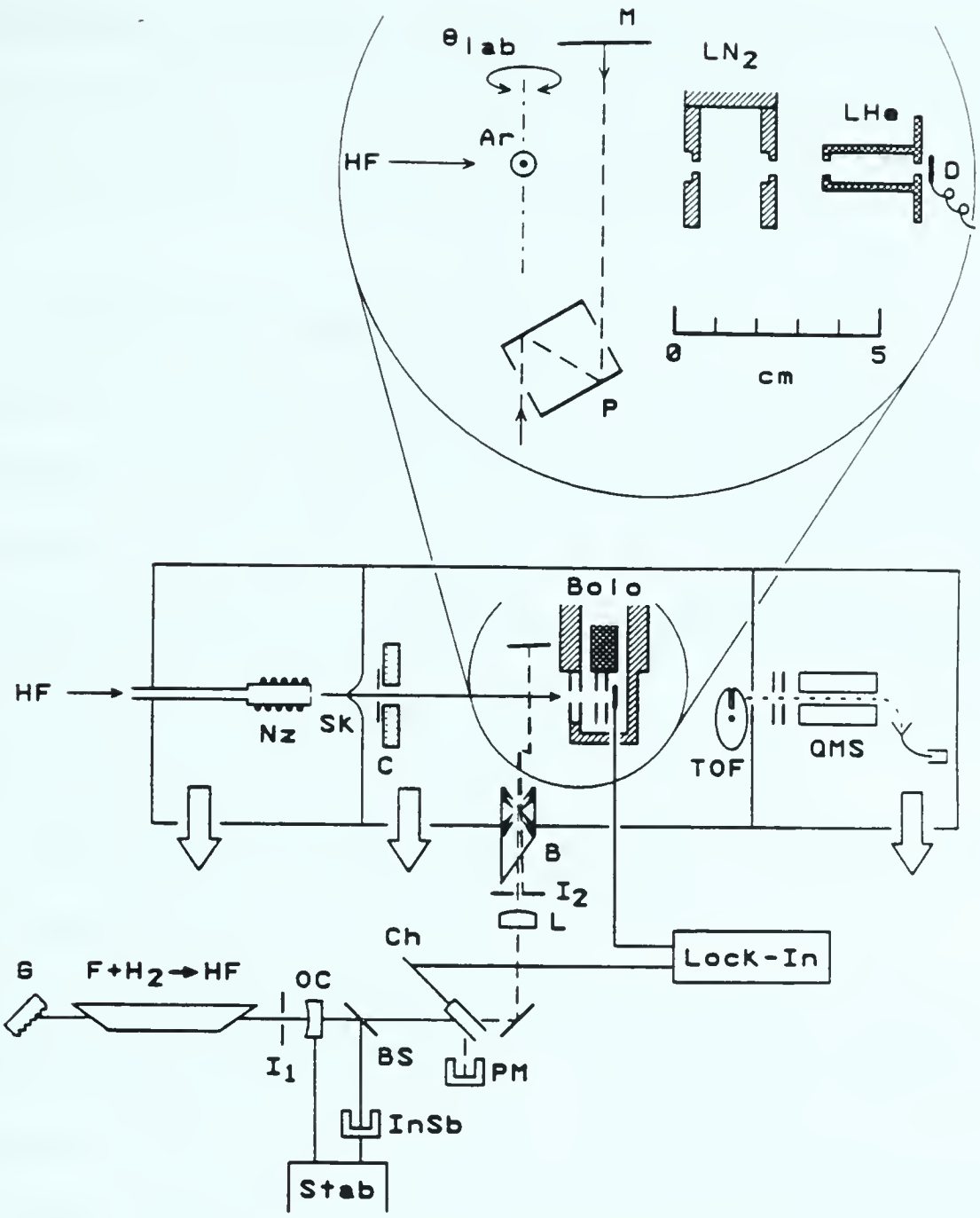

Figure 4.1: Schematic side-view of the scattering apparatus. The cw chemical laser fueled by the $\mathbf{F + H_2 \longrightarrow HF^{\dagger} + H}$ chemical reaction is shown at the lower left: **G**—diffraction grating; **OC**—output coupler; $\mathbf{I_1}$—intra-cavity iris; **BS**—beam splitter; **InSb**—infrared detector; **Stab**—laser frequency stabilizer; **Ch**—tuning fork chopper; **PM**—power meter; **L**—collimating lens; $\mathbf{I_2}$—blocking iris; **B**—Brewster-angle vacuum window and light baffle. The HF molecular beam is introduced at the left through the **Nz**—nozzle; **Sk**—skimmer; and **C**—collimator. This beam may be characterized by the **TOF**—time-of-flight chopper and **QMS**—quadrupole mass spectrometer, when the bolometer detector is rotated away from the incident beam. Heavy arrows denote diffusion pumping for each vacuum chamber. The rotating laser+bolometer detection system **(Bolo)** is shown in the inset, together with its collimating apertures and laser mirrors: $\mathbf{LN_2}$—liquid nitrogen-cooled apertures; **LHe**—liquid helium-cooled apertures; **P**—periscope; **M**—double-pass mirror; and **D**—semi-conducting bolometer detector. All five of these components rotate as a rigid assembly about an axis that passes through the collision zone and is perpendicular to the scattering plane formed by the HF and Ar beams, the latter emerging from the plane of the figure. Components within the inset are drawn to scale, as shown.

this background gas is Ar because the HF is efficiently cryo-pumped by liquid N_2-cooled surfaces inside the scattering chamber. For applying background corrections, the Ar beam is periodically interrupted by a flag placed between the skimmer and collimator.

The HF nozzle pressure is regulated by the vapour pressure from a monel cylinder thermostatted at 10.0 ± 0.5°C, while the Ar gas flow is regulated using a mass flow controller. Mass spectrometric time-of-flight techniques are used to determine beam velocity distributions. The mass spectrometer is also used to check that HF cluster formation $[(HF)_n,\ n \geq 2]$ is sufficiently repressed; this is achieved by heating the HF nozzle to 500°K. Also, we note that HF dimers, the most common clusters, are not excited by the chemical laser.[50]

Beam angular distributions are measured by flowing HF at low pressure through the nozzles, while monitoring the laser+bolometer signal as the bolometer is scanned across the beam. We note that these measurements include convolution over the rather wide bolometer acceptance angle. To avoid thermally overloading the bolometer while measuring incident HF beam rotational distributions, we replace the beam collimators by 0.1 mm–diameter apertures. For on-beam characterization of angular or rotational distributions, the bolometer is operated at 4.2°K. Molecular beam operating conditions are reported in Table 4.1, and the distribution of HF rotors measured in the incident beam is compiled in Table 4.2. By convoluting the beam velocity and angular distributions, we calculate a most-probable collision energy of 120 meV. Given that the $\nu = 0$ rotational constant of HF is 2.55 meV ($= 20.56\,\mathrm{cm}^{-1}$), rotational excitation is thermodynamically limited to $j' \leq 6$ for 86% of the incident HF (*i.e.*, from $j \leq 2$), and vibrational excitation is not accessible at all.

The detector is a composite Ge bolometer (Infrared Laboratories) mounted on a rotating flange to allow detection in the (horizontal) plane defined

Table 4.1 Molecular Beam Operating Conditions

	HF	Ar
Nozzle temperature (°K)	500±10	302
Nozzle diameter (mm)	0.10	0.30
Nozzle pressure (atm)	0.74	0.64
Nozzle–skimmer distance (mm)	14	18
Skimmer diameter (mm)	0.73	1.03
Most probable velocity (km/sec)[a]	1.21	0.56
Velocity FWHM $\left(\frac{\Delta v}{v_{\mathrm{mp}}}\right)$[a]	0.21	0.079
Collimator diameter (mm)	2.41	2.56
Angular divergence (deg)[b]	3.0	3.3
Nozzle–scattering centre distance (mm)	63	66
Dimer/monomer signal ratio[c]	0.06	0.004

[a] The corresponding most probable relative velocity is 1.31 km/sec, with a FWHM spread of 17%. The calculated collision energy is 120 meV.

[b] Calculated.

[c] For HF, this is the measured $\frac{m}{e} = 21 : 20$ ratio. Most likely this provides only a lower limit for the true dimer : monomer ratio due to fragmentation in the mass spectrometer.

Table 4.2 HF Beam Rotational Distribution

j	Population (%)[a]
0	28
1	37
2	21
3	10
4	3.2
5	0.7

[a] Calculated from the measured on-beam bolometer signals as described in Sec. 4.3.B. This distribution may be characterized by a rotational "temperature" of 55° K for $j = 0 - 1$, and 170° K for $j = 3 - 5$.

by the two intersecting molecular beams. Defining the incident HF and Ar beams as 0° and 90° respectively, accessible scattering angles range from −10° to +96°. The bolometer views the collision zone through two 2.4 mm–diameter collimating apertures located 35 and 83 mm from the molecular beams intersection point. For scattering measurements, the bolometer must be made as sensitive as possible. This is achived by pumping on the liquid He dewar to lower its temperature to ~ 1.5°K, simultaneously improving responsitivity[51] and reducing microphonic noise.

The cw line-tuneable HF chemical laser has been described in a previous publication,[49] but a short description is also warranted here. The lasing action is obtained from the $F + H_2 \longrightarrow HF^{\dagger} + H$ chemical reaction, where $HF^{\dagger}$ denotes vib-rotationally excited HF in the ground electronic state. Flourine atoms are generated *in situ* from a mixture of SF_6 in He passing through a 2450 MHz microwave discharge. Hydrogen is mixed into the flow channel, which is maintained at ~ 5.5 Torr by a 165 litre/sec Roots pump backed by a 60 litre/sec mechanical pump (both Leybold-Heraeus). The optical cavity consists of a 300 lines/mm diffraction grating (Milton Roy) mounted in the first-order Littrow configuration, and a ZnSe output coupler (Two-Six) mounted on a piezoelectric translator (PZT, Lansing). These optics are separated by three Invar rods mounted on an optical table. To reduce mechanical vibrations, the optical table does not touch the laser mixing channel, mechanical pumps, or microwave generator.

A small portion of the laser output power is fed into an InSb detector (Infrared Associates) to allow active frequency stabilization (Sec. 4.2.B). The laser beam is mechanically chopped at 39.6 Hz for synchronous lock-in detection using the bolometer. Light reflected off the chopper during its closed period is used for simultaneously monitoring the laser power. The laser is collimated with a long focal length CaF_2 lens, and is directed into the scattering chamber in a (vertical) direction perpendicular to the plane of the molecular beams. Scattered light is suppressed

using a CaF_2 Brewster-angle window and conical light baffles. The entire extra-cavity light path is flushed with dry N_2 to reduce absorption by atmospheric water vapour.

Operating characteristics unique to this particular chemical laser but nevertheless important for the present experiments include lasing in the R–branch[49] and active stabilization of the laser frequency.[29]

4.2.B Laser Stabilization

Of central concern to the present experiments is efficient matching of the laser emission wavelength with the molecular beam absorption. On the one hand, the free-running laser emission is $\sim 400\,\mathrm{MHz}$ wide due to Doppler broadening within the laser cavity,[52] whereas the molecular beam absorption is inherently sub-Doppler due to the narrow range of out-of-plane scattering angles seen by the bolometer. The absorption may be suitably broadened using multiple non-orthogonal laser crossings with the molecular beam. However, such an arrangement is stricken by increased scattered light and use of an inherently multi-mode Doppler-broadened laser beam.[49] We have opted to use an optical cavity-length stabilization loop to narrow the laser emission instead.

We achieve "single-frequency" laser operation by shortening the optical cavity so that it can sustain only a single longitudinal mode, as well as controlling transverse modes using an intra-cavity iris. The higher-gain laser lines require a smaller iris size, which is adjusted to give $\sim 60\,\mathrm{mW}$ of laser power for each line. This power is sufficient for optical saturation (Sec. 4.3.B).[29] Spatial scans confirm TEM_{00} operation, with a measured $\frac{1}{e}$ laser diameter of $1.9\,\mathrm{mm}$ at the molecular beam. Under these conditions, slowly scanning the optical cavity length using the PZT—while monitoring the molecular beam absorption signal with the bolometer—shows the laser spectral width to be $\sim 15\,\mathrm{MHz}$. In addition, the laser power output shows a prominent Lamb dip located at the maximum bolometer signal.[49] Locking

the cavity length to the minimum of the Lamb dip then yields laser emission that is spectrally narrow *and* is "automatically" matched to the sub-Doppler molecular beam absorption.

We find that stabilizing the laser output frequency is facilitated by averaging the very fast feedback signal from the InSb detector. The averaged signal is then smooth enough to provide laser powers and bolometer signals that are stable over the $> 10\,\mathrm{hr}$ length of each day's scattering experiment. Error signals for correcting the cavity length are generated by 520 Hz modulation imposed on the PZT holding the output coupler. This frequency is too fast to be followed by the bolometer, whose time constant is $\sim 15\,\mathrm{msec}$.

As can be seen from Fig. 4.1, the present stabilization scheme is considerably simpler for the line-tunable HF laser than for continuously tunable colour-centre lasers in this wavelength region,[53] as well as providing more power.[49] Conversely, the line tunability restricts the chemical laser to probing a severely limited number of molecules (*e.g.*, HF, DF and HCl).[54]

The use of a stabilized laser engenders important modifications to the experimental design. In a previous publication, we reported preliminary inelastic scattering measurements obtained by running the laser in a multi-mode configuration with power levels up to 10× higher for some of the stronger laser lines. Also, the molecular beam was formerly excited by a dozen (non-orthogonal) passes through the molecular beam.[49] We have now replaced the multiple-pass cell with a single mirror, enabling the laser to make two orthogonal crossings through the molecular beam. This latter design reduces scattered laser light to nearly immeasurable levels, but sacrifices $\sim 40\%$ of the scattered signal from our preliminary measurements. Offsetting this loss is the achievement of optical saturation with the much-improved spectral overlap.

The Gaussian beam profile of the TEM_{00} mode being used in the current laser configuration implies that all laser lines have the same spatial energy

distribution. This allows the rotational state populations to be calculated directly from the bolometer signals,[29] enabling DCS measurements for HF scattered into different rotational states to be compared. Such comparisons could not easily be accomplished previously, since each laser line has a different mode structure and size when operated multi-mode.

Because the incident HF beam consists of a few rotational states, aiming the laser at the intersection point of the two molecular beams would promote some of the incident HF flux to $\nu = 1$ *before* colliding with the Ar. Such an arrangement would then yield a modulated bolometer signal with a component independent of whatever rotational state the HF is scattered into. To eliminate this problem, we mounted a two-mirror periscope onto the same rotating flange as the bolometer. This displaces the laser 16.5 mm away from the intersection point of the molecular beams, but along the direction taken by HF scattered into the bolometer detector—regardless of the scattering angle.

4.2.C Alignment and Background Suppression

Alignment of the periscope, and of the laser along the bolometer's rotating axis, is crucial in ensuring constant angular sensitivity for the laser+bolometer combination detector: mis-alignment could allow the laser beam to wander off the direct path between the scattering center and the bolometer.

To verify proper alignment, we constructed an angular sensitivity calibration source. This calibrator is a sealed tube attached to the rotating flange and extending vertically to the collision center. A small hole drilled in the side of the tube aims HF at the scattering center and into the bolometer, thus providing molecular flux independent of the bolometer's rotation angle. Under these test conditions, the variation of angular sensitivity was measured to be $< 2\%$ throughout the range of accessible scattering angles, and was repeatable for several laser re-alignments.

The stringent alignment requirements forced us to abandon our earlier use of pneumatic levelling for the optical table;[49] fortunately the laser stability does not suffer. Finally, we note that slight mis-alignment of the laser beam returning off the double-pass mirror is necessary to avoid optical feedback into the laser cavity. This mis-alignment displaces the laser $\sim 0.3\,\mathrm{mm}$ along the direction of the HF that is scattered into the bolometer. Since the double-pass mirror also rotates with the bolometer, the laser displacement is maintained regardless of scattering angle and neither reduces the signal level nor changes the angular sensitivity.

Early measurements of scattered HF were hindered by large background signals that were present with the Ar beam flagged open or closed. This background was attributed to HF bouncing from walls near the collision zone, through the laser beam, and into the bolometer—thus acquiring the same modulation frequency and phase as possessed by HF bouncing directly off the Ar beam. Although the background contribution is removed by subtracting the Ar beam-off from beam-on signal, the measurable signal-to-noise ratio is degraded and the possibility of systematic errors is increased.

We remove most of this background contribution by employing a cylindrical liquid N_2–cooled Al mesh that partially surrounds the collision zone, shown as the stippled area adjacent to the collimator in Fig. 4.1. This mesh (Energy Research and Generation) has the appearance of a sponge, with a labyrinthine cross section that enhances the HF trapping efficiency. Two holes drilled into the sponge allow the HF and Ar beams into the collision zone, and the entire half opposite the beam inlet holes is cut away to allow for detection and adequate pumping. In this way, the bolometer always "looks at" the cold Al sponge. Test measurements indicate that background suppression exceeds 90% when the sponge is kept below 100°K.

To avoid excessive HF condensation on the beam collimator, which is mounted to the same liquid N_2–cooled post as the Al sponge, the collimator is

thermally isolated, and remains above $-50°$C. Nevertheless, the high incident flux of HF partially obscures the beam after $4-6$ hr continuous operation. At this stage, we thaw the sponge to $> 150°$ K for a few minutes before re-cooling it and resuming scattering measurements.

4.3 DATA ACQUISITION and ANALYSIS

4.3.A Measurement Technique

DCS measurements of HF scattered into a particular state j' within $\nu = 0$ are conducted by tuning the laser to the $\nu = 0, j' \longrightarrow \nu = 1, j' \pm 1$ transition, as shown schematically in Fig. 4.2. The bolometer is placed at the desired laboratory scattering angle to measure the modulated signal. This signal corresponds to the energy flux impinging on the detector as a consequence of the laser excitation (Sec. 4.3.B). To obtain measurable signal levels, the bolometer collimating apertures are made large enough to ensure that the detector viewing cone encompasses the entire scattering volume. Considering the sizes of both molecular beams and the laser, as well as the bolometer apertures, we estimate an overall apparatus angular resolution of 3° FWHM. Consequently, we perform most scattering signal measurements at 5° intervals. We do not expect to resolve rapid quantum oscillations, which are spaced by only $\sim 1.6°$ for the analogous Ne+Ar system.[45]

In order to reduce signal fluctuations due to long-term drifts in beam intensities and detector sensitivity, we periodically (every $\sim {}^1/_2\,\mathrm{hr}$) measure the scattering signal at 30° with the laser tuned to the $R_1(0)$ line. This particular angle was chosen because of negligible background despite high signal levels, and inconsequential errors in the event of imperfect angular placement. Using the $R_1(0)$ line as a reference for each of the final rotational states examined provides the means to compare the DCS scattered into each j', relative to that for $j' = 0$, without further normalization.

On average, the reference signal is stable to within $\pm 10\%$ between successive references and on successive days, but a slow decrease in signal intensity is usually observed during the course of each day's experiment. We assume this is caused by gradual HF and Ar condensation on the bolometer surface. However, larger changes sometimes occur in the reference signal level, paticularly because

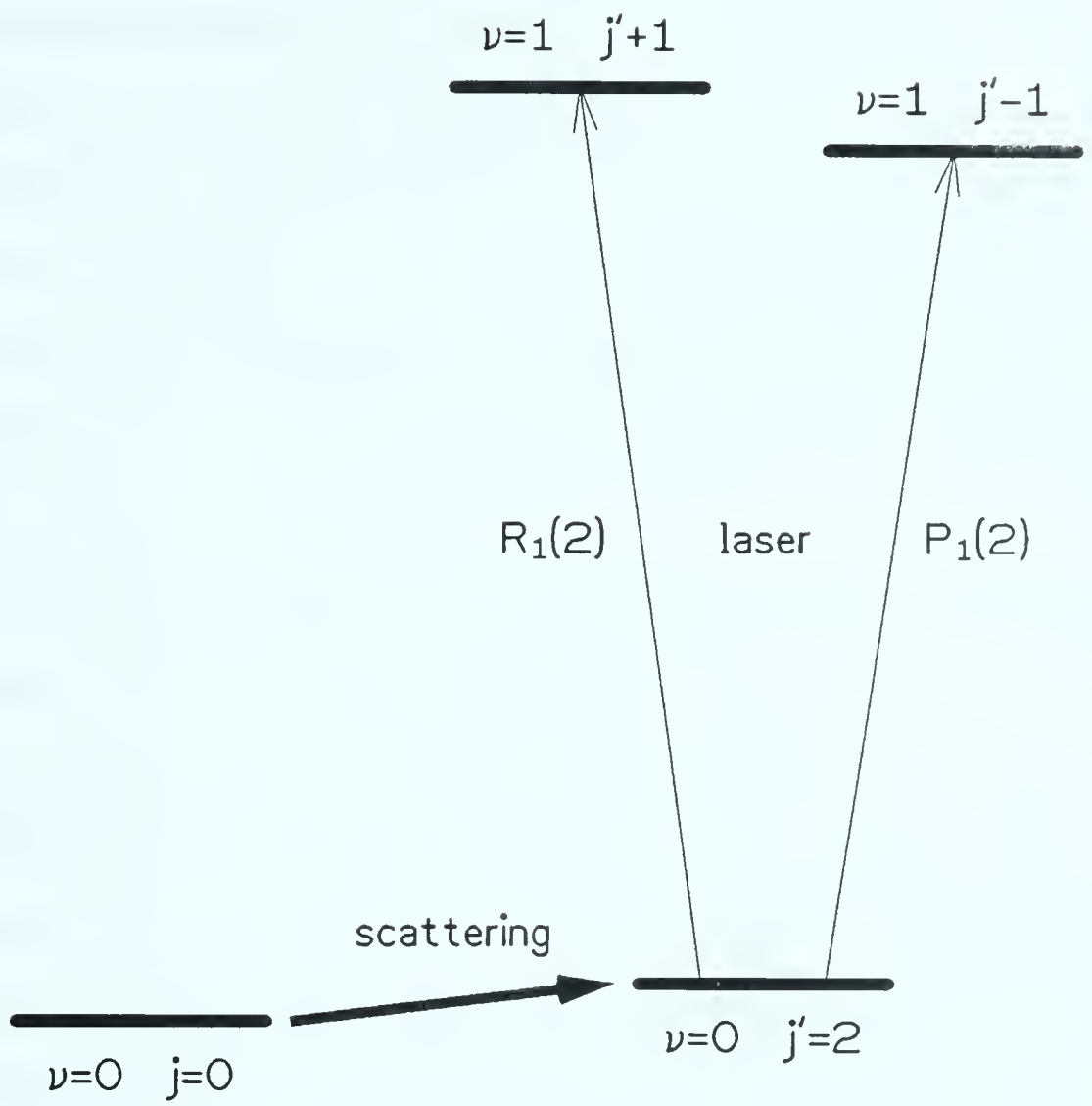

Figure 4.2: Illustration of the laser-based bolometric detection scheme for rotationally inelastic scattering. In the example shown here, HF molecules initially in $j = 0$ are scattered into the final $j' = 2$ state, both within $\nu = 0$. This final state is probed by the chemical laser operating on either the $R_1(2)$ or $P_1(2)$ transition, thereby promoting the inelastically scattered HF to $\nu = 1$. The excess vibrational excitation is then conveyed to the bolometer for detection.

of partial blockage of the HF beam by condensation (Sec. 4.2.C). If the change between successive reference measurements exceeds 25%, then all data gathered between those references is rejected; this affects $< 10\%$ of the data accumulated.

In order to obtain statistically meaningful results, we performed four or five independent measurements of the intensity at each laboratory scattering angle. Integration times for each of these measurements were $40 - 2000$ sec (including background subtraction). The longer integration times corresponded to low signal levels at wide scattering angles and/or high j' states. To obviate possible systematic errors, the measurements were conducted on two or three different days. After all the data were gathered and averaged, 1σ error bars were constructed by slightly smoothing the statistical errors.

Accuracy of the laboratory scattering angle is dictated by the HF beam centreline accuracy and by reproducibility of the detector positioning. A fully automated feedback system ensures that the latter error is kept to within $\pm 0.02°$. However, the former error is more difficult to characterize. Beam angular scans do not accurately determine the centreline, owing to drifting bolometer sensitivity when exposed directly to the incident HF beam. Unfortunately, our angular range is insufficient, with the broad beams being used here, for us to apply symmetry considerations for the scattering measurements on both sides of the HF beam.[48] From our beam angular scans, we estimate the absolute error for the laboratory scattering angle to be $\pm 1°$. This has substantial consequences only for the steeply angular-dependent measurements at 10° and 15° (Sec. 4.4.C).

For these experiments, modulated signals can be generated by HF scattered from residual Ar present in the scattering chamber and by scattered laser light. Both these background signals are removed by flagging off the Ar atomic beam before the scattering centre and subtracting this signal from that obtained without blocking the Ar. For all but the smallest scattering angles of $\theta_{\rm lab} = 10°$

and 15°, the measured background constitutes $\sim 20\%$ of the true scattered (*i.e.*, difference) signal.

For small scattering angles, one further complication arises from the bolometer's wide viewing cone and the broad HF molecular beam. For $\theta_{\rm lab} \leq 15°$, a minute part of the molecular beam impinges directly onto the bolometer surface. Because some of the HF beam is attenuated by the Ar beam, opening the Ar flag reduces the incident HF beam flux onto the bolometer, thereby spuriously depressing the measured on/off difference signal. In the present experiment, the Ar beam attenuates the HF incident flux by 2.1%, as measured on the mass spectrometer. Under these conditions, the error introduced by the Ar beam flagging procedure will be only $\sim 2\%$, even for background signals amounting to 50% of the background+scattered signal. With statistical error bars of $\sim 5-10\%$ at low angles, we should be able to ignore this particular background correction problem.

4.3.B Conversion to Populations

The bolometer is a thermal detector responding to the total energy content of the incident molecules and to heat from optical sources. The total molecular energy content includes kinetic and internal energy, as well as the heats of adsorption and condensation. The following discussion assumes that this total molecular energy content is accomodated upon the cold bolometer surface independently of internal state. Under such circumstances, utilizing lock-in detection attuned to the laser chopper then eliminates all the molecular contributions except for molecular internal energy. Periodic flagging of the crossed Ar beam eliminates scattered laser light also, which is the only modulated optical source. The lock-in signal obtained is then proportional to N_2, the population actually promoted by the laser to the $\nu = 1$ excited state,

$$S_{\rm bolo} \propto N_2 \Delta E_{12}, \qquad (4-1)$$

where $\Delta E_{12} \equiv E_2 - E_1$ and E_1 and E_2 are the vib-rotational energy contents of the ground and excited states, respectively.

In the present case, the large vibrational term value of HF ensures that the energy difference ΔE_{12} depends only slightly upon the rotational state being probed and upon the choice of R– or P–branch excitation. However N_2, the flux of HF molecules actually excited to $\nu = 1$, depends upon the laser power, spectral width and molecule+laser interaction time, as well as the HF absorption and emission coefficients.[29] Nevertheless, under conditions of optical saturation, these dependencies are eliminated, and only the rotational degeneracies of the $\nu = 0$ and $\nu = 1$ states are important.[55] We have shown previously that the frequency stabilized chemical laser operating at $\sim 50\,\mathrm{mW}$ is sufficiently bright to ensure that the HF optical absorption is saturated within the $\sim 1.6\,\mu\mathrm{sec}$ interaction time. Since the $\nu = 1$ excited state is completely empty before the laser interaction, the bolometer signal for saturated optical transitions is given simply by

$$S_{\mathrm{sat}} \propto \frac{N g_2 \Delta E_{12}}{g_1 + g_2}, \qquad (4-2)$$

where g_1 and g_2 are the degeneracies of the ground and excited states respectively, and N is the population, before laser excitation, residing in the rotational state being probed.[29] Equation (4–2) is then used, with appropriate expressions for ΔE_{12}, to convert the measured bolometer signals to rotational state populations. The rotational degeneracy factor $\frac{g_2}{g_1+g_2}$ is larger for R–branch excitation than for the corresponding P–branch transition, so we use the former for $j' \leq 2$. For $j' \geq 3$ however, the chemical laser produces enough power only in the P–branch.[29,49]

We note that the bolometer, though nominally an energy flux detector, operates as a number flux detector under two limiting circumstances: either the molecular beam is chopped and its accomodation energy upon the bolometer vastly exceeds its internal and kinetic energy; or the laser beam is chopped and the optical

transition is saturated.[55] The "total" (unresolved elastic+inelastic) DCS measurements of Vohralik, Miller, and Watts[27] closely match the first set of criteria, whereas the present experiments satisfy the second set.

The validity of the above procedure for extracting rotational state populations from measured bolometer signals was verified by measuring the rotational distribution for HF effusing from the molecular beam source chamber at a few Torr. The fitted rotational temperature was very close to that of the source chamber walls. In addition, our measured incident beam population distribution, presented in Table 4.2, is very similar to that reported in the literature under similar operating conditions.[27,56] Finally, we performed on-beam measurements for $j = 1$ and 2 using both R– and P–branch excitation. The corresponding populations calculated from Eqn. (4–2) agree to within $\pm 10 - 15\%$ (despite bolometer signals differing by a factor of 2.5), which we then take as a reasonable estimate of the error in comparing populations from the different rotational states.[29]

4.3.C Polarization Considerations

Rotationally inelastic scattering of molecules can preferentially orient the molecular plane of rotation. This is especially true for interactions governed by hard-ellipsoid potential energy surfaces,[57–59] or those characterized by a deep attractive well in the linear atom+molecule configuration[16,17] (such as Ar+HF[19,37]).

The influence of such preferential orientation has been considered in detail by Altkorn and Zare for laser-induced fluorescence detection.[55] Experimentally, this requires use of a plane-polarized laser. Test measurements indicate that the chemical laser polarization is preserved with respect to the laboratory frame (to $> 99\%$) as the periscope and bolometer detector are rotated together about the collision zone. In principle therefore, molecular orientation effects ought to be observable using the present experimental configuration. In practice however, Altkorn and Zare concluded that—in the strongly saturated limit—the detection sensitivity

for most orientation distributions is only weakly dependent upon the laser polarization. This conclusion is not strictly applicable to the present case, since our detection scheme involves excitation but not emission. Specifically, the bolometer intercepts molecules excited by the laser regardless of the direction in which they will emit, effectively integrating over the emission anisotropy. This integration tends to further reduce effects of the exciting laser's polarization.

One other set of test measurements was conducted to assess the possible rôle played by orientation effects in the inelastic scattering. If molecular orientation occurs as a result of inelastic scattering, then the scattered HF would have excess population in some $m_{j'}$ levels. In this case, probing the final j' rotational state with $R_1(j')$ and $P_1(j')$ laser transitions would result in different populations if Eqn. (4–2) is used to interpret the measured signals (Sec. 4.3.B). This difference is caused by the plane-polarized laser output, implying a spectral selection rule of $\Delta m_j = 0$.[55,60]

Scattering measurements were performed for $j' = 1$ and $j' = 2$ using both R– and P–branch laser excitation at four different scattering angles. The measured $P_1(j') : R_1(j')$ population ratio obtained using Eqn. (4–2) was 1.09 ± 0.02 for $j' = 1$ and 1.09 ± 0.05 for $j' = 2$, with no discernable angular dependence. We conclude that possible orientation of the scattered HF has an insignificant effect on the present results (Sec. 4.3.B). Future measurements as a function of laser polarization may allow more accurate determinations of such orientation effects, but more precise measurements would be required.

4.4 RESULTS and DISCUSSION

4.4.A Experimental Results

Differential cross section results for scattering angles ranging from $10° - 70°$ with respect to the incident HF beam direction are reported in Table 4.3, and displayed in Fig. 4.3. These are all calculated from the measured bolometer signals as described in Sec. 4.3.C, and are then normalized to the *single* reference intensity defined for $\theta = 30°$ and $j' = 0$. The only thermodynamically accessible rotational state not included in the measurements is $j' = 6$, due to prohibitively low signal-to-noise ratios (Sec. 4.4.B). The lower rotational states ($j' \leq 2$) have excellent S/N ratios, comparable to those of wide-angle elastic DCS measurements (albeit with poorer angular resolution[48]). Due to low signal levels and hence large proportional error bars, a logarithmic plot for $j' = 5$ is not meaningful, and these measurements are given only in tabular form.

Several interesting trends in the DCS results are immediately apparent. Firstly, we observe strong forward scattering for all j'. In addition, a shoulder is clearly evident for the $j' = 0$ DCS in the $\theta \approx 25° - 40°$ region. Also evident is an evolution in the shape of the DCS as a function of j': for $j' = 0$ and 1, the DCS drops steadily at wide scattering angles, whereas it becomes roughly constant for $j' = 2$ and 3. Finally, the $j' = 4$ and 5 DCS's exhibit minima for intermediate scattering angles, and then increase for $\theta \geq 40°$ and $\theta \geq 70°$ respectively. For $j' = 5$, the latter statement relies on the integrity of the single measurement at $\theta = 70°$: all the $j' = 5$ measurements shown in Table 4.3 for $20° \leq \theta \leq 60°$ are very close to zero within our signal-to-noise ratio (average S/N $\simeq$ 1). Nevertheless, the emergence of the DCS for $\theta = 70°$ above this noise level is clearly evident, with a very carefully determined S/N $\simeq$ 3.5.

The present scattering experiments determine only the final rotational state, while the initial state is given by the cooled distribution recorded in Table 4.2.

Table 4.3 Measured Differential Cross Sections[a]

Final State	Laboratory Scattering Angle 10°	15°	20°	25°	30°	35°
$j' = 0$	1305.1	288.5	132.7	107.0	100.0[b]	92.4
$j' = 1$	2831.2	608.9	294.5	206.1	153.4	118.4
$j' = 2$	892.9	181.9	106.6	83.8	71.2	63.2
$j' = 3$	291.2	72.1	52.1	41.0	38.1	34.9
$j' = 4$	64.7	13.6	10.1	—	8.8	—
$j' = 5$	11.5	—	0.5	—	3.0	—

Final State	Laboratory Scattering Angle 40°	45°	50°	60°	70°	Error[c]
$j' = 0$	81.1	68.3	58.5	39.6	23.4	$\pm$ 5 − 10%
$j' = 1$	97.9	89.9	76.3	64.1	54.5	$\pm$ 5 − 10%
$j' = 2$	53.7	52.3	49.5	46.6	46.4	$\pm$ 5 − 10%
$j' = 3$	40.2	37.3	38.6	29.3	31.7	$\pm$10 − 20%
$j' = 4$	14.0	—	16.7	20.1	25.2	$\pm$20 − 30%
$j' = 5$	1.6	—	2.6	1.9	7.2	± 2[d]

[a] Measured signals converted to rotational state populations, as discussed in Sec. 4.3.B.

[b] Reference angle and rotational state used for arbitrary normalization of populations as functions of scattering angle and final rotational state j'.

[c] These statistical error bars are generally largest for the widest scattering angles. At the lowest scattering angles ($\theta \leq 15°$), there may also be systematic errors (Secs. 4.3.A and 4.4.C).

[d] Minimum noise level achieved in these experiments, equivalent to a sensitivity of ~50000 HF molecules/sec per quantum state impinging on the bolometer (see Ref. 29).

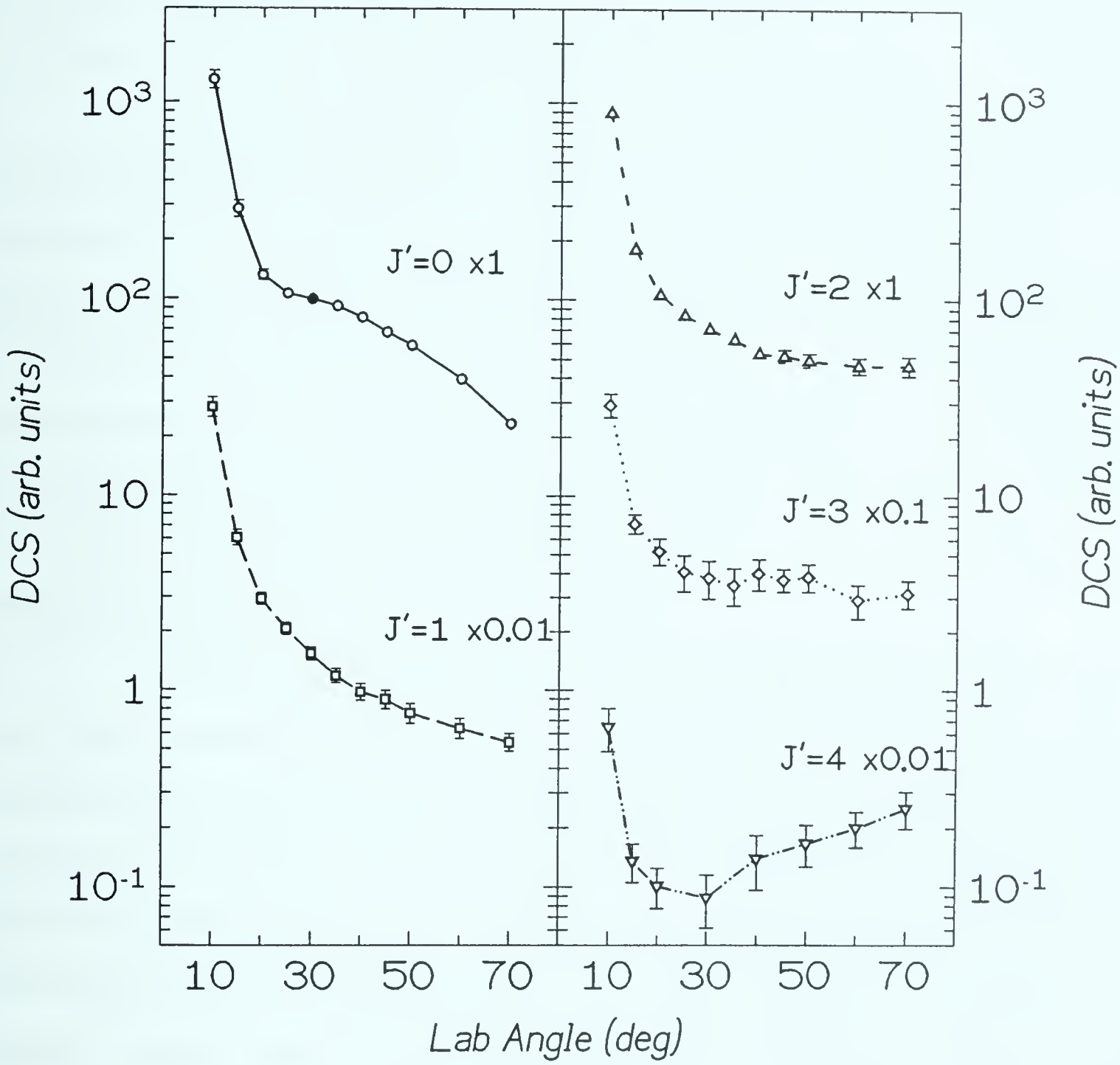

Figure 4.3: Measured differential cross section data for HF scattered by Ar into rotational states $j' = 0 - 4$. Each data point is normalized to the scattering signal intensity measured for $j' = 0$ at a laboratory scattering angle of 30°, shown by the filled symbol. Data for $j' \neq 0$ have also been adjusted to reflect rotational state populations rather than averaged bolometer signals, as discussed in Sec. 4.3.B. Vertical shifts for cross sections into each j' are for clarity of display, as are the connecting lines.

It is therefore evident that the measured DCS's are weighted averages over several possible rotational transitions, including one that is elastic. For example, the $j' = 2$ measured DCS includes contributions from the $j = 0, 1 \longrightarrow j' = 2$ translation-to-rotation cross sections, and the $j \geq 3 \longrightarrow j' = 2$ rotation-to-translation cross sections, as well as the $j = 2 \longrightarrow j' = 2$ elastic cross section.

For the collision energy used for the present experiments, the elastic DCS for mass combinations corresponding to HF+Ar is strongly peaked in the forward direction.[27,45] We may therefore expect that the low-angle DCS measurements are heavily influenced by elastic scattering from the distribution of initial rotational states in the incident beam (Table 4.2), at least for the low rotational states ($j' \leq 2$). Elastic scattering is much less evident for the higher rotational states, even for low scattering angles, since they are initially present in much lower proportion. For $j' \geq 3$, the observed forward peak intensity relative to the wide-angle scattering is much smaller than for $j' \leq 2$.

In Fig. 4.4, we again present the scattering measurements, this time in a manner emphasizing how the distribution amongst HF final rotational states changes with the scattering angle. This figure shows, even for low scattering angles and low j', that the HF rotational distribution in the incident beam is significantly altered by collision with the Ar crossed beam. This requires either that there are substantial inelastic contributions even at low angles, or that the elastic DCS is strongly dependent upon the initial rotational state.[41] Conversely, the increasing proportion of high rotational states ($j' \geq 2$) for wide scattering angles is almost certainly due to predominantly inelastic scattering.

In common with many other systems, large rotational inelasticities are most clearly evident at wide scattering angles.[14] Classically, large-angle deflection corresponds to scattering off the hard repulsive core of the potential energy (PE) surface, which can impart significant torque and hence rotational excitation. If the

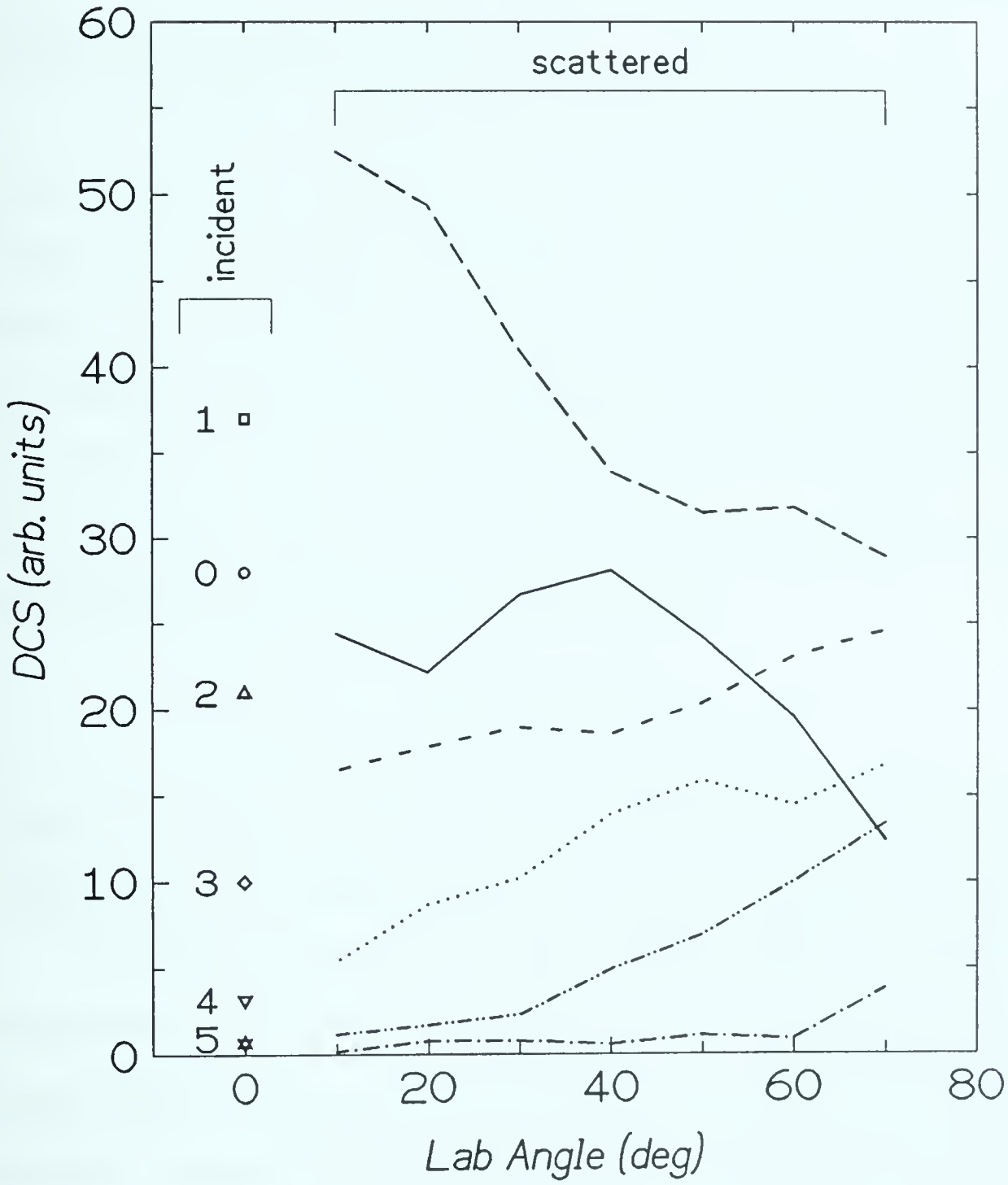

Figure 4.4: Incident and scattered rotational state populations, as percentages of the total HF detected at each laboratory scattering angle (0° denotes the incident beam). Symbol and line types are identical to those in Fig. 4.3.

wide-angle scattering into $j' = 4$ and 5 really does originate from $j = 0$, these rotational inelasticities correspond to transferring very large fractions—42% and 64% respectively—of the available kinetic energy into rotation.

4.4.B Kinematic Transformations

Particularly for inelastic scattering it can be important to realize that the DCS, as measured in the laboratory frame, may be significantly distorted from the DCS in the centre-of-mass (CM) frame. Since experimental DCS's are often compared to those calculated from proposed PE surfaces in the CM scattering frame, we discuss such distortions in this section. We base our discussion on the kinematic "Newton" diagram shown in Fig. 4.5. It is useful to note that, for the present experimental conditions, the CM scattering angle $\theta_{\rm CM}$ is related to the laboratory angle $\theta_{\rm lab}$ by a very simple rule-of-thumb:

$$\theta_{\rm CM} \simeq 1.5\, \theta_{\rm lab} \qquad (4-3)$$

over most of the range of $\theta_{\rm lab}$ and j' states for which we have measured the DCS. This rule-of-thumb deteriorates significantly only for $j' \geq 4$ and $\theta_{\rm lab} \leq 20°$.

In addition to the angle transformation, the CM $\rightarrow$ lab intensity transformation must be considered. These Jacobian factors become especially large for laboratory scattering angles nearly tangent to the Newton circles. In this experiment, the corresponding singularities can occur only for the highly inelastic $j = 0 \longrightarrow j' = 6$ transition, since we are detecting the light scattering partner (the $j = 0 \longrightarrow j' = 5$ transition falls just inside the lab origin in the figure).

The above discussion suggests that neither the angle nor the intensity transformations drastically alter the shape of the measured DCS upon transformation into the CM frame. Before performing such transformations however, one further complication must be recognized. Since the initial rotational state is not

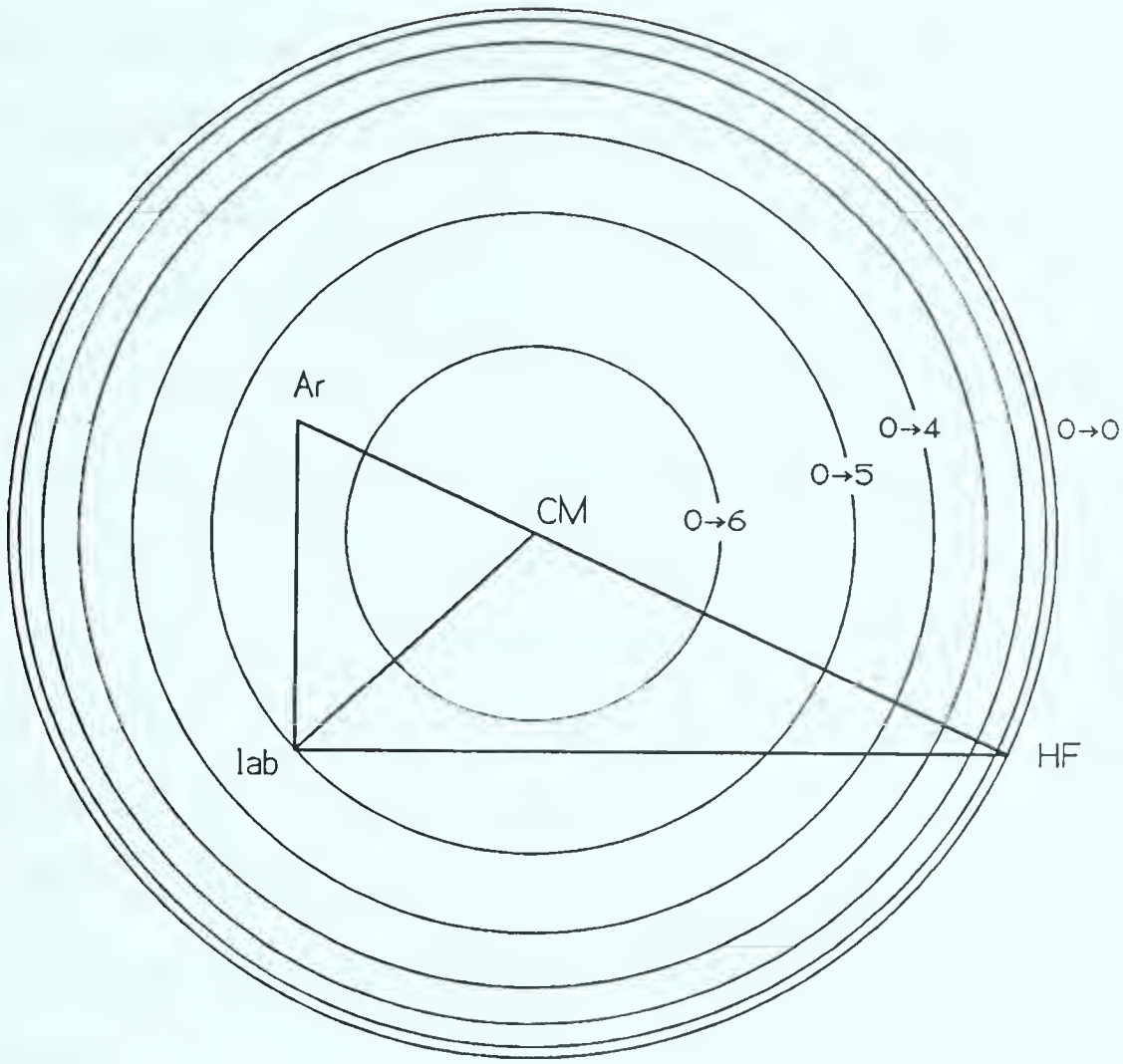

Figure 4.5: Inelastic Newton diagram showing all thermodynamically accessible rotational transitions from an incident $j = 0$ state. Newton circles for $j \neq 0$ may be estimated by interpolation. Molecular beam velocities correspond to those listed in Table 4.1.

specified precisely, neither is the inelasticity for whichever particular j' is being detected. This implies that the Newton circle depends on the j state assumed to give rise to the scattering. To quantify the effect of such an uncertainty, we perform the lab $\rightarrow$ CM transformations separately under two independent assumptions: the scattering originates from $j = 0$, or from $j = 4$. The latter assumption would overstate the uncertainty associated with the transformations, since it is responsible for $< 4\%$ of the initial HF rotors (Table 4.2).

The results of these two assumptions are shown in Fig. 4.6 for the $j' = 0$ and $j' = 4$ measured DCS's. It is readily apparent that the *shape* of the corresponding CM-frame DCS's is not affected by any reasonable choice for the initial rotational state. The actual CM-frame DCS should lie somewhere in a band enclosed by the DCS plotted for the $j = 0$ and $j = 4$ assumptions. It is apparent that both the $j' = 0$ shoulder and the resurgence of wide-angle scattering into $j' = 4$ are not kinematic artifacts. The figure also demonstrates that the CM scattering angles attained in the present experiments are rather large (θ_{CM} up to 110°), corresponding to collisions governed mostly by the repulsive wall of the HF+Ar PE surface.

For quantitative comparison to theoretical scattering results in the CM frame, the uncertainty caused by the experimental distribution of initial rotational states may nevertheless be difficult to overcome. One notices that the CM-frame DCS's shown in Fig. 4.6 are reasonably parallel, but the steepness of the low-angle scattering implies that θ_{CM} is shifted significantly by the initial state selected for the transformations. Consequently, we believe that the present experimental results would best be compared to theoretical scattering calculations after transforming the latter to the laboratory frame.

For quantum mechanical scattering calculations, lab-frame comparisons would involve separate transformations for each $j \longrightarrow j'$ transition, followed by an averaging procedure over beam velocities and angles that differs for each such $j \longrightarrow j'$.

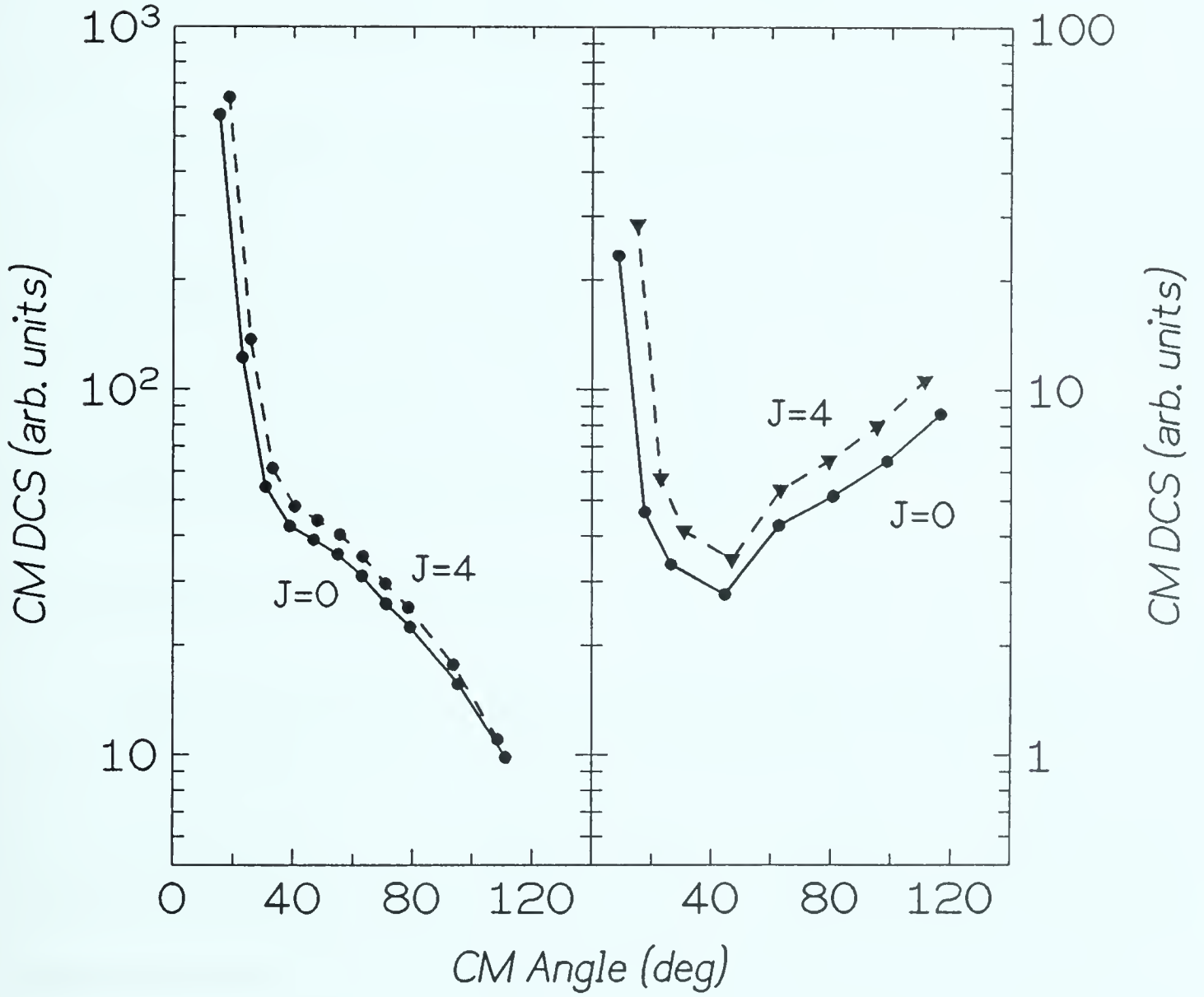

Figure 4.6: Differential cross sections transformed into the centre-of-mass (CM) frame for scattering into $j' = 0$ and $j' = 4$ final states. In each panel, the two sets of data correspond to lab $\rightarrow$ CM transformations constructed assuming initial states of $j = 0$ and $j = 4$ respectively, as described in Sec. 4.4.B.

On the other hand, classical trajectory calculations could profitably use Monte Carlo techniques to sample the velocity and angle distributions, and then use these to perform the CM $\rightarrow$ lab transformation after integrating each individual trajectory. Just such simulations are currently being performed.[61] We remark here that, for CM $\rightarrow$ lab transformations, only a single θ_{CM} can contribute to a given θ_{lab}, as long as $j' \leq 5$. Conversely, Fig. 4.5 shows that, for low scattering angles and $j' > j$, a given absolute value of θ_{CM} can contribute to two different θ_{lab}, both of which are positive.

Referring again to Fig. 4.5, it is apparent that the $j = 0 \longrightarrow j' = 6$ DCS should be strongly enhanced at laboratory scattering angles near $\theta_{\mathrm{lab}} \simeq 10°$ and 75°. Accordingly, we measured the scattering intensity at these two angles with the laser tuned to $j' = 6$, but were unable to distinguish any signal above the noise level. We conclude that the DCS into $j' = 6$ is therefore very small, at least near the corresponding CM scattering angles of $\theta_{\mathrm{CM}} \simeq 60°$ and 165°.

4.4.C Comparison to Previous Results

Scattering studies for several rare-gas+hydrogen halide systems have been performed in varying degrees of detail.[30,40–43] For HF+Ar, such measurements include the integral state-to-state rotational energy transfer cross sections of Barnes *et al.*[39] These measurements, except for the $j = 1 \longrightarrow j' = 0$ cross section, were found to be rather insensitive to the PE surface.[27] Since we did not measure the state-to-state DCS for all scattering angles, we cannot compare directly to the Barnes *et al.* results. More recently, Vohralik, Miller, and Watts measured the HF+Ar DCS under scattering conditions similar to ours, though their DCS was rotationally unresolved.[27] A comparison to these data is possible if we sum our results over all j', for each laboratory scattering angle. Such a summation effectively removes our rotational state sensitivity, at least for purposes of this comparison.

Some manipulation of the Vohralik *et al.* DCS results is also necessary for comparing to the present data. In particular, we must remove the Ar contribution to their scattering signal (using Fig. 8 of Ref. 27), since our laser-induced signals are totally insensitive to the scattered Ar. Secondly, we note that the bolometer accomodation energy of $\sim 430\,\mathrm{meV}$ assumed by Vohralik *et al.* almost ensures that their DCS corresponds to scattered particle flux, as do the current measurements (Sec. 4.3.B). Nevertheless, accounting for the acceleration of (elastically) scattered HF in the laboratory frame indicates that the bolometer is $\sim 7\%$ more sensitive at $\theta_{\mathrm{lab}} = 40°$ than at $10°$ for the Vohralik *et al.* data. Thirdly, we adjust their measured DCS to reflect our apparatus angular resolution, since it is wider than for the Vohralik *et al.* measurements. Finally, we normalize their results to ours at $\theta_{\mathrm{lab}} = 30°$ for convenience. We note that the distribution of rotational states in the incident HF beam is very similar for the two experiments.

The resulting comparison between the Vohralik *et al.* "total" DCS and the present summation over rotationally resolved DCS's is shown in Fig. 4.7. The agreement is excellent for $\theta_{\mathrm{lab}} \geq 20°$, but becomes poorer in the steeply rising region ($\theta_{\mathrm{lab}} \leq 15°$). We have already mentioned that our results for precisely these scattering angles could be adversely affected by difficulties in background compensation and by imprecise determination of the HF beam centreline (Sec. 4.3. A). In addition, the steep low-angle DCS renders our choice of apparatus angular resolution used in convoluting the Vohralik *et al.* results particularly crucial. It appears to us that any one of these three possible errors could account for $10 - 20\%$ of the discrepancy seen at $\theta_{\mathrm{lab}} = 10°$, implying that at least two of the above errors lead to systematic exaggeration of the present measurements for $\theta_{\mathrm{lab}} \leq 15°$. These errors are likely to be much lower for $j' \geq 3$ because the background populations in the incident molecular beam are much lower, and because the DCS at low scattering angles is much less steep. We remark here that since the Vohralik *et al.* data actually begin at $\theta_{\mathrm{lab}} = 3°$, it is unlikely that their results are systematically depressed

for $10° \leq \theta_{lab} \leq 15°$, unless they have grossly over-estimated the HF accomodation energy upon the bolometer.

Even if the present results are indeed exaggerated for $\theta_{lab} \leq 15°$ as suggested above, the qualitative shape of the DCS measurements is unaltered for each j'. Indeed, the present summed DCS shifted by 0.9° would reproduce the total Vohralik *et al.* DCS results almost exactly. Despite the errors apparent in the present measurements, we regard the agreement shown in Fig. 4.7 as quite gratifying, given the nature of the experiments and the manipulations required for comparing the corresponding results.

Detailed comparisons to spectroscopic results can only be made indirectly, through scattering patterns calculated from various PE surfaces proposed for HF+Ar. Such comparisons will be the subject of future reports.[61]

4.4.D Rainbow Scattering

For elastic atom+atom scattering in classical mechanics, rainbow structure in the DCS arises from an extremum in the deflection angle as a function of the impact parameter. Since this minimum in the classical deflection function cannot occur for any interaction that is purely repulsive, such "impact parameter" rainbows have been used extensively to characterize weak van der Waals attractive minima for many atom+atom interactions.[62] In the present case of atom+diatom scattering, the PE surface has one extra degree of freedom, assuming that we neglect the molecular bond length. The dependence of the interaction potential upon the atom+molecule orientation angle breaks the central field symmetry of the atom+atom case, allowing the collision to exert a torque on the molecule and thereby inducing some rotational inelasticity. The amount of this inelasticity may also exhibit extrema as a function of the molecular orientation, giving rise to "rotational rainbow" scattering.[9,10] Obviously such rainbows arise only for inelastic scattering (though an attractive well

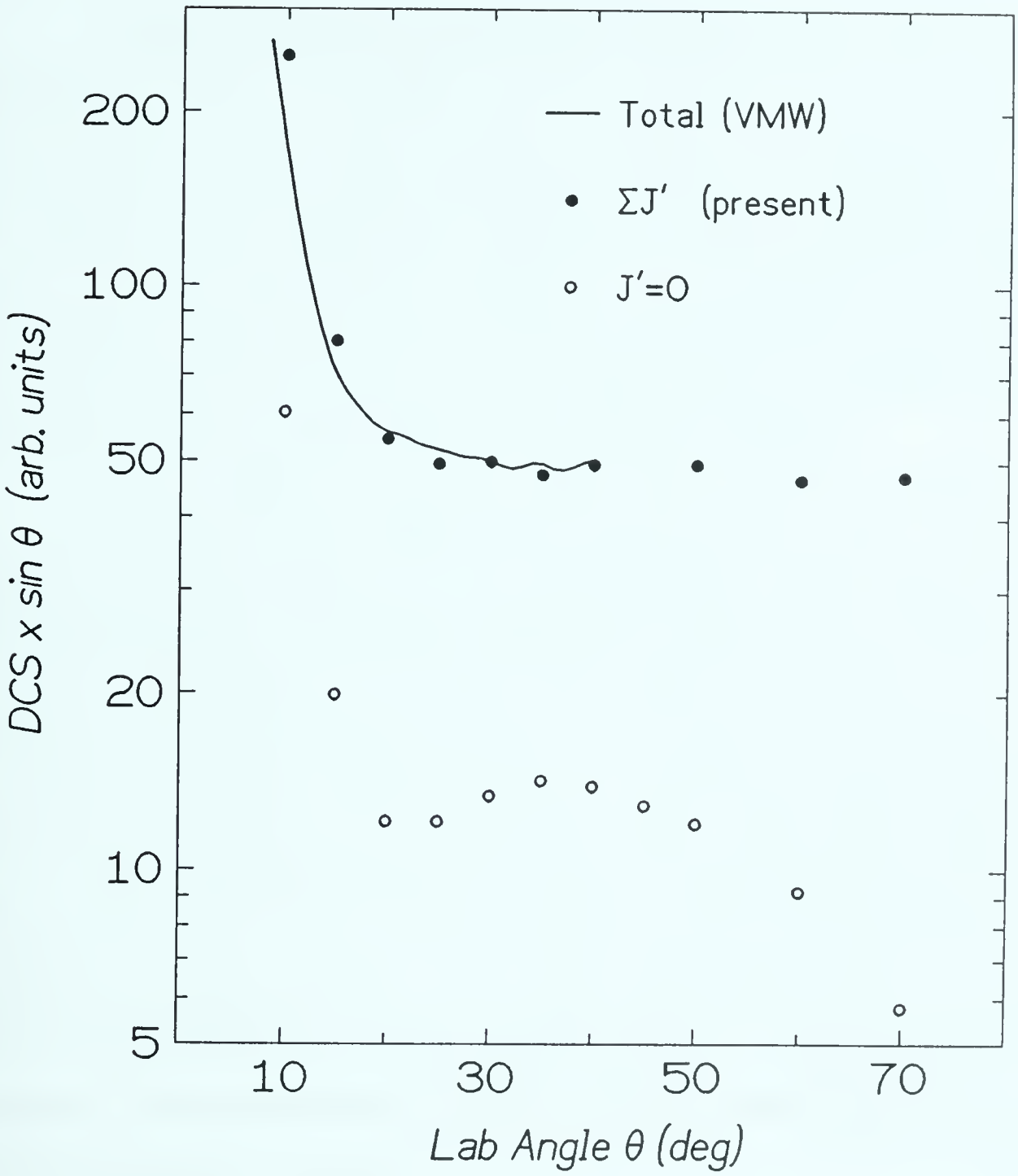

Figure 4.7: Comparison of HF+Ar "total" differential cross sections. Adjustments to the "VMW" data of Vohralik, Miller, and Watts (Ref. 27) are necessary for this comparison, and are described in Sec. 4.4.C. Data from the present work are summed over the populations measured into each j' final state. The two sets of data are arbitrarily normalized at a laboratory scattering angle of 30°. Also included is the $j' = 0$ state-resolved differential cross section demonstrating the loss of structure encountered by summing over j'. The vertical displacement is due to the population difference in $j' = 0$ relative to the total summed population.

is not required in this case), whereas impact parameter rainbows may arise for both inelastic and elastic scattering.[14,17]

4.4.D.1 The DCS for j′=0

Impact parameter rainbows have been observed in total DCS measurements for both HF+Ar[27] and HCl+Ar,[40,42] as well as for HF+Xe.[41] These DCS's all exhibited a shoulder, without complete resolution of the rainbow maximum [at least not on a plot of $I(\theta)$ *vs.* θ]. In all these cases, the angular position of the rainbow was reasonably well predicted by assuming an effective spherical potential for the HX+Rg interaction, and using the approximation that $\theta^r_{\rm CM} \simeq \frac{2\epsilon}{E_{\rm rel}}$ where ϵ is the attractive well depth and $E_{\rm rel}$ is the collision energy.[63]

For a collision energy just 17% higher than ours, Vohralik *et al.* anticipated a rainbow angle of $\sim 7°$ in the laboratory scattering frame using the spherically averaged ϵ for HF+Ar, very close to their observed rainbow at 5.5°.[27] These scattering angles are too close to the incident HF beam to be observed in the present experiments. They are also much too low to account for the shoulder observed in the present $j' = 0$ DCS in the $\theta \approx 25° - 40°$ region (Fig. 4.3). Even using $\epsilon = 26.5\,\text{meV}$,[19,37] the absolute minimum of the PE surface,[14] the rainbow is predicted to occur at $\theta^r_{\rm CM} \simeq 25°$. This is equivalent to only 17° in the laboratory scattering frame. It therefore appears that the $j' = 0$ shoulder cannot be explained as an impact parameter rainbow, at least not one based on any reasonable spherically symmetric potential.

For better visualization of impact parameter rainbows, the scattering data are sometimes plotted as $I(\theta)\cdot\sin\theta$ *vs.* θ, where $I(\theta)$ is the DCS. The minimum displayed in the $j' = 0$ cross section in Fig. 4.7 is obviously on the high scattering angle side of the impact parameter rainbow, since the ordinate must vanish as $\theta \to 0°$ due to the $\sin\theta$ weighting. Conversely, the $I(\theta)\cdot\sin\theta$ *vs.* θ plot for our data summed over j' is completely flat for $\theta \geq 25°$, demonstrating the increased structure

observable by resolving the rotational state of the scattered HF. The exaggerated angular dependence for the $j' = 0$ data shown in Fig. 4.7 reveals a prominent maximum around $\theta_{\rm lab} \simeq 35°$. This feature is somewhat reminiscent of the "hump" at 20° described by Buck and Schleusener[42] for their measurements of the HCl+Ar total DCS, but is much more prominent in the present $j' = 0$ results. So far as we know, this hump or shoulder has not yet been attributed to any specific feature of the PE surface, nor has it been labelled as any kind of a rainbow.

Early calculations performed by Buck and McGuire[44] for rotationally inelastic DCS scattering also show the presence of such a feature on model PE surfaces for HCl+Ar. Only model surfaces could be considered, since even the global topology characterizing the HCl+Ar surface was not known with assurance until two years later.[65,66] Consequently, the model surfaces were constructed with their absolute minima lying (a) nearly perpendicular to the HCl molecular axis, and along it in either the linear (b) Ar $\cdots$ ClH or (c) Ar $\cdots$ HCl configuration. The calculations showed the hump appearing most prominently for model potential (c), precisely the one now known to be correct.[20(a)] Indeed, Buck and McGuire adjusted their model PE surface for qualitative agreement[44] with the total DCS measured by Farrar and Lee,[40] and obtained (12 years earlier!) a well depth anisotropy qualitatively agreeing with Hutson's most accurate HCl+Ar PE surface.[20(a)]

The above discussion suggests that the $j' = 0$ shoulder for HF+Ar may contain useful information on the attractive anisotropy of the HF+Ar PE surface. We note that the shoulder is much more evident in the present experiments (it is just as prominent as the low-angle oscillation shown in Fig. 1 of Ref. 42), which also attain a higher degree of rotational state specificity than the HCl+Ar total DCS data.[40,42] On the other hand, the HF+Ar *attractive* anisotropy is already known much more accurately from detailed spectroscopic analysis[19,37] than scattering experiments are likely to provide for quite some time. Thus, the real utility of the

shoulder observed for $j' = 0$ probably lies in whatever sensitivity it has to the *interplay* between attractive and repulsive regions of the HF+Ar PE surface.

We also remark on the importance of realizing that some proportion of the observed DCS is caused by rotational de-excitation into $j' = 0$, since the incident beam has a significant population of $j = 1$ rotors. In this context, it is again interesting to note that the $j = 1 \longrightarrow j' = 0$ integral cross section appears to be particularly sensitive to attractive regions of the PE surface.[39]

4.4.D.2 The DCS for $j' \geq 4$

As j' increases, the DCS's displayed in Fig. 4.3 exhibit progressively weaker forward intensity relative to the wide-angle scattering. By the time we reach $j' = 4$, we see a rather small forward peak, and then a virtual disappearance of signal in the $\theta \approx 20° - 30°$ region. Finally the signal "re-appears" for $\theta \gtrsim 40°$, and then monotonically increases up to our maximum attainable scattering angle. For $j' = 5$, we cannot even see the signal at intermediate scattering angles, and it "re-appears" only for much wider scattering angles of $\theta \gtrsim 70°$, corresponding to $\theta_{CM} \gtrsim 110°$. It is therefore reasonable to suggest that such "hard" collisions sample the repulsive wall of the potential as if its attractive components hardly matter.

Under conditions of scattering off purely repulsive PE surfaces, rotational rainbows appear with the following typical characteristics: (a) they are "dark" on the low-angle side of the rainbow, *i.e.,* there is less intensity for scattering below the rainbow angle; and (b) the rainbow shifts to higher scattering angles as the rotational inelasticity increases[10,17] (the former behaviour is in contradistinction to impact parameter rainbows, which are "bright"—more intense—on the low-angle side[64]). If we attribute the small forward peak to some residue of elastic scattering, these two characteristics of rotational rainbows are precisely those observed for the $j' = 4 - 5$ DCS's.

Rotational rainbows have been shown to provide direct probes for the repulsive core anisotropy of the PE surface, and have often been successfully modeled by assuming a rigid ellipsoid to characterize the surface.[10] This assumption might also work for HF+Ar in collisions producing large j', thus avoiding effects due to attractive regions of the PE surface. Unfortunately for the present discussion, these models are usually based on the infinite-order sudden approximation (IOSA) in which rotational energy levels are approximated as being degenerate.[67] Such an approximation is unlikely to be quantitatively accurate for scattering of HF,[27] with its large rotational constant. This is especially true for the $j' = 4 - 5$ states being considered, since the difference between them constitutes 21% of the collision energy for the present experiments. Although we have not yet attempted to model the wide-angle features observed in the $j' = 4 - 5$ DCS's, we note that the appearance of rotational rainbows is not limited to IOSA theory. Rainbow structure is also evident for close-coupling and coupled-states calculations, appearing for example in both inelastic and elastic channels for HF+Ar.[27]

Modifications to rainbow structure in the presence of an attractive well have so far[1(b)] only been studied using model systems and classical[17,68] and/or sudden[68] approximations. Although quantal effects can significantly distort the classical DCS's, particularly for scattering of He–containing systems,[68] all these calculations show just the type of behaviour being observed experimentally, namely: "bright...dark" impact parameter rainbows for low j', then a flattening of the DCS as j' increases, followed finally by "dark...bright" rotational rainbows for high j'.[17] The results strongly suggest that the features seen for $j' = 4-5$ are indeed rotational rainbows, and that they provide rather direct probes for the repulsive regions of the HF+Ar PE surface.

4.5 SUMMARY and CONCLUSIONS

This work presents measurements for HF+Ar scattering into specific rotational states of the HF as a function of the scattering angle. The rotational distribution in the incident HF beam (*i.e.*, before scattering) is cooled by supersonic jet expansion, and resides mostly in $j = 0$ and 1. For the particular laser+bolometer detection scheme used, the scattering signals are analyzed to yield final rotational state-resolved differential cross sections (DCS). The most interesting features of the results are discussed in terms of:

(a) Strong forward scattering for all rotational states, though decreasing in prominence as j' increases. This is probably due mostly to elastic scattering;

(b) A broad shoulder in the $j' = 0$ DCS in the $25° - 40°$ region, perhaps attributable to the highly anisotropic attractive potential energy surface for HF+Ar;

(c) Significant scattering at the highest scattering angles accessible in the present experiments, equivalent to $\sim 110°$ in the centre-of-mass scattering frame; and

(d) Rotational rainbow structure for the highly inelastic transitions into $j' = 4$ and 5. These transitions correspond to transferring into rotation up to 42% and 64% respectively, of the available kinetic energy.

Concerted attempts to detect scattering into $j' = 6$, the maximum rotational state thermodynamically attainable, proved unsuccessful. This was despite potentially large kinematic enhancements near the laboratory-frame scattering angles at which these attempts were made. Conversely, kinematic distortion of the results is shown to be minor for the $j' \leq 5$ results, and the features (b) and (d) enumerated above transform intact into the centre-of-mass scattering frame under a variety of reasonable assumptions.

The state-resolved results are summed for comparison to the recent measurements of a rotationally unresolved HF+Ar DCS reported by Vohralik, Miller, and Watts.[27] The agreement is excellent except for 10° and 15°, the two lowest scattering angles included in the present measurements. The disagreement appears to be caused by some combination of high background near our rather wide HF beam, and to difficulties we encounter in directly comparing the two sets of experimental results. Nevertheless, agreement at 10° and 15° would be almost perfect if the HF beam centrelines for the two experiments were different by 0.9°; such a shift would not disturb the excellent agreement for any of the other scattering angles. Accordingly, we place an uncertainty of ±1° on the angular scale for the forward scattering peak in the present results. This error becomes insignificant for scattering angles beyond 15°, due to the much flatter appearance of the wide-angle DCS.

Currently underway are experiments with the HF beam seeded in He, yielding higher collision energies ($\sim 330\,\mathrm{meV}$) and co-incidentally also cooling the initial rotational distribution somewhat.[29,69] These experiments should allow further insights regarding the influence of the attractive well on the scattering. We are also conducting model scattering calculations in order to elucidate the dependence of the observed features on regions of the HF+Ar potential energy surface.[61]

It is readily apparent that the present results would provide an even more useful probe of the HF+Ar potential energy surface if the initial population distribution could be prepared with higher rotational state purity. Such state-to-state experiments may be achievable by using a second laser to pump the incident HF beam to a specific j state within $\nu = 1$ before the collision zone. Rotationally inelastic scattering would then occur within the $\nu = 1$ vibrational state, and the probe laser would be tuned to an $R_2(j')$ or $P_2(j')$ transition. Since the optical transitions are saturated, such an experiment might not be crippled by an overly severe loss of

signal intensity. Indeed, this type of arrangement—similar to the optical pumping experiments of Bergmann[70] and Pritchard and Kinsey[71] and their co-workers—may simultaneously allow state-to-state DCS measurements for scattering from the depleted rotational state within $\nu = 0$, provided that vibrational-to-translational energy transfer cross sections are small.[39]

REFERENCES:

1. For recent overviews, see

   (a) U. Buck, in *Atomic and Molecular Beam Methods Vol. 1*, edited by G. Scoles (Oxford University Press, Oxford, 1988), Chapter 18;

   (b) U. Buck, *ibid.*, Chapter 21;

   (c) P. J. Dagdigian, *ibid.*, Chapter 23.

2. U. Buck, F. Huisken, J. Schleusener, and H. Pauly, *Phys. Rev. Lett.* **38**, 680 (1977); U. Buck, *Faraday Disc. Chem. Soc.* **73**, 187 (1982).

3. W. R. Gentry and C. F. Giese, *J. Chem. Phys.* **67**, 5389 (1977).

4. M. Faubel, K.–H. Kohl, J. P. Toennies, K. T. Tang, and Y. Y. Yung, *Faraday Disc. Chem. Soc.* **73**, 205 (1982); M. Faubel, *Adv. At. Mol. Phys.* **19**, 345 (1983).

5. K. Bergmann, R. Engelhardt, U. Hefter, P. Hering, and J. Witt, *Phys. Rev. Lett.* **40**, 1446 (1978); U. Hefter, P. L. Jones, A. Mattheus, J. Witt, and K. Bergmann, *Phys. Rev. Lett.* **46**, 915 (1981); P. L. Jones, E. Gottwald, U. Hefter, and K. Bergmann, *J. Chem. Phys.* **78**, 3838 (1983).

6. W. D. Phillips, J. A. Serri, D. J. Ely, D. E. Pritchard, K. R. Way, and J. L. Kinsey, *Phys. Rev. Lett.* **41**, 937 (1978); W. P. Moskowitz, B. Stewart, R. M. Bilotta, J. L. Kinsey, and D. E. Pritchard, *J. Chem. Phys.* **80**, 5496 (1984).

7. J. Andres, U. Buck, F. Huisken, J. Schleusener, and F. Torello, *J. Chem. Phys.* **73**, 5620 (1980).

8. R. Schinke, W. Müller, W. Meyer, and P. McGuire, *J. Chem. Phys.* **74**, 3916 (1981); R. Schinke, W. Müller, and W. Meyer, *J. Chem. Phys.* **76**, 895 (1982).

9. L. D. Thomas, *J. Chem. Phys.* **67**, 5224 (1977).

10. R. Schinke and J. M. Bowman, in *Molecular Collision Dynamics*, edited by J. M. Bowman (Springer-Verlag, Berlin, 1982), Chapter 4.

11. M. Faubel and G. Kraft, *J. Chem. Phys.* **85**, 2671 (1986).

12. U. Buck, H. Meyer, M. Tolle, and R. Schinke, *Chem. Phys.* **104**, 345 (1986).

13. U. Buck, D. Otten, and R. Schinke, *J. Chem. Phys.* **82**, 202 (1985).

14. H. J. Loesch, *Adv. Chem. Phys. 52*, 421 (1980).

15. U. Buck, *Comments At. Mol. Phys.* **17**, 143 (1986).

16. M. Keil and H. R. Mayne, *Chem. Phys. Lett.* **85**, 456 (1982).

17. H. R. Mayne and M. Keil, *J. Phys. Chem.* **88**, 883 (1984).

18. For a recent and comprehensive review, see A. D. Buckingham, P. W. Fowler, and J. M. Hutson, *Chem. Rev.* **88**, 963 (1988).

19. D. J. Nesbitt, M. S. Child, and D. C. Clary, *J. Chem. Phys.* **90**, 4855 (1989).

20. (a) J. M. Hutson, *J. Chem. Phys.* **89**, 4550 (1988);

    (b) J. M. Hutson, *J. Chem. Phys.* **91**, 4448 (1989).

21. S. E. Novick, P. Davies, S. J. Harris, and W. Klemperer, *J. Chem. Phys.* **59**, 2273 (1973).

22. G. T. Fraser and A. S. Pine, *J. Chem. Phys.* **85**, 2502 (1986).

23. R. L. Robinson, D. Gwo, D. Ray, and R. J. Saykally, *J. Chem. Phys.* **86**, 5211 (1987).

24. M. D. Marshall, A. Charro, H. O. Leung, and W. Klemperer, *J. Chem. Phys.* **83**, 4924 (1985).

25. Z. S. Huang, K. W. Jucks, and R. E. Miller, *J. Chem. Phys.* **85**, 6905 (1986).

26. B. J. Howard and A. S. Pine, *Chem. Phys. Lett.* **122**, 1 (1985).

27. P. F. Vohralik, R. E. Miller, and R. O. Watts, *J. Chem. Phys.* **90**, 2182 (1989).

28. T. E. Gough, R. E. Miller, and G. Scoles, *Appl. Phys. Lett.* **30**, 338 (1977).

29. Y. B. Fan, L. J. Rawluk, Y. Apelblat, and M. Keil, *J. Opt. Soc. Am. B* **8**, 1218 (1991).

30. C. V. Boughton, R. E. Miller, P. F. Vohralik, and R. O. Watts, *Mol. Phys.* **58**, 827 (1986).

31. T. A. Dixon, C. H. Joyner, F. A. Baiocchi, and W. Klemperer, *J. Chem. Phys.* **74**, 6539 (1981).

32. S. J. Harris, S. E. Novick, and W. Klemperer, *J. Chem. Phys.* **60**, 3208 (1974).

33. M. R. Keenan, L. W. Buxton, E. J. Campbell, A. C. Legon, and W. H. Flygare, *J. Chem. Phys.* **74**, 2133 (1981).

34. C. M. Lovejoy, M. D. Schuder, and D. J. Nesbitt, *J. Chem. Phys.* **85**, 4890 (1986).

35. C. M. Lovejoy, M. D. Schuder, and D. J. Nesbitt, *Chem. Phys. Lett.* **127**, 374 (1986).

36. C. Douketis, J. M. Hutson, B. J. Orr, and G. Scoles, *Mol. Phys.* **52**, 763 (1984).

37. J. M. Hutson and B. J. Howard, *Mol. Phys.* **45**, 791 (1982).

38. A. Kumar and W. J. Meath, *Mol. Phys.* **54**, 823 (1985).

39. J. A. Barnes, M. Keil, R. E. Kutina, and J. C. Polanyi, *J. Chem. Phys.* **72**, 6306 (1980); **76**, 913 (1982).

40. J. M. Farrar and Y. T. Lee, *Chem. Phys. Lett.* **26**, 428 (1974).

41. C. H. Becker, P. W. Tiedmann, J. J. Valentini, Y. T. Lee, and R. B. Walker, *J. Chem. Phys.* **71**, 481 (1979).

42. U. Buck and J. Schleusener, *J. Chem. Phys.* **75**, 2470 (1981).

43. W. D. Held, E. Piper, G. Ringer, and J. P. Toennies, *Chem. Phys. Lett.* **75**, 260 (1980).

44. U. Buck and P. McGuire, *Chem. Phys.* **16**, 101 (1976).

45. L. Beneventi, P. Casavecchia, and G. G. Volpi, *J. Chem. Phys.* **84**, 4828 (1986).

46. L. Beneventi, P. Casavecchia, F. Vecchiocattivi, G. G. Volpi, D. Lemoine, and M. H. Alexander, *J. Chem. Phys.* **89**, 3505 (1988).

47. L. J. Danielson, K. M. McLeod, and M. Keil, *J. Chem. Phys.* **87**, 239 (1987).

48. L. J. Danielson and M. Keil, *J. Chem. Phys.* **88**, 851 (1988).

49. L. J. Rawluk and M. Keil, *J. Opt. Soc. Am. B* **6**, 1278 (1989).

50. T. Ellenbroek, J. P. Toennies, M. Wilde, and J. Wanner, *J. Chem. Phys.* **75**, 3414 (1981).

51. H. B. Sachse, *Semiconducting Temperature Sensors and Their Applications* (Wiley, New York, 1975), pp.99 – 104.

52. J. J. Hinchen, *J. Appl. Phys.* **45**, 1818 (1974).

53. Z. S. Huang, K. W. Jucks, and R. E. Miller, *J. Chem. Phys.* **85**, 3338 (1986).

54. O. Svelto, *Principles of Lasers* (Plenum, New York, 1982), pp. 247 – 250.

55. R. Altkorn and R. N. Zare, *Ann. Rev. Phys. Chem.* **35**, 265 (1984).

56. R. E. Miller, *Ph.D. Thesis* (University of Waterloo, 1980).

57. P. Eckelt and H. J. Korsch, *J. Phys. B* **10**, 741 (1977); R. Schinke and H. J. Korsch, *Chem. Phys. Lett.* **74**, 449 (1980).

58. V. Khare, D. J. Kouri, and D. K. Hoffmann, *J. Chem. Phys.* **74**, 2275 (1981); **76**, 4493 (1982).

59. A. Mattheus, A. Fischer, G. Ziegler, E. Gottwald, and K. Bergmann, *Phys. Rev. Lett.* **56**, 712 (1986).

60. K. Bergmann, in *Atomic and Molecular Beam Methods Vol. 1*, edited by G. Scoles (Oxford University Press, Oxford, 1988), Chapter 12.

61. J. J. Barrett, H. R. Mayne, L. J. Rawluk, and M. Keil, *to be published.*

62. R. A. Aziz, in *Inert Gases: Springer Series in Chemical Physics* **34**, edited by M. L. Klein, (Springer-Verlag, Berlin, 1984), Chapter 2.

63. M. A. D. Fluendy and K. P. Lawley, *Chemical Applications of Molecular Beam Scattering* (Chapman and Hall, London, 1973), Chapter 2.

64. R. B. Bernstein, *Adv. Chem. Phys.* **10**, 75 (1966).

65. A. M. Dunker and R. G. Gordon, *J. Chem. Phys.* **64**, 354 (1976).

66. S. L. Holmgren, M. Waldman, and W. Klemperer, *J. Chem. Phys.* **69**, 1661 (1978).

67. D. J. Kouri, in *Atom–Molecule Collision Theory*, edited by R. B. Bernstein (Plenum, New York, 1979), Chapter 9.

68. R. Schinke, H. J. Korsch, and D. Poppe, *J. Chem. Phys.* **77**, 6005 (1982).

69. T. E. Gough and R. E. Miller, *J. Chem. Phys.* **78**, 4486 (1983).

70. K. Bergmann, U. Hefter, and J. Witt, *J. Chem. Phys.* **72**, 4777 (1980).

71. J. A. Serri, C. H. Becker, M. B. Elbel, J. L. Kinsey, W. P. Moskowitz, and D. E. Pritchard, *J. Chem. Phys.* **74**, 5116 (1981); J. A. Serri, J. L. Kinsey, and D. E. Pritchard, *J. Chem. Phys.* **75**, 663 (1981).

CHAPTER 5

QUANTUM EFFECTS in the INELASTIC SCATTERING of HF and DF by ARGON†

5.1 INTRODUCTION

Intermolecular potential energy (PE) surfaces for atom+diatom van der Waals interactions are usually probed by either spectroscopic or scattering techniques. Dramatic improvements to the PE surface around the equilibrium geometry of bound complexes[1] are being achieved as spectroscopic studies attain higher resolution,[2] while state-to-state scattering serves a complementary role in characterizing PE surfaces with hardly any attraction at all.[3] For the weakly anisotropic and weakly attractive hydrogen–rare gas systems, it has been possible to characterize both attractive and repulsive regions simultaneously.[4]

For more strongly attractive PE surfaces, scattering measurements have not yet combined high precision with simultaneous resolution of rotational inelasticities.[5–7] Interactions on attractive PE surfaces are expected to exhibit features typical both of attractive systems (*e.g.*, the impact parameter rainbows familiar from atom+atom scattering), and of repulsive systems (*e.g.*, rotational rainbow structure).[8] Scattering studies of such interactions are then particularly important[9] in elucidating the balance[10] between attractive and repulsive forces during collisions that induce energy transfer.

This chapter compares exact quantum close-coupling (CC), infinite order sudden (IOS) approximation, and classical trajectory (CT) scattering calculations with previous measurements of the rotationally-resolved differential cross

† Part of this work has been published.
L.J.Rawluk, M. Keil, M. H. Alexander, H. R. Mayne and J. J. C. Barrett,
Chem. Phys. Lett. **202**, 291 (1993).

section (DCS) for crossed-beam scattering of HF by Ar.[11] Earlier measurements of the total (*i.e.*, rotationally unresolved) DCS[12] correspond to summing over the final rotational state of the scattered HF, which completely obscures the prominent quantal structure that appears in the rotationally-resolved scattering data.

This structure is most apparent in the elastic and weakly-inelastic DCS's originating in $j = 0$. Corresponding neither to diffraction oscillations[4,7] nor to rotational rainbows,[3,13,14] this structure is due to novel interference effects in rotationally inelastic scattering. The CC calculations also show particular sensitivity to isotopic substitution of HF by DF. Finally, the scattering measurements complement extensive and very detailed spectroscopic data for the strongly anisotropic attractive well of the HF+Ar PE surface,[1] and may be useful in improving its repulsive wall.

5.2 APPARATUS and CALCULATIONS

The crossed molecular beams apparatus and experimental parameters used to measure DCS's for HF scattered by Ar are described elsewhere in detail.[11,15] Both the atomic and molecular beams are supersonic: most of the incident HF beam is cooled into the $j = 0$ and $j = 1$ rotational states, with rapidly diminishing populations up to $j = 5$. The collision energy is 120 meV; the distribution of collision velocities peaks at 1.31 km/sec with a FWHM spread of 17% after convolution over all instrumental parameters. Beam angular divergences are 3°, as is the detector acceptance angle. The rotational state of the scattered HF is resolved by chemical laser excitation[16,17] between the scattering zone and a rotatable liquid He-cooled bolometer detector.

To compare signals measured for rotationally state-resolved inelastic scattering[11] to corresponding calculated DCS's, four different PE surfaces for the HF+Ar interaction proposed in the recent literature are used (displayed in Figure 5.1). Three of these potentials are based primarily on spectroscopic observations of the HF•Ar van der Waals complex.[1,18,19] The fourth is based on Hartree–Fock calculations for the repulsive wall,[12] and is adjusted for agreement with some of the spectroscopic observations.[20] The most recent and detailed of these four PE surfaces is Hutson's H6(4,3,2) potential[1] (abbreviated hereafter as "H6").

State-to-state DCS's for collisions of Ar with the closed-shell HF molecule are generated in the center-of-mass frame using fully-converged CC calculations.[21] For each initial rotational level j ($0 \leq j \leq 5$), four different collision energies are required to properly average over the beam velocity and angular distributions. This necessitates calculations at 24 different total energies in the range of $82 - 242$ meV. In all cases the number of rotational levels included in the channel expansion include one (and at the lower energies, two) energetically inaccessible levels. For convergence of the elastic cross sections in the forward direction, it is necessary to determine scattering S matrices at up to 400 values of the

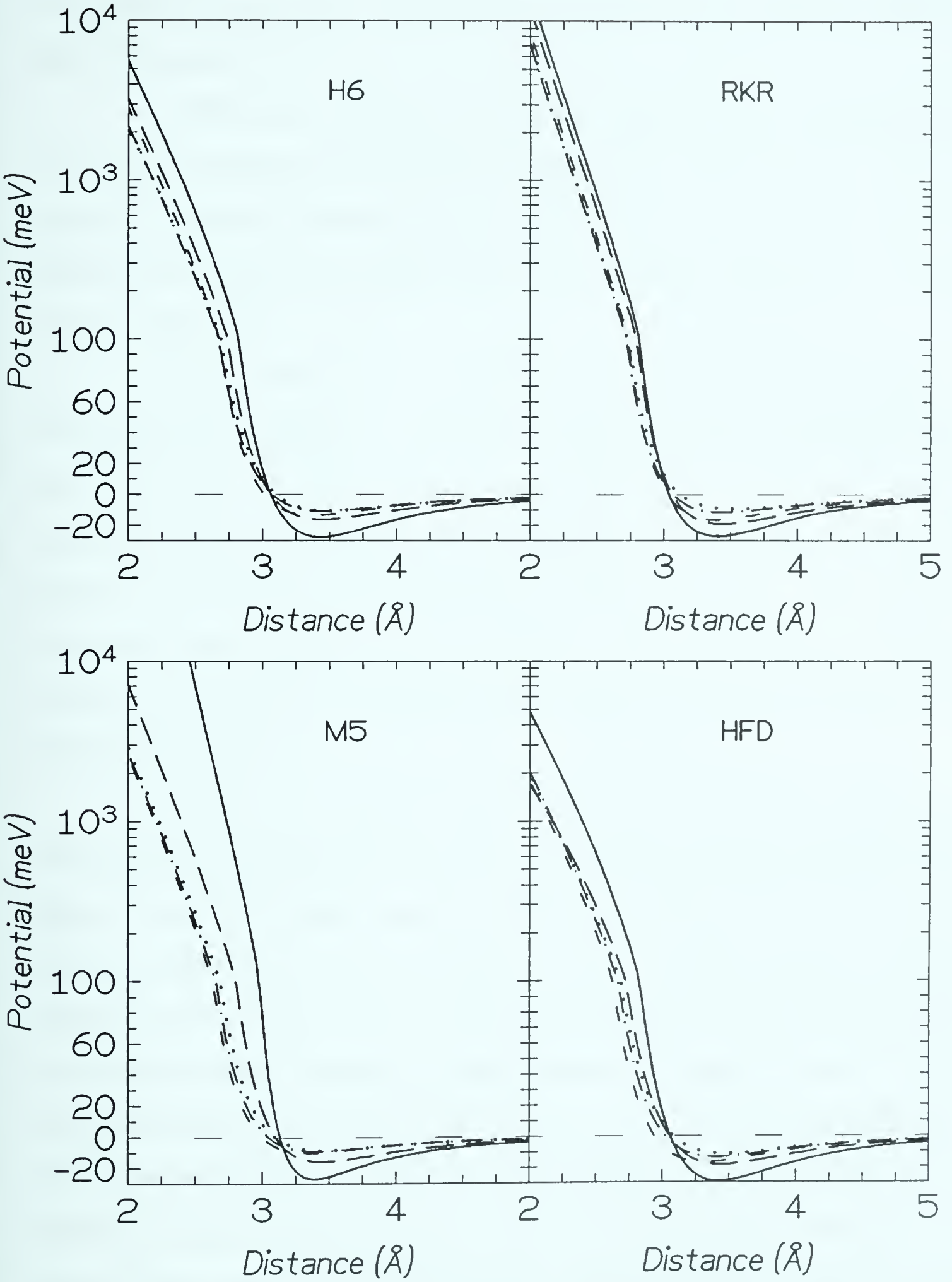

Figure 5.1. Potential energy as a function of HF–Ar separation at different angles for Ref. 1 (H6); Ref. 18 (M5); Ref. 19 (RKR); Ref. 20 (HFD).
Solid – 0°; long-dashed – 45°; dotted – 90°; dash-dotted – 135°; short-dashed – 180°.

total angular momentum J. All calculations are carried out using the HIBRIDON scattering package.[22]

State-to-state DCS's for the HF+Ar system are also calculated in the center-of-mass frame using the IOS approximation.[23] Four different energies are required to properly average over beam velocities and angular distribution. Two rotational levels above the energetic limit were included in inelastic $0 \rightarrow j''$ cross section summations.

The calculated state-to-state DCS's, determined every 0.1° for angles up to 60° and every 1° thereafter, are subsequently transformed to the laboratory frame and summed over the initial rotational states weighted by the measured rotational population.[11] This procedure properly reproduces the experimental conditions of detecting one particular HF rotational state after the collision. To account for the arbitrary intensity scale of the measurements, the experimental and calculated DCS's are normalized to one another using a single scaling factor, common to all final rotational states j'.

Additional CC calculations are performed for state-to-state transitions, without energy averaging and without direct reference to the experimental measurements. These DCS's exhibit quantum diffraction oscillations having a 1° angular frequency, which could be observed only with a high-resolution apparatus.[7] By averaging over a 2° angular window, these rapid oscillations in the calculated DCS's are removed to avoid obscuring the broad features that might be observable in future experiments. The surviving quantum effects are examined by comparison with classical trajectory (CT) calculations. The rigid-rotor trajectory calculations are carried out using a standard program,[10] with the rotational action "binned" to the nearest integer value.[24] To obtain the DCS, variable angular bin sizes are chosen so that the relative error in each bin is roughly the same. Also, isotope effects for the CC calculations are examined by substituting DF for HF. All state-to-state

calculations are conducted at a single fixed collision energy of 135 meV on the H6 PE surface.[1] Finally, a series of analytical modifications to the H6 PE surface are incorporated to help understand which parts of the PE surface most strongly influence the state-to-state DCS's.

5.3 RESULTS and DISCUSSION

5.3.A Laboratory Frame

There is a clear trend in the experimental data that is believed to be of fundamental significance in the scattering of a rigid-rotor by a structureless particle. The $j' = 0$ DCS has a strong forward peak followed by a shoulder at intermediate angles, and a fall in intensity at high angles. Through $j' = 1, 2,$ and 3 we see the forward peak declining, and the wide angle DCS flattens out. The $j' = 4$ and 5 DCS's show declining forward intensity and both display minima at $\theta_{\rm lab} = 20 - 30°$, followed by a resurgence of signal at wide scattering angles. Understanding this pattern will be the focus of the remainder of this chapter.

Table 5.1 provides a statistical overview for the ability of several PE surfaces to reproduce the experimental measurements using two different calculational techniques. The CC results are clearly better than the IOS, and the best PE surface is Hutson's H6 potential.[1] Figures 5.2a – 5.2d present a visual comparison of the experimentally measured DCS's to those calculated via the CC technique for all four potentials. Note that though the CC calculations reproduce several prominent features of the experiment, agreement is not quantitative everywhere.

The origin of each potential may, in part, explain its ability to reproduce the experimental observations: the H6 PE surface (Figure 5.2a) is obtained by doing a simultaneous multiproperty fit of several different spectroscopic properties, namely vibrational frequencies, rotational and centrifugal distortion constants, dipole moments, and spin-spin coupling constants. The repulsive wall slope is determined from *ab initio* calculations,[12] and is adjusted to smoothly join with the potential in the attractive well. This large data set is most likely the reason why it is best at reproducing the present scattering results. The M5[18] PE surface is the poorest at regenerating the experimental features (Figure 5.2b). Most likely, this observation goes hand-in-hand with the fact that the M5 surface is obtained by fitting

Table 5.1. Potential Energy Surfaces and their Predictive Quality for the DCS's.

	H6	RKR	HFD	M5
Reference	1	19	20	18
$CC\ \delta$[a]	2.4	3.0	3.9	7.8
$CC\ \delta$ w/o $j'=0$[a,b]	2.0	1.8	2.7	4.9
$IOS\ \delta$[a,c]	6.7	9.1	8.8	6.5
$\Delta r_{\pi/2}$ (Å)[d]	0.13	0.08	0.14	0.29
Δr_{π} (Å)[d]	0.15	0.09	0.20	0.35

[a] A weighted, dimensionless measure of predictive quality discussed in Ref. 15; $\delta \leq 1$ corresponds, on average, to reproducing all the DCS data to within their error bars.

[b] Calculated without including the experimental data for the j'=0 DCS.

[c] Calculated using the experimental error in j'=0,1, and 2 DCS's only. This limited data set is necessary for the purpose of comparison since inclusion of all ($0 \leq j' \leq 5$) DCS's in the fitting procedure results in an overly large, and thus numerically indistinguishable, fitting quality δ for each PE surface.

[d] Change in position of the repulsive wall from the 0° orientation (corresponding to Ar···HF) to 90°, or to 180°, at a potential energy of 100 meV.

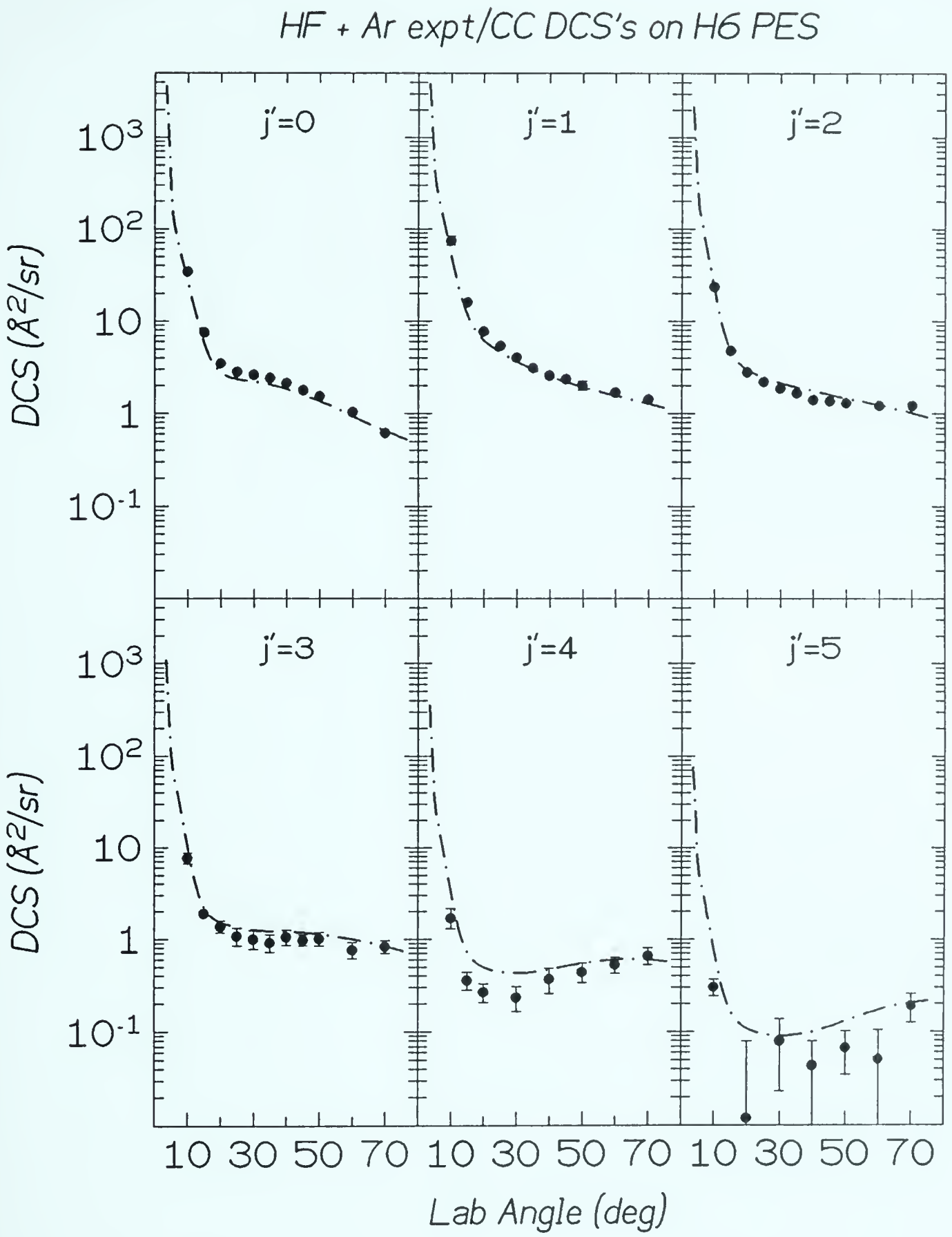

Figure 5.2a. Experimental differential cross section measurements from Ref. 11 as functions of the laboratory scattering angle $\theta_{\rm lab}$ and the final HF rotational state j'. The curves for all j' are generated from the close-coupling calculations for the H6 PE surface[1].

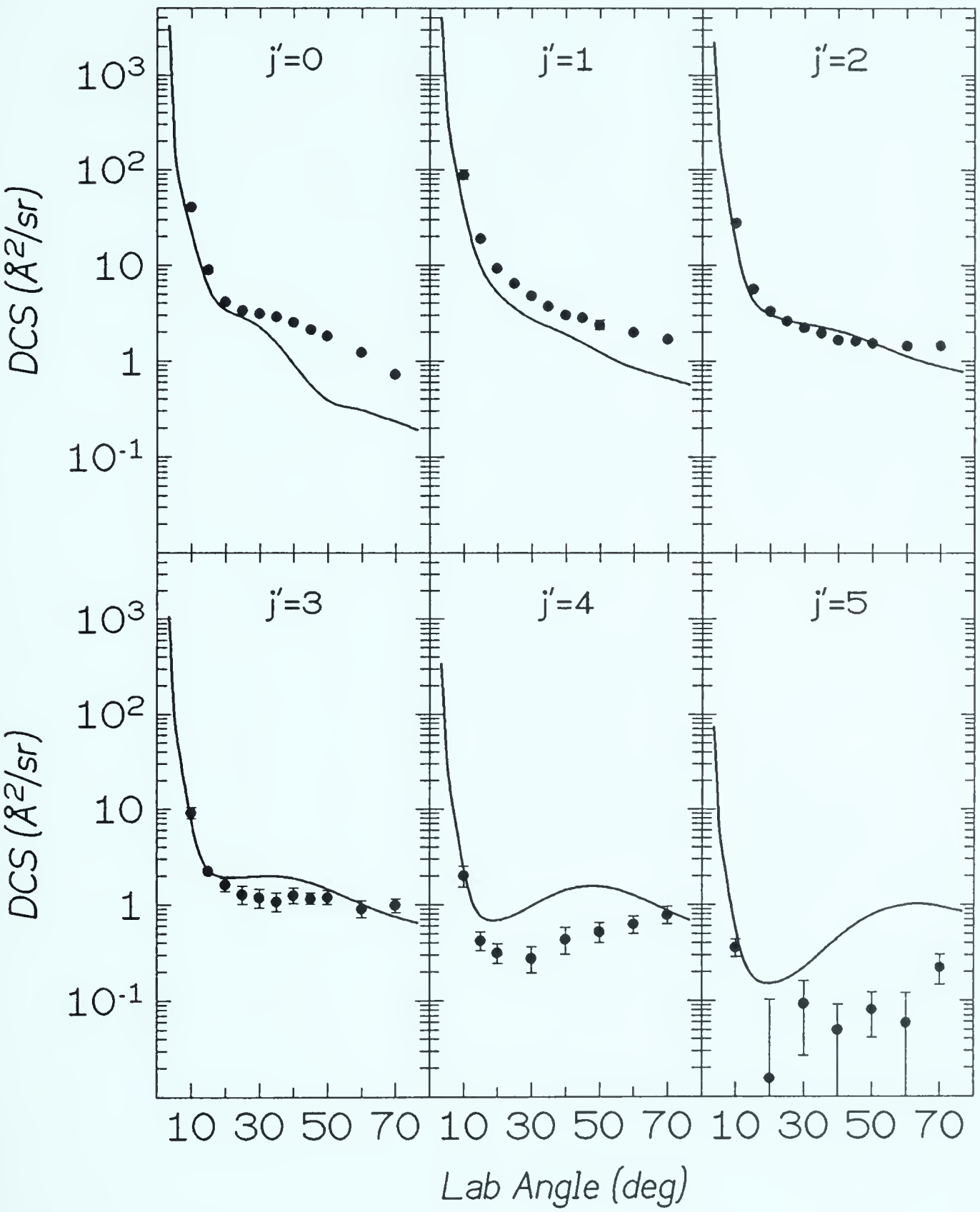

Figure 5.2b. Experimental differential cross section measurements from Ref. 11 as functions of the laboratory scattering angle $\theta_{\rm lab}$ and the final HF rotational state j'. The curves for all j' are generated from the close-coupling calculations for the M5 PE surface[18].

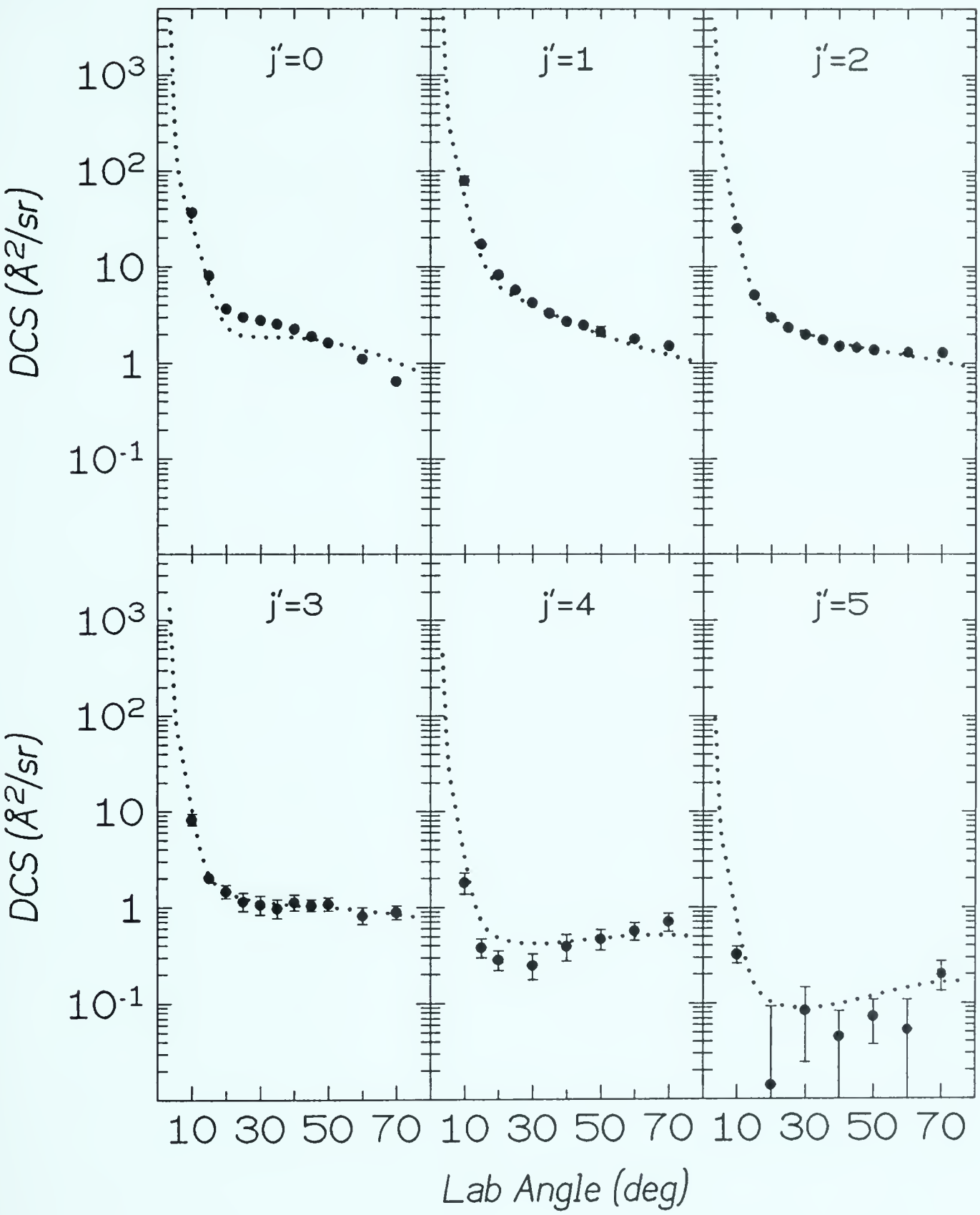

Figure 5.2c. Experimental differential cross section measurements from Ref. 11 as functions of the laboratory scattering angle $\theta_{\rm lab}$ and the final HF rotational state j'. The curves for all j' are generated from the close-coupling calculations for the RKR PE surface[19].

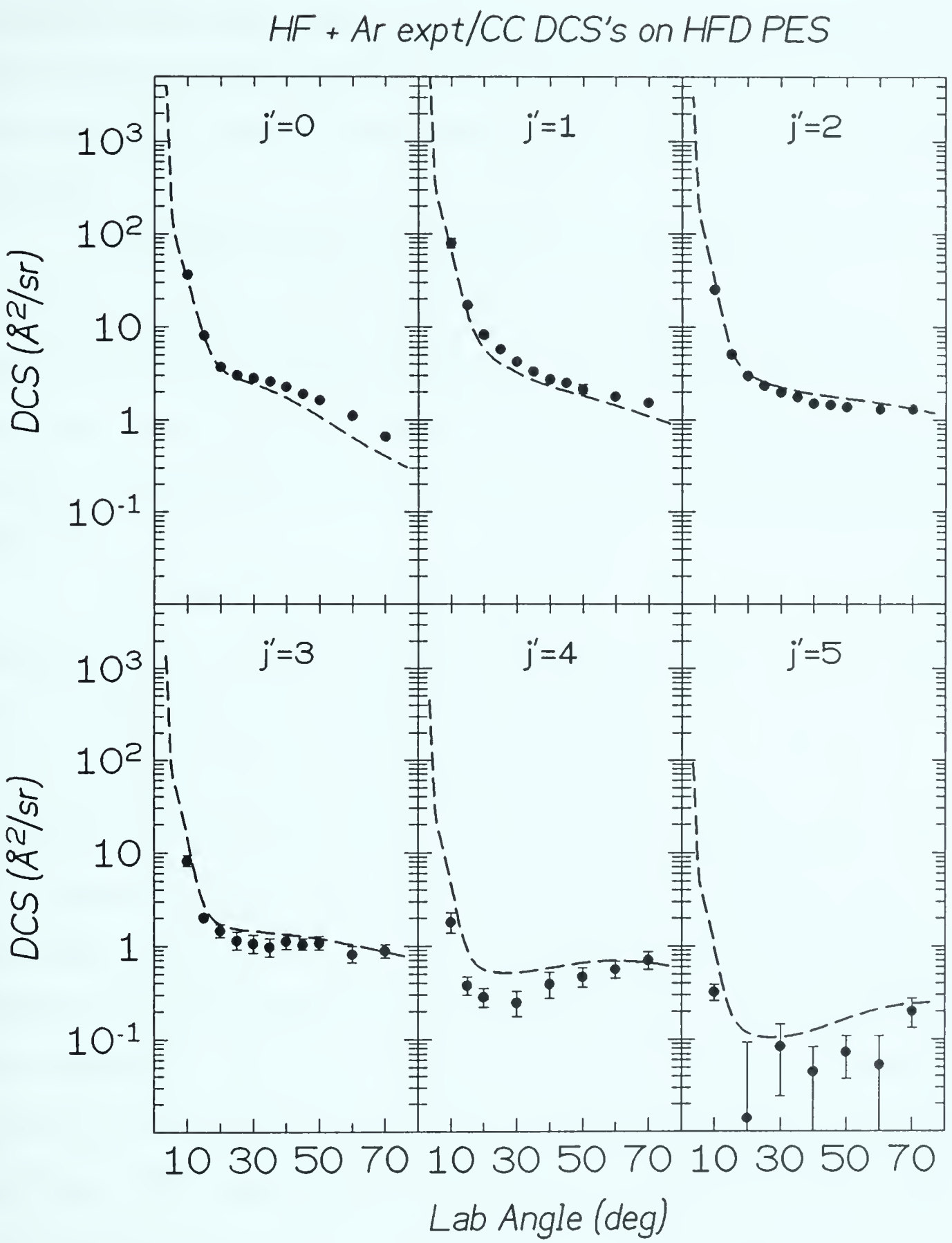

Figure 5.2d. Experimental differential cross section measurements from Ref. 11 as functions of the laboratory scattering angle $\theta_{\rm lab}$ and the final HF rotational state j'. The curves for all j' are generated from the close-coupling calculations for the HFD PE surface[20].

a general potential energy function (the Maitland-Smith parameterization[25,26]) to a small experimental data set sensitive exclusively to the absolute Ar $\cdots$ HF potential well minimum (*i.e.*, molecular beam rotational spectra of the HF•Ar van der Waals molecule[27]).

The RKR[19] (Figure 5.2c) and HFD[20] (Figure 5.2d) potentials both fail to accurately reproduce the measured DCS for scattering into $j' = 0$, even though they are experimentally indistinguishable from the H6 results for DCS's into $j' > 0$. On the other hand, if one only considers the limited circumstance of $j' > 0$ DCS's, the RKR PE surface most accurately reproduces the experimental measurements (Table 5.1).

The RKR PE surface was determined by studying the infrared absorption spectroscopy of the HF•Ar van der Waals molecule with the HF molecule in the $\nu = 1$ vibrational state. Inversion of this data gave the potential well shape near the minimum as a Legendre expansion up to the P_2 term. The long range attraction is represented by a simple r^{-6} term, and the repulsive wall is given by $e^{-\alpha r}$ which is spliced to the inner branch inversion data. The fact that this potential was developed with HF in the $\nu = 1$ vibrational state lends itself to questioning the reliability of scattering calculations where the HF is in $\nu = 0$. To answer this question, additional CC calculations using Hutson's H6 vibrationally excited ($\nu_{HF} = 1$) PE surface[1] were carried out. The calculations suggest only modest changes, confined to $\theta_{lab} > 30°$, would result if the RKR ($\nu_{HF} = 1$) potential could be adjusted for scattering of ground-state HF (Figure 5.3). It is also noted that treatment of the HF as a rigid rotor or as having zero point vibrational energy makes little difference to the scattering calculations since all vibrational channels are energetically closed under the experimental scattering conditions.[23]

The poorer agreement obtained for DCS's calculated using the HFD potential may reflect its origin. The repulsive wall is obtained from Hartree-Fock

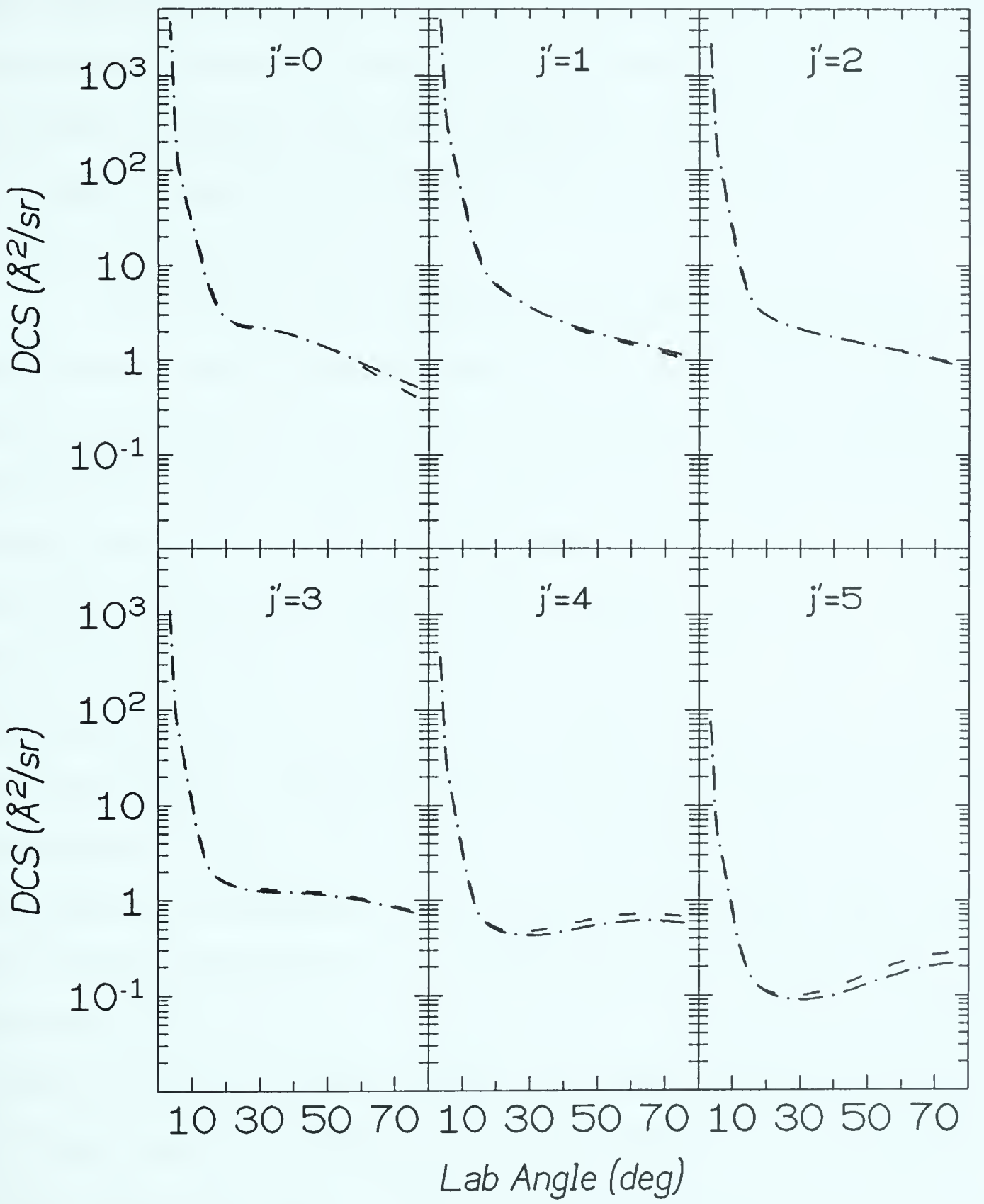

Figure 5.3. CC DCS's on the H6 PE surface[1] for HF in $\nu = 0$ (dash-dotted line) versus the same calculation, but with HF in $\nu = 1$ (dashed line). Note the marginal differences in the DCS's restricted to wide angle scattering only.

self-consistant-field calculations, while the attractive well is a two-center dispersion series. The potential was used to calculate a set of spectroscopic constants obtained from molecular beam rotational spectra,[27] and the lack of agreement was corrected by arbitrarily adjusting the dispersion coefficients by 27% to provide the best fit to the rotational spectra data. This limited data set most likely results in a less accurately characterized PE surface.

Figures 5.4a – 5.4d compare the measured DCS's to those calculated by the IOS method using the same four potentials. The calculations are particularily poor in quantitatively or even qualitatively reproducing the most prominent experimental features such as the shoulder at $\sim 30°$ for $j' = 0$ or the resurgence of signal at large angles for $j' = 4$ and 5. All PE surfaces fit the experimental data very poorly, and a non-linear least-squares fit of an arbitrary scaling factor used to adjust the calculated results to the experimental data demonstrates that an inversion in fitting quality has occured with the M5 PE surface most accurately agreeing with experiment (Table 5.1). Most likely this is the result of it being the only surface that generates a shoulder in the $j' = 0$ IOS calculation. Also, only $j' = 0, 1, 2$ were included in the least-squares fitting algorithm, even though it readily appears that the M5 PE surface would also provide the best fit to the high j' data. The descrepancy between experiment and calculation if all j' are included in the fitting procedure is so great for all four PE surfaces that there is no numerical distinction in the fitting quality δ, and therefore, the results in Table 5.1 are obtained with a truncated experimental data set to allow for at least a cursory evalution of the quality of the PE surfaces. Further discussion of final rotational state resolved IOSA DCS's is limited due to the relative inability to reproduce experimental features.

Returning to the discussion of the close-coupling results, it is evident when decomposing the rotational state summed CC DCS's into their state-to-state contributions that an odd situation arises in the $j' = 0$ and $j' = 1$ plots in Figure 5.5.

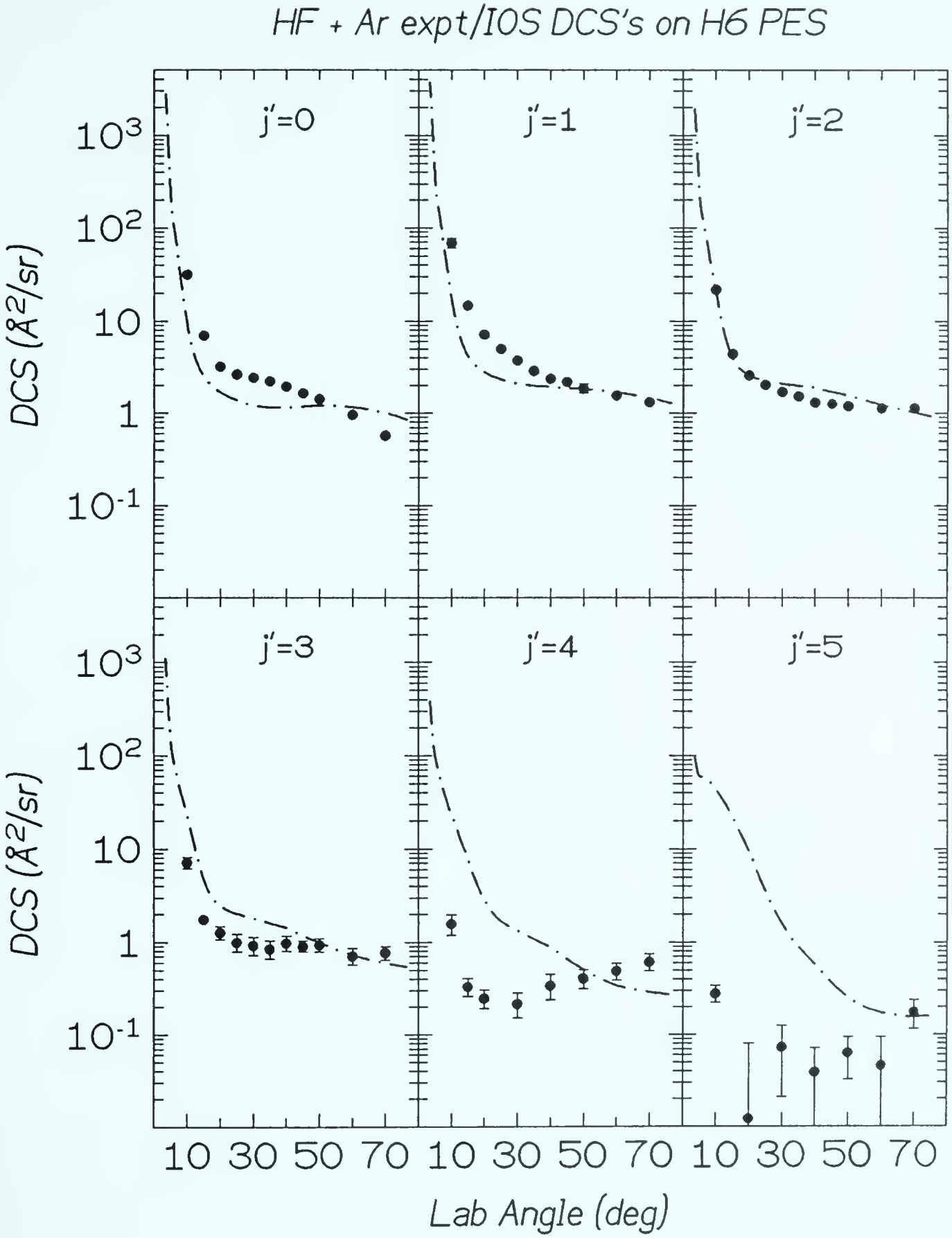

Figure 5.4a. Experimental differential cross section measurements from Ref. 11 as functions of the laboratory scattering angle $\theta_{\rm lab}$ and the final HF rotational state j'. The curves for all j' are generated from the infinite order sudden approximation calculations for the H6 PE surface[1].

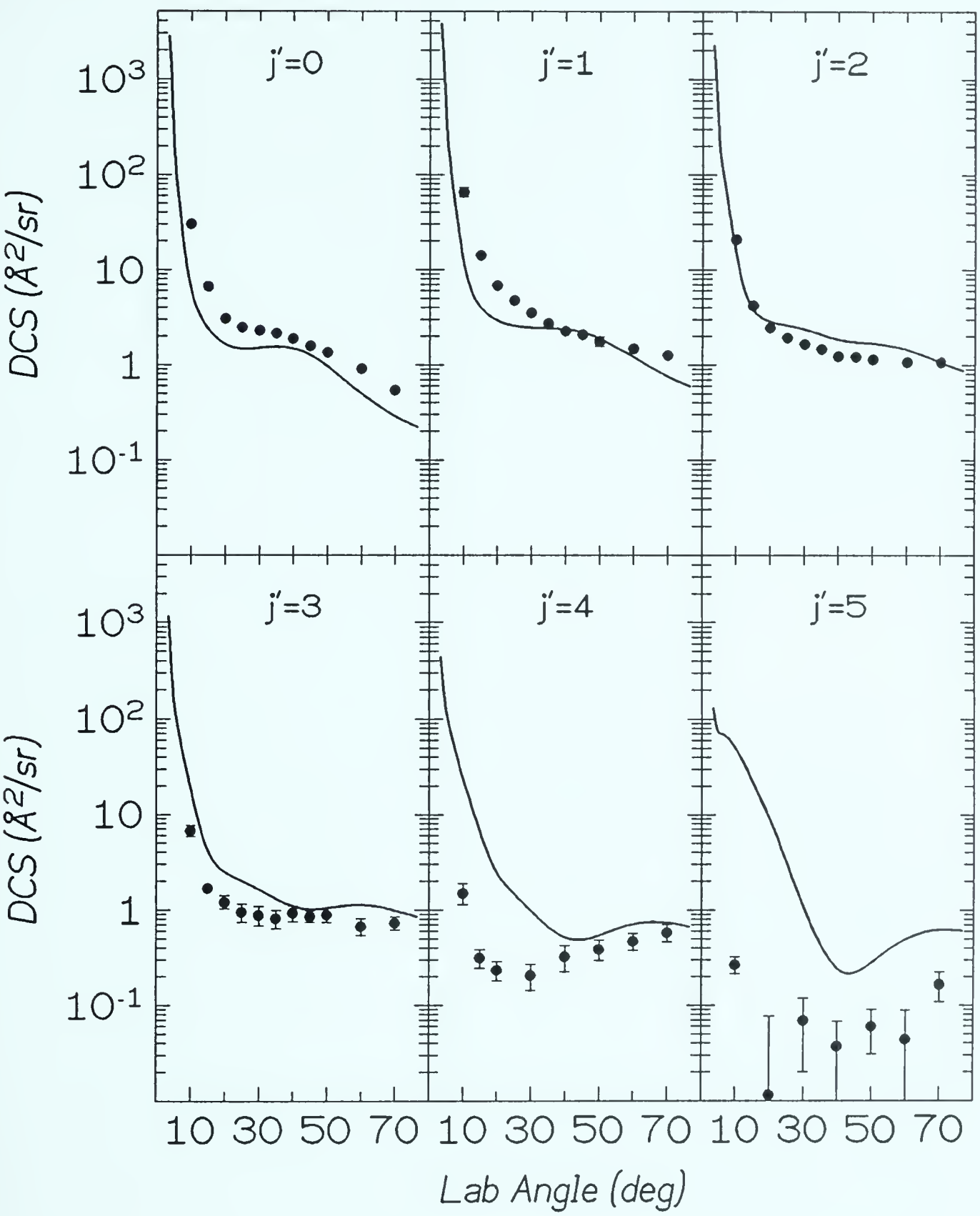

Figure 5.4b. Experimental differential cross section measurements from Ref. 11 as functions of the laboratory scattering angle $\theta_{\rm lab}$ and the final HF rotational state j'. The curves for all j' are generated from the infinite order sudden approximation calculations for the M5 PE surface[18].

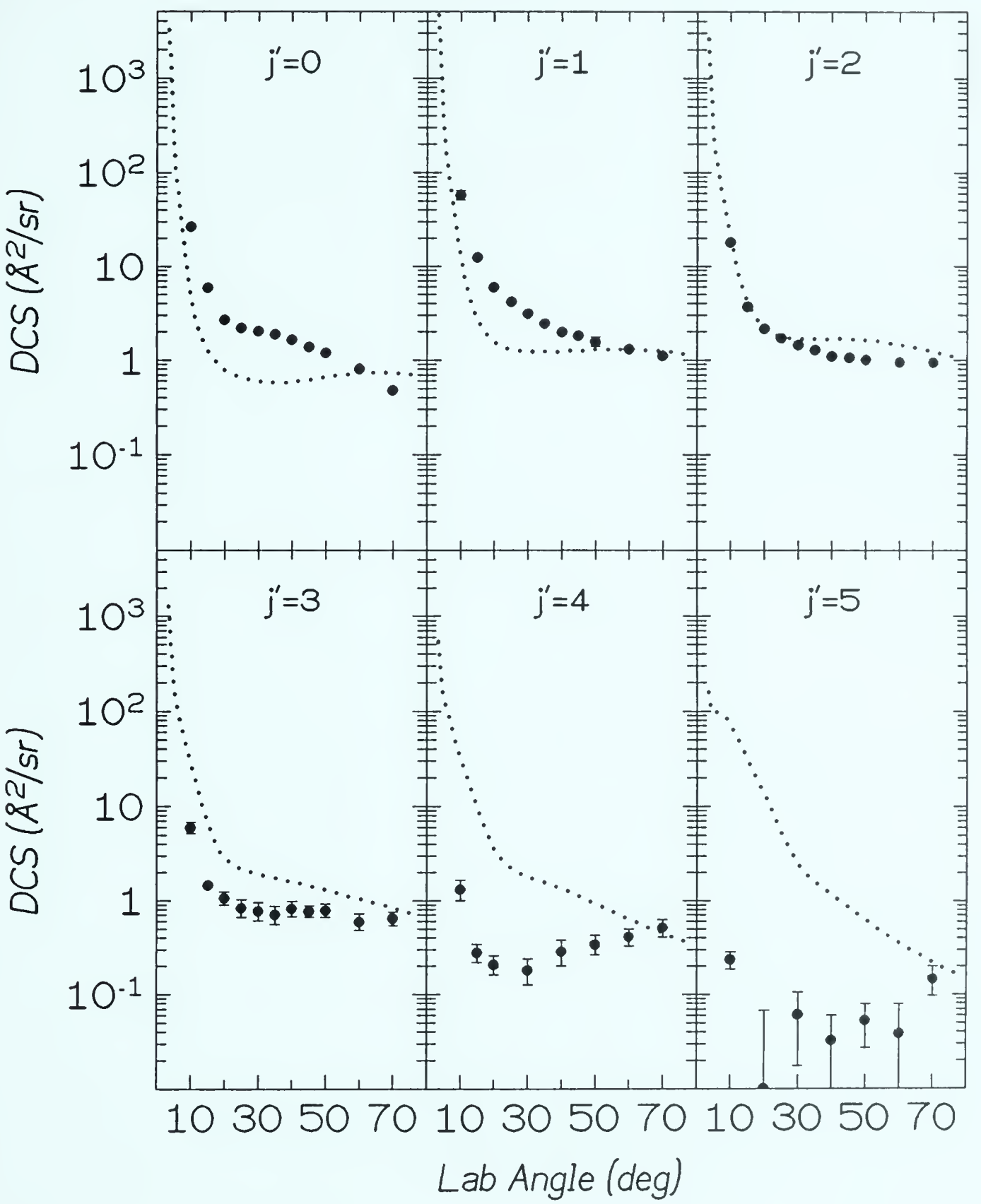

Figure 5.4c. Experimental differential cross section measurements from Ref. 11 as functions of the laboratory scattering angle $\theta_{\rm lab}$ and the final HF rotational state j'. The curves for all j' are generated from the infinite order sudden approximation calculations for the RKR PE surface[19].

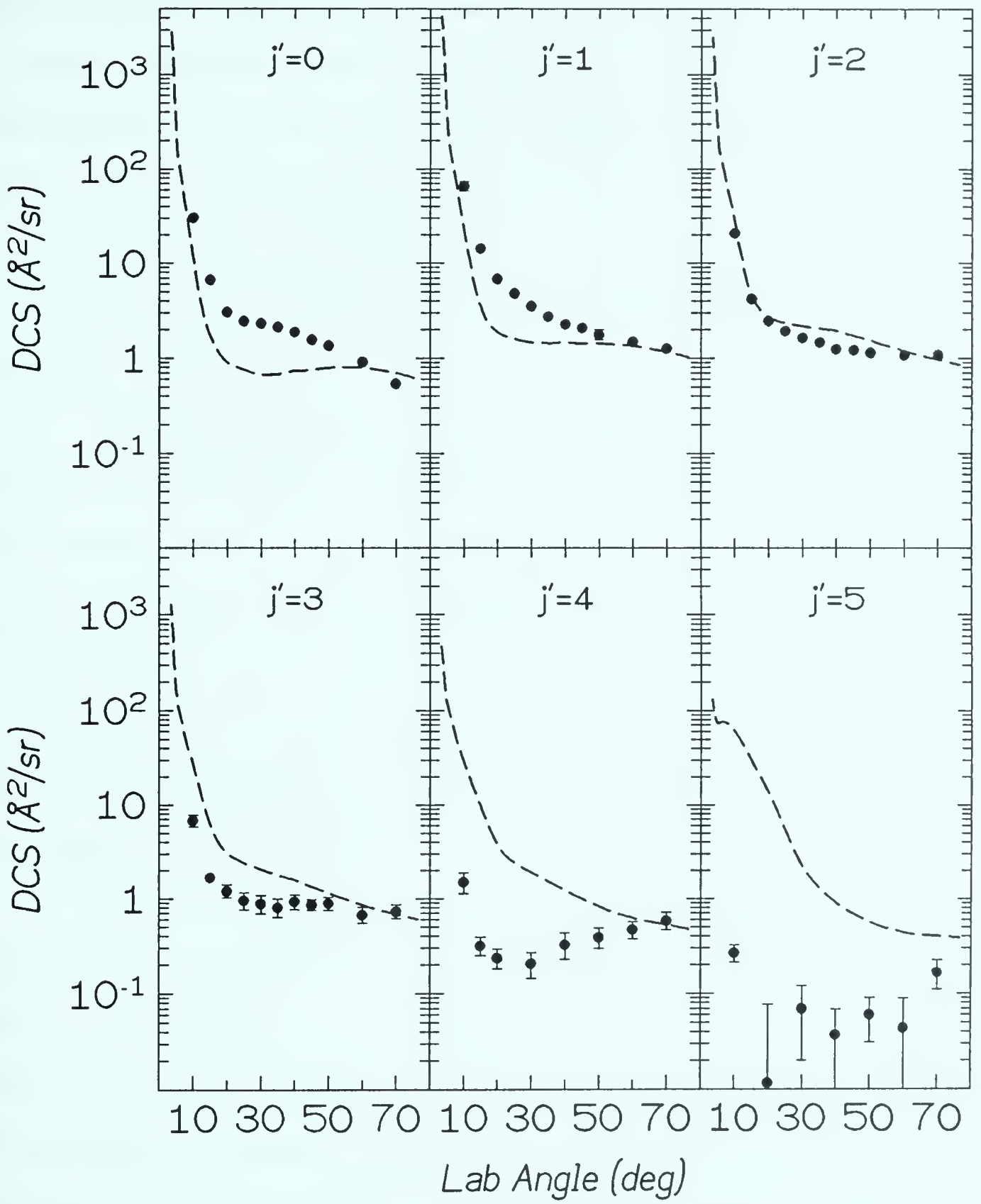

Figure 5.4d. Experimental differential cross section measurements from Ref. 11 as functions of the laboratory scattering angle $\theta_{\rm lab}$ and the final HF rotational state j'. The curves for all j' are generated from the infinite order sudden approximation calculations for the HFD PE surface[20].

The elastic contributor (*i.e.*, $j = 0 \rightarrow j' = 0$ or $j = 1 \rightarrow j' = 1$) and the first slightly inelastic contributor (*i.e.*, $j = 1 \rightarrow j' = 0$ or $j = 0 \rightarrow j' = 1$) have a reciprocal relationship in their percentage of the final state-summed DCS. This unusual behavior, plus the fact that the $j' = 0$ DCS is composed almost exclusively of the $j = 0 \rightarrow j' = 0$ and $j = 1 \rightarrow j' = 0$ state-to-state DCS's, directs one to examine these state-to-state DCS's in more detail in order to attempt to uncover the reason for the shoulder in the $j' = 0$ state-summed DCS. This point will be further discussed in Section 5.3.B.

Figure 5.5 also shows that the small angle scattering for $j' \geq 2$ is almost exclusively elastic scattering, and much of the $j' < 2$ scattering is elastic at all angles. As angle and/or j' increases, the proportion of inelastic scattering also steadily increases. This type of behaviour is typical of rotational rainbow scattering from the repulsive potential core.[13] Previous experimental observations have been restricted to systems with only weakly attractive PE surfaces,[3] unlike the HF+Ar potential, while calculational studies[10,14] have exhibited rotational rainbow scattering even on strongly attractive PE surfaces.

Summing over the experimental state-summed differential cross sections gives the total differential cross section. Vohralik *et al.*[12] have measured the total DCS for HF+Ar scattering using only a bolometer (energy flux) detector (*i.e.*, without laser-based rotational state sensitivity). This reported DCS contains contributions from Ar scattering (found to be approximately linear with angle) and is uncorrected for the changing kinetic energy of HF as a function of angle. After removing the Ar contribution and any artificial increase in signal due to the kinematic increase in HF velocity, the Vohralik *et al.* data is cosine squared angle averaged over a 3.11° window to compare to the experimental averaging in our experiments. The results are presented in Figure 5.6. The excellent agreement between the two different techniques is testimony to the accuracy of each laboratory, however for

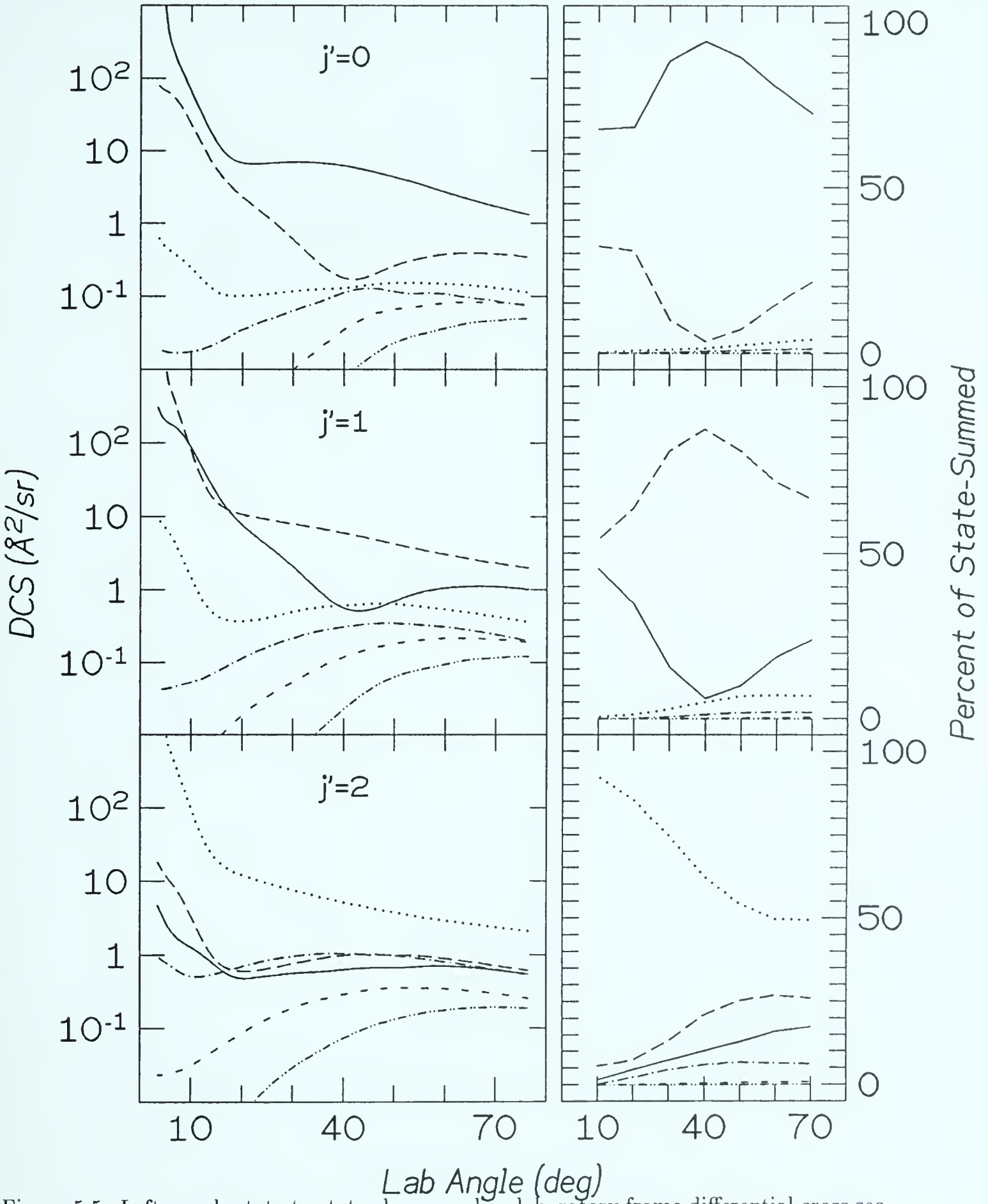

Figure 5.5. Left panel: state-to-state close-coupling laboratory frame differential cross sections (DCS) for transitions out of all possible initial j and into the experimentally detected final j'. Right panel: the percentage composition of each state-to-state DCS weighted by rotational population relative to the rotational state-summed DCS

Line types are: solid—$j = 0$; long dash—$j = 1$; dotted—$j = 2$; dash dot—$j = 3$; short dash—$j = 4$; dash double-dot—$j = 5$.

Continued on next page.

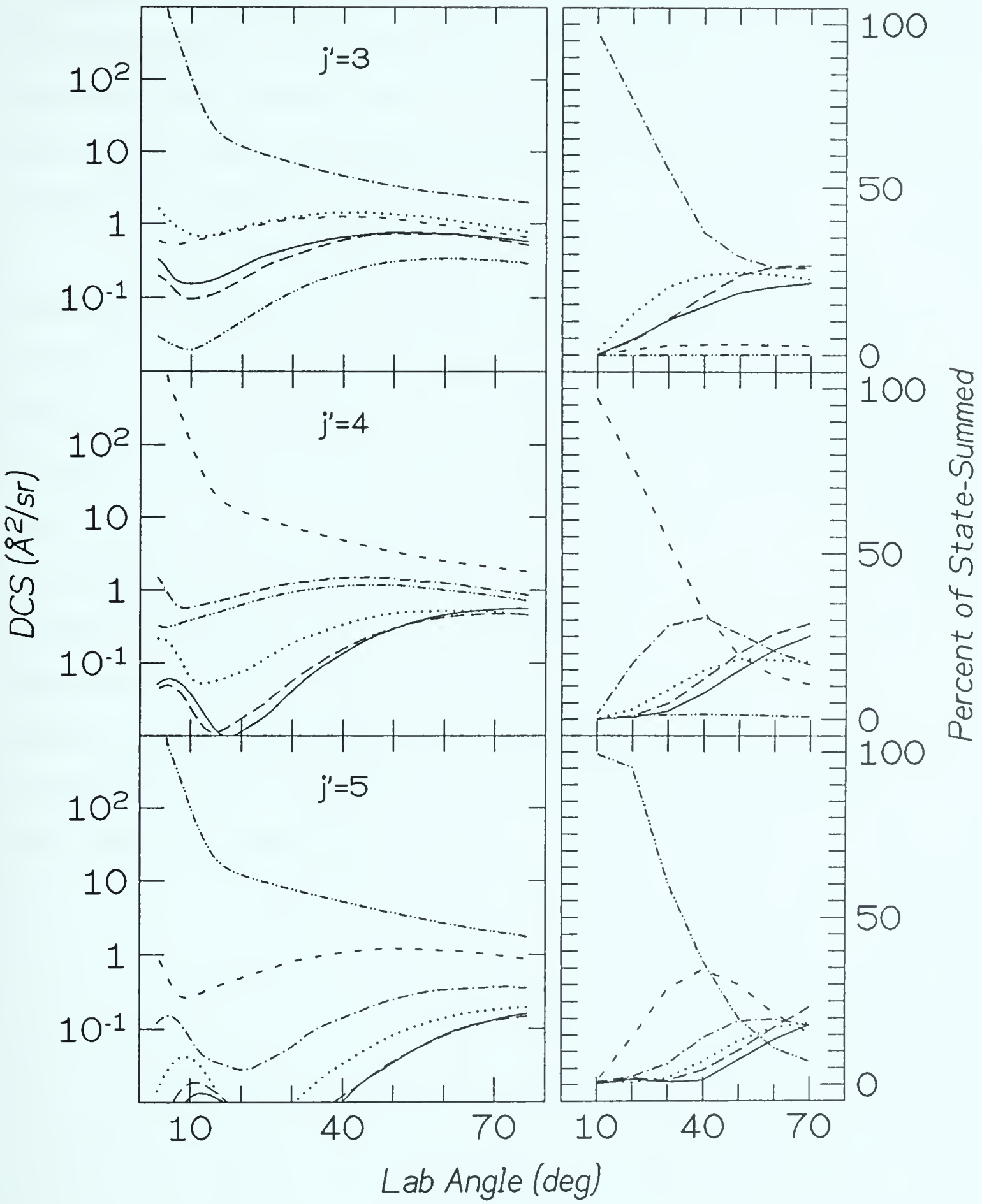

Figure 5.5. ... *Continued* ...
Line types are: solid—$j = 0$; long dash—$j = 1$; dotted—$j = 2$; dash dot—$j = 3$; short dash—$j = 4$; dash double-dot—$j = 5$.

low angle scattering (*i.e.*, 10°) there is a slight difference in the DCS's (Figure 5.6). An angular shift of $\sim -0.9°$ is required to move the DCS of this lab into perfect agreement with the Vohralik *et al.* DCS. This discrepancy is taken to be the error in the angular zeroline of our apparatus since the Vohralik *et al.* angular resolution is considerably narrower.

It is possible calculate the total differential cross section using all four potentials and both the CC and IOS calculational methods. The results are presented in Figures 5.7 and 5.8. Two immediate conclusions are drawn: the removal of final rotational state specificity diminishes the value of doing more complex CC calculations versus the relatively easy IOS approximation. Indeed, based on Figures 5.7 and 5.8 one may even suggest that the IOS calculations are better than the exact quantum CC results, which is clearly unanticipated considering the premise on which the IOS calculation is constructed (Section 1.4.B). The second observation is that the total DCS cannot distinguish between the different PE surfaces with regards to which is most useful for scattering calculations. Thus, knowing the final rotational state of the scattered HF molecules is necessary in analyzing the merits of the various potentials in the literature.

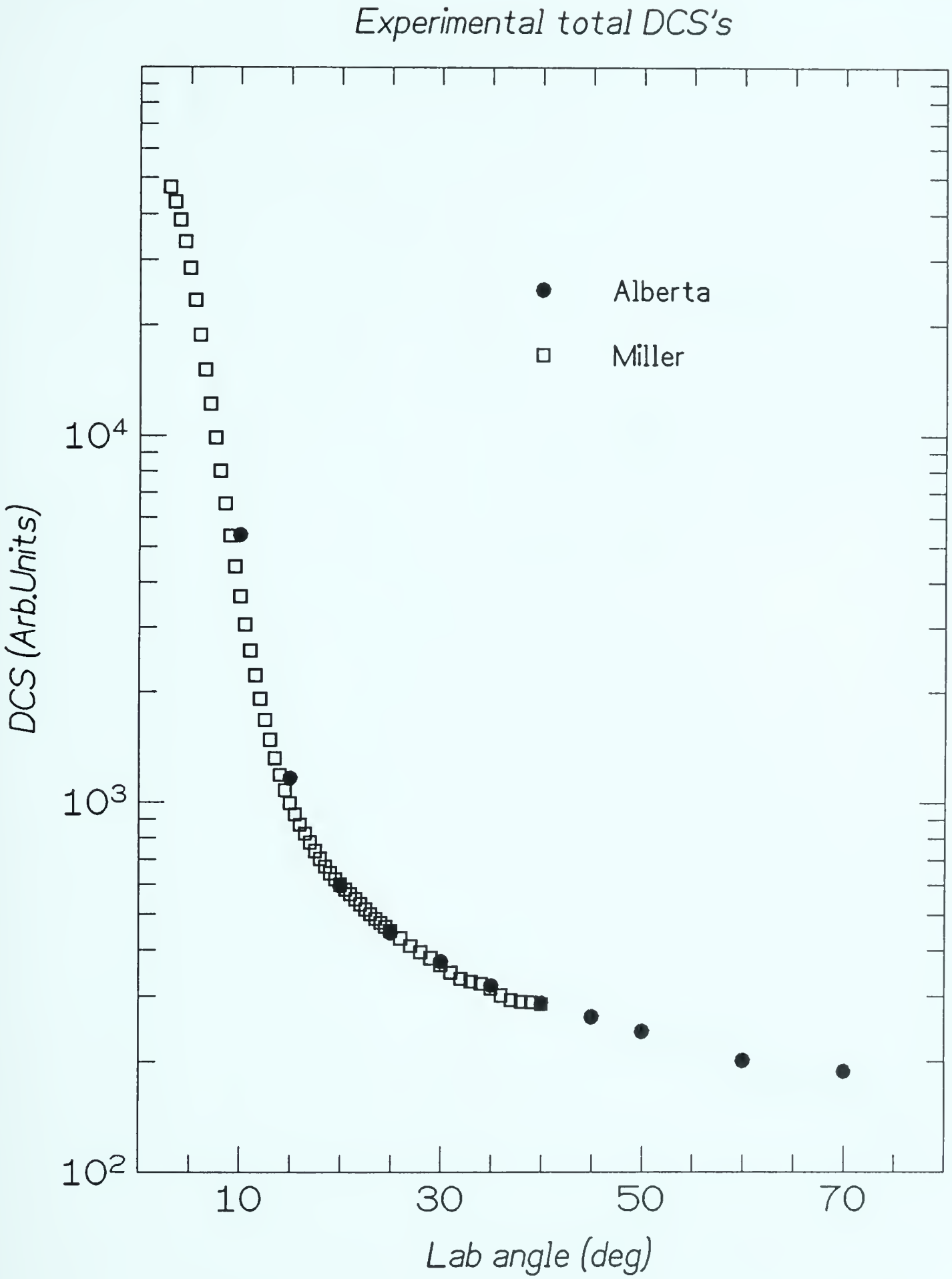

Figure 5.6. Experimental total differential cross section obtained by summing over the measured final rotational state resolved differential cross sections. Square symbols represent data from Vohralik *et al.*[12].

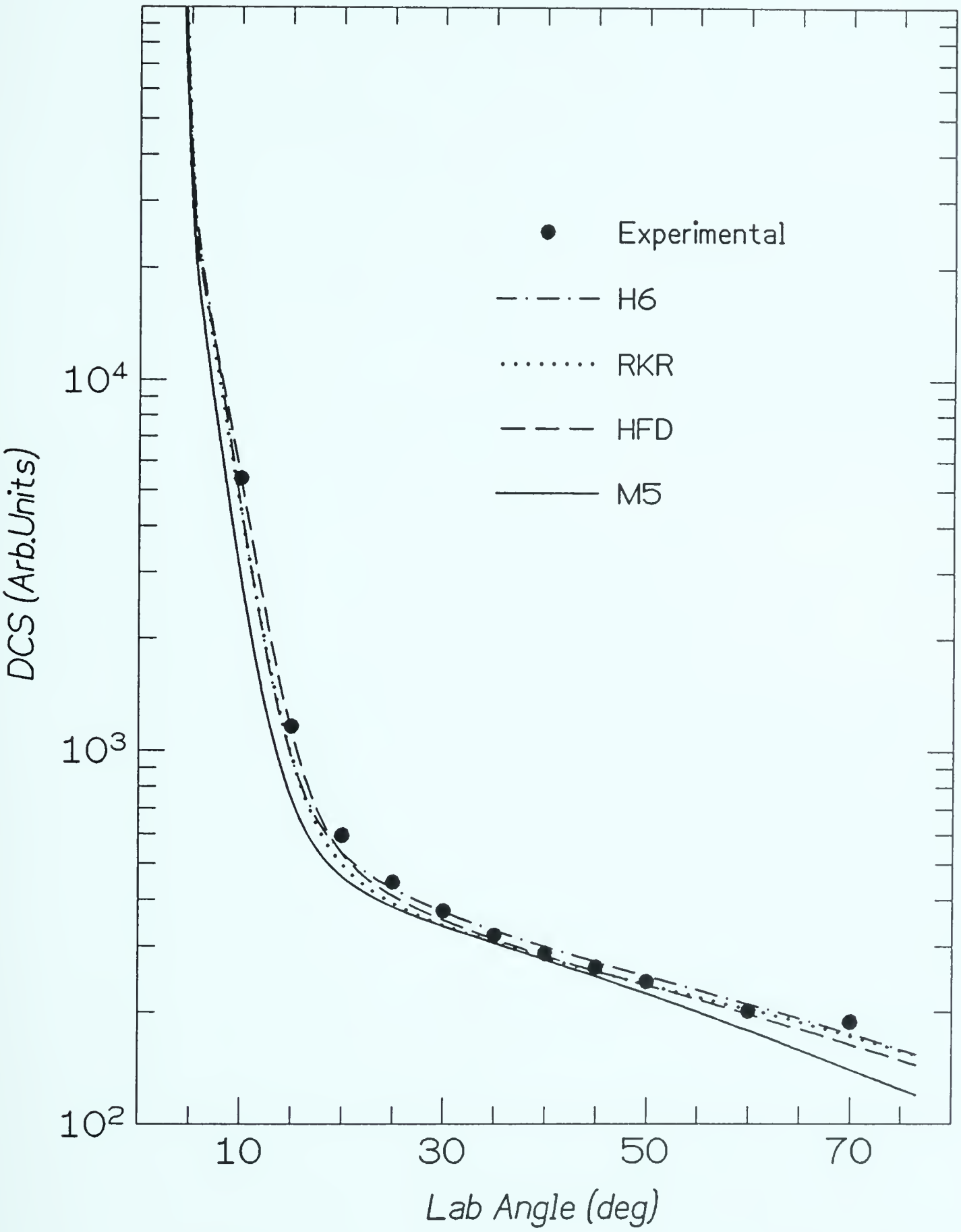

Figure 5.7. Lab frame total differential cross sections for the four different potential surfaces calculated using close-coupling techniques.

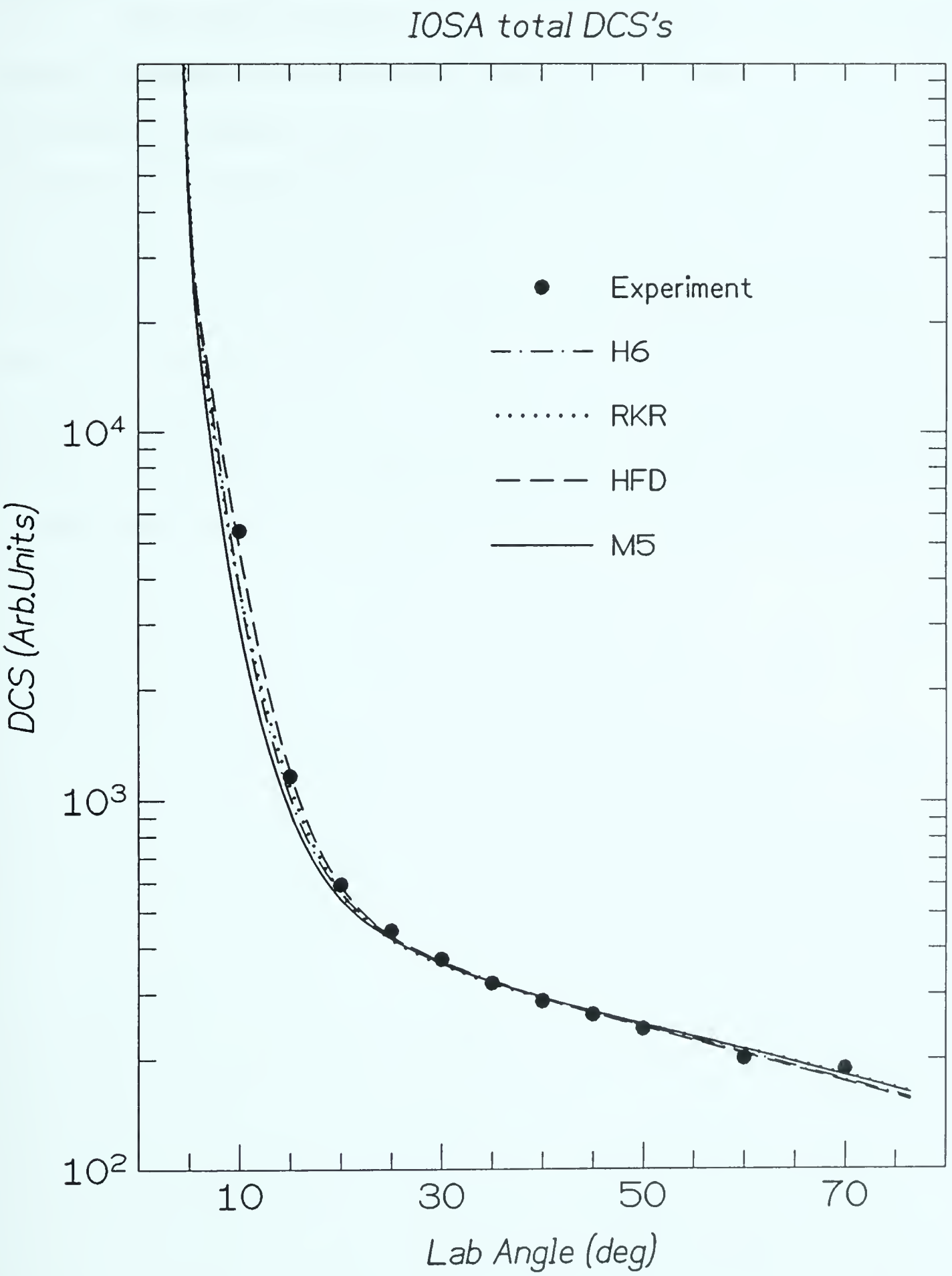

Figure 5.8. Lab frame total differential cross sections for the four different potential surfaces calculated using the infinite order sudden approximation.

5.3.A.1 Conclusion from Laboratory Frame Results

The results of Figures 5.2a - 5.2d and Table 5.1 verify that the H6 potential, developed from spectroscopic fitting, is also the most useful for differential scattering calculations. Because of its mainly spectroscopic origin, it is largely insensitive to the repulsive anisotropy, and needs some modification to reproduce the $j' = 4$ and $j' = 5$ rotational rainbows. For example, the H6 potential predicts a minimum in the $j' = 4$ DCS only half as deep as that observed experimentally. In contrast, the strongest rotational rainbows calculated occur using the M5 potential,[18] (Figure 5.2) which also has the most anisotropic repulsive wall (Table 5.1). This suggests that somewhat stronger repulsive anisotropy in the H6 potential would improve its agreement with the experimental results.

5.3.B Center-of-Mass Frame

The rotational rainbow feature of the experimental DCS's can be readily confirmed by looking at the calculational results presented in the laboratory frame (Section 5.3.A). The origin of the shoulder experimentally observed near $\theta_{\rm lab} = 30°$ in the $j' = 0$ DCS is not so easily addressed, and bears further investigation to gain understanding as to its origin. To avoid any complications that may arise from kinematic transformations, it is best to study the $j' = 0$ shoulder by looking at calculational results in the center of mass reference frame.

It has already been shown in Section 4.4.D.1 that this shoulder cannot be explained as an impact parameter rainbow, familiar from atom+atom elastic scattering and observed at $\theta_{\rm lab} = 5.5°$.[12] Since the H6 potential gives the best fit to the experiment, and in particular since it is the only PE surface to reproduce the observed shoulder, it is used for all the investigative dynamical calculations presented below.

For DCS's scattered into $j' = 0$, Figure 5.5 shows that $\gtrsim 95\%$ of the observed signal is due to the $j = 0 \rightarrow j' = 0$ and $j = 1 \rightarrow j' = 0$ state-to-state transitions. Hence, the observed shoulder must be due to features appearing in these two DCS's. To simplify further investigation of these two DCS's, the $j = 0 \rightarrow j' = 1$ inelastic DCS is calculated instead of the $j = 1 \rightarrow j' = 0$ DCS. The former is more convenient for the classical trajectories (CT) studies since a single set of trajectories provides the probability of transitions from a given initial rotational state to all final rotational states. (*i.e.*, Studying $j = 0 \rightarrow j' = 0$ and $j = 1 \rightarrow j' = 0$ would require two calculational runs, whereas both the $j = 0 \rightarrow j' = 0$ and $j = 0 \rightarrow j' = 1$ DCS's are obtained from the same initial conditions, which saves both time and effort.) Also, the rotational to translational energy transition in the $j = 1 \rightarrow j' = 0$ event is relatively improbable in comparison to the translational to rotational transition in the $j = 0 \rightarrow j' = 1$ event (approximately one-third as

probable due to the rotational degeneracy), and so a larger number of trajectories would have to be run to get meaningful statistics for the former inelastic transition. The close-coupling calculations at a single energy are sufficiently fast to allow one to readily calculate any desired DCS.

Any question that the $j = 1 \rightarrow j' = 0$ and $j = 0 \rightarrow j' = 1$ cross sections do not represent the same information can be easily answered by realizing their close relation through microscopic reversibilility. The two cross sections are calculated at the same relative translational energy and therefore nearly the same total energy. Their relative magnitude is related by their rotational degeneracy factors,[23] and these DCS's should be in a 1:3 ratio over the entire anglular range. Table 5.2 shows this comparison at one of the studied energies.

To further simplify the analysis, the calculations are not transformed to the laboratory frame, nor are they averaged over the instrumental energy distribution. However, a 2° angle averaging over a cosine squared profile is applied to remove rapid quantum oscillations. Study of the $j = 0 \rightarrow j' = 0$ and the $j = 0 \rightarrow j' = 1$ state-to-state DCS's is done directly in the centre-of-mass scattering frame using a collision energy of 135 meV. This is not exactly the average energy of the collision, but it is one of four energies which is used for experimental averaging and is thus a convenient choice.

Figure 5.9 displays CC, IOS and CT results for these two DCS's. The CC results show the shoulder in the $j = 0 \rightarrow j' = 0$ DCS, and at the same angle the $j = 0 \rightarrow j = 1$ DCS shows a prominent minimum. In strong contrast, the CT results are smooth and monotonic and display no feature resembling either a shoulder or a minimum. The conclusion garnered is that these features must be quantum mechanical in nature. The interest in this phenomenon is that experimentally this feature is observed, (*i.e.*, the shoulder in the $j' = 0$ lab-frame DCS), but for such a heavy collision system (reduced mass 13.3 amu), one would expect only classical effects to be observable (Section 4.3.A).

Table 5.2. $j = 1 \rightarrow j' = 0$ **DCS** / $j = 0 \rightarrow j' = 1$ **DCS at 135 meV.**

Angle	Ratio	Angle	Ratio	Angle	Ratio	Angle	Ratio	Angle	Ratio
0	0.350	37	0.326	73	0.390	109	0.344	145	0.327
1	0.345	38	0.325	74	0.391	110	0.343	146	0.328
2	0.344	39	0.323	75	0.390	111	0.341	147	0.329
3	0.369	40	0.321	76	0.387	112	0.340	148	0.330
4	0.386	41	0.319	77	0.386	113	0.340	149	0.332
5	0.381	42	0.317	78	0.383	114	0.339	150	0.333
6	0.373	43	0.315	79	0.382	115	0.339	151	0.333
7	0.365	44	0.314	80	0.381	116	0.338	152	0.333
8	0.355	45	0.311	81	0.379	117	0.338	153	0.334
9	0.350	46	0.307	82	0.376	118	0.338	154	0.334
10	0.341	47	0.303	83	0.372	119	0.337	155	0.335
11	0.337	48	0.300	84	0.369	120	0.336	156	0.336
12	0.331	49	0.297	85	0.368	121	0.336	157	0.336
13	0.325	50	0.295	86	0.366	122	0.335	158	0.334
14	0.325	51	0.294	87	0.362	123	0.334	159	0.333
15	0.316	52	0.293	88	0.358	124	0.333	160	0.332
16	0.320	53	0.294	89	0.356	125	0.332	161	0.332
17	0.314	54	0.298	90	0.355	126	0.330	162	0.331
18	0.316	55	0.304	91	0.353	127	0.328	163	0.331
19	0.317	56	0.312	92	0.351	128	0.326	164	0.331
20	0.316	57	0.322	93	0.352	129	0.326	165	0.329
21	0.323	58	0.335	94	0.353	130	0.324	166	0.328
22	0.319	59	0.346	95	0.354	131	0.322	167	0.329
23	0.327	60	0.353	96	0.355	132	0.320	168	0.328
24	0.325	61	0.359	97	0.356	133	0.317	169	0.323
25	0.329	62	0.368	98	0.357	134	0.316	170	0.321
26	0.329	63	0.374	99	0.360	135	0.316	171	0.326
27	0.330	64	0.378	100	0.361	136	0.317	172	0.332
28	0.332	65	0.379	101	0.361	137	0.316	173	0.331
29	0.330	66	0.379	102	0.360	138	0.317	174	0.326
30	0.333	67	0.378	103	0.359	139	0.320	175	0.326
31	0.330	68	0.378	104	0.356	140	0.321	176	0.324
32	0.331	69	0.381	105	0.352	141	0.322	177	0.317
33	0.329	70	0.385	106	0.349	142	0.323	178	0.311
34	0.329	71	0.388	107	0.346	143	0.323	179	0.303
35	0.328	72	0.389	108	0.344	144	0.324	180	0.298
36	0.327								

Average ratio of differential cross sections is 0.339 ± 0.023. Note that this ratio is calculated after a 2° angular averaging removes the rapid quantum oscillations.

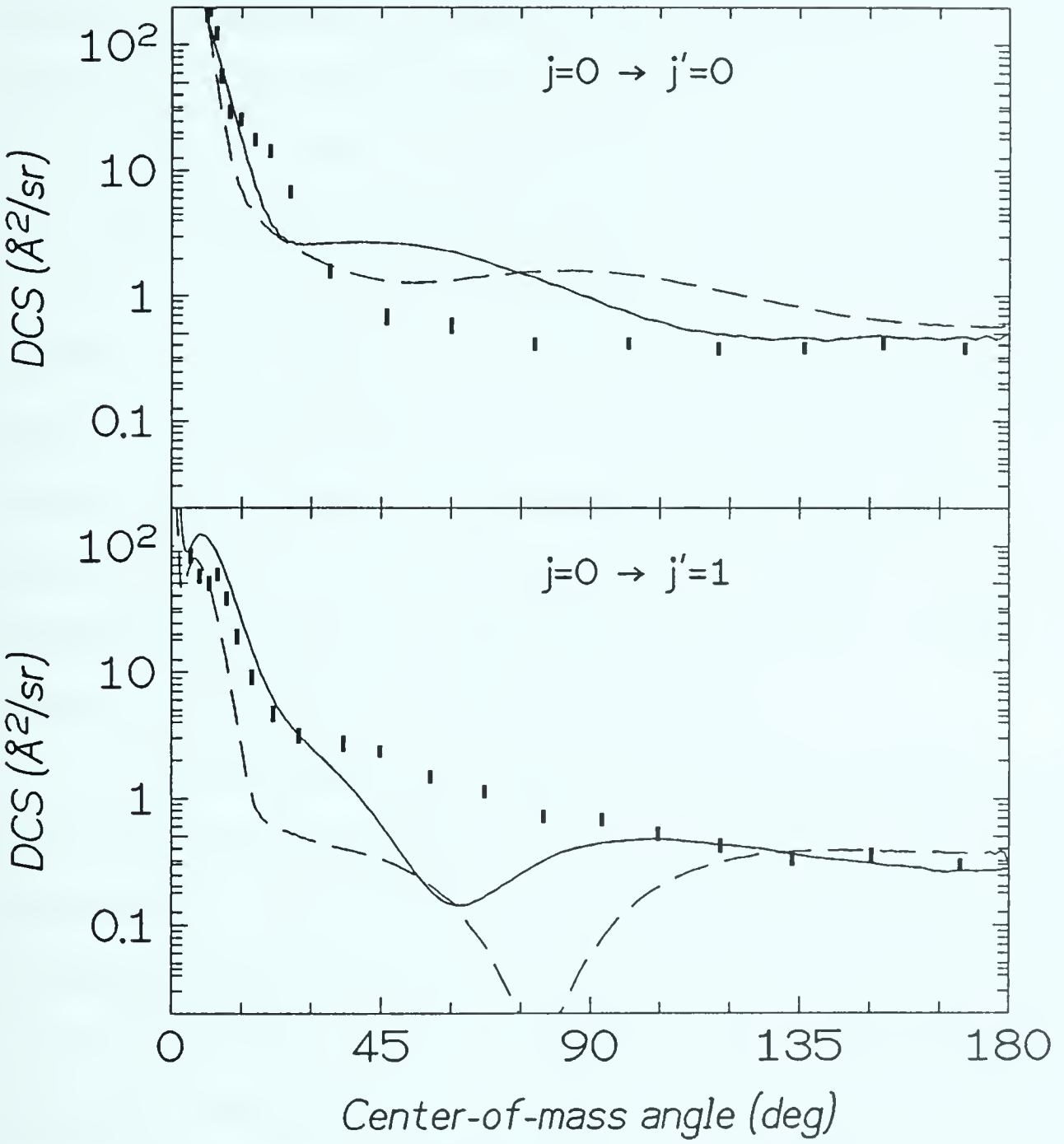

Figure 5.9. Calculated state-to-state differential cross sections as a function of the center-of-mass scattering angle $\theta_{\rm cm}$ for elastic $j = 0 \rightarrow j' = 0$ and weakly-inelastic $j = 0 \rightarrow j' = 1$ scattering. The curves present the theoretical results (solid: exact close-coupling; dashed: infinite-order sudden). The classical trajectory results appear as heavy bars whose height indicates the associated 1σ statistical error. No energy averaging is performed, but a 2°—wide angular average is applied to all the quantum results to smooth out diffraction oscillations. Lab- and cm-frame scattering angles are related by $\theta_{\rm cm} \simeq 1.5 \times \theta_{\rm lab}$ over most of the angular range. All calculations are conducted using the H6 potential of Ref. 1 at a collision energy of 135 meV.

The new structures shown in Figure 5.9 are not consistent with rainbows seen in previous experiments[3] or calculations.[10,14] The HF+Ar PE surface, with deep wells in both the Ar···HF and Ar···FH collinear geometries, represents a qualitatively different type of potential than those analyzed previously. If the new features were due to a resonance, then they should be sharp functions of the collision energy. It would be fortuitous that the energy selected to study the state-to-state DCS's would exactly be the energy of a resonance. Figure 5.10 shows the DCS's as a function of energy (the four energies chosen to properly average over experimental conditions). We see that the new features appear to be rainbow-like rather than resonant, in that both the $j = 0 \rightarrow j' = 0$ shoulder and the $j = 0 \rightarrow j' = 1$ minimum show a regular and monotonic displacement as a function of collision energy.[28] However, at this point it is not certain if these are rainbow features, and no further conclusion can be made than to say that the "shoulder" and "hole" behave in a way reminiscent of rainbow features.

Even though the IOS approximation provides a minimal amount of insight at the final rotational-state resolved level, the value of the IOS at the state-to-state level for this system was unknown. Further investigation was inspired by the knowledge that several types of structures in rotationally inelastic DCS's have been examined in the literature. For systems governed by purely repulsive PE surfaces, rotational rainbows and associated supernumary rainbows have been observed,[3] with elegant explanations[13] based on the IOS approximation.[23] Even richer structure has been predicted for systems governed by attractive PE surfaces,[14] though few such structures have yet been confirmed experimentally.[9] As shown in Figure 5.9, IOS calculations are qualitatively successful in reproducing both the $j = 0 \rightarrow j' = 0$ shoulder and the $j = 0 \rightarrow j' = 1$ minimum, but the location and magnitude of these features are grossly inaccurate relative to the exact CC calculations.

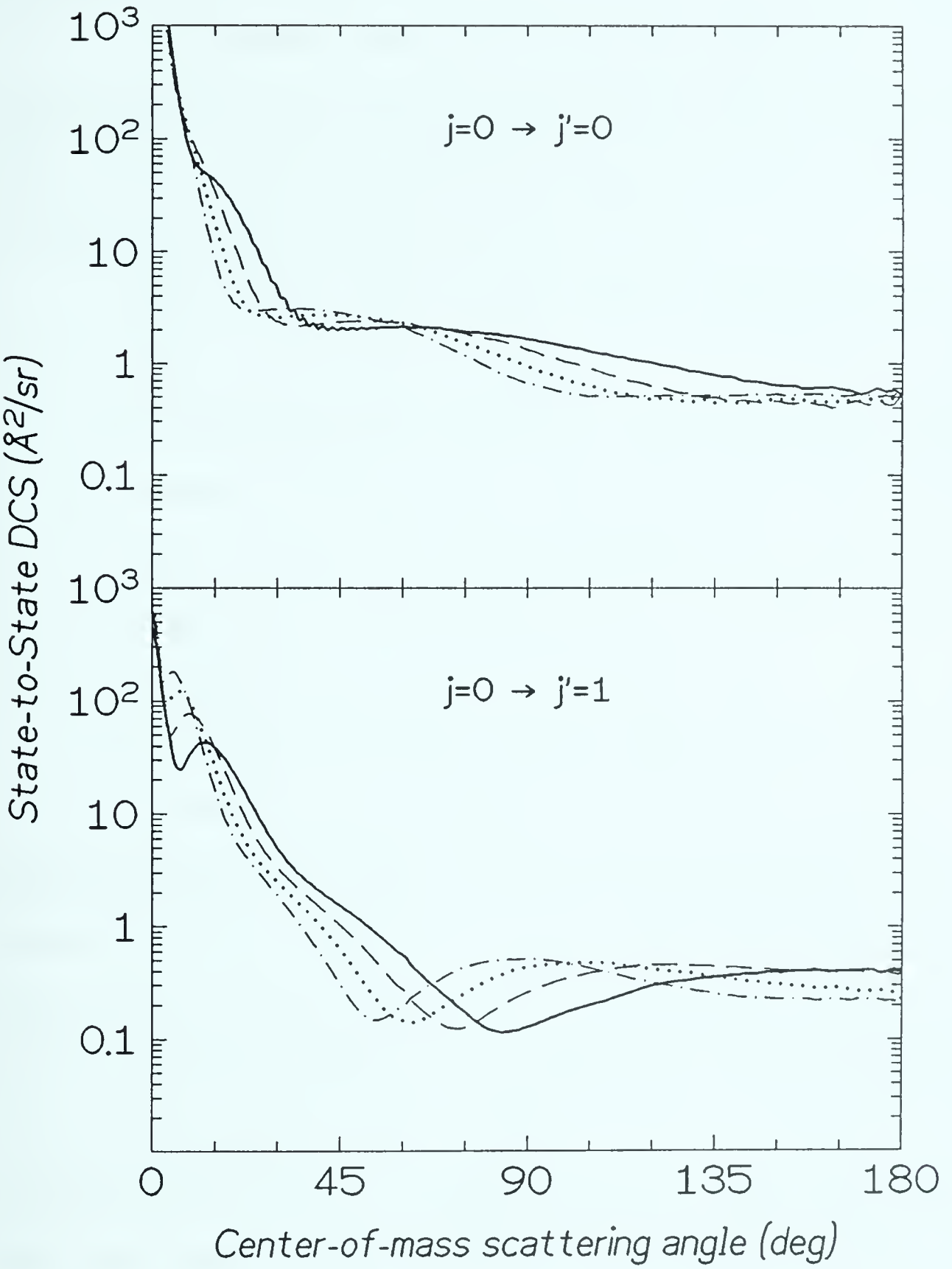

Figure 5.10. The same calculated CC state-to-state differential cross sections as shown in Figure 5.9, but varying the collision energy. The angular positions of the "shoulder" and "hole" move as a function of energy, just as expected for a rainbow feature.[28] Collision energy is identified by line type: solid – 82.43 meV; dashed – 107.04 meV; dotted – 134.85 meV; dash-dotted – 165.88 meV.

5.4 ISOTOPE EFFECT

The sensitivity of the $j = 0 \rightarrow j' = 0$ shoulder and the $j = 0 \rightarrow j' = 1$ minimum features to the scattering dynamics can be further explored computationally by isotopic substitution of DF for HF. Several important differences arise in the dynamics from the isotopic substitution. They are:

i. DF+Ar has a slightly larger collisional reduced mass (13.3 amu for HF+Ar and 13.7 amu for DF+Ar).

ii. Changes in the H6 potential due to lower DF zero point energy.[1]

iii. Different rotational energy level spacing. $B_e^{HF} = 20.56\,cm^{-1}$, while $B_e^{DF} = 10.86\,cm^{-1}$. It may be instructive to note that over a collision range of 10 Å, the flight time is $\sim 8 \times 10^{-13}$ sec. During this time an HF(DF) molecule in $j = 1$ executes $\sim 1.3(0.7)$ complete rotations.

iv. The center-of-mass of the DF PE surface lies 0.041 Å further from the F atom than does the center-of-mass of the HF PE surface.

Explicit calculation of the DF+Ar DCS's with a reduced mass of 13.3 amu, and calculation of the HF+Ar DCS's with a 13.7 amu reduced mass display no perceptible differences from the cases of using the correct reduced mass. Therefore, the reduced mass does not have any influence in the isotopic effects observed for the scattering. To answer the second item, the DCS's calculated with the $\nu = 1$ HF+Ar PE surface are nearly identical to the $\nu = 0$ DCS's (Figure 5.3). Hence, the different DF zero point energy should not have any effect on the scattering calculations. Items (iii) and (iv) are the two most important PE surface differences, and are considered in greater detail below.

Figures 5.11a and 5.11b show CC calculations at 135 meV for the four combinations of rotational constant with PE surface. These DCS's can be used to separate anisotropy effects due to the 0.041 Å shift of the PE surface from the

influence of the rotational constant. The HF+Ar and DF+Ar PE surfaces are shown in Figure 5.12 for angular cuts at 90° intervals.

Within Figure 5.11a, HF+Ar DCS's on the HF+Ar PE surface versus DCS's on the DF+Ar PE surface display vast differences. The less anisotropic DF+Ar surface causes the $j = 0 \rightarrow j' = 0$ shoulder to slightly decrease in prominence by broadening in angular range. The $j = 0 \rightarrow j' = 1$ DCS shows the biggest change with the "hole" at $\sim 60°$ being completely destroyed. The small and large angle parts remain essentially unchanged except for small differences in the magnitude of the cross section. In Figure 5.11b the same significant differences between HF+Ar versus DF+Ar DCS's are present, but on the DF+Ar PE surface this time. The conclusion drawn is that the less anisotropic DF+Ar PE surface (0.041 Å shift towards the D) causes a loss in "quantum" features as observed in the decrease in shoulder clarity, and the destruction of the $j = 0 \rightarrow j' = 1$ minimum.

Comparison between Figures 5.11a and 5.11b demonstrates the effect of changing the rotational constant of the diatom in the collision. For the $j = 0 \rightarrow j' = 0$ DCS's, the change from the HF+Ar system to the DF+Ar system clearly shows an exaggeration and sharpening of quantum features occurs if the rotational constant is smaller. For instance, the HF+Ar shoulder (Figure 5.11a, left panels) has been resolved into a distinct minimum in the DF+Ar DCS's (Figure 5.11b, left panels). The $j = 0 \rightarrow j' = 1$ DCS's display the same trend. The "hole" in the HF+Ar DCS (Figure 5.11a, upper right panel) is significantly sharper with the DF+Ar rotational constant (Figure 5.11b, upper right panel). There is no appreciable intermediate and wide angle difference in comparing $j = 0 \rightarrow j' = 1$ cross sections on the DF+Ar PE surface. One would suspect that calculations done with an even smaller rotational constant (for instance that of tritium fluoride) would show even more highly exaggerated quantum features.

One additional note of interest is that for all of the above scattering system + PE surface combinations, the small oscillation at $\sim 7°$ is present in the

$j = 0 \rightarrow j' = 1$ DCS. It corresponds to that observed in the final rotational state-summed measurements,[12] but is not seen in our experiments since it occurs below the accessible experimental angular range for the state-resolved results.[11] This is most likely a classical impact-parameter rainbow, as suggested by Vohralik *et al.* and by the CT data shown in Figure 5.9. One other interesting note is that this feature appears far more prominently in the inelastic DCS than in the elastic one; the latter shows an oscillation only if the angular dependence is greatly exaggerated.[12]

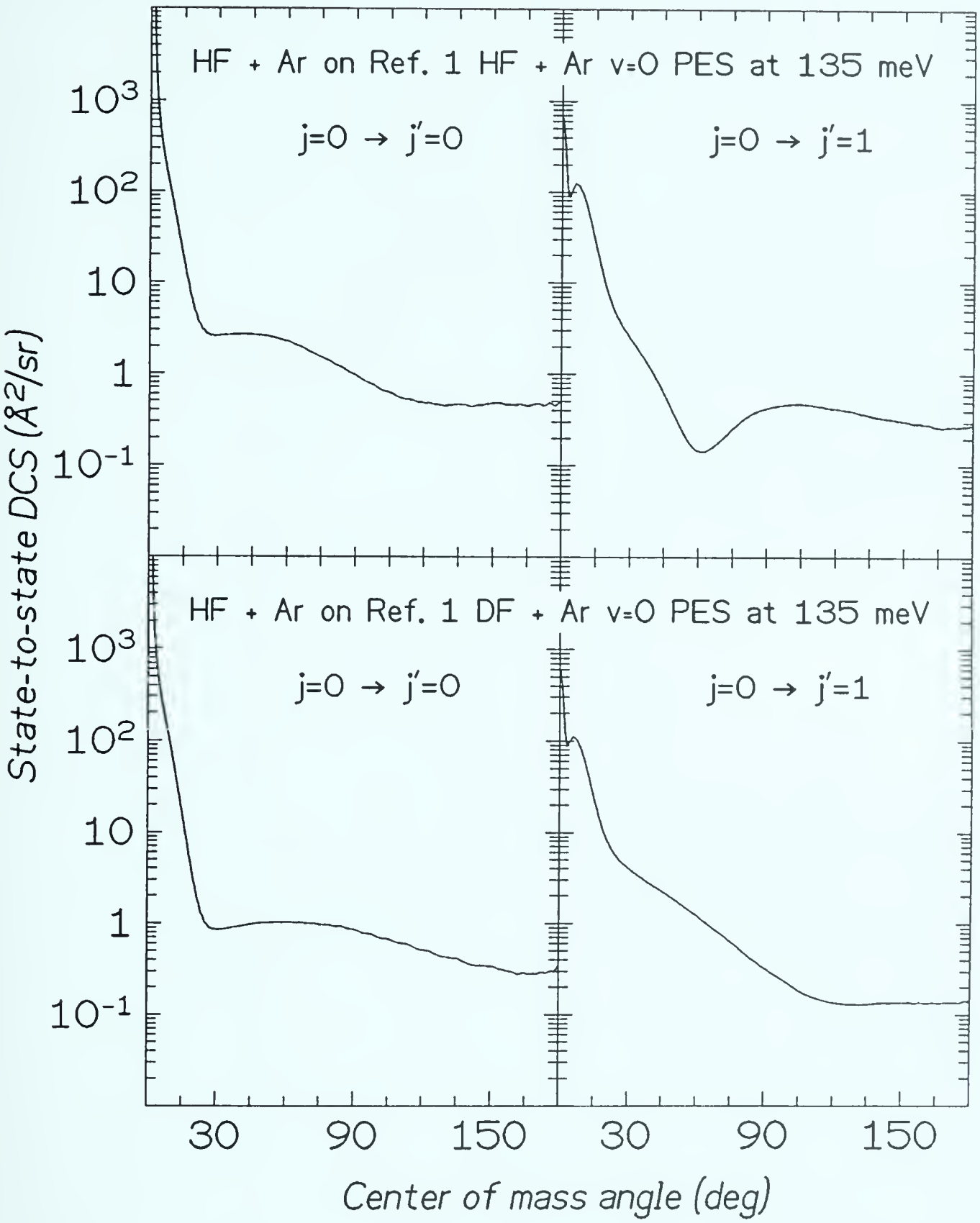

Figure 5.11a. $j = 0 \rightarrow j' = 0$ and $j = 0 \rightarrow j' = 1$ state-to-state close-coupling differential cross sections. Top panels show DCS's for the calculation using the HF+Ar reduced mass and rotational constant. The potential energy surface is for the HF+Ar scattering system. Lower panels show DCS's for the calculation using the HF+Ar reduced mass and rotational constant. The potential energy surface is for the DF+Ar scattering system. The total energy is 134.8 meV, which is one of four used to properly energy average over experimental conditions.

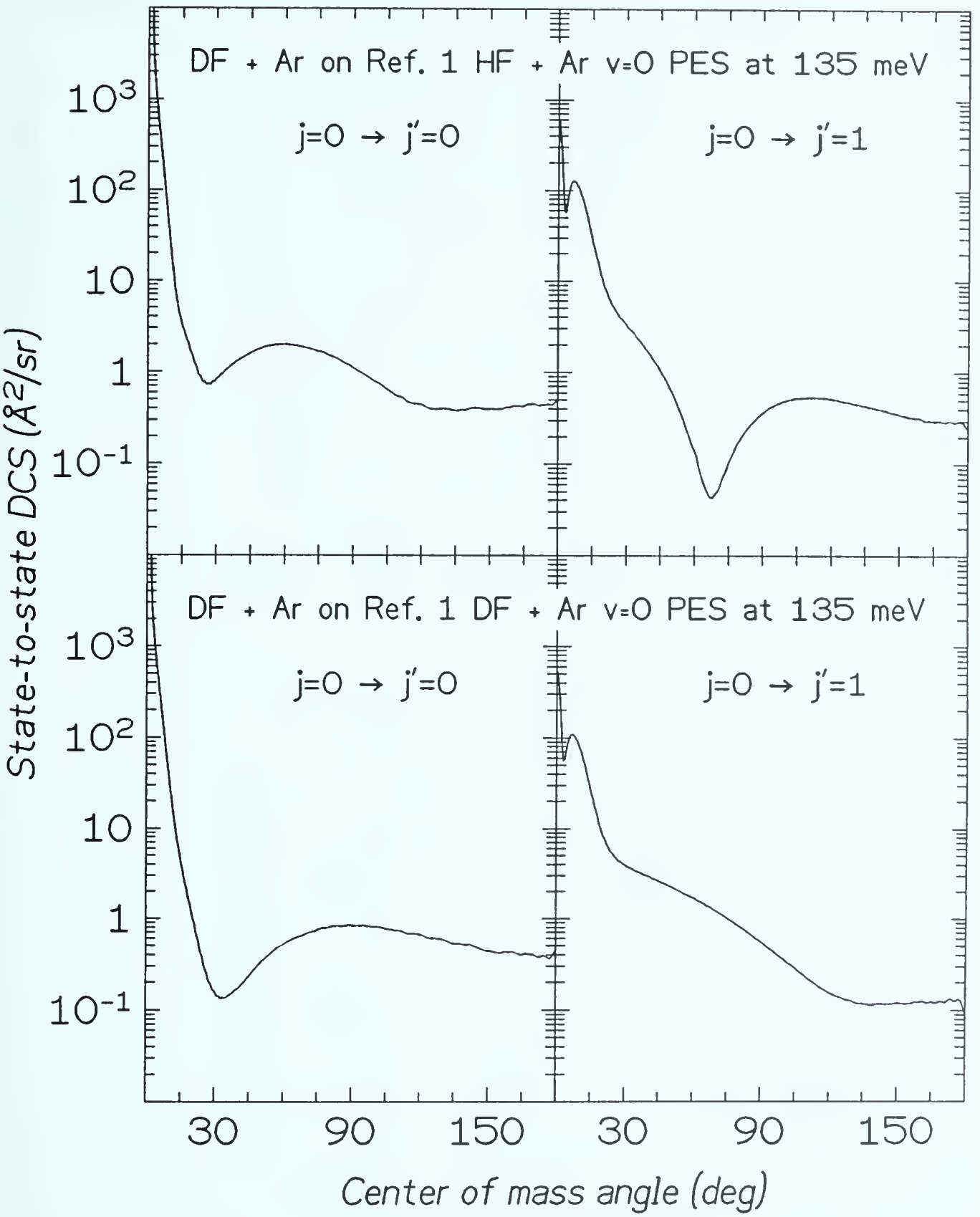

Figure 5.11b. $j = 0 \rightarrow j' = 0$ and $j = 0 \rightarrow j' = 1$ state-to-state close-coupling differential cross sections. Top panels show DCS's for the calculation using the DF+Ar reduced mass and rotational constant. The potential energy surface is for the HF+Ar scattering system. Lower panels show DCS's for the calculation using the DF+Ar reduced mass and rotational constant. The potential energy surface is for the DF+Ar scattering system. The total energy is 134.8 meV, which is one of four used to properly energy average over experimental conditions.

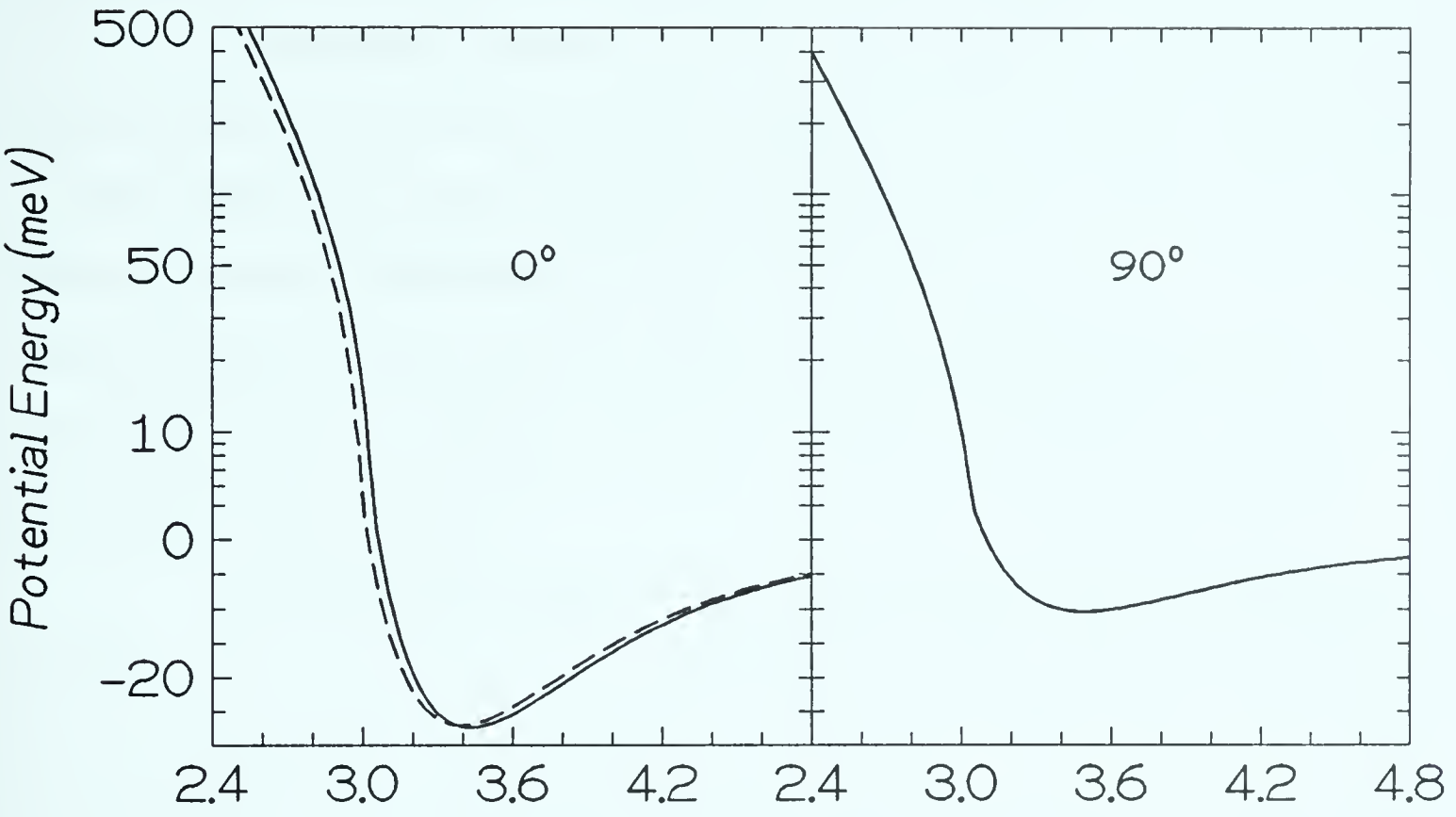

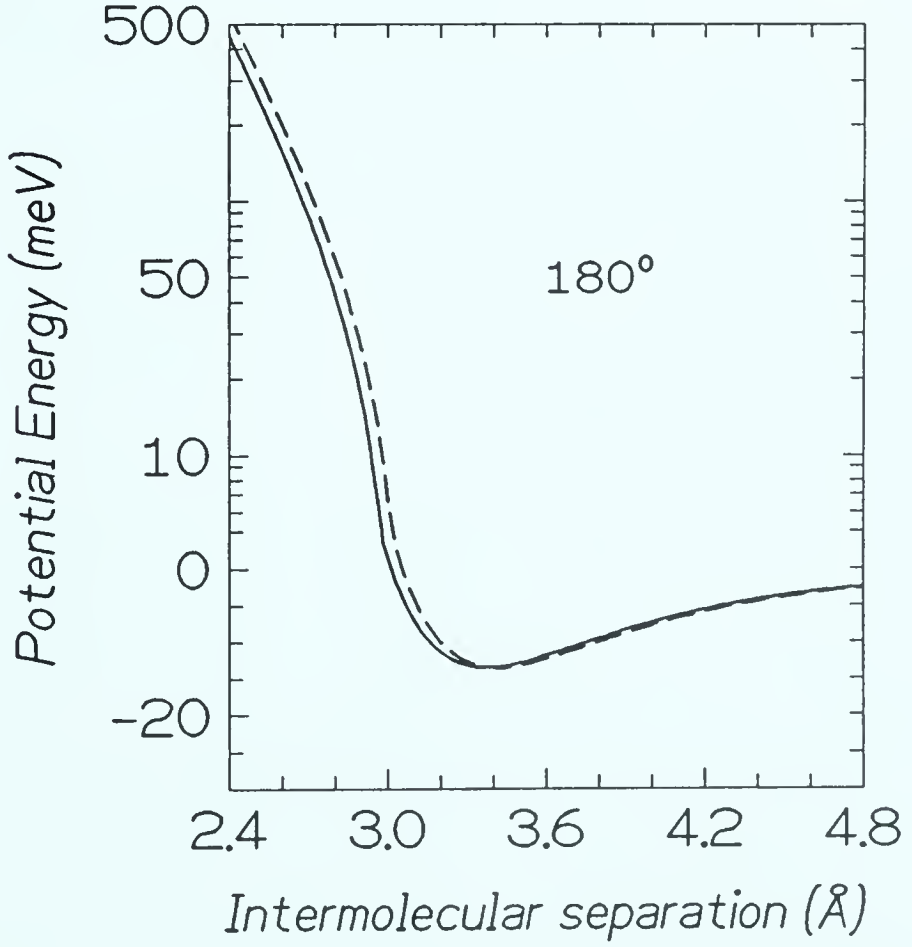

Figure 5.12. H6 (Ref. 1) HF+Ar (solid line) intermolecular potential versus the DF+Ar (dashed line) intermolecular potential at three different interaction angles of 0, 90, and 180°. The 0°orientation corresponds to a collinear geometry of $Ar \cdots H - F(D)$. The 180°orientation corresponds to a collinear geometry of $Ar \cdots F - H(D)$. The radial displacement between the curves is 0.041Å at the 0° and 180° orientations.

5.5 SENSITIVITY TO FEATURES OF THE PE SURFACE

The exploratory calculations of the preceding section were based on using the hydrogen or deuterium isotope of hydrogen fluoride. The PE surfaces had very little difference in shape, and only a small 0.041 Å shift in position towards the D atom. Even more information can be obtained by adjusting the H6 PE surface in dramatic fashion. Table 5.3 provides mathematical details for the modifications performed. Figures 5.14a – 5.14h show the various PE surfaces with the accompanying HF+Ar close-coupled DCS's.

By comparing the DCS's of each of the modifications to the original unmodified work, it is possible to make conclusions as to which parts of the potential have the largest effect upon the quantum observations. To simplify the evaluation, each state to state DCS is individually analyzed to monitor the effects of the PE surface modifications.

Table 5.3. H6 Potential Modifications

Modification #	Effect	Equation form	Range
0	Unmodified PE surface	Ref. 1	
1	Eliminate attractive well	$V = V(r,\gamma)$	$r < r_{sw}(\gamma)$
		$V = 0$	$r > \sigma(\gamma)$
		$V = A(r-\sigma)^2$	$r_{sw}(\gamma) < r < \sigma(\gamma)$
$r_{sw}(\gamma)$ is the distance at which $V(r,\gamma) = 30$ meV $\sigma(\gamma)$ is the distance at which $V(r,\gamma) = 0$ meV with negative slope			
2	Isotropic attractive well at γ_{sph} value	$V = V(r,\gamma)$	$r < r_{sw}(\gamma)$
		$V = V(r,\gamma_{sph})$	$r > \sigma(\gamma_{sph})$
		$V =$ cubic spline*	$r_{sw}(\gamma) < r < \sigma(\gamma_{sph})$
$r_{sw}(\gamma)$ is the distance at which $V(r,\gamma) = 30$ meV $\sigma(\gamma_{sph})$ is the distance at which $V(r,\gamma_{sph}) = 0$ meV; $\gamma_{sph} = 90^\circ$			
3	Attractive well is anisotropic, but symmetric	$V = V(r,\gamma)$	$\gamma < 90^\circ$
		$V = V(r,\gamma)$	$\gamma > 90^\circ$ and $r < r_{sw}(\gamma)$
		$V = V(r,180^\circ - \gamma)$	$\gamma > 90^\circ$ and $r > \sigma(180^\circ - \gamma)$
		$V =$ cubic spline*	$\gamma > 90^\circ$ and $r_{sw}(\gamma) < r < \sigma(180^\circ - \gamma)$
$r_{sw}(\gamma)$ is the distance at which $V(r,\gamma) = 30$ meV $\sigma(180^\circ - \gamma)$ is the distance at which $V(r,180^\circ - \gamma) = 0$			
4a	Remove frontside attractive well anisotropy	$V = V(r,\gamma)$	$\gamma > \gamma_{sph}$
		$V = V(r,\gamma)$	$r < r_{sw}(\gamma)$ and $\gamma < \gamma_{sph}$
		$V = V(r,\gamma_{sph})$	$r > \sigma(\gamma_{sph})$ and $\gamma < \gamma_{sph}$
		$V =$ cubic spline*	$r_{sw}(\gamma) < r < \sigma(\gamma_{sph})$ and $\gamma < \gamma_{sph}$
$r_{sw}(\gamma)$ is the distance at which $V(r,\gamma) = 30$ meV $\sigma(\gamma_{sph})$ is the distance at which $V(r,\gamma_{sph}) = 0$ meV; $\gamma_{sph} = 90^\circ$ γ_{sph} is the angle below which the potential is angle independent			
4b	Remove backside attractive well anisotropy	$V = V(r,\gamma)$	$\gamma < \gamma_{sph}$
		$V = V(r,\gamma)$	$r < r_{sw}(\gamma)$ and $\gamma > \gamma_{sph}$
		$V = V(r,\gamma_{sph})$	$r > \sigma(\gamma_{sph})$ and $\gamma > \gamma_{sph}$
		$V =$ cubic spline*	$r_{sw}(\gamma) < r < \sigma(\gamma_{sph})$ and $\gamma > \gamma_{sph}$
$r_{sw}(\gamma)$ is the distance at which $V(r,\gamma) = 30$ meV $\sigma(\gamma_{sph})$ is the distance at which $V(r,\gamma_{sph}) = 0$ meV; $\gamma_{sph} = 90^\circ$ γ_{sph} is the angle above which the potential is angle independent			
5	Remove repulsive wall anisotropy	$V = V(r,\gamma_{sph})$	$r < r_{sw}(\gamma_{sph})$
		$V = V(r,\gamma)$	$r > \sigma(\gamma)$
		$V =$ cubic spline*	$r_{sw}(\gamma_{sph}) < r < \sigma(\gamma)$
$r_{sw}(\gamma_{sph})$ is the distance at which $V(r,\gamma) = 30$ meV γ_{sph} is the angle which the potential is isotropic (90°) $\sigma(\gamma)$ is the distance at which $V(r,\gamma) = 0$ meV			
6	Spherical average	$V = \frac{1}{2}\int_0^\pi V(r,\gamma)\sin\gamma\, d\gamma$	for all γ

* The cubic spline equation is $V = a_1 + (r - r_{sw})\{a_2 + (r - \sigma)[a_3 + (r - r_{sw})\, a_4]\}$

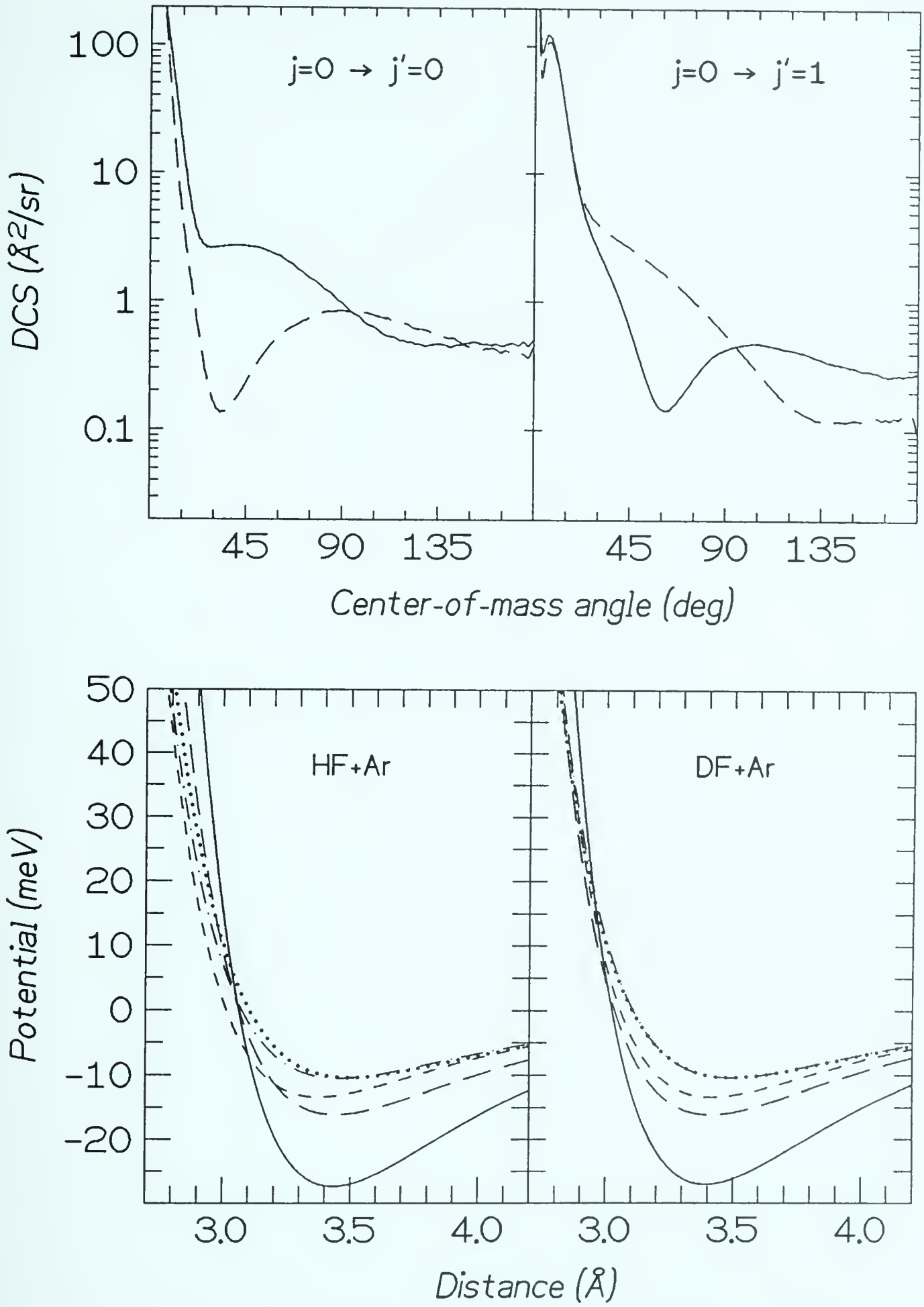

Figure 5.13a Top panels show $j = 0 \rightarrow j' = 0$ and $j = 0 \rightarrow j' = 1$ state to state differential cross sections for the unmodified H6 PE surface. This figure is a basis for comparison for all of the modifications described in Table 5.3. For this and all subsequent plots for Figure 5.13, the line types are: DCS's $\Rightarrow$ HF+Ar (solid), DF+Ar (dashed); Angular cuts for the PE surfaces $\Rightarrow$ 0° – solid, 45° – long dash, 90° – dots, 135° – dot-dash, 180° – short dash.

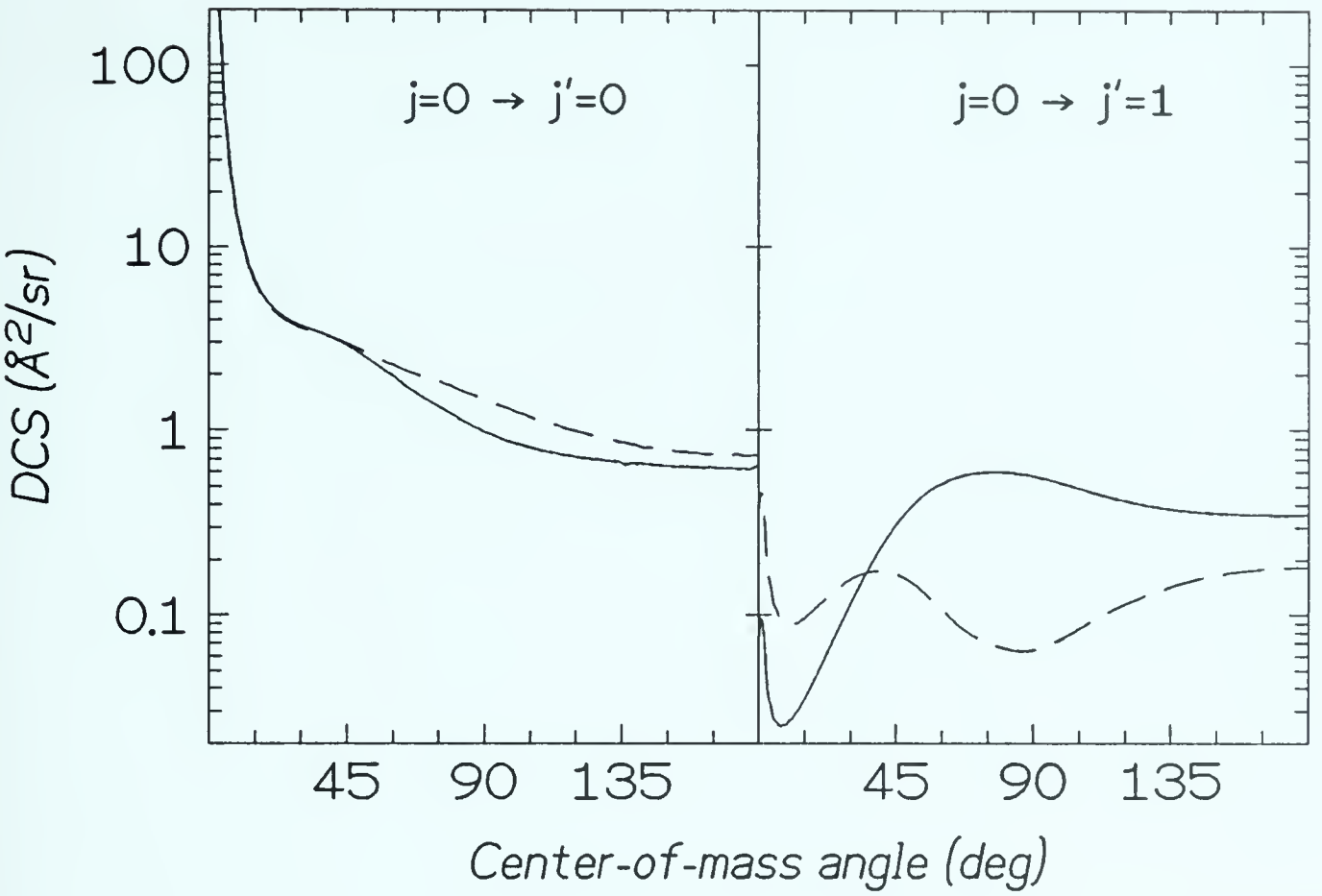

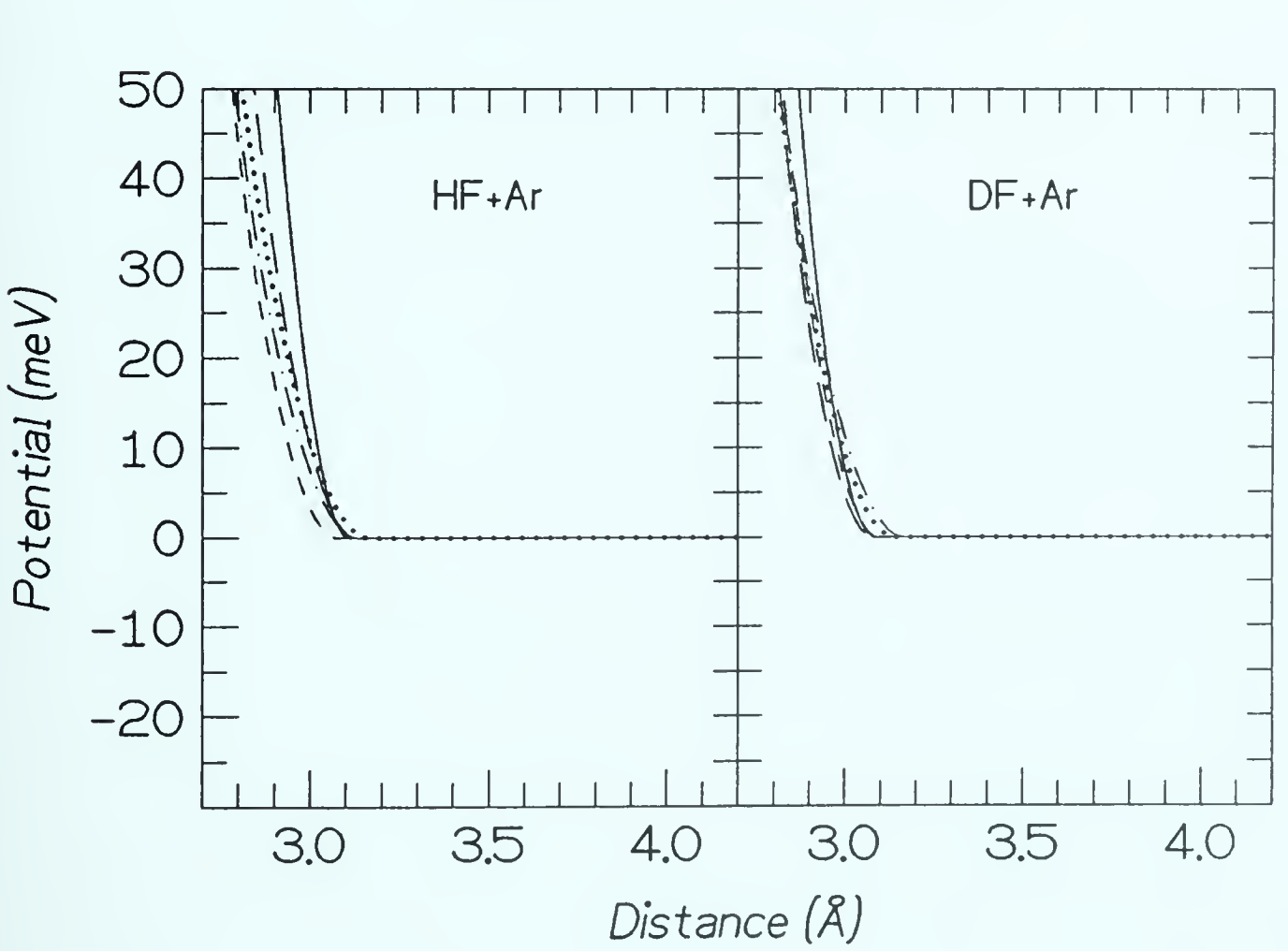

Figure 5.13b $j = 0 \rightarrow j' = 0$ and $j = 0 \rightarrow j' = 1$ state to state differential cross sections for the H6 PE surface with modification #1 from Table 5.3. The potential well has been removed by smoothly joining the repulsive wall to a parabolic form which goes to zero. Line types are identical to those in Figure 5.13a.

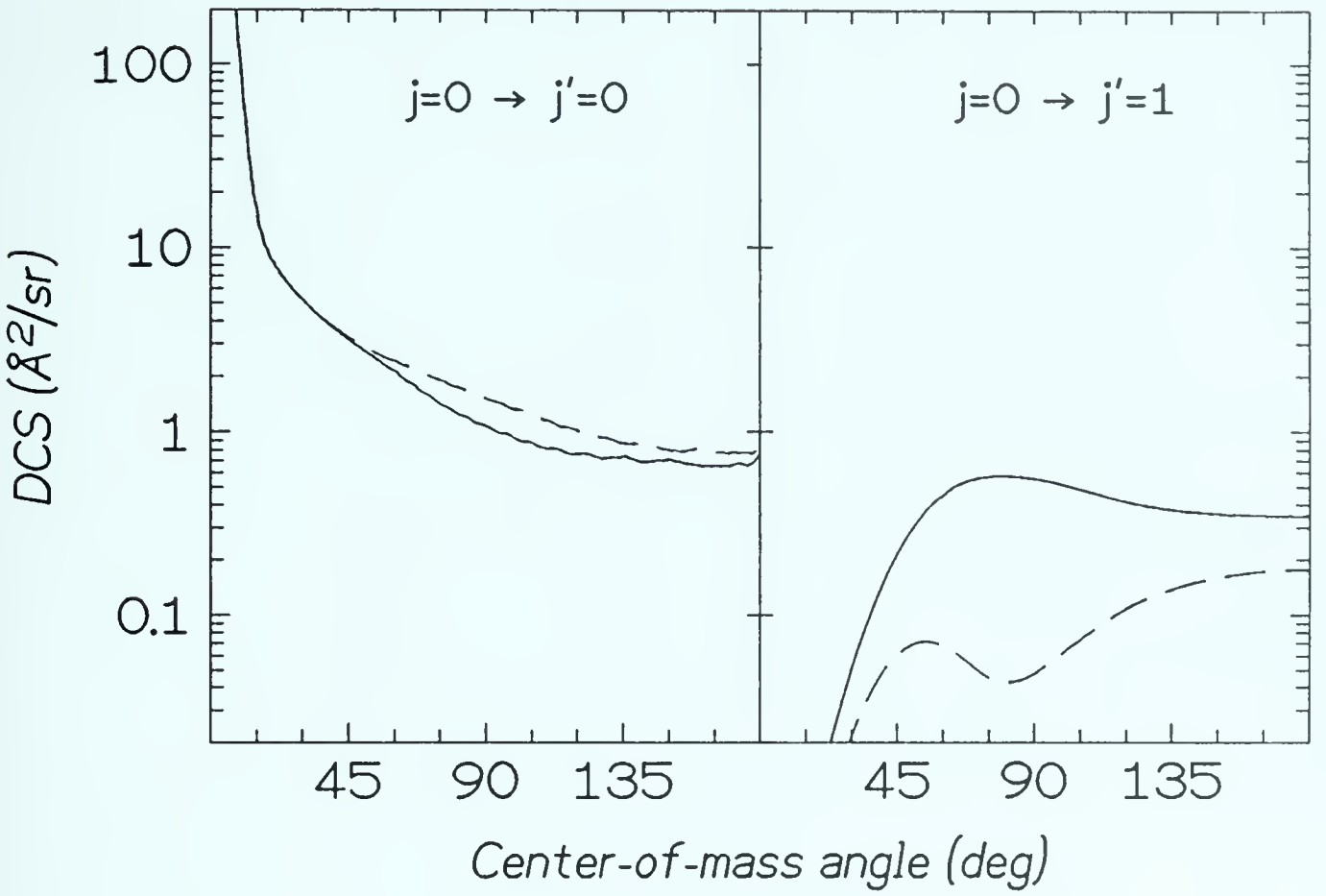

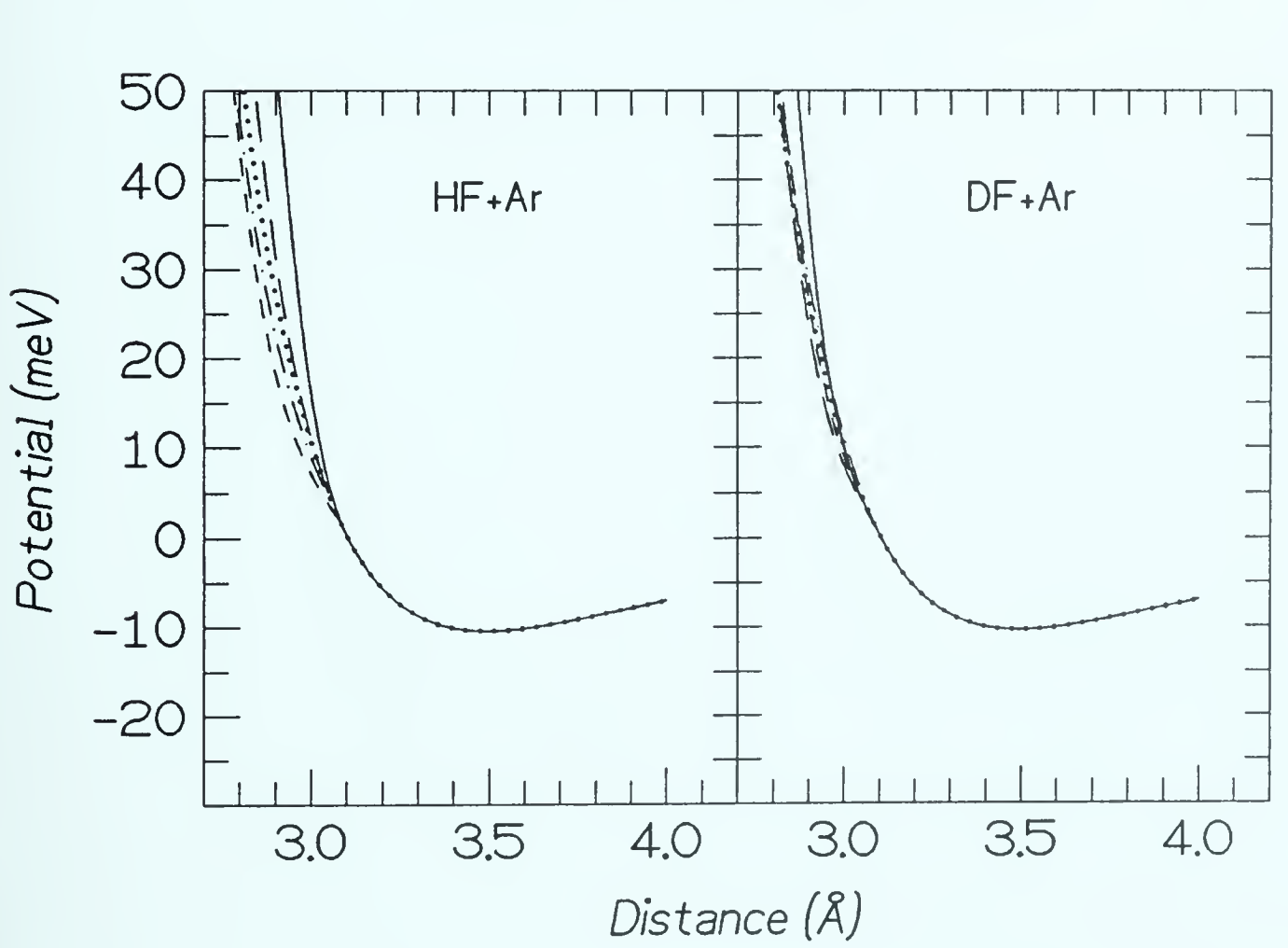

Figure 5.13c $j = 0 \rightarrow j' = 0$ and $j = 0 \rightarrow j' = 1$ state to state differential cross sections for the H6 PE surface with modification #2. The anisotropic repulsive wall is switched starting at 30 meV to an isotropic attractive well equal to the 90° contour.

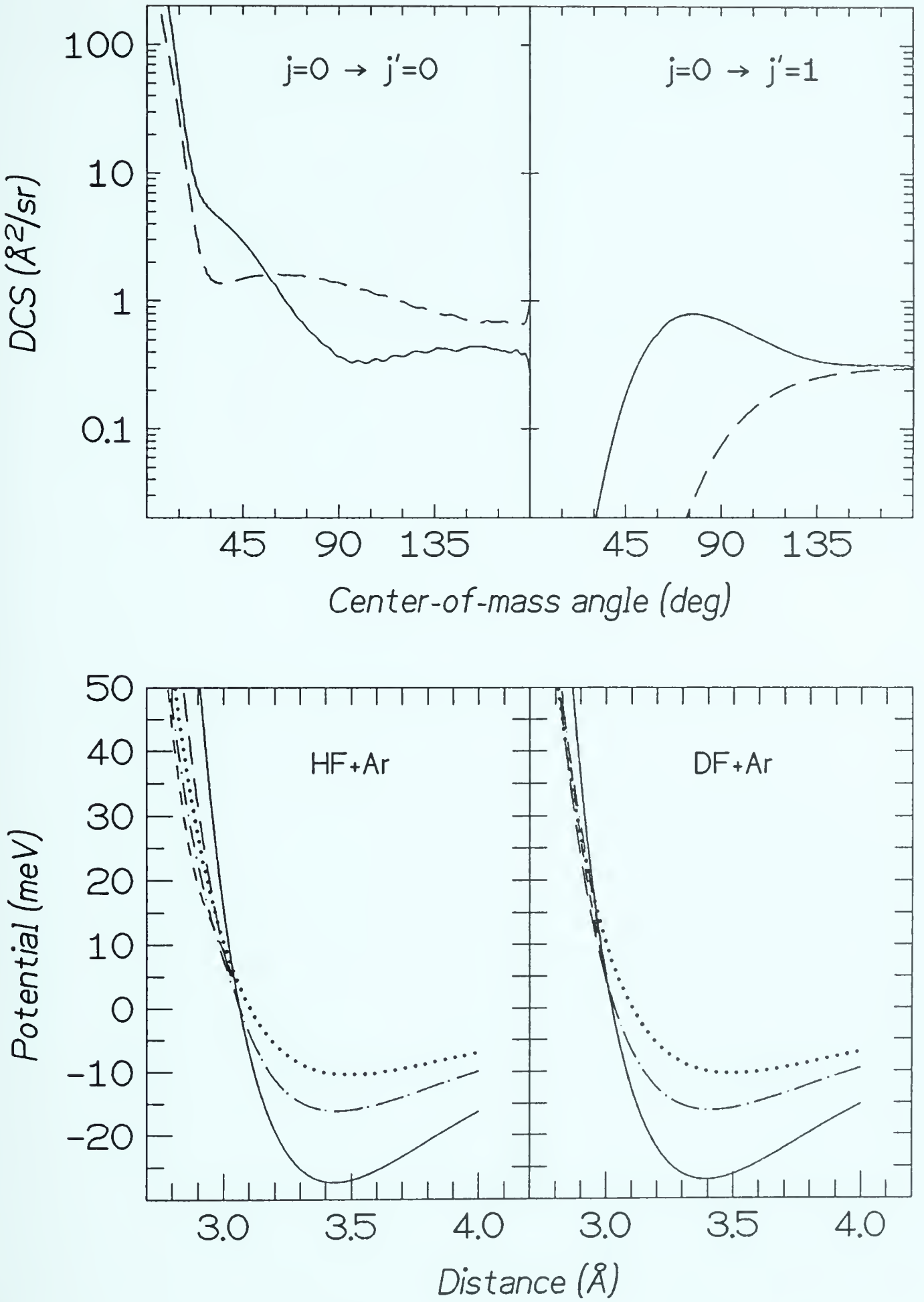

Figure 5.13d $j = 0 \rightarrow j' = 0$ and $j = 0 \rightarrow j' = 1$ state to state differential cross sections for the H6 PE surface with modification #3. The attractive well is symmetric. For interactions in the angular range of 0° to 90°, the PE surface is unchanged. For angles greater than $\gamma = 90^\circ$, the repulsive wall below 30 meV is smoothly switched to a well corresponding to the $180^\circ - \gamma$ orientation.

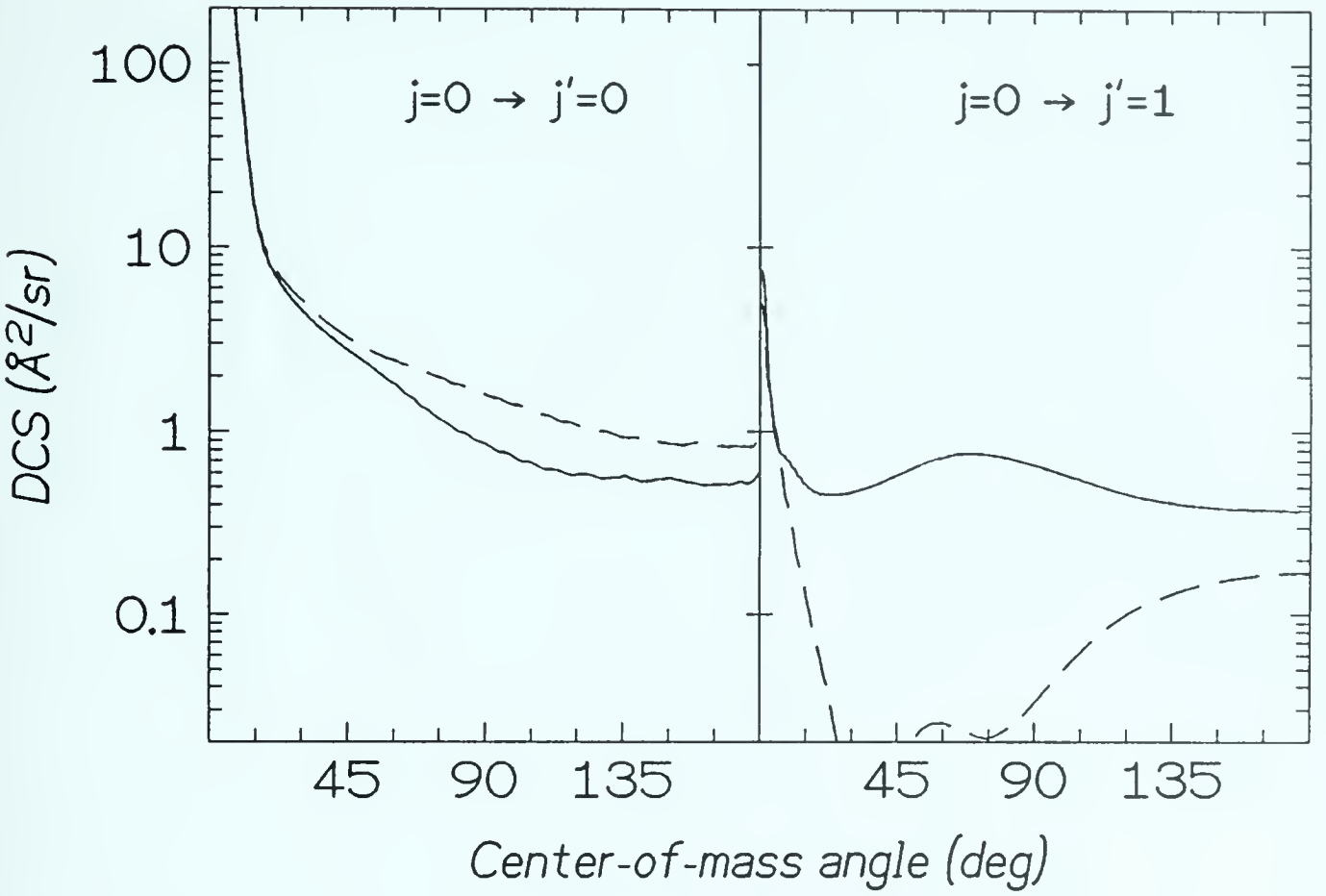

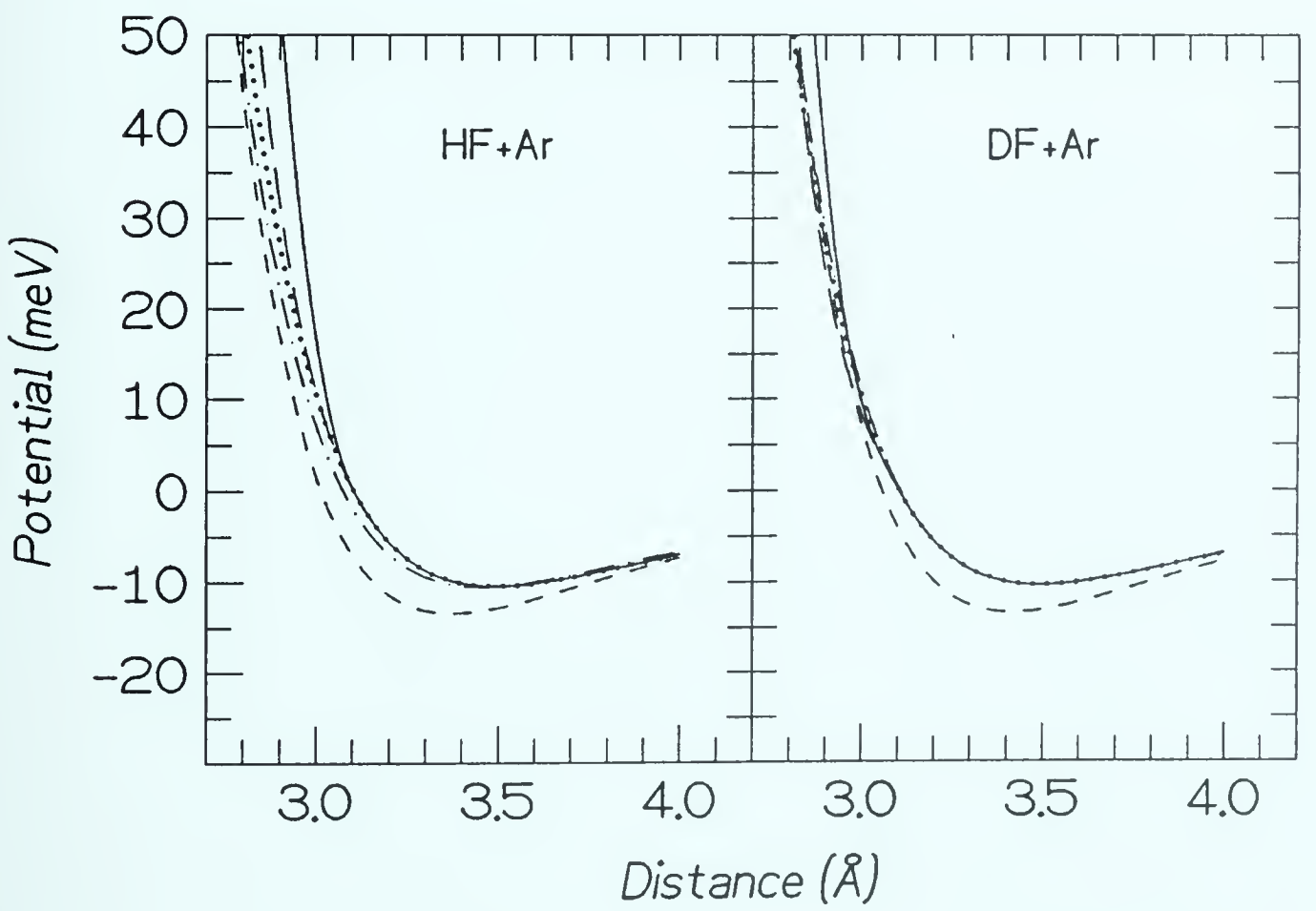

Figure 5.13e $j = 0 \rightarrow j' = 0$ and $j = 0 \rightarrow j' = 1$ state to state differential cross sections for the H6 PE surface with modification #4a. For interactions in the angular range of 90° to 180°, the PE surface is unchanged. For angles less than 90°, the repulsive wall below 30 meV is smoothly switched to an isotropic well corresponding to the 90° orientation.

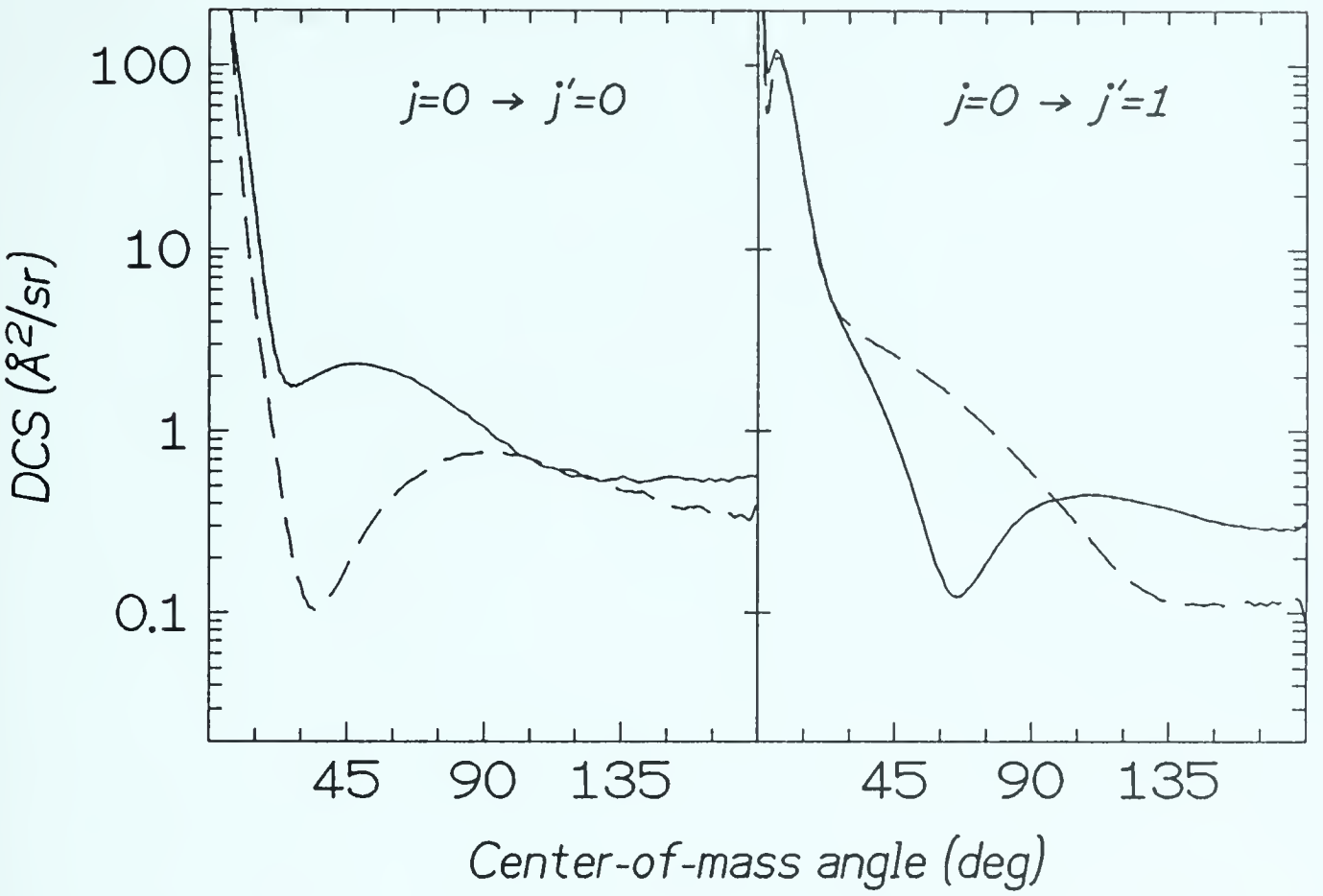

Figure 5.13f $j = 0 \rightarrow j' = 0$ and $j = 0 \rightarrow j' = 1$ state to state differential cross sections for the H6 PE surface with modification #4b. For interactions in the angular range of 0° to 90°, the PE surface is unchanged. For angles greater than 90°, the repulsive wall below 30 meV is smoothly switched to an isotropic well corresponding to the 90° orientation.

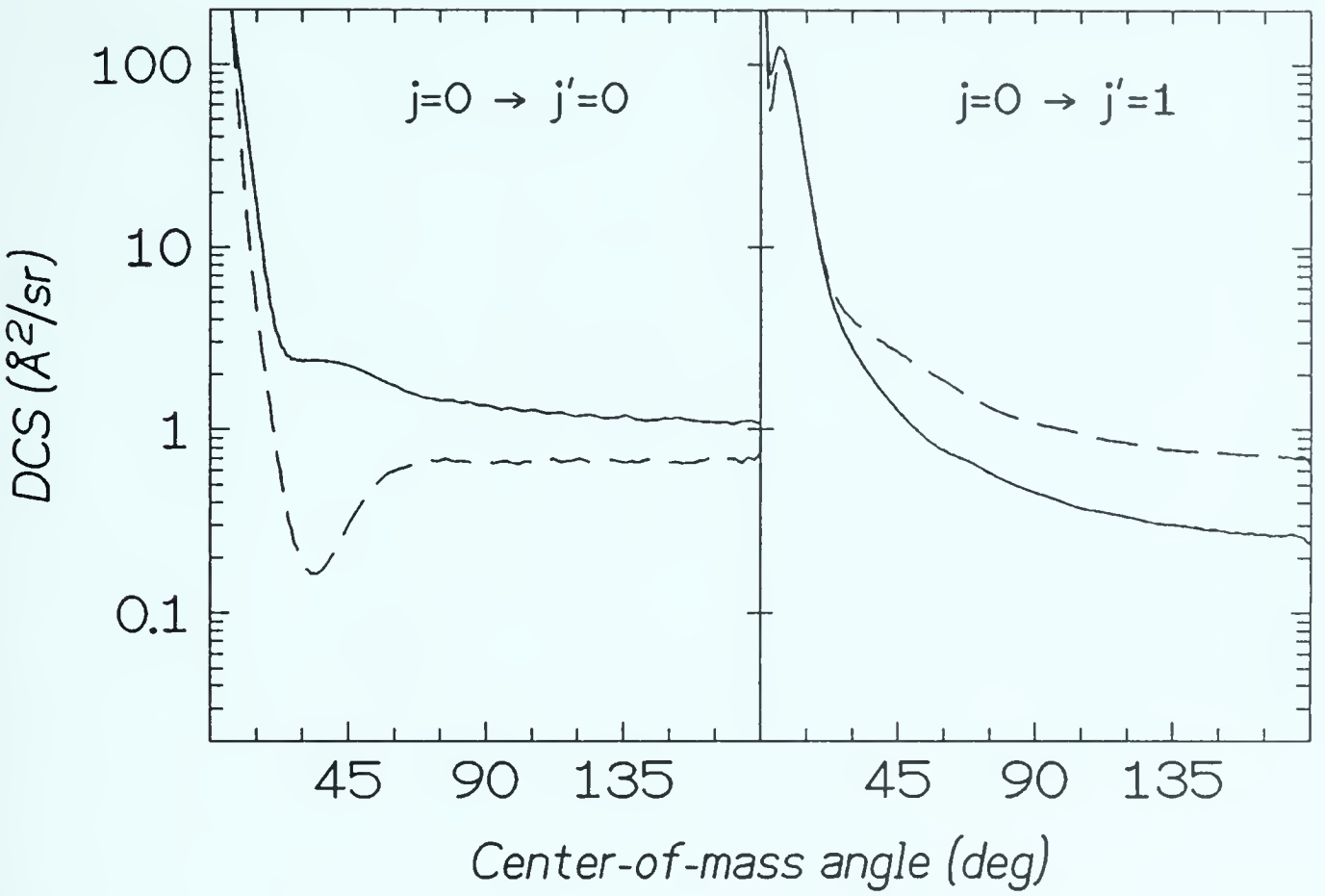

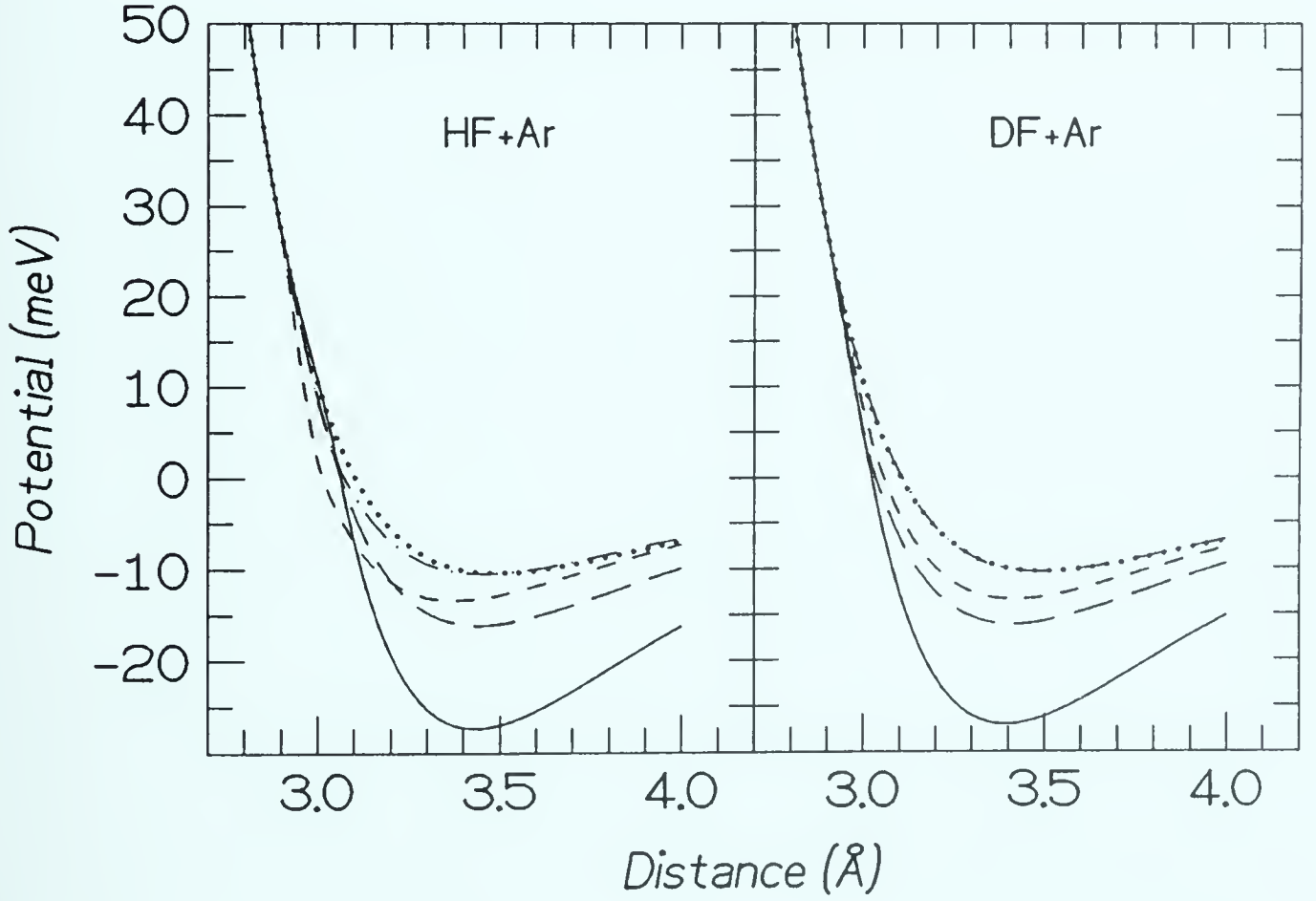

Figure 5.13g $j = 0 \rightarrow j' = 0$ and $j = 0 \rightarrow j' = 1$ state to state differential cross sections for the H6 PE surface with modification #5. The repulsive wall above 30 meV is isotropic, and has the shape corresponding to the 90° contour.

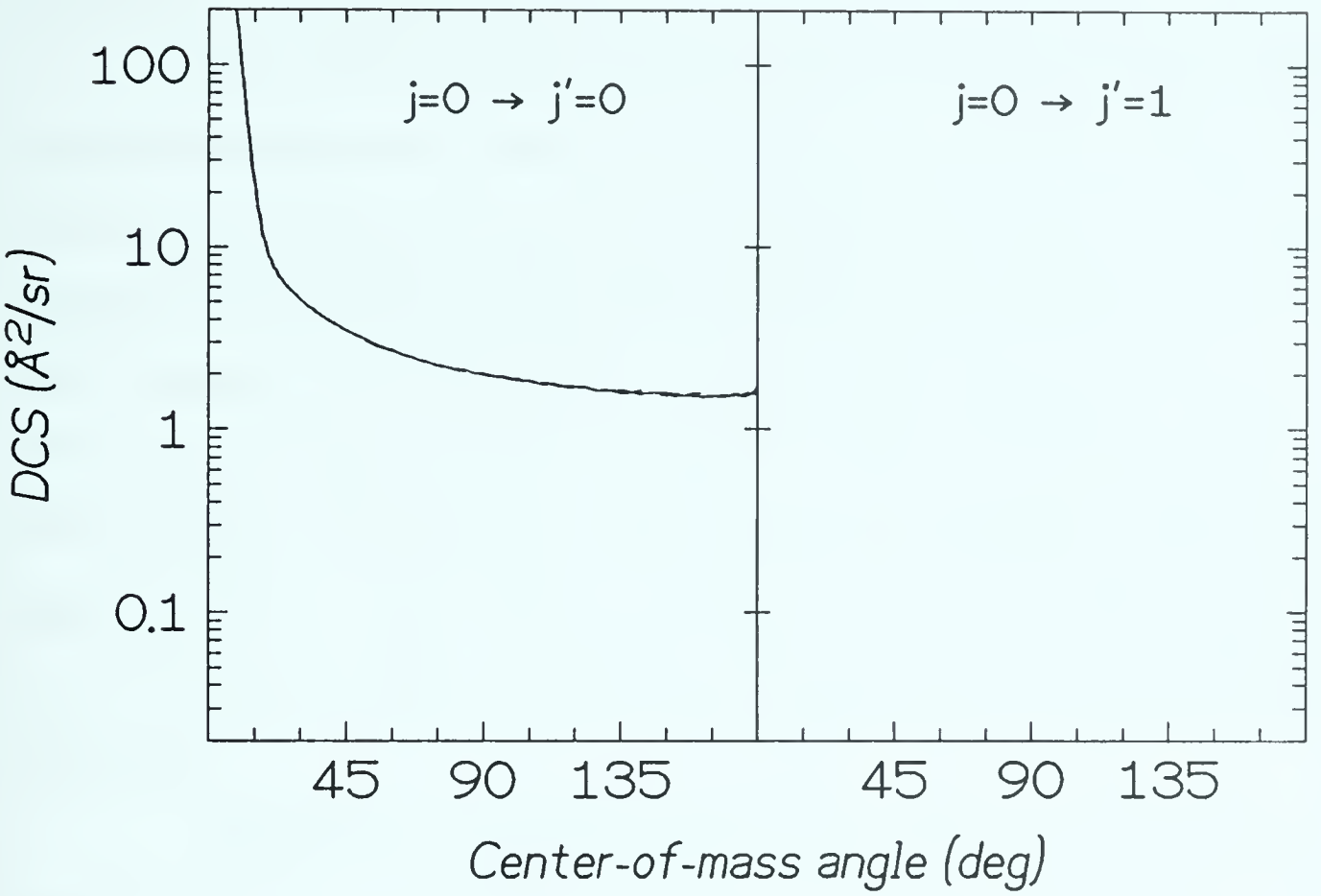

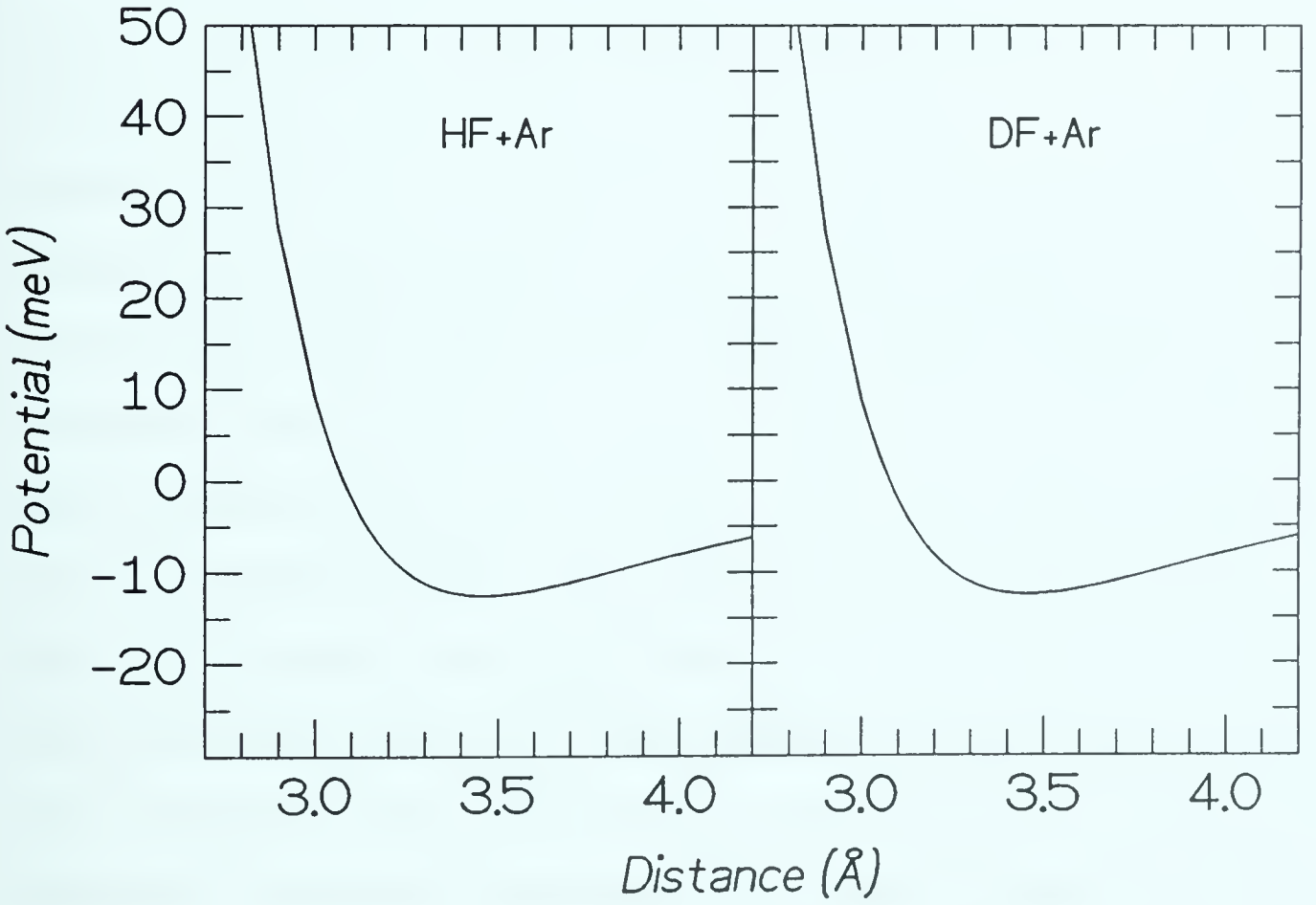

Figure 5.13h $j = 0 \rightarrow j' = 0$ (*i.e.*, elastic) differential cross sections for the spherical average of the H6 PE surface for HF+Ar (solid) and DF+Ar (dashed). (The two curves differ imperceptibly at all angles.) This interaction duplicates the scattering of two structureless particles. Note that by definition the $j = 0 \rightarrow j' = 1$ DCS's do not exist for these PE surfaces.

5.5.A $j = 0 \rightarrow j' = 0$ DCS

The plots of Figures 5.14a to 5.14h provide a very large basis for extracting information about various parts of the potential. One feature common to all of the cross sections is the presence of a strong forward peak due to large impact parameter collisions. The more interesting feature of a shoulder in the 60°range is highly dependent on the PE surface. The unmodified potential is the most highly anisotropic and both the HF+Ar (shoulder) and DF+Ar (minimum) DCS's show a prominent feature in Figure 5.13a. The most extreme opposite case is the spherical potential of Figure 5.13h, where no striking feature in the DCS is seen. Therefore, the HF+Ar shoulder and DF+Ar minimum must be due to anisotropy in the PE surface.

Modification of the PE surface by completely removing the attractive well (Figure 5.13b, modification #1) leaves only a hint of the HF+Ar shoulder, but none of the DF+Ar minimum remains. The well must then be essential to the mid-angle features. Maintaining an attractive well that is isotropic (Figure 5.13c, modification #2) does not reinstate the shoulder (HF+Ar) or dip (DF+Ar), thus confirming that anisotropy in the attractive well is required. If the anisotropy is made to be symmetric (Figure 5.13d, modification #3), the shoulder and dip begin to reappear but they are not as strong as in Figure 5.13a. Modification #4a gives a slightly anisotropic attractive well, and the DCS's (Figure 5.13e) are almost identical to the ones of Figure 5.13c. This modification does not have enough attractive anisotropy to reproduce the original DCS's. However, Figure 5.13f (modification #4b) has an attractive well with almost its full anisotropy, and the reproduction of the unmodified work is essentially exact. The conclusion is that the attractive well must be both anisotropic and highly asymmetric to observe the shoulder in the HF+Ar DCS or the minimum in the DF+Ar DCS.

It is possible that the repulsive wall can affect mid-angle elastic scattering. Figure 5.13g (modification #5) shows scattering with a spherical repulsive

wall. The HF+Ar shoulder and the DF+Ar minimum exist, but they are smaller in magnitude than for the full PE surface. This indicates that the repulsive wall must also be anisotropic, though no comment on symmetry can be made. From the series of figures displayed, it is clear that the $j = 0 \rightarrow j' = 0$ rotationally elastic DCS is influenced by both the attractive well and repulsive wall of the PE surface, and anisotropy is a key characteristic in determining the DCS.

5.5.B $j = 0 \rightarrow j' = 1$

Studying this state-to-state DCS instantly reveals that the various PE surfaces described in Table 5.3 generate vastly different cross sections. The most prominent features on the unmodified PE surface are the HF+Ar minimum at $\sim$ 60°, the slight shoulder for DF+Ar in the range of 45° to 120°, and the oscillation for both systems at $\sim$ 10°. DCS's from the spherical PE surface are not included in this discussion since an isotropic PE surface does not give rise to rotational transitions.

One can again step through the PE surface modifications in Table 5.3 to further clarify the origin of the $j = 0 \rightarrow j' = 1$ features. Removal of the attractive well (Figure 5.13b, modification #1) removes the large forward cross section and destroys the intermediate angle shape. Only the wide-angle part ($\geq$ 150°) of the DCS for both HF+Ar and DF+Ar shows qualitative agreement with the unmodified DCS. This is as expected since the wide angle DCS is mostly comprised of strongly repulsive interactions, and the repulsive part of the potential is unaltered. Also, it is believed that the oscillatory DCS shape in Figure 5.13b is a rotational rainbow, reminiscent of calculations conducted for hard sphere scattering.[29,30]

Figure 5.13c (modification #2) shows the DCS's calculated from the PE surfaces when they have isotropic attractive wells. Note the lack of similarity to the original DCS's, whereby only a rotational rainbow for the HF+Ar, and a rotational rainbow plus what appears to be a supernumery rotational rainbow[13,14,30] for the DF+Ar are visible, with no forward scattering occuring in either case. Making the attractive well anisotropic but symmetric shows little change (Figure 5.13d, modification #3) relative to Figure 5.13c. More interesting observations result from modification #4a. The slightly anisotropic and asymmetric PE surface generates the DCS's in Figure 5.13e, and the beginning of the forward scattering is evident. The most anisotropic and asymmetric PE surface (Figure 5.13f, modification #4b) most closely displays the features seen only in the unmodified work.

Rendering the repulsive wall isotropic (Figure 5.13g, modification #5) retains the oscillation at $\sim 10°$, but features in the 45° to 90° range are absent. Hence, the anisotropic repulsive wall affects the mid-angle scattering.

The conclusion from studying the $j' = 0 \rightarrow j' = 1$ DCS is similar to that of Section 5.5.A. The contributions to the quantum features in the $j = 0 \rightarrow j' = 1$ are affected by both the repulsive wall and attractive well, and the two effects cannot be separated. However, again the PE surface must be anisotropic, and that this anisotropy must also be asymmetric for the observed features in the $j' = 0 \rightarrow j' = 0$ and $j' = 0 \rightarrow j' = 1$ DCS's for both HF+Ar and DF+Ar scattering.

5.6 CONCLUSION

Four different potential energy (PE) surfaces recently proposed in the literature[1,18,19,31] were studied. Using these PE surfaces, reproduction of experimentally measured DCS's via the infinite order sudden approximation technique has proven to be less than satisfactory. Thus, exact quantum calculations are required to provide acceptable theoretical agreement with experiment (see Table 5.1). Within this context, the most recently proposed PE surface by Hutson[1] is clearly demonstrated to be the most accurate in reproducing the experimental results.

The most notable experimental state-summed DCS features are the "shoulder" in the $j' = 0$ DCS and the resurgence of wide-angle signal in the $j' = 4$ and $j' = 5$ DCS's. The latter feature is believed to be the result of highly inelastic collisions, while the former is not readily explained. Attempts to decompose the rotational state summed $j' = 0$ DCS into its component state-to-state DCS's clearly show that the shoulder is a remnant of the $j = 0 \rightarrow j' = 0$ state-to-state DCS. Isotopic substitution of DF for HF show that this feature is dependent upon the magnitude of the diatomic rotational constant, as well as the degree of anisotropy in the PE surface. Analysis of two parts of the PE surface (*i.e.*, attractive well versus repulsive wall) show that asymmetric anisotropy coupled with a complex interplay between the attractive well and repulsive wall are responsible for the experimentally observed shoulder in the $j' = 0$ DCS.

REFERENCES:

1. J. M. Hutson, *J. Chem. Phys.* **96**, 6752 (1992).
2. For the case of HF+Ar, see C. M. Lovejoy and D. J. Nesbitt, *J. Chem. Phys.* **91**, 2790 (1989) and other sources listed in Ref. 1.
3. P. L. Jones, U. Hefter, A. Mattheus, J. Witt, K. Bergmann, W. Müller, W. Meyer, and R. Schinke, *Phys. Rev. B* **26**, 1283 (1982); P. L. Jones, E. Gottwald, U. Hefter, and K. Bergmann, *J. Chem. Phys.* **78**, 3838 (1983), and references therein.
4. U. Buck, H. Meyer, and R. J. LeRoy, *J. Chem. Phys.* **80**, 5589 (1984).
5. M. Faubel and G. Kraft, *J. Chem. Phys.* **85**, 2671 (1986).
6. U. Buck, D. Otten, and R. Schinke, *J. Chem. Phys.* **82**, 202 (1985); U. Buck, H. Meyer, M. Tolle, and R. Schinke, *Chem. Phys.* **104**, 345 (1986).
7. L. Beneventi, P. Casavecchia, F. Vecchiocattivi, G. G. Volpi, D. Lemoine, and M. H. Alexander, *J. Chem. Phys.* **89**, 3505 (1988).
8. H. J. Loesch, *Adv. Chem. Phys.* **52**, 421 (1980).
9. U. Buck, *Comments At. Mol. Phys.* **17**, 143 (1986).
10. M. Keil and H. R. Mayne, *Chem. Phys. Lett.* **85**, 456 (1982); H. R. Mayne and M. Keil, *J. Phys. Chem.* **88**, 883 (1984).
11. L. J. Rawluk, Y. B. Fan, Y. Apelblat, and M. Keil, *J. Chem. Phys.* **94**, 4205 (1991).
12. P. F. Vohralik, R. E. Miller, and R. O. Watts, *J. Chem. Phys.* **90**, 2182 (1989).
13. R. Schinke and J. M. Bowman, in *Molecular Collision Dynamics*, edited by J. M. Bowman (Springer-Verlag, Berlin, 1982), Chapter 4.
14. R. Schinke, H. J. Korsch, and D. Poppe, *J. Chem. Phys.* **77**, 6005 (1982).
15. L. J. Danielson and M. Keil, *J. Chem. Phys.* **88**, 851 (1988).
16. L. J. Rawluk and M. Keil, *J. Opt. Soc. Am. B* **6**, 1278 (1989).
17. Y. B. Fan, L. J. Rawluk, Y. Apelblat, and M. Keil, *J. Opt. Soc. Am. B* **8**, 1218 (1991).
18. J. M. Hutson and B. J. Howard, *Mol. Phys.* **45**, 791 (1982).
19. D. J. Nesbitt, M. S. Child, and D. C. Clary, *J. Chem. Phys.* **90**, 4855 (1989).

20. C. Douketis, J. M. Hutson, B. J. Orr, and G. Scoles, *Mol. Phys.* **52**, 763 (1984).

21. W. A. Lester Jr., *Meth. Comp. Phys.* **10**, 211 (1971), and references contained therein.

22. HIBRIDON is a package of programs for the time-independent quantum treatment of inelastic collisions and photodissociation written by M. H. Alexander, D. E. Manolopoulos, H.–J. Werner, and B. Follmeg, with contributions by P. F. Vohralik, D. Lemoine, G. Corey, B. Johnson, T. Orlikowski, W. Kearney, A. Berning, A. Degli-Esposti, C. Rist, and P. Dagdigian.

23. G. A. Parker and R. T Pack, *J. Chem. Phys.* **68**, 1585 (1978).

24. The center-of-mass classical trajectory results were transmitted to us by Dr. Howard Mayne of the University of New Hampshire, and are used as provided with no further calculational modifications.

25. J. M. Hutson and B. J. Howard, *Mol. Phys.* **45**, 769 (1982).

26. G. C. Maitland and E. B. Smith, *Chem. Phys. Lett.* **22**, 443 (1973).

27. S. J. Harris, S. E. Novick, and W. Klemperer, *J. Chem. Phys.* **60**, 3208 (1974); T. A. Dixon, C. H. Joyner, F. A. Baiocchi, and W. Klemperer, *J. Chem. Phys.* **74**, 6539 (1981); M. R.Keenan, L. W. Buxton, E. J. Campbell, A. C. Legon, and W. H. Flygare, *J. Chem. Phys.* **74**, 2133 (1981).

28. Page 50 of M. A. D. Fluendy and K. P. Lawley, in *Chemical Applications of Molecular Beam Scattering*, (Chapman and Hall Ltd., London, 1973).

29. R. Schinke, *J. Chem. Phys.* **73**, 6117 (1980).

30. H. J. Korsch and R. Schinke, *J. Chem. Phys.* **75**, 3850 (1981).

CHAPTER 6

GENERAL DISCUSSION

This thesis is a study of the experimental and theoretical aspects of HF+Ar rotationally inelastic differential scattering. This is a specific example of highly anisotropic interactions between an atom and a diatom. In many studies such as this,[1,2] the atom is a member of the inert gas family. For weak van der Waals interactions, the diatom has been varied from H_2[3,4], to N_2,[5,6] to alkali dimers such as Na_2.[7,8] The hydrogen halides represent a different type of interaction since the permanent dipole makes the system much more attractive. For example, the well depth $\epsilon \approx 1.7$ meV for H_2 + He[9]; $\epsilon \approx 1.2$ meV for Na_2 + He[10]; $\epsilon \approx 4.0$ meV for HF + He[11] which is more than double the other attractive wells, and clearly shows how the permanent dipole increases the attraction in the system.

The HF + Ar system includes two very interesting potential energy (PE) surface features: short-range repulsion with significant long-range attraction, and strong angular dependence in the PE surface. Measuring the final rotational state-resolved differential cross sections for $j' = 0 - 5$ is one way of probing both the radial and angular dependence of the PE surface. The interest in systems which couple strong attraction and strong angular dependence makes this project valuable to the scientific community.[12–14]

The continuous wave hydrogen fluoride chemical laser has proven to be an excellent infrared radiation source (centered at $\sim 2.5\mu$m) for these inelastic DCS experiments. The most obvious feature is the natural spectral overlap between the emission of the laser and the HF molecules being probed. The amount of usable laser power is directly related to the laser emission bandwidth. Contributing to the laser emission bandwidth is Doppler broadening in the laser cavity ($\sim$ 370MHz), the natural line width on the order of tens of hertz, and the collisional broadening

of $\sim$ 5 MHz. The laser cavity length (the distance from the output coupler to the diffraction grating) is 26 cm, therefore allowing only one longitudinal mode to oscillate since the spacing between adjacent modes[15] is given by $\frac{c}{2L} = 580$ MHz. Thus, the laser output profile (power *vs.* frequency spectrum) reflects its Doppler profile.

The absorption spectrum of HF molecules in the molecular beam is on the order of tens of megahertz wide due to the narrow collimation of the molecular beam, and so it is experimentally advantageous to narrow the laser emission spectrum below its Doppler breadth. This is done by exploiting the Lamb dip[15] superimposed on the Doppler profile. This phenomenon is due to molecules in the laser cavity reabsorbing some of the stimulated emission radiation, and the resulting power curve as a function of cavity length is shown in Figure 2.3. The output power profile with Lamb dip as a function of cavity length is used to generate a discriminator signal which allows active stabilization of the output frequency on the center of the emission/absorption profile. The laser output is referred to as optically bright owing to the frequency spread being $\lesssim$ 15 MHz rather than its Doppler width. This narrow band emission is now intense enough to saturate the transition in the molecular beam.

Another important laser feature is the presence of R–branch lasing with sufficient power for studying $R_1(0)$, $R_1(1)$, and $R_1(2)$ transitions. In particular, the $R_1(0)$ line is crucial because it allows study of the HF rotor population in $j = 0$, which could otherwise not be done if only P–branch transitions were available. Also important are the $R_1(1)$ and $R_1(2)$ transitions since they explore the same HF molecules as do $P_1(1)$ and $P_1(2)$. This gives rise to the possibility of comparing signals obtained from probing with one type of transition (*e.g.*, R–branch) versus the other type (*e.g.*, P–branch), as is shown in Sections 3.3 and 3.4.

The actual molecular beam detection technique is a marriage between the HF laser and a low temperature (1.5K) bolometer detector. The bolometer is

an energy flux detector,[16] where the energy can be kinetic and/or internal energy of molecules, or thermal energy from a light source. Before any interaction with the laser, the HF molecules have kinetic energy and internal energy from rotation. When an HF molecule strikes the detector surface, some proportion of the kinetic energy, internal energy and the heat of condensation in going from the gas to the solid phase is given up to the detector surface. When laser absorption occurs, the HF molecules are excited from the ground state ($\nu = 0, j$) to an upper level ($\nu = 1, j+1$ for the R–branch or $\nu = 1, j-1$ for the P–branch). If such an excited molecule now impinges onto the detector, the same amount of kinetic energy and heat of condensation are released as before pumping, but a different amount of internal energy is liberated. Chopping the laser generates a modulated signal directly proportional to the number of molecules that have excess internal energy. Note that such a chopped signal is independent of both the kinetic energy and the adsorption energy, as well as their accomodation on the cold bolometer surface.

In Chapter 3 the theory is developed showing the mathematical relation between the number of molecules in the upper and lower state if the pumping mechanism couples an isolated two-level system (Equation 3-2) . This connection is crucial since the goal of this investigation is to determine the relative number of HF molecules in a particular $\nu = 0$ rotational state after scattering (*i.e.*, the energetically lower level before laser interaction in the two level system being considered).

Equation 3–5 (repeated here) relates the bolometer signal to the population of the j state being probed (refer to Chapter 3 for symbol definitions).

$$S_{\text{bolo}} \propto \frac{N B_{12} \rho \Delta E_{12}}{A_{21} + (B_{21} + B_{12})\rho} \left[1 - e^{-[A_{21} + (B_{12} + B_{21})\rho]t}\right]. \qquad (3-5)$$

Note that in the exponential term both interaction time t and energy density ρ affect the relation of signal S_{bolo} to population N. Measurements of how each factor influences this relation are shown in Figure 3.3. The displacement between the two

curves indicates that for shorter interaction times (*i.e.*, the fast molecular beam) a higher laser power is needed to achieve the same excitation levels as with the slow molecular beam. A laser power of $\sim 50 - 60$ mW is needed to saturate the optical transitions for the slow molecular beam, and this is the same range of power used in normal operation of the scattering experiment. This is also the maximum laser power obtainable in single mode TEM_{00} operation. The combination of these factors yielded maximum signal levels with the simplest configuration for data analysis (*i.e.*, $S_{\text{bolo}} \leftrightarrow N(j')$).

Either one of two conditions is most ideal when converting bolometer signal to the population:

i. the laser power is low enough that bolometer signal varies linearly with power,

ii. the laser power is high enough to saturate the optical transition of the absorbing molecules.

Item *i* requires that the analysis equations include a term for power dependence. Contrary to this is the condition of item *ii* where the power term can be removed, thus making the Einstein A and B factors of Equation 3–5 no longer required. Coincidently then, the experimental signal becomes insensitive to modest laser power variations. This dependence on power was not examined before selecting this research project, so it may be considered somewhat fortuitious that the HF vib-rotational transitions are saturated at such low power levels.

It is possible that the most appealing way to carry out molecular dynamics studies would be to conduct "real time"[17] experiments. The quantum states of the molecules are followed as the scattering event evolves in time. This technique typically involves lasers whose pulse duration is on the order of femtoseconds. In contrast, the chemical laser output in these experiments is continuous in time, meaning that "real time" experiments are not possible. Rather, the HF rotational

state distribution before the scattering event is measured, followed by measuring the post-collision DCS for each particular final rotational state. In this way the change in rotational state distribution can be followed as a function of scattering angle. The "real time" behavior can then be generated theoretically from quantum dynamical calculations using PE surfaces realistic enough to reproduce both the scattering results and high-resolution spectroscopy of bound-state Ar•HF.

The experimentally measured DCS's are shown in Figure 4.3, with several features that bear close inspection. First of all, the DCS for each j' shows a strong forward peak followed by a drop of intensity as the scattering angle is increased. This observation is similar to the DCS's generated from classical mechanics for atom-atom scattering where the large intensity-low angle DCS is due to large impact parameter collisions since they have the greatest probability of occurance. Also, from Figure 4.4 there is evidence that for lab scattering angles up to $\sim 40°$ the scattering is mostly elastic. This is in agreement with sampling mainly the attraction of the PE surface. For larger scattering angles ($\theta_{\rm lab} \gtrsim 50°$), a larger extent of the repulsive core is sampled, and these impulsive collisions give rise to a greater fraction of rotationally inelastic collisions.

The change in DCS shape when switching from $j' = 0$ up to $j' = 5$ reflects the change in the type of scattering (*i.e.*, predominantly elastic to predominantly inelastic). The $j' = 0$ DCS has a strong forward peak followed by the quantum mechanical shoulder at intermediate angles and then a monotonic decline in intensity at wide angles. The $j' = 1$ DCS behaves likewise except for the absence of the mid-angle shoulder. $j' = 2$ and 3 DCS's show a flattening out of the DCS at wide angles, and $j' = 4$ and 5 DCS's have a weak forward intensity, a hole at intermediate angles and a resurgence of signal at wide angles. This behavior is very typical of DCS's having a large composition of inelastic scattering, and for these large j' a rotational rainbow is evident.[12]

The most interesting DCS feature is the shoulder in the $j' = 0$ DCS. Attempts to explain this shoulder as being a remnant of an elastic "L-type" (impact parameter) rainbow fail because the angular range of the shoulder ($30 - 40°$) is very different than that of the L-type rainbow ($\sim 7°$) observed by Vohralik *et al.*[1] and calculated classically and quantum mechanically.[18] Rationalizing the shoulder as a rotational rainbow is not possible either since the collisions giving rise to this cross section are mostly elastic and also since the intensity drops at wide angles. A further understanding of the $j' = 0$ shoulder is left to a theoretical study.

The initial theoretical attempt at explaining the HF+Ar scattering dynamics was done with the infinite order sudden (IOS) approximation.[19] These calculations, which include the development of the center-of-mass to laboratory transformations and the coding of the inelastic IOS approximation DCS's, were carried out for rotationally inelastic scattering on four PE surfaces in the literature[20–23] and compared to the scattering results (Figures 5.4a–d). The relatively poor reproduction of experimental DCS's by any of the four PE surfaces is one of the first indicators that the IOS dynamics are insufficient for this system. In particular, only the Hutson and Howard[20] PE surface displays a broad shoulder in the $j' = 0$ DCS. None of the newer potentials (which are presumably better characterized) displays even a hint of a shoulder. The flattening out of the DCS for $j' = 2$ and 3 is not seen for any calculated IOS DCS, and only the Hutson and Howard[20] PE surface shows structure which resembles a rotational rainbow in the $j' = 4$ and 5 DCS's. The very poor low-angle quantitative agreement, coupled with the knowledge that the large HF rotational constant is detrimental to the success of the IOS approximation, has made these calculations unreliable for comparisons to experimental results. Also noted is that the fitting parameter δ presented in Table 5.1 is very large for all PE surfaces. An attempt to categorize the PE surfaces according to their ability to calculate DCS's (and other properties) is useless with such a poor dynamical approximation.

Exact quantum dynamics are the best way to examine the HF+Ar differential scattering. Calculations done with the HIBRIDON code of Professor Millard H. Alexander at the University of Maryland show that the most recent HF+Ar PE surface[23] is the best in reproducing the experimental DCS's. In particular, the $j' = 0$ shoulder is accurately reproduced, and the rotational rainbow in $j' = 4$ and 5 is qualitatively evident. The close-coupling and experimental results complement each other very well because each independent study so closely reproduces the results of the other, and thus lends credence to the other work. As suspected, the earliest potential of Hutson and Howard[20] is shown to do the poorest job of reproducing the experimental features.

Further examination of the $j' = 0$ shoulder by decomposing the DCS into a sum of state to state DCS's shows that the $j = 0 \rightarrow j' = 0$ and $j = 1 \rightarrow j' = 0$ DCS's contribute $\geq 95\%$ of the state summed DCS. The shoulder is present in the $j = 0 \rightarrow j' = 0$ DCS while simultaneously the $j = 1 \rightarrow j' = 0$ DCS has a "hole" at the same angular region. This combination of features between the two DCS's is what gives the shoulder in the final rotational state summed experimental DCS. A similar comparison of the $j = 1 \rightarrow j' = 1$ and $j = 0 \rightarrow j' = 1$ DCS's (*i.e.*, the main components of the $j' = 1$ state-summed DCS) shows no shoulder in the $j = 1 \rightarrow j' = 1$ DCS, and only a shallow "hole" in the $j = 0 \rightarrow j' = 1$ DCS. Thus, a shoulder in the $j' = 1$ state-summed DCS is non-existant.

Comparison of the exact quantum $j = 0 \rightarrow j' = 0$ DCS to the same DCS obtained from classical trajectory studies[24] show the shoulder to be a quantum mechanical effect. Further investigations into which part or parts of the PE surface dictate the shoulder's presence have thus far led only to the conclusion that it is a result of a complicated interaction between attractive and repulsive anisotropic components of the potential (see Chapter 5).

In conclusion, this careful examination of HF + Ar scattering has provided fundamental knowledge about the energy transfer process. The past generation of elastic experiments and IOSA calculations[25] provided the footing on which the developments presented herein stand. The success of the inelastic scattering experiments is largely due to the discovery of the $R_1(0)$ laser transition and the subsequent ability to actively stabilize the output frequency of the HF chemical laser. Incorporating the laser + bolometer detection scheme[26] presented in Chapters 2 and 3 allowed the accurate measurement of final rotational-state resolved DCS's to be determined.[27] Finally, a thorough theoretical investigation using quantum dynamics concludes the analysis of the HF + Ar scattering system.

REFERENCES:

1. P. F. Vohralik, R. E. Miller, and R. O. Watts, *J. Chem. Phys.* **90**, 2182 (1989).

2. P. L. Jones, U. Hefter, A. Mattheus, J. Witt, K. Bergmann, W. Müller, W. Meyer, and R. Schinke, *Phys. Rev. B* **26**, 1283 (1982); P. L. Jones, E. Gottwald, U. Hefter, and K. Bergmann, *J. Chem. Phys.* **78**, 3838 (1983), and references therein.

3. U. Buck, F. Huisken, J. Schleusener, and H. Pauly, *Phys. Rev. Lett.* **38**, 680 (1977); U. Buck, *Faraday Disc. Chem. Soc.* **73**, 187 (1982).

4. W. R. Gentry and C. F. Giese, *J. Chem. Phys.* **67**, 5389 (1977).

5. M. Keil, J. T. Slankas, and A. Kupperman, *J. Chem. Phys.* **70**, 541 (1979).

6. A. J. Banks, D. C. Clary, and H. -J. Werner, *J. Chem. Phys.* **84**, 3788 (1986).

7. K. Bergmann, R. Engelhardt, U. Hefter, P. Hering, and J. Witt, *Phys. Rev. Lett.* **40**, 1446 (1978); U. Hefter, P. L. Jones, A. Mattheus, J. Witt, and K. Bergmann, *Phys. Rev. Lett.* **46**, 915 (1981); P. L. Jones, E. Gottwald, U. Hefter, and K. Bergmann, *J. Chem. Phys.* **78**, 3838 (1983).

8. W. D. Phillips, J. A. Serri, D. J. Ely, D. E. Pritchard, K. R. Way, and J. L. Kinsey, *Phys. Rev. Lett.* **41**, 937 (1978); W. P. Moskowitz, B. Stewart, R. M. Bilotta, J. L. Kinsey, and D. E. Pritchard, *J. Chem. Phys.* **80**, 5496 (1984).

9. P. Schafer and R. G. Gordon, *J. Chem. Phys.* **58**, 5422 (1973).

10. E. Berbenni and P. McGuire, *Chem. Phys. Lett.* **45**, 84 (1977).

11. W. R. Rodwell, L. T. Sin Fai Lam and R. O. Watts, *Molec. Phys.* **44**, 225 (1981).

12. R. Schinke and J. M. Bowman, *Molecular Collision Dynamics*, edited by J. M. Bowman (Springer-Verlag, Berlin, 1982), Chapter 4.

13. U. Buck, *Com. At. Mol. Phys* **17**, 143 (1986). **68**, 1585 (1978).

14. R. J. Cross, *J. Chem. Phys* **52**, 5703 (1970).

15. O. Svelto, *Principles of Lasers, Third Edition* (Plenum Press, New York, 1989). Chapter5, Sections 5.1 - 5.3.

16. *Atomic and Molecular Beam Methods*, edited by G. Scoles (Oxford University Press, New York, 1988). Chapter 10.

17. L. R. Khundkar, J. L. Knee, D. D. Smith and A. H. Zewail, *J. Chem. Phys.* **87**, 77 (1987); N. F. Scherer and A. H. Zewail, *J. Chem. Phys.* **87**, 87 (1987); J. L. Knee, L. R. Khundkar and A. H. Zewail, *J. Chem. Phys.* **87**, 115 (1987); N. F. Scherer, L. R. Khundkar, R. B. Bernstein and A. H. Zewail, *J. Chem. Phys.* **87**, 1451 (1987); M. Dantus, M. J. Rosker and A. H. Zewail, *J. Chem. Phys.* **87**, 2395 (1987); M. Gruebele and A. H. Zewail, *Physics Today* **43**, 24 (1990).

18. L.J.Rawluk, M. Keil, M. H. Alexander, H. R. Mayne and J. J. C. Barrett, *Chem. Phys. Lett.* **202**, 291 (1993).

19. G. A. Parker and R. T Pack, *J. Chem. Phys.*

20. J. M. Hutson and B. J. Howard, *Mol. Phys.* **45**, 791 (1982).

21. C. Douketis, J. M. Hutson, B. J. Orr, and G. Scoles, *Mol. Phys.* **52**, 763 (1984).

22. D. J. Nesbitt, M. S. Child, and D. C. Clary, *J. Chem. Phys.* **90**, 4855 (1989).

23. J. M. Hutson, *J. Chem. Phys.* **96**, 6752 (1992).

24. H. R. Mayne and J. J. C. Barrett, Univerisity of New Hampshire. Private communication.

25. L. J. Danielson, *Determination of Interatomic and Intermolecular Potential Energy Surfaces from Crossed Molecular Beam Scattering*, Ph.D. thesis, University of Alberta, 1988.

26. T. E. Gough, R. E. Miller, and G. Scoles, *Appl. Phys. Lett.* **30**, 338 (1977).

27. L. J. Rawluk, Y. B. Fan, Y. Apelblat, and M. Keil, *J. Chem. Phys.* **94**, 4205 (1991).

28. (a) *Atom-Molecule Collision Theory: A Guide for the Experimentalist*, edited by R.B. Bernstein (Plenum, New York, 1979); (b) R.B. Bernstein, *Chemical Dynamics via Molecular Beam and Laser Techniques* (Clarendon, Oxford, 1982).

APPENDIX A

EXPERIMENTAL DETAILS

The experiments presented in this thesis are the result of two individual and unrelated pieces of equipment being brought together. The first is the continuous wave hydrogen fluoride chemical laser which had not been used previously in a narrow emission bandwidth configuration.[1] The second is a crossed beam apparatus with a bolometer detector that had its experimental origin in high-resolution elastic crossed beam experiments and was well described earlier.[2] The union of the laser + bolometer in the optothermal detection scheme[3] had already been presented in the literature, but not previously incorporated in this particular apparatus.

A.1 CONTINUOUS WAVE HF CHEMICAL LASER

The HF chemical laser has been previously described in Sections 2.2 and 3.2. Refering to Figures 2.1 and 3.1, a mixture of He (600 atm-cm^3/sec) and SF_6 (15 atm-cm^3/sec) pass through an alumina tube (1.6 cm I.D. $\times$46 cm long) running through the cross section of an aluminum waveguide. Compressed air ($\sim$60 psig) is blown into the waveguide through a $\sim$ 0.5 cm hole in the movable stub to prevent the alumina tube from cracking due to thermal stress. A magnetron (Hitachi M57D11 operating at 2450 MHz) is positioned with its emission dome inside the waveguide. It delivers $\sim$ 1200 W of microwave power to the alumina tube. The magnetron is powered by a highly regulated 4 kV DC power supply. After the flow of the He/SF_6 mixture is established, the power supply to the magnetron is turned on. The voltage applied to the magnetron adjusted to a setting of $\sim$ 3.2 kV, with a DC current of $\sim$ 0.6 A. While increasing the voltage to operating conditions, the He/SF_6 in that portion of the alumina tube inside the waveguide should form a plasma that causes the alumina tube to glow a dull orange/yellow color. The intensity of the

plasma glow should be constant in time providing the mixture of He/SF_6 does not change. Inside the plasma, the SF_6 is broken down into smaller fractions, the most important of which is F atoms. Further characterizations as to the temperature of the plasma or the actual decomposition of the SF_6 into smaller fragments were not attempted due to the extremely corrosive nature of F at high temperatures.

The alumina tube is attached to the laser cavity body using a Cajon O-ring compression fitting threaded into a water-cooled collar. The water-cooled collar is necessary to prevent the O-ring from overheating and cracking, thereby destroying the vacuum seal. The hot F atoms enter the laser cavity and fan out into a horizontal plane. They are immediately bombarded by H_2 (300 atm-cm^3/sec) injected through a row of holes (62 holes $\times$0.5 mm each) from both above and below the plane of travel. The flow channel here is 115 mm wide by 4 mm high. A rapid chemical reaction takes place,

$$H_2 + F \longrightarrow HF^{\dagger} + H,$$

to produce vibrationally excited $HF^{\dagger}$ in a wide variety of rotational states[4] (see Figure 2.2 for all of the rotational states that are experimentally observed). Brewster angle CaF_2 windows are mounted with centers 5 mm downstream of the H_2 injection holes to allow the emission of the excited HF to escape the laser cavity. Small injection holes in the vicinity of the Brewster windows introduce He to sweep out any vibrationally deactivated HF. The pressure inside the laser cavity is 5.5 Torr, which is maintained by a Leybold-Heraeus WAU500 Roots pump (rated speed 165 L/sec) backed by a Leybold-Heraeus S160C mechanical pump (rated speed 60 L/sec). The pumps are kept in a room separate of the laboratory to reduce noise and mechanical vibrations. The tubing ($\sim$ 4 m of 10 cm I.D. PVC narrowing down to $\sim$ 1 m of 5 cm I.D. reinforced rubber) is rigidly bolted to the laboratory wall with a frame constructed of heavy gauge 2 inch angle iron to further assist in damping mechanical vibrations being transmitted to the laser table. It is of interest to note that

the first 90° elbow in the pumping line immediately after the laser cavity would slowly clog with crystalline sulfur since it is the first cool surface that the gaseous sulfur atoms come in contact with downstream of the plasma. This elbow (along with a filter screen directly above the Roots pump) should be checked and cleaned after every $\sim 200 - 300$ hours of laser operation. The above laser components (*i.e.*, microwave discharge and laser cavity body) are rigidly held in place by bolting to a 1.2 cm thick steel plate supported by a free standing steel structure which does not make any contact with the laser optics table.

The breadboard laser optics table (Newport GS-34) is freestanding and does not make any physical contact to the outer table supporting the laser body and microwave generator. It was originally mounted on pneumatic legs, but the required positional reproducibility of < 0.2 mm forced the pneumatic feature to be discarded. All optical components needed for the generation and alignment of the HF laser are mounted on this table.

The laser optical cavity consists of a gold coated diffraction grating and a partially reflective mirror called an output coupler. The diffraction grating is manufactured by Bausch & Lomb and has 300 rulings per millimeter of surface with a blaze angle of 22.2°. It is held in the first-order Littrow configuration by an adjustable mirror mount (Newport 600A-3). The output coupler (Two-Six) is supported on the opposite side of the laser body by a second identical mount. It is a 2.5 cm diameter ZnSe circular mirror whose front side has a 3 m radius of curvature. It is coated to provide 90% reflectance at 2.7 μm, and the reflectance drops to 87% at 2.43 μm and 2.91 μm. Generating the laser beam is quite straightforward: newly created vibrationally excited HF molecules in the laser body spontaneously emit photons as they descend to a lower vibrational state. This electromagnetic (e.m.) radiation oscillates in the optical cavity formed by the diffraction grating and the output coupler. The e.m. radiation (present as a plane wave) is amplified with each

cycle through the optical cavity, but a certain percentage ($\sim$ 10% for our laser) of the e.m. radiation is extracted from the cavity by passing through the partially reflecting output coupler. This forms the laser beam.

There does not exist a way in which one could select the vibrational and/or rotational state of the excited HF formed in the laser body. Rather, a distribution of excited states is formed. By tuning the angle of the diffraction grating, the spontaneous emission of one specific dipole allowed transition is reflected many times in the optical cavity. The different frequencies (and corresponding wavelengths) available with this chemical laser are shown in Table A.1.

The mirror mounts supporting the laser cavity optics are rigidly held by three Invar rods (2.5 cm diameter), although relative motion along the optical cavity axis due to thermal expansion is accomodated by a ball-bearing bushing arrangement supporting one end of the Invar rods. The distance between the diffraction grating and the output coupler is kept as short as is physically possible (26 cm) to prevent more than one longitudinal mode from oscillating at the same time. The frequency spacing between two successive longitudinal modes is given by the difference in frequency between a cavity with n nodes of a standing wave versus $n+1$ nodes. This frequency difference[5] is given by $\Delta\nu_{\mathrm{long}} = \frac{\mathrm{c}}{2\mathrm{L}}$, where c is the speed of light and L is the cavity length (26 cm). For this laser cavity, the frequency difference between two adjacent longitudinal modes is calculated to be 580 MHz (often this is referred to as the free spectral range).

One can calculate whether more than one longitudinal mode will oscillate by simply calculating the expected linewidth of the laser output. The linewidth of the laser is controlled by three different broadening mechanisms: collisional broadening and the natural linewidth due to spontaneous emission are each homogeneous broadening; the fact that inside the laser cavity the HF molecules are propagating in random directions gives rise to Doppler broadening, which falls in the class of

Table A.1 Observed HF Chemical Laser Output Frequencies

Notation[1]	$\nu'^{\dagger}$	$j'^{\dagger}$	$\nu^{\dagger}$	$j^{\dagger}$	Wavelength[2] (μm)	Power[3] (W)
$R_1(0)$	1	1	0	0	2.49928	0.14
$R_1(1)$	1	2	0	1	2.47579	0.15
$R_1(2)$	1	3	0	2	2.45372	0.07
$R_1(3)$	1	4	0	3	2.43304	0.01
$P_1(1)$	1	0	0	1	2.55071	0.21
$P_1(2)$	1	1	0	2	2.57874	0.66
$P_1(3)$	1	2	0	3	2.60837	0.82
$P_1(4)$	1	3	0	4	2.63966	0.91
$P_1(5)$	1	4	0	5	2.67266	0.41
$P_1(6)$	1	5	0	6	2.70743	0.90
$P_1(7)$	1	6	0	7	2.74404	1.05
$P_1(8)$	1	7	0	8	2.78256	0.20
$P_1(9)$	1	8	0	9	2.82306	0.07
$P_2(1)$	2	0	1	1	2.66678	0.04
$P_2(2)$	2	1	1	2	2.69627	0.50
$P_2(3)$	2	2	1	3	2.72747	0.96
$P_2(4)$	2	3	1	4	2.76044	1.05
$P_2(5)$	2	4	1	5	2.79522	1.34
$P_2(6)$	2	5	1	6	2.83189	1.21
$P_2(7)$	2	6	1	7	2.87052	0.82
$P_2(8)$	2	7	1	8	2.91118	0.20

[1] The notation indicates the diatomic going from a lower energy state to a higher energy state (*i.e.*, a pumping process), and is a commonly used designation for allowed spectroscopic transitions in a vibrating rotor. The "R" or "P" notation indicates the change in rotational state: R implies $\Delta j = +1$; P implies $\Delta j = -1$. The subscripted integer is the upper vibrational state where $\Delta\nu = +1$. The full sized integer is the lower rotational (j) state.

[2] Output wavelengths obtained from Helios Inc. HF CW Chemical Laser product information sheet (Helios Inc., 1822 Sunset Plaza, Longmont, CO 80501), and are measured under vacuum conditions.

[3] Measured with the intracavity iris fully open, and the laser operating in a multi-transverse mode configuration (see Figure 2.2).

[†] Note that these laser lines are generated by relaxation of excited HF molecules in the laser cavity, but the notation implies the energy required to optically promote an HF molecule from a lower to a higher energy state. The primed (*e.g.*, ν' and j') notation denotes the higher energy vibrational/rotational state, while the unprimed notation denotes the lower energy state.

inhomogeneous broadening. Using the equations given in Reference 5, the collisional linewidth is ~80 MHz, the natural linewidth is $\sim 30 \times 10^{-6}$ MHz, and the Doppler linewidth is ~370 MHz (all calculated for the $R_1(0)$ line). Clearly, the Doppler broadening is the most significant, but it is sufficiently small to allow only one longitudinal mode to oscillate.

The optical cavity can also support the oscillation of many transverse modes. Experimental control over these modes is maintained by an intracavity iris used to restrict the laser beam diameter. It has been found that if the intracavity iris is kept at diameters of ~0.4 cm or less, then no additional transverse modes oscillate, and only the TEM_{00} mode will lase. This can be confirmed in three ways. The easiest and most convienient method is to examine the laser spot shape for roundness on ultraviolet sensitized infra-red visualizer paper. The second method is to direct the laser into the scattering chamber while slowly sweeping the optical cavity length to allow the laser to oscillate on successive longitudinal modes. At the same time an HF molecular beam is impinging upon the bolometer. If only the TEM_{00} mode is oscillating, then a single sharp peak will be observed in the bolometer signal during the lasing of the TEM_{00} transverse mode at each longitudinal mode. Observation of more than one sharp peak in the bolometer signal while each longitudinal mode lases implies that two (or more) transverse modes are oscillating. The third method of confirming that only the TEM_{00} mode is lasing is by scanning the spatial distribution of power within the laser beam. If no additional transverse modes are oscillating, the power distribution will be gaussian in shape along the cross section of the beam. Figure A.1 displays such a scan.

With the laser oscillating on the TEM_{00} mode, the next requirement is to narrow the laser emission bandwidth, which has the effect of increasing the power per unit frequency range. This was accomplished by taking advantage of a phenomenon specific to gas lasers – the Lamb dip. After an HF molecule in the

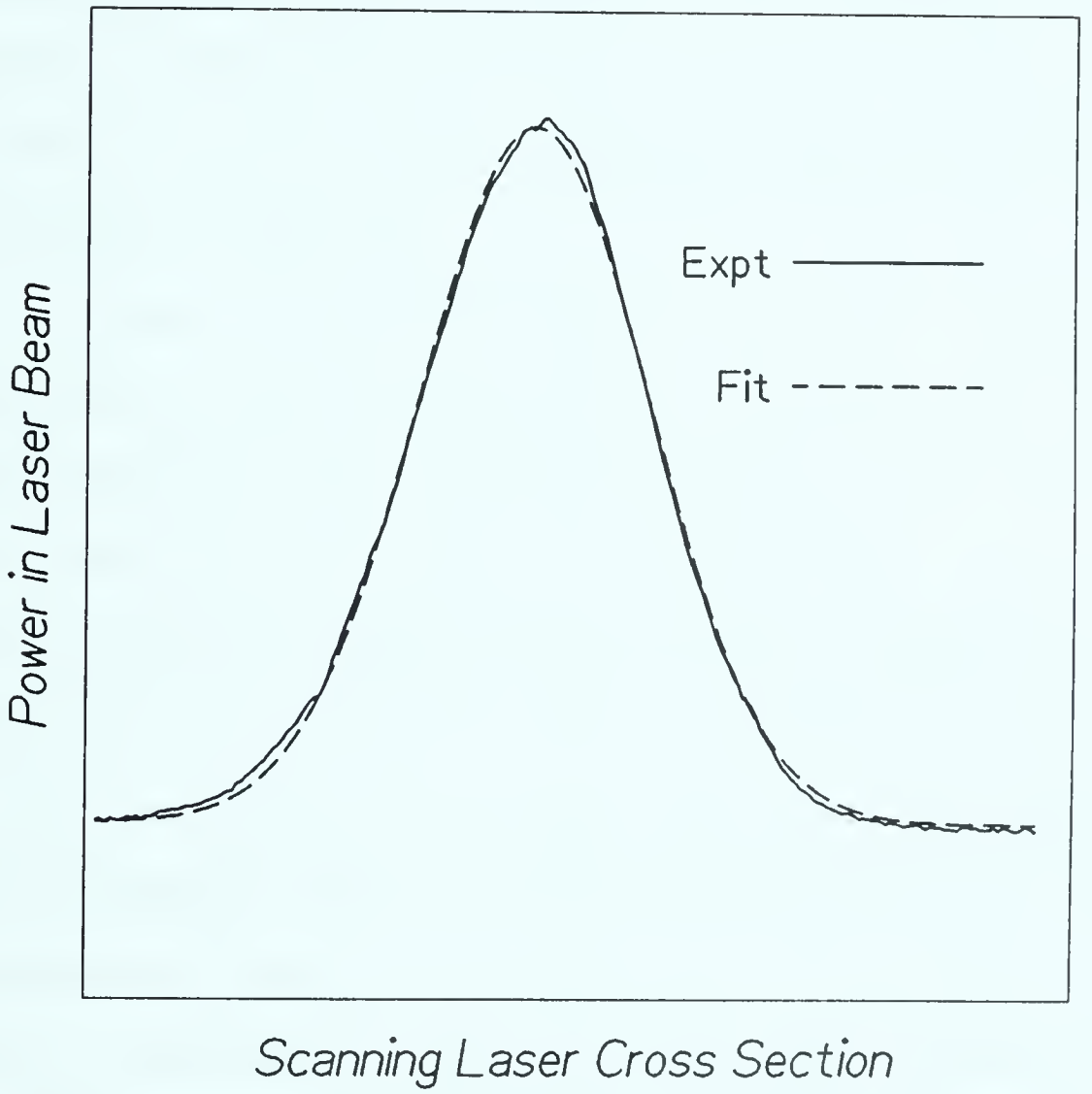

Figure A.1 The solid curve displays the laser power as a small circular aperture (0.3 mm diameter) is scanned across the cross section of the laser beam with the intracavity iris closed down to allow only the TEM_{00} transverse mode to oscillate. The dashed curve is a non-linear least-squares fit of a gaussian functional form to the experimental data. The agreement between the two curves is excellent, indicating that the laser is truly oscillating on the TEM_{00} mode (see reference 5). The e^{-1} width of the laser is found to be 1.9 mm, calculated from the fitted equation.

laser body has emitted a photon, it is possible for the molecule to reabsorb a second photon before it is removed by the vacuum pumps from the region of electromagnetic oscillation. The frequency that the molecule will absorb is dependent upon its velocity relative to the velocity of the photon being absorbed. All frequencies oscillating in the cavity will be reabsorbed by relaxed molecules to a certain extent, but at exactly the line center frequency the extent of reabsorption is roughly twice that of all other frequencies since the photon can be absorbed by the same group of molecules regardless of its direction of propagation in the cavity. The resulting power curve as a function of cavity length (*i.e.,* tuning across the Doppler gain profile) is shown in Figure 2.3

To take advantage of the Lamb dip in the power curve, a small fraction ($< 5\%$) of the laser beam was reflected off a 1.2 cm thick CaF_2 window (located immediately after the output coupler) and directed into an InSb detector cooled to 77K (Infrared Associates). The output from the InSb detector was averaged slightly by a boxcar integrator (Stanford Research Systems) and then fed back to a Lock-in Stabilizer (Lansing 80-214). The stabilizer would electronically differentiate the power curve as a function of cavity length. This discriminator signal is then used to actively control the length of the optical cavity by mounting the output coupler on a piezoelectric translator. The resulting frequency bandwidth as measured by absorption on the bolometer is found to be $\lesssim$ 15 MHz, and could not be determined any lower since the residual Doppler broadening of the HF molecular beam is $\sim$ 10 MHz. This frequency stabilization technique was used for all scattering experiments reported here.

The actively stabilized laser emerges from the optical cavity plane polarized owing to the diffraction grating and Brewster angle windows on the ends of the laser body. It is directed via a series of five mirrors into the crossed molecular beams scattering apparatus through a CaF_2 window held at Brewster's angle to

minimize reflective losses at this surface. Before the first mirror, the laser is mechanically chopped by a tuning fork chopper operating at 39.6 Hz. The output of the chopper is used as a reference signal for the lock-in amplifier (Stanford Research Systems SR-510). Between the first and second mirrors a CaF_2 planoconvex lens (1.0 m focal length; 1.05 m downstream of the output coupler) is inserted to collimate the laser beam as it propagates into the scattering chamber. The second and third mirrors, mounted on the optical table, are used to raise the laser from the optical table to the level of the fourth and fifth mirrors mounted to the scattering chamber. They are also used to align the laser through two irises also mounted to the scattering chamber before the fourth mirror. The fourth and fifth mirrors then direct the laser into the scattering chamber along the bolometer's rotation axis. The entire path from the output coupler to the Brewster window is flushed with dry N_2 to restrict laser attenuation due to water vapor absorption. Inside the scattering chamber the laser is displaced away from the scattering center on the direct line to the bolometer detector chip. This is accomplished via a two mirror arrangement which functions much like a periscope (see Section A.2.C) mounted to the bolometer. After interacting with the HF molecular beam, the laser is reflected from a mirror back onto itself except for a slight ($\sim 0.5°$) misalignment needed to eliminate feedback into the optical cavity.

Since the HF laser operates in the infrared region, it is necessary to use a HeNe laser (Uniphase) as a tracer for alignment purposes. The HeNe and HF lasers are made collinear at the beam splitter used to extract a small portion of the laser for the lock-in stabilizer. Ultraviolet sensitized infrared sensitive visualizer paper (Infrared Associates) is used to locate the HF laser, and the HeNe is adjusted to coincide (*i.e.,* along the entire pathlength). The visible HeNe (632.8 nm) can then be aligned into the scattering chamber, or directed to a far wall of the laboratory to ensure proper overlap of the HF and HeNe lasers. Alignment of the two lasers with

respect to each other, as well as alignment into the scattering apparatus is crucial to the experimental integrity, and thus checked on the day of each new experiment.

A.2 MOLECULAR BEAMS APPARATUS

The molecular beam scattering apparatus used in these rotationally inelastic scattering experiments is largely unchanged from the description given by L.J.Danielson in his PhD thesis.[6] It consists of two supersonic molecular beam sources intersecting at 90°. Each source chamber is rigidly bolted to the scattering chamber in prealigned machined steps. Inside the scattering chamber is a rotatable liquid helium cooled bolometer detector whose motion lies in the plane formed by the supersonic beams, and rotates about the intersection point of these beams. The laser beam is admitted through a window at the bottom of the scattering chamber, and is aligned so that the laser beam is perpendicular to each supersonic beam. The three beams (two molecular and one laser) intersect at one unique point in space–the scattering center, although later apparatus modifications required the laser beam to be displaced towards the bolometer (Section A.2.C). For the purpose of supersonic beam characterization, a mass spectrometer can be bolted to the scattering chamber directly opposite of either supersonic beam.

The two source chambers are essentially identical. They appear as a vertical cylinder (~54 cm diameter by ~53 cm long) being intersected by a horizontal cylinder (~40 cm diameter). The diffusion pump (Varian VHS-400 rated at 8000 L/sec for air) is unbaffled and bolted directly to the vertical section. It is backed by a Leybold-Heraeus S160-C pump (60 L/sec) through ~5 m of ~15 cm PVC tubing. The top covering to the source chamber is a 1.8 cm thick aluminum disc with a 2.54 cm thick Perspex window containing several vacuum feed-through connections providing the beam inlet gas, water cooling, and electrical power to the nozzle assembly inside. The end cover is also a 1.8 cm aluminum disc with a 2.54 cm thick Perspex window containing a rod on a threaded mount used to adjust the nozzle-skimmer distance. With no beam gases flowing, the pressures inside these chambers is $\sim 2 \times 10^{-7}$ torr, and the backing pressure is ~60 mtorr. The source

chamber pressures were not measured under experimental running conditions, but they are expected to be on the order of $\sim 5\times 10^{-4}$ torr[6]. The backing pressures measured at the diffusion pump exhaust is ~150 mtorr for the Ar beam. For the HF beam, at the start of an experiment the backing pressure would be ~90 mtorr. As the experiment progressed, the backing pressure would continue to rise and usually be allowed to reach ~250 mtorr due to dissolving of HF in the mechanical pump oil. Purging with dry nitrogen for ~10 minutes would help to bring the backing pressure back to ~150 mtorr, and would allow the remainder of the day's run to be completed (~ 10 hr).

The scattering chamber is box-like in appearance with dimensions of ~60 cm long ×~60 cm wide ×~41 cm high. It contains four machined ports (one per side) to which the two source chambers and the mass spectrometer are bolted to in pre-aligned positions. The fourth port is covered with a Perspex window and is used mainly for viewing the inside of the scattering chamber when evacuated. The bolometer is mounted on a rotating flange on the top of the scattering chamber. Vacuum is maintained by a Varian VHS-10 diffusion pump (5000 L/sec) backed by a Leybold-Heraeus D8A rotary vane mechanical pump (~3 L/sec). With no gas load, the scattering chamber pressure is maintained at $\sim 2\times 10^{-7}$ torr with a backing pressure of $\sim 30-50$ mtorr. Under experimental conditions the scattering chamber pressure is $\sim 3\times 10^{-6}$ torr with a backing pressure of $\sim 60-100$ mtorr.

The mass spectrometer is constructed with an inner and outer chamber, where the shape of the outer chamber is similair to the source chambers. This outer chamber is pumped by an NRC-6 diffusion pump (~ 1500 L/sec) which maintains a pressure of $\sim 1\times 10^{-6}$ torr. This diffusion pump is backed by the same Leybold-Heraeus D8A pump which backs the scattering chamber VHS-10. The inner chamber, which contains the mass spectrometer components (Extrel 041-1 ionizer, EAI 200 quadrupole mass filter, and Gallileo 4770 channeltron), is pumped

by an Edwards 6 inch Diffstak (700 L/sec) charged with Santovac 5 oil, and backed by a separate D8A mechanical pump. The Diffstak is closed off by a butterfly valve when the mass spectrometer is not in use, and a Varion I-3 Triode Vacion pump (20 L/sec) maintains the vacuum in the inner chamber. This assists in keeping the mass spectrometer inner components free of contamination from backstreaming diffusion pump oil, and is convienient to use since it requires no cooling services.

A.2.A Molecular Beam Angular Resolution

The scattering apparatus is shown schematically in three different illustrations representing the development of the experiments presented in Chapters 2, 3 and 4 (Figures 2.1, 3.1, and 4.1 respectively). The most important configuration is that which was used to conduct the molecular beam scattering experiments presented in Chapter 4. Figure A.2 presents a scale drawing of the important collimating apertures that determine the angular resolution of the apparatus.

In this configuration, the skimmer is the aperture which limits the angular divergence of each beam. Using trigonometry, one can calculate the angular divergence of the HF beam to be 3.0°, and for the Ar beam it is 3.3°. The theoretical calculations can be compared to attempts to measure the angular divergence of the molecular beam using the bolometer detector. To do this, a very low pressure HF beam is made in one source chamber, while simultaneously the laser (typically using the $R_1(0)$ line) propagates into the scattering chamber. A weak molecular beam is used to avoid overloading the bolometer, which is seen as a dip in the angular profile even for the bolometer operated at 4.2 K. The bolometer is then slowly rotated so that its apertures pass through the molecular beam, and the measured bolometer signal is directly proportional to the intensity of the molecular beam. Figures A.3a and A.3b display this measurement for the set of apertures used for the HF molecular beam and the Ar atomic beam.

One shortfall of this technique is that the bolometer signal's measured angular width is a convolution over the molecular beam width and the width of the smallest bolometer aperture. However, knowing that the molecular beam distribution obeys a cosine squared angular dependence[6] allows one to deconvolute these two widths via geometry considerations. By realizing that the smallest bolometer aperture has a diameter of 2.42 mm (Figure A.2), the experimentally deconvoluted angular divergence of the HF molecular beam is ~3.1°. This is in excellent

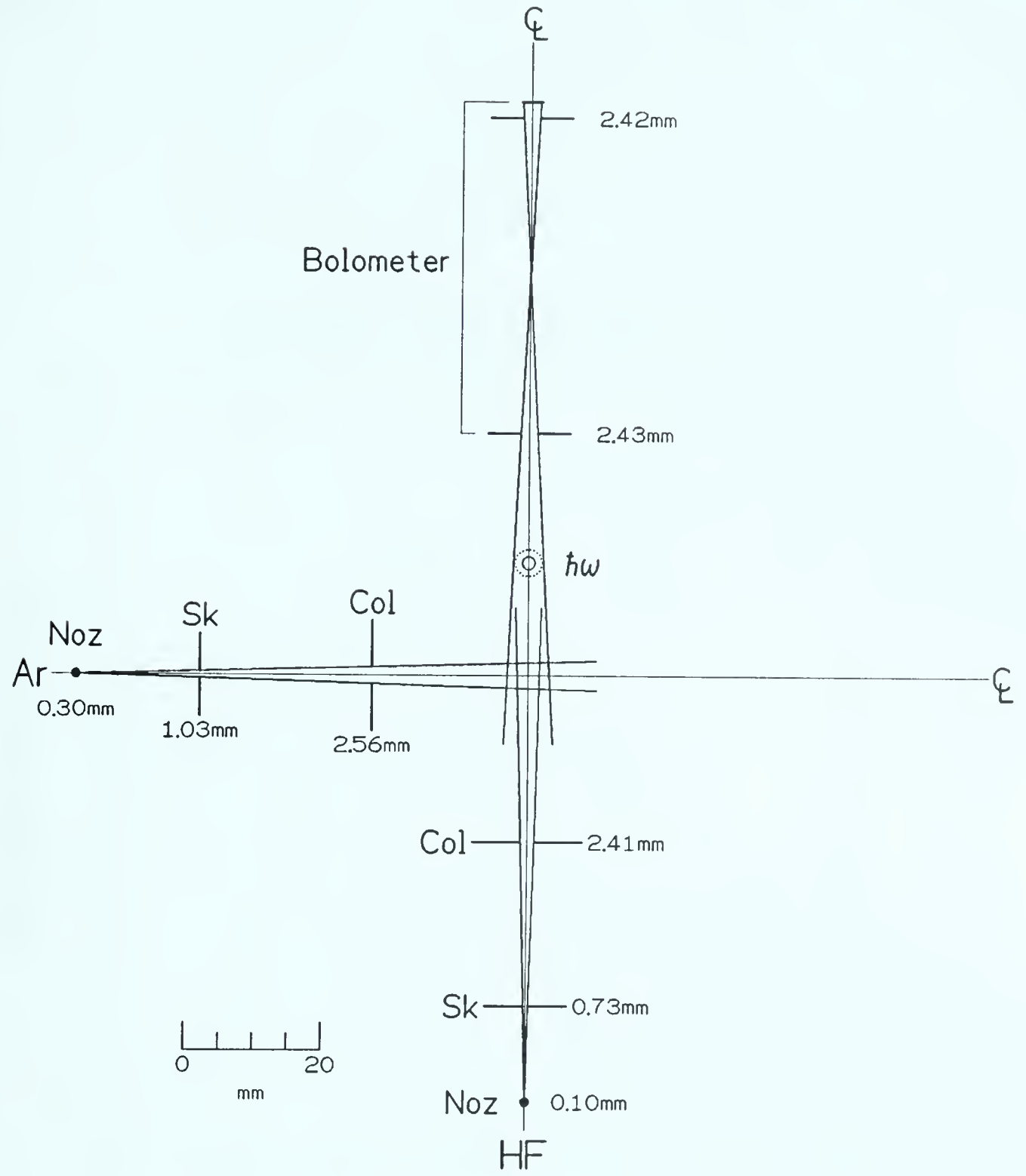

Figure A.2 Scale drawing showing all apertures which contribute to the collimation of the molecular beams. The HF molecular beam is depicted as propagating up the page; the Ar atomic beam propagates horizontally across the page. Nz–nozzle; Sk–skimmer; Col–liquid nitrogen cooled beam collimator; bolometer collimator nearest to the scattering center is liquid nitrogen cooled; bolometer collimator farthest from the scattering center is liquid helium cooled; $\hbar\omega$–continuous wave HF chemical laser propagating in the direction perpendicular to the plane formed by the intersection of the Ar and HF beams. The solid circle depicts the $\frac{1}{e}$ spot size of 1.9 mm. The dotted circle represents the laser spot size at 1% of the centerline power. All apertures are circular in shape with the diameter in millimeters next to the aperture. The molecular beam cones, as well as the bolometer viewing cone are outlined and appear as triangular sections.

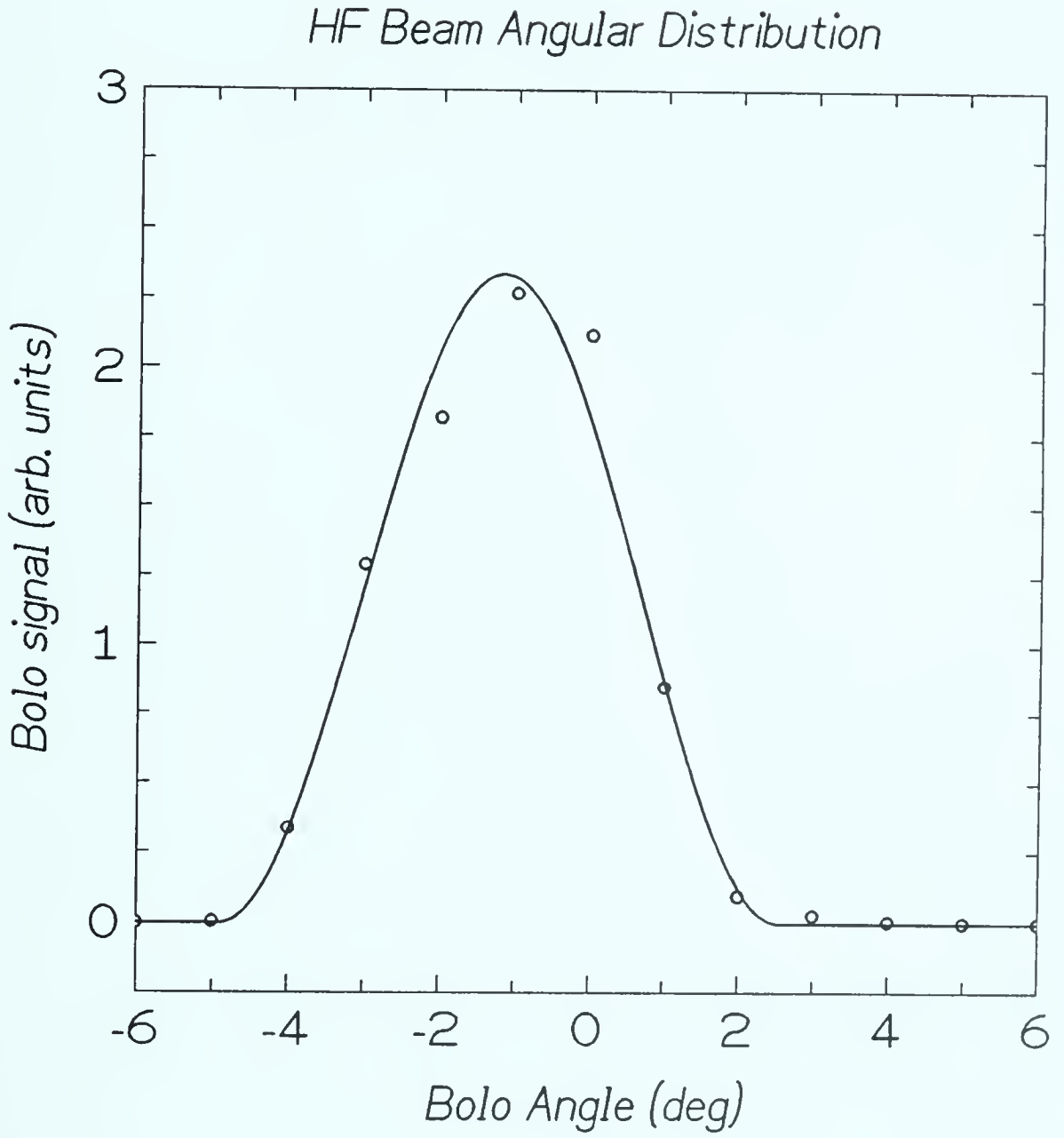

Figure A.3a Angular divergence of the HF molecular beam as measured by rotating the bolometer through the molecular beam axis while flowing a weak HF beam which is excited by the HF laser. The circles are experimental data points; the solid line is a least squares fit of the function "$S = S_0 + \alpha \cos^2(\beta(x - x_0)\,\frac{\pi}{2})$". The best fit values are: $S_0 = 0.00$ (not varied); $\alpha = 2.340$; $\beta = 0.268$; $x_0 = -1.18$. From this equation form, the full width at half maximum for the distribution is 3.7°. Note that the shift in zeroline (*i.e.*, $x_0 = -1.18°$) is in good agreement with the angular shift required to move our total DCS into agreement with that of Vohralik *et al.* (Section 5.3.A).

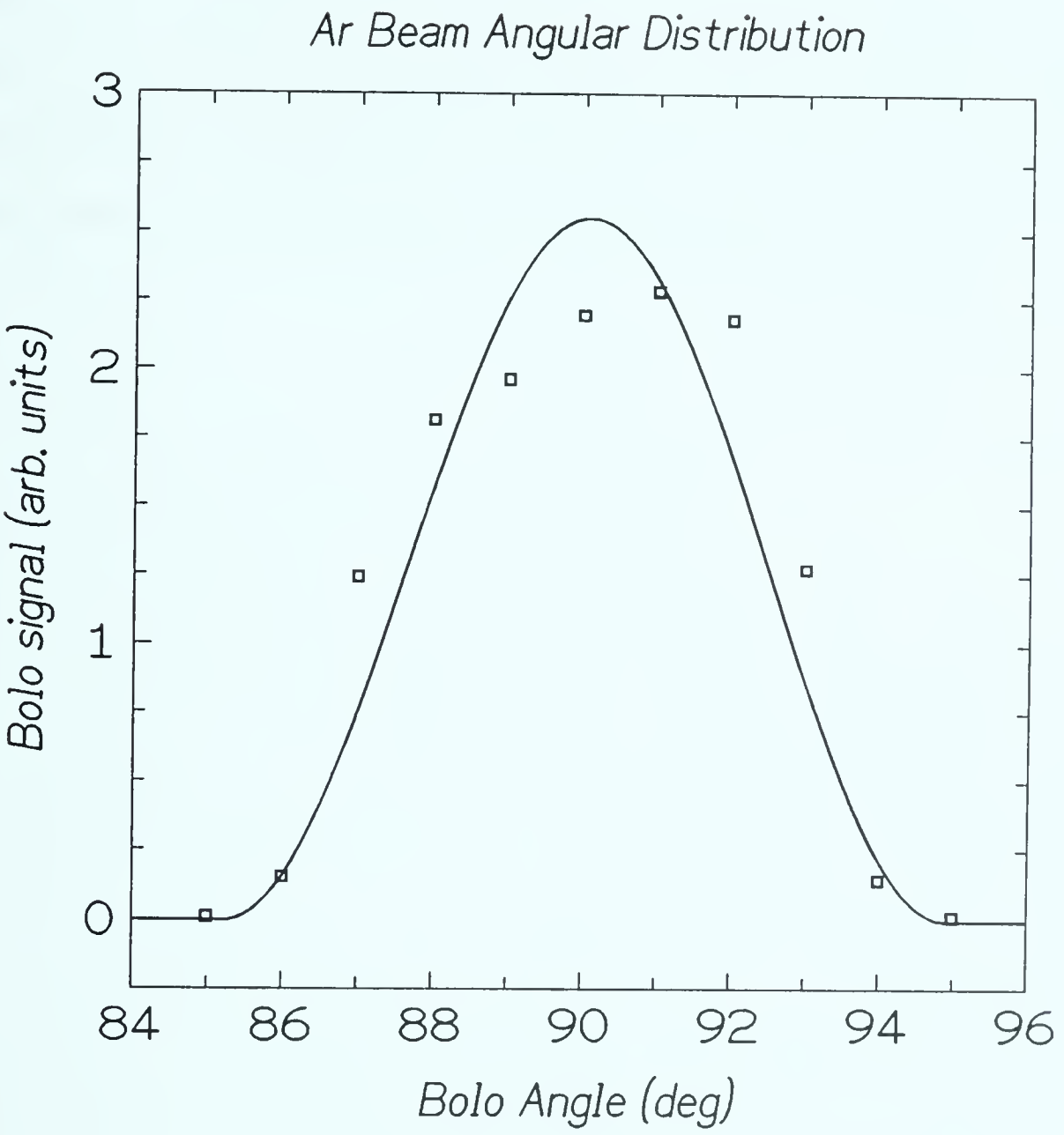

Figure A.3b Angular divergence of the Ar atomic beam as measured by rotating the bolometer through the molecular beam axis while flowing a weak HF beam which is excited by the HF laser. The squares are experimental data points; the solid line is a least squares fit of the function "$S = S_0 + \alpha \cos^2(\beta(x - x_0)\,\frac{\pi}{2})$". The best fit values are: $S_0 = 0.00$ (not varied); $\alpha = 2.555$; $\beta = 0.206$; $x_0 = 90.07$. From this equation form, the full width at half maximum for the distribution is $4.8°$.

agreement with the calculated divergence of 3.0°presented above and in Chapter 4. For the Ar apertures, the experimentally deconvoluted angular divergence is ~4.2°, which is slightly larger than that shown in Chapter 4. A possible explanation is that the larger flux of HF molecules passing through this set of apertures causes the bolometer's response to be saturated, and thus an artificially high signal level as the bolometer is moved away from the beam centerline is observed. Such an event would explain the skewing of data visible in Figure A.3b. Nevertheless, there was sufficient agreement between the calculated and experimentally determined divergence to allow the scattering experiment to proceed confidently.

A.2.B Molecular Beam Formation and Characterization

One cannot simply "turn on" a molecular beam and begin scattering experiments. Rather, several factors must be considered when producing a molecular beam with optimized expansion parameters. Amongst these factors are the nozzle size, nozzle temperature, nozzle pressure, and the nozzle-skimmer distance. The mass spectrometer has been used to establish the beam qualitities of relative intensity, velocity, and velocity distribution. Ideally, one wants as large an intensity as possible, coupled with as narrow a velocity distribution (and hence a narrow relative collision energy distribution) as attainable. Time-of-flight (TOF) techniques are used to directly determine the velocity and velocity distribution of a molecular beam, and can also simultaneously determine relative intensity.

The TOF chopper is a 4.50" diameter two bladed brass wheel with a narrow slot (0.015" wide) cut into the center of each blade. The chopper is aligned to intersect the molecular beam at a radial distance of 2.0" from the center of the wheel. This wheel is rotated at 200 Hz, meaning that the "open" time between blades is 1.25 msec, and the "open" time for a slot is 6 μsec. The "on–off" function provided by the blades is used to determine the beam intensity using the lock-in amplifier, and the slot is used to determine the velocity and velocity distribution of the beam. Artificial broadening of the velocity distribution due to the angular divergence of the beam is removed by placing a narrow slit (same width as the slot in the TOF chopper blade) between the TOF chopper and the entrance to the mass spectrometer.

Calibration of the mass spectrometer is via the method of Blais *et al.*[7], with a very thorough description of this technique given by L.J. Danielson[8]. It is noted that here Ar is used to provide the flight time of the neutral up to the mass spectrometer ionizer, with Ar^+ and Ar^{2+} providing the ion flight times. He gas is used as a second neutral species to calibrate the distance from the chopper to the

mass spectrometer. The equation relating the actual flight time to the observed flight time is found to be

$$t_{actual} = t_{obs} - 4.44 \times \left(\frac{m}{e}\right)^{\frac{1}{2}} - 19.7\mu sec.$$

From this actual flight time, the flight distance is calculated to be 65.69 cm. After calibration is complete, one is ready to optimize beam conditions, and determine the velocity and velocity distribution.

The experimental parameters necessary to produce the most intense Ar atomic beam were not investigated for this work. Rather, an optimized Ar beam was produced in earlier elastic scattering experiments in this lab[6] and these parameters were used in the inelastic experiments. Only the nozzle-skimmer distance was checked for the Ar beam, and Figure A.4 displays this scan. Figure A.5 shows the TOF measurement determining the velocity and velocity distribution for the optimized Ar beam.

Prior to doing any optimization of the HF beam, an unexpected complication arises: commercially available HF is liquified, so the vapor phase HF above the liquid must be extracted for beam formation. Attempts to control the flow of gaseous HF via mass flow controllers[6] (Tylan) proved to be fruitless since the pressure drop required across the mass flow controllers was too difficult to maintain throughout the gas feed line. To circumvent this difficulty, liquid HF was distilled from a large storage cylinder to a small 500 mL stainless steel cylinder. This small cylinder is easily immersed in a thermostatic bath which controls the vapor pressure of the liquid HF, and ultimately controls the pressure of HF in the nozzle. 95% ethanol was used as the thermostatic liquid since it readily allowed bath temperatures to be set below 0°C. A scan of bath temperature (and thus nozzle pressure) versus relative beam intensity on the mass spectrometer is displayed in Figure A.6.

Test runs done with varying nozzle sizes showed little difference in HF molecular beam intensity on the mass spectrometer. Comparing a 100 μm nozzle

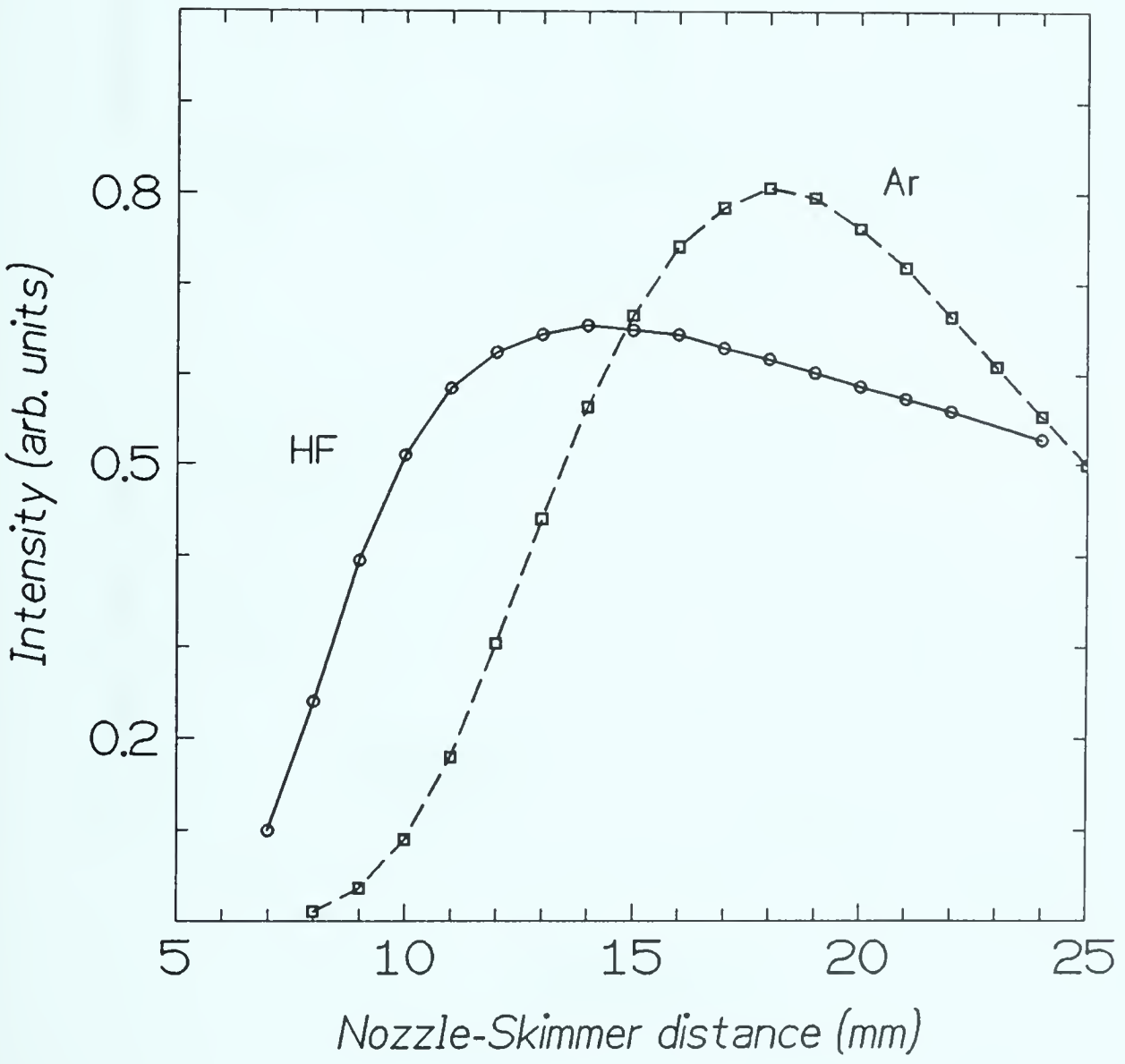

Figure A.4 Circles and solid line: HF molecular beam intensity measured on the mass spectrometer at $\frac{m}{e} = 20$ versus the nozzle-skimmer distance with the following conditions—nozzle diameter 100 μm; nozzle pressure 550 torr; nozzle temperature 230°C.
Squares and dashed line: Ar atomic beam intensity measured on the mass spectrometer at $\frac{m}{e} = 40$ versus the nozzle-skimmer distance with the following conditions—nozzle diameter 300 μm; nozzle pressure 505 torr; nozzle temperature 25°C (ambient).
Intensity differences between the curves is not meaningful.

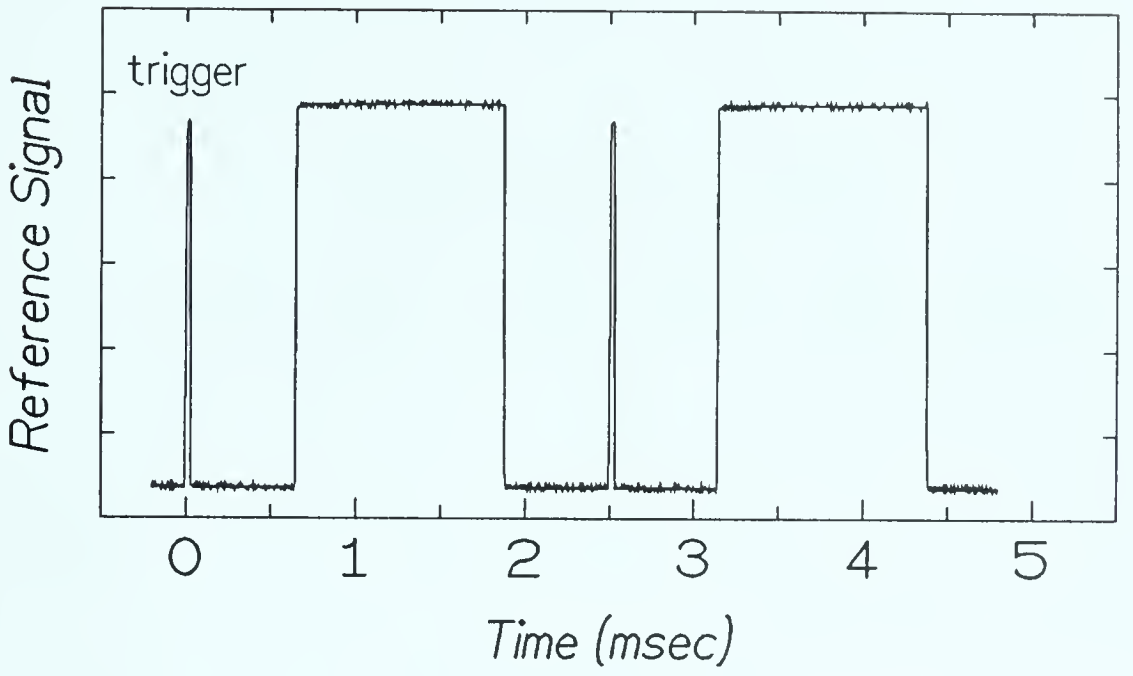

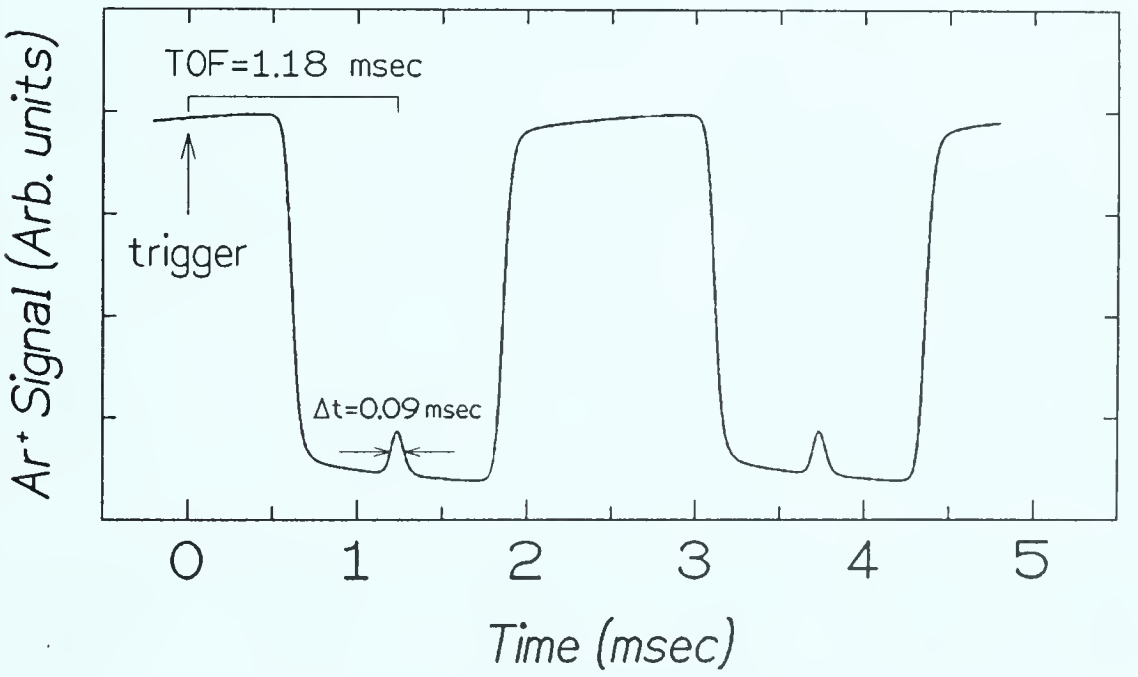

Figure A.5 Upper trace shows the reference signal from the TOF chopper generated by a photodiode positioned to be exactly opposite the point on the chopper wheel where the molecular beam is striking the chopper. This reference signal is exactly in phase with the molecular beam intensity allowed to pass by the chopper. The narrow spike results from the slot passing through the photodiode, and is designated to be time zero. The lower curve is the intensity (arbitrary units) of the Ar beam on the mass spectrometer at $\frac{m}{e} = 40$. The horizontal offset between the two curves is the observed time-of-flight. Expansion of the peaked region from the burst of Ar gas passing through the slot shows the velocity full width at half maximum FWHM to be 7.9% of the most probable Ar velocity.

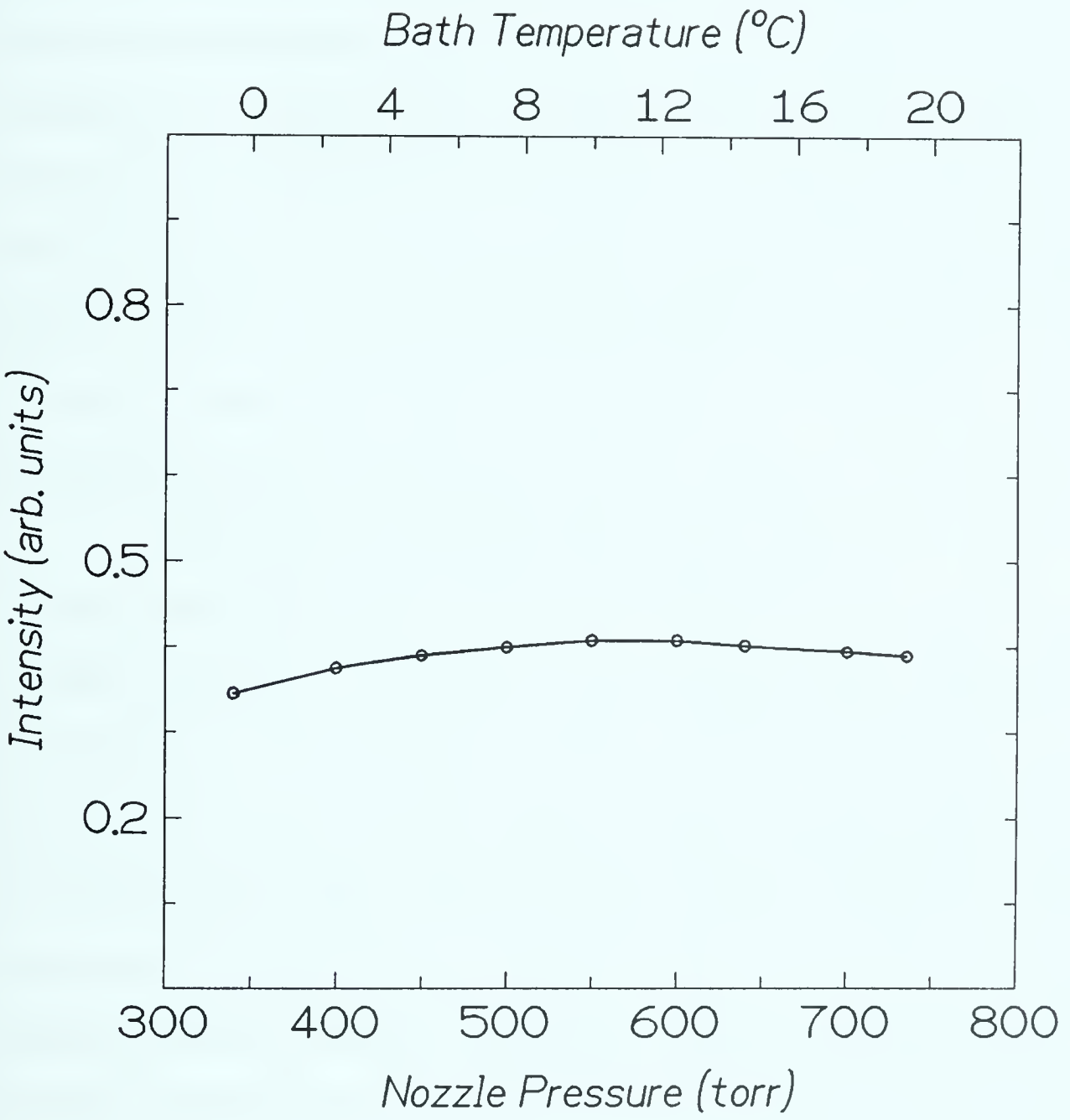

Figure A.6 HF Molecular beam intensity measured on the mass spectrometer at $\frac{m}{e} = 20$ versus the nozzle pressure (thermostatic bath temperature) under the following conditions: nozzle diameter 100 μm; nozzle temperature 230°C; nozzle-skimmer distance 17 mm.

to a 300 μm nozzle displayed a 3% difference in molecular beam intensity, and only a slight difference in the velocity spread ($\frac{\Delta v}{v}$ = 20.0% for 100 μm versus $\frac{\Delta v}{v}$ = 20.4% for 300 μm measured with the same TOF technique as described for Ar in Figure A.5) for the best measurements made. Also, the mass spectrometer signal at $\frac{\mathrm{m}}{\mathrm{e}} = 21$ (which is a measure of the population of HF dimers in the molecular beam while keeping in mind that this signal can be distorted by the fragmentation of polymers) is $\sim$ 6.2% of the $\frac{\mathrm{m}}{\mathrm{e}} = 20$ signal for the 100 μm nozzle, whereas the same ratio is $\sim$ 11.3% for the 300 μm nozzle. Considering these above findings, and since the nozzle pressure is the same for either size of nozzle diameter, it was decided to use the 100 μm nozzle because this would greatly reduce the flow of HF, and thus significantly lessen the requirements on the pumping system, while simutaneously providing the lowest proportion of dimers in the molecular beam.

The temperature of the nozzle can play a significant role in the success of these experiments by counteracting negative effects caused by more vigorous beam expansion conditions. In particular, increasing the nozzle pressure will provide better beam expansion resulting in a narrower velocity spread in the beam particles. However, the increase in nozzle pressure is usually accompanied by an increase in the percentage of polymers (dimers being the most prominent) in the molecular beam, especially for HF which has large intermolecular forces. To counteract the increased polymer population, the nozzle temperature is also increased. This has been done with the HF beam with the intention of increasing the intensity of the monomer, while decreasing the polymer population. Figure A.7 displays the HF monomer intensity as a function of nozzle temperature. The dimer composition (uncorrected $\frac{\mathrm{m}}{\mathrm{e}} = 21 : 20$) in the molecular beam was measured to be $\sim$30% for a nozzle temperature of 25°C, $\sim$6% for a nozzle temperature of 230°C, and $\sim$2% for a nozzle temperature of 400°C. As seen in Figure A.7, the greatest intensity for HF monomer is at $\sim$300°C. However, considering that the difference in dimer

concentration is quite small (~2%) between 230°C and 300°C, 230°C was chosen as the nozzle temperature for scattering experiments since this same temperature was used in a similar DCS experiment by Voharlik *et al.*[9], and comparisons between the two experiments are easiest if as few parameters differ as possible.

The experimental HF nozzle-skimmer distance is set for an optimum beam intensity entering the scattering chamber. This distance was determined by placing the mass spectrometer directly opposite the HF source chamber. The scan of relative HF intensity on the mass spectrometer versus the nozzle-skimmer distance is shown in Figure A.4.

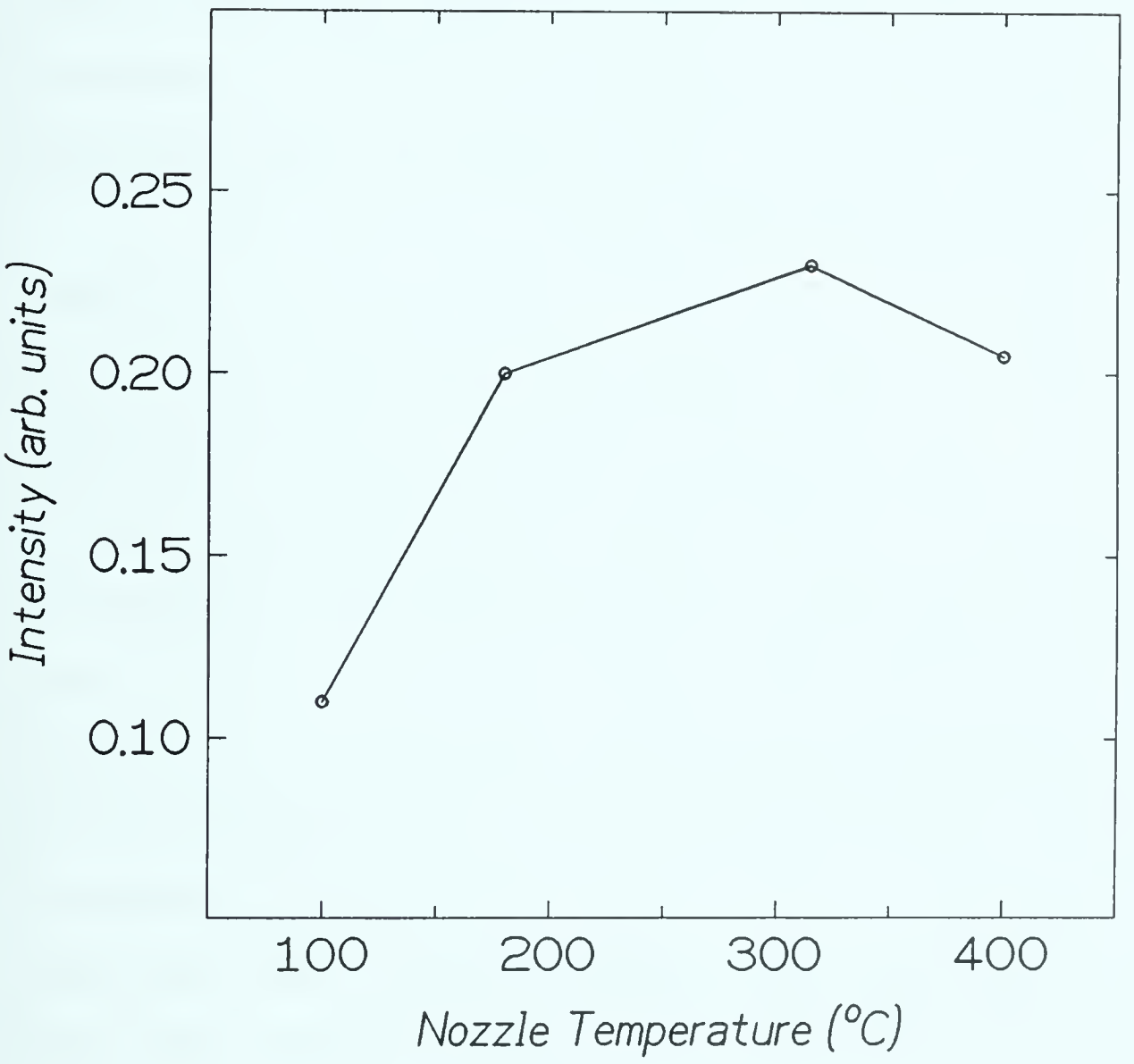

Figure A.7 HF molecular beam intensity measured on the mass spectrometer at $\frac{m}{e} = 20$ versus the nozzle temperature under the following conditions: nozzle diameter 100 μm; nozzle pressure 340 torr; nozzle-skimmer distance 17 mm.

A.2.C Laser – HF Molecular Beam Interaction

The optothermal detection technique[3] used for these experiments is centered upon the frequency overlap between the emission spectrum of the HF chemical laser and the absorption spectrum of HF molecules in the molecular beam. The key advantage of using the HF chemical laser is the ease of keeping the emission frequency constant within the Doppler absorption width if the laser is stabilized and operated single mode. Control of the emission bandwidth of the laser is managed by the frequency stabilization mechanism which locks onto the Lamb dip in the laser's power output curve (Section A.1).

The absorption bandwidth of HF molecules in the molecular beam is controlled by two separate factors. One is the natural absorption width, which is known to be very narrow from tabulated values of the Einstein absorption coefficients.[10,11] The second factor is the Doppler absorption width due to the absorbing molecules having velocity components either with or against the direction of laser propagation. Remembering that the three-dimensional shape of the molecular beam is similair to a cone, it is possible for an HF molecule at the edge of the scattering volume (*i.e.*, either above or below the plane defined by the two molecular beam centerline axes) to have a velocity which is not parallel to the beam centerline. The maximum angular difference between the center and the edge of the scattering volume, such that an HF molecule originating from either position is geometrically able to strike the detector surface, is $\sim 2.0°$. This implies that the angle between HF molecules and the laser can be in the range of $\sim 88.0°$ to $\sim 92.0°$. Therefore, since the HF molecules have a velocity of $\sim$1.21 km/s $\pm$22%) their Doppler absorption width[12] is $\sim$34 MHz ($\pm$22%) if $R_1(0)$ radiation is absorbed. This would imply that there is good spectral overlap between the laser emission ($\sim$ 15 MHz width) and the molecular beam absorption, and that theoretically (at least) all of the laser output can be absorbed by the molecular beam.

One of the complicating factors which arose when establishing the optothermal detection scheme was the presence of scattered laser light incident upon the detector. This scattered light would have the same modulation and phase as the excited HF molecules, and would therefore be an artifact of the scattered signal. Without any preventive measures, the scattered light was on the order of the scattered signal ($\sim$ 0.5 mV on the lock-in amplifier). Efforts to reduce the amount of scattered light include painting all bolometer and scattering chamber surfaces near the scattering center with flat black paint, using Brewster angle windows on all interfaces between vacuum and atmosphere, anodizing the periscope mirror mount, painting the retro mirror mount flat black, and using a set of conical baffles to trap any scattered light entering the scattering chamber through the lower Brewster window. All of these features combined to reduce the amount of scattered light by a factor of 50, thus making our lock-in amplifier detection limit on the order of 10 μV under normal operating conditions.

A second complicating factor of the optothermal detection scheme was the difficulty with high background signals, and thus lowered signal-to-noise ratios. It is believed that HF not in the molecular beam would bounce off walls in the vicinity of the scattering center, interact with the laser, and subsequently impinge upon the bolometer. To overcome this problem, an OFHC (oxygen free high conductivity) Cu post mounted on a liquid nitrogen cooled plate supported an aluminum mesh (Energy Research and Generation) surrounding $\sim \frac{1}{3}$ of the scattering zone on the side opposite the bolometer. An oversized hole was drilled through the mesh to allow each molecular beam to pass through unimpeded, and the bolometer would always "view" a cold ($\sim$ 80K) surface. Any stray HF in the vicinity of the bolometer would eventually collide with the mesh, be trapped on the cold surface, and not have a chance of striking the bolometer. The effectiveness of the mesh in reducing the

amount of stray HF arriving at the bolometer is amazing–nearly 100% of the background signal is removed if the mesh is kept around liquid nitrogen temperatures. Figure A.8 shows a plot of background signal versus mesh temperature.

An unexpected difficulty in using the Al mesh to suppress background was the presence of HF stalactites growing on the edge of the hole drilled through the mesh for the HF molecular beam. After ~6 hours of continuous beam operation, the stalactites would grow large enough to begin to attenuate the HF beam. The stalactite would then grow very rapidly and within minutes block most of the molecular beam directly striking the cold surface. Blowing out the liquid nitrogen from the heat sink reservoir, followed with heating the mesh to $\sim -100°C$ would vaporize the growth and allow the experiment to continue. For convenience, at this time that the mechanical pump backing the diffusion pump in the HF source chamber would be flushed with dry nitrogen (see Section A.2).

The original alignment of the laser was such that it propagated through the scattering center perpendicular to the plane formed by the molecular beams. In practice this is the easiest arrangement to construct, although it is deficient in the following way: it is possible that as an HF molecule enters the scattering volume, it can first interact with an Ar atom, and then be excited by the laser as it travels to the bolometer detector. This is the sequence that one wishes to study. However, with equal probability the reverse order of events can also occur, namely the HF molecule enters the scattering volume, is excited by the laser to a $\nu = 1, j$ state, and is then scattered by the Ar. Two problems with this second set of events are that it probes the scattering of vibrationally excited HF by Ar rather than probing ground state HF scattered by Ar, and does not provide resolution of the final rotational state (*i.e.*, after scattering).

The solution to this problem was to build a periscope-like arrangement to displace the laser parallel to its original path, but downstream (*i.e.*, towards the

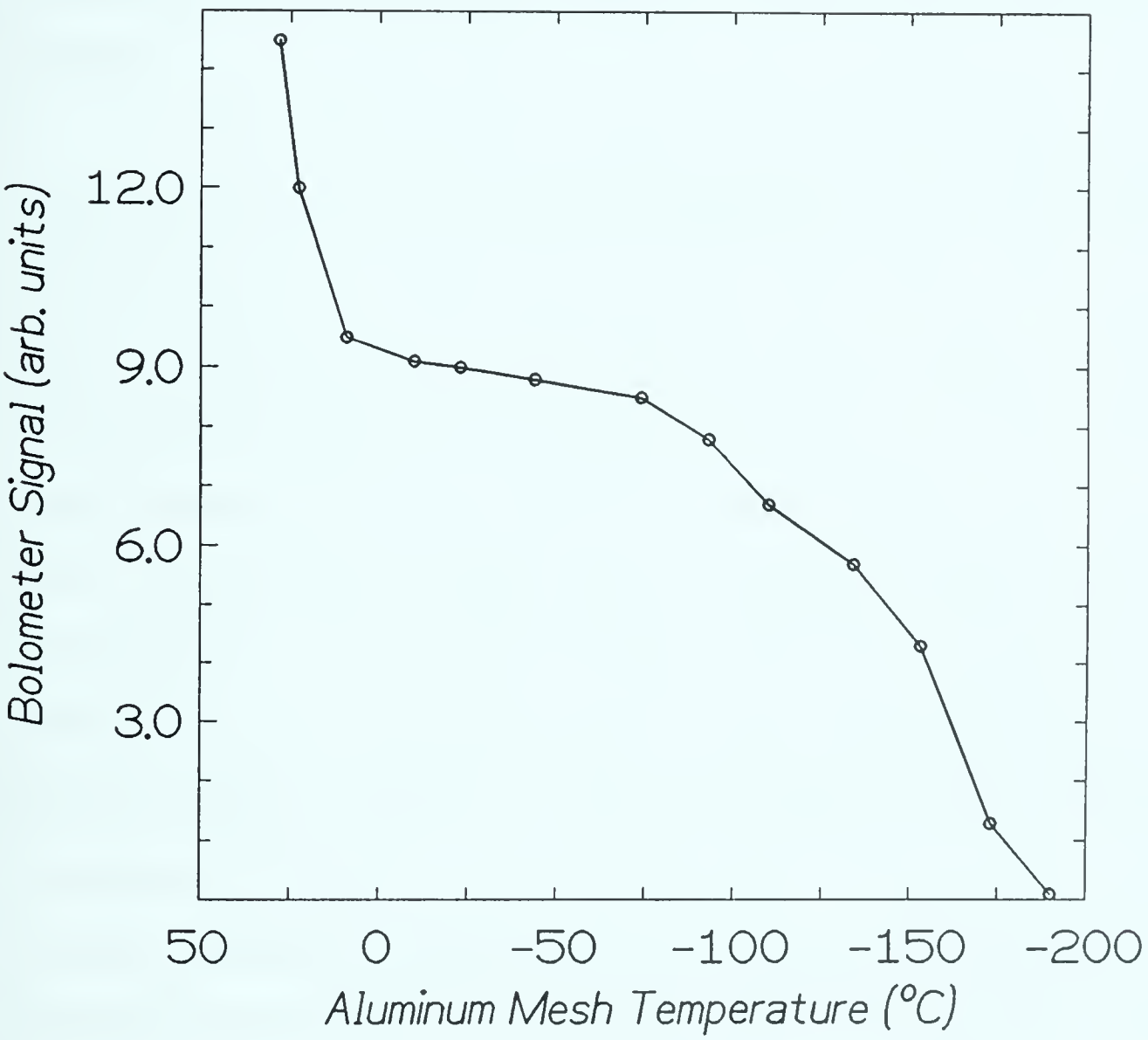

Figure A.8 Background signal on the bolometer as the aluminum mesh surrounding the scattering center is cooled to liquid nitrogen temperature. The bolometer is positioned at 30° away from the HF beam; the HF beam is operated at a nozzle pressure of 330 torr (thermostatic bath temperature of 0°C), nozzle heated to 230°C, and the nozzle-skimmer distance set to 100 mm to reduce the amount of HF in the bolometer region. This same observation is seen if the HF molecular beam is prepared under scattering conditions (*i.e.*, nozzle-skimmer distance of 15 mm and nozzle pressure of $\sim$ 560 torr), or if an effusive source of HF is inlet into the scattering chamber through a port on the top of the scattering chamber.

bolometer) of the scattering center by 16 mm. Attaching the periscope to a warm (*i.e.*, $\sim$ 300 K) bracket on the rotating bolometer ensured that the laser displacement remained on the line between the scattering center and the bolometer detector during rotation, as well as keeping the optical surfaces free of infrared absorbing diffusion pump oil would otherwise coat a cold mirror surface. This scheme to physically displace the laser assures that the HF molecules are excited only after the scattering event has occured (a crucial point regarding the optothermal detection scheme).

Two calibration checks were run on the periscope setup to ensure signal integrity as the bolometer was rotated through different scattering angles. The first involves the polarization of the laser since use of Brewster angle windows and the diffraction grating in the laser cavity produces a plane polarized HF laser beam. The polarization of this beam was maintained as the laser is steered into the scattering chamber, and thus the excitation of HF molecules is via the polarized HF laser. It is important to check whether the periscope would in some way affect the polarization of the laser as the bolometer and periscope orientation are rotated through all accessible scattering angles. Use of a polarized HeNe laser and a polarized photography lens in front of a sensitive photodiode detector showed that laser polarization with respect to the laboratory frame is fully maintained throughout the entire angular range of detection. (Actual measurements show that after passage through the periscope the laser remains 100% polarized with the bolometer at 0°, $\sim$ 99% polarized when the bolometer is at 45°, and 100% polarized when the bolometer is at 90°.)

The second calibration check was designed to investigate whether the laser would wander away from the line joining the scattering center and the bolometer as the bolometer is rotated. The source of HF for this test was a closed tube attached to the rotating flange supporting the bolometer with a small hole ($\sim$ 0.5 mm)

drilled through the wall of the tube. This small hole was positioned to be on the line joining the scattering center to the bolometer, and ensured a constant flux of HF into the detector regardless of its angular position. A low pressure of HF was inlet into the scattering chamber through this hole, and the laser would excite the HF as the molecules travelled to the bolometer resulting in a given signal level. The measurement was repeated at several different angles throughout the detector's range. The results are shown in Table A.2. It is evident that the periscope does not introduce any systematic errors in the bolometer signal level, and this was true even after several realignments of the laser. From these tests it was concluded that the periscope could be used to employ the optothermal detection scheme properly and not be a source of error in the measured signal.

With assurance that the laser+bolometer detection system is functioning error-free, one is ready to begin experimental runs for the purpose of characterizing the HF molecular beam. The ultimate goal is to make a connection between the measured bolometer signal and the relative number of HF molecules in a particular rotational state. A necessary condition for this to be possible is to establish the relation between the bolometer signal for a given transition and the amount of laser power being input into the scattering chamber. An investigation of this type was carried out for two different HF molecular beams, one of which is used in the scattering studies presented here. (Note that in order to prevent the bolometer from being thermally overloaded, it was operated at 4 K to reduce sensitivity in addition to the nozzle-skimmer distance being set at 100 mm.) The laser power entering the scattering chamber was varied by placing neutral density filters of differing optical densities in the laser beam path, and the bolometer signal for the weak HF beam is measured. The results are shown in Figure 3.3 for HF molecules traveling at two different velocities. The most important finding was that under single mode (*i.e.*, TEM_{00}) laser beam conditions, the electric dipole transition undergone by HF

Table A.2 Check of Periscope Alignment During Bolometer Rotation

Bolometer Angle (°)	Bolometer Signal (% of 0°)
Condition #1	
0	100.0
10	99.8±1.6
20	101.3±2.7
45	104.9±2.6
90	99.1±1.3
Condition #2	
0	100.0
10	99.3±2.7
20	103.2±4.5
45	102.3±4.1
90	101.3±1.3

Condition #1: The aluminum sponge used to suppress background HF is kept at ambient temperature. Laser is operated on the $P_1(2)$ transition.

Condition #2: The aluminum sponge is cooled to liquid nitrogen temperature ($\sim -190°C$). Laser is operated on the $P_1(2)$ transition.

molecules due to being excited by the laser beam was saturated. In other words, the laser power per unit frequency range is sufficient to excite all molecules capable of being promoted for a given rotational state in the molecular beam. The equations and conclusions presented in Chapter 3 were developed from this information.

With the relationship between bolometer signal and relative rotor population well understood, one is now ready to determine the rotational state population distribution in the supersonic expansion. The HF molecular beam is prepared under optimized expansion conditions, but one important apparatus modification was required to restrict the amount of HF striking the bolometer surface. This was done by epoxying a 0.1 mm Pt nozzle onto a collimator plate (Col in Figure A.2) whose normal aperture size is ~2.4 mm. This small aperture restricted the flux of HF enough so that the bolometer could be positioned directly in line with the incoming HF molecular beam. With the laser operating under single mode conditions, the bolometer signal is integrated for ~50 sec per laser line. Appreciable bolometer signals, and hence a measurable rotational state population, were obtained for the laser tuned to the $R_1(0)$, $R_1(1)$, $R_1(2)$, $P_1(1)$, $P_1(2)$, $P_1(3)$, $P_1(4)$, and $P_1(5)$ transitions. The results of the rotational distribution study are presented in Chapter 3 and again in Chapter 4. Note that the relative population in $j = 1$ and $j = 2$ is probed by both R-branch or P-branch transitions. This allowed for a consistency check to the equations derived in Chapter 3.

A.3 HF+AR SCATTERING

An experimental day starts at ~5 a.m. when a timer switch automatically opens a solenoid valve and allows $N_{2(\ell)}$ to cool the radiation shielding attached to a liquid nitrogen dewar on the bolometer. At ~7 a.m. this dewar can be manually filled, and the transfer of liquid helium from a storage dewar to a second dewar on the bolometer is begun. Details of the transfer procedure are contained in reference 6.

While the liquid helium transfer is underway, the thermostatic bath for the HF cylinder is regulated to $10.0 \pm 0.5°C$, and the HF nozzle heater is switched on. Also, the microwave discharge is struck to allow the laser components to warm up to operating temperature before doing an alignment of the tracer HeNe laser and the HF chemical laser. After the liquid helium transfer is completed in $\sim \frac{1}{2}$ hour (usually collect ~1.1 L), the inner dewar containing the liquid helium is pumped down to ~6.5 torr to lower the detector temperature to 1.5K. The bolometer is rotated to the 0° position (directly opposite the primary HF molecular beam), and the tracer laser is carefully aligned first to the HF laser, then through the two irises under the scattering chamber. The returning laser is slightly misaligned in a downstream direction (~0.4°) to prevent its feedback into the optical cavity. Without this misalignment, locking of the laser frequency to the Lamb dip minimum is impossible.

With the laser ready for the experiment, the HF molecular beam and the Ar atomic beam are turned on to give the beam conditions described earlier. A scattering angle of 30° with the laser tuned to the $R_1(0)$ transition is used as a reference, so this data point is usually measured twice to ensure good reproducibility for this day, and to previous days. The bolometer is then rotated, under computer control (IBM PC-AT), to the desired scattering angle, while the diffraction grating is rotated to the desired position (also under computer control) to give the needed

laser transition. The laser frequency is manually locked to the Lamb dip minimum, and the measurement of scattering signal is begun. Signal integration times vary from 200 sec to 1000 sec depending on their strength. The Ar beam is periodically flagged off to allow for subtraction of background signals. After every two or three data points (or after every data point for long integration times), the bolometer and laser are moved back to their reference postions and a reference data point is taken. This is needed to compensate for long term drift of the detection system sensitivity, as well as to keep track of any short term increases/decreases in signal. With all aspects operating properly, an experimental day would usually last for ~10 hours of data taking until the liquid helium in the bolometer was gone.

Approximately 8 to 10 data points are collected for each scattering angle at each j' that is measured ($0 \leq j' \leq 5$). This large number of data is collected to ensure that a good statistical sampling is obtained, and that if data is to be rejected for some reason (*e.g.*, laser power too low or too high, or data point is removed with a Q-test) then there will remain a sufficient number of data points to still have a statistically meaningful error bar.

The raw data is stored in an archive file on the computer's hard disk. The program ARCNORM reads through this file to normalize the data based upon reference signal levels. If two successive reference signals vary by a preset limit (usually ±25% of the first of the two points), then the data gathered between these two reference points is automatically rejected. For this experiment, the signal obtained with the laser tuned to $R_1(0)$ and the bolometer rotated to 30° is chosen to be the reference. The normalized data is then collated and averaged according to final rotational state and scattering angle. The program ERRBAR takes the average data whose error bars represent one standard deviation and 3-point smooths the error bars for all scattering angles for a given j'. This produces the data presented in Chapter 4.

REFERENCES:

1. Previous unstabilized and low resolution work completed with this laser is reported in J. A. Barnes, M. Keil, R. E. Kutina, and J. C. Polanyi, *J. Chem. Phys.* **72**, 6306 (1980); **76**, 913 (1982).
2. L. J. Danielson and M. Keil, *J. Chem. Phys.* **88**, 851 (1988); M. Keil, L. J. Danielson, U. Buck, J. Schleusener, F. Huisken and T. W. Dingle, *J. Chem. Phys.* **89**, 2866 (1988); L. J. Danielson, K. M. M^{c}Leod and M. Keil, *J. Chem. Phys.* **87**, 239 (1987); L. J. Danielson, M. Keil and P. J. Dunlop, *J. Chem. Phys.* **88**, 4218 (1988).
3. T. E. Gough, R. E. Miller and G. Scoles, *Appl.Phys.Lett.* **30**, 338 (1977).
4. J. C. Polanyi, *Chemica Scripta* **27**, 229 (1987).
5. O. Svelto, *Principles of Lasers* (Plenum, New York, 1976), pp. 96 – 99.
6. L. J. Danielson, *Determination of Interatomic and Intermolecular Potential Energy Surfaces from Crossed Molecular Beam Scattering*, Ph.D. thesis, University of Alberta, 1988.
7. N. C. Blais, J. B. Cross, and G. H. Kwei, *J. Chem. Phys* **66**, 2488 (1977).
8. See Reference 6, in particular Appendix A, pages 268 and 269.
9. P. F. Vohralik, R. E. Miller, and R. O. Watts, *J. Chem. Phys.* **90**, 2182 (1989).
10. K. Tamagake and D. W. Setser, *J. Chem. Phys.* **83**, 1000 (1979).
11. A. Corney, *Atomic and Laser Spectroscopy* (Oxford University Press, 1977).
12. D. Halliday and R. Resnick, *Fundamentals of Physics, 2nd Ed., Extended Version* (John Wiley and Sons, Toronto, 1981). Chapter 38.

APPENDIX B

CALCULATIONAL DETAILS

Many hundreds of lines of computer code had been written in this laboratory (mainly by Dr. Mark Keil) to calculate the differential cross section for atom-atom scattering. This code was subsequently expanded to use the infinite-order-sudden (IOS) approximation to calculate the "total" (*i.e.*, rotationally unresolved) differential cross section for atom-linear molecule scattering. The experiments reported here contain results from rotationally inelastic differential scattering experiments, and as a result the computer code was further modified to include this calculational requirement. The most informative reference for this calculation is given by Parker and Pack.[1]

An outline of the input and output parts of the calculational scheme is presented below in Section B.1. Section B.2 is intended to provide an introduction to the calculational method used to generate differential cross sections in the laboratory-frame averaged over all experimental conditions.

B.1 Experimental Input

The upper box in Table B.1 indicates the experimental details that need to be input to characterize the system being studied under a given energy distribution.

HF beam: this is the primary beam, known as such since it contains the particles that are detected by the bolometer.

i. HF mass = 20.006 g/mole is needed to calculate the reduced mass of the HF+Ar scattering system.

ii. Rotational constant of ground state (*i.e.*, $\nu = 0$) HF = 20.56 cm^{-1} (from Herzberg[2]). No other dependence on quantum numbers is in-

Table B.1 Input to Scattering Program

Input Experimental Details
HF Primary Beam particle mass; rotational constant; rotational distribution; velocity; velocity distribution; beam angular divergence; heat of condensation.
Ar Secondary Beam particle mass; velocity; velocity distribution; beam angular divergence.
Apparatus Parameters beam intersection angle; detector angular resolution.

↓

Input Calculational Parameters
angular grid to select θ_{cm}; angular grid for θ_{lab} output;
number of points and cutoff limits for primary and secondary beam angular and velocity distributions used to construct Newton diagrams;
number of points and cutoff limits for primary and secondary beam velocities and intersection angle to construct relative velocity distribution.
number of collision energies for which a center-of-mass frame DCS is calculated.
number of interaction angles for IOS integration.
number of interaction angles for scattering amplitude Legendre expansion coefficients.
WKB phase shift parameters for IOS calculation of DCS in center-of-mass frame.†

↓

Interaction Potential
interaction potential as a function of "r" and "γ"

↓

Output
laboratory-frame final rotational state selected DCS averaged over all experimental conditions.

† The HIBRIDON code (see Chapter 5) can be used here to calculate the close-coupling center-of-mass frame DCS in place of the IOS technique of calculating the center-of-mass frame DCS.

cluded here. This value is necesary to quantify the amount of rotational energy transfered during a scattering event, used only in the center-of-mass to laboratory-frame transformation since the IOS approximation is rotationally degenerate.

iii. Incident rotational distribution needed to properly sum the contributions of various state-to-state DCS's to a particular final rotational state-summed DCS. The incident rotational distribution is given in Chapter 3, and again in Chapter 4.

iv. Due to the supersonic expansion of the molecular beam, the distribution of molecular velocities is non-Boltzmann. The actual distribution of beam particle velocity is needed to construct the distribution of the relative collisional energy.

v. The two molecular beams nominally intersect at 90°, but the angular divergence of each molecular beam implies the existence of interactions occuring over a distribution of angles near 90°.

vi. The amount of heat liberated when an HF molecule strikes the bolometer detector surface and is frozen to the surface (taken to be 431 meV[3]) is needed to properly convert the scattered flux in the center-of-mass (c.m.) frame to a corresponding signal due to HF in the laboratory reference frame.

Ar beam: this is the secondary beam, known as such since it contains the particles that are not detected by the bolometer.

i. Ar mass = 39.948 g/mole is needed to calculate the reduced mass of the HF+Ar scattering system.

ii. Due to the supersonic expansion of the molecular beam, the distribution of velocities is non-Boltzmann. The actual distribution of beam particle velocity is needed to construct the distribution of the relative collisional energy.

iii. The two molecular beams nominally intersect at 90°, but the angular divergence of each molecular beam implies the existence of interactions occuring over a distribution of angles near 90°.

Apparatus: the bolometer detector has a series of appertures which restrict unwanted particles or radiation from impinging on the liquid He cooled surface. These apertures define the angular resolution of the detector, which is calculated to be 3.11°. This number represents the maximum deflection that an HF molecule in the wing of the HF beam can be deflected and still reach the detector under single collision conditions if the bolometer is positioned directly opposite the HF molecular beam.

B.2 Calculational Aspects

The second box of Table B.1 depicts the scattering program using the information of the first box to integrate over experimental conditions. This constitutes the majority of the calculational effort.

The calculation begins by first constructing a vector of center-of-mass (c.m.) scattering angles beginning at 0° and ending at 180°. The vector of angles can be divided into two parts with each having a different increment between adjacent angles if desired. This is necessary to allow for sufficient angular fineness in calculating the highly oscillatory c.m. DCS for low angles ($0° \leq \theta_{cm} \leq 60°$), but then allowing a coarser angular grid at large angles ($60° < \theta_{cm} \leq 180°$) where the DCS is usually monotonic. Also, the initial and final laboratory angles, along with an incremental stepsize, are specified to produce a vector of laboratory angles to which the c.m. DCS's are transformed.

The next step is to employ the molecular beam conditions in constructing the Newton diagrams used to transform the c.m. DCS's to the laboratory-frame. This involves four steps:

i. Using the angular divergence of the HF beam to provide the range of possibilities, select 4 angles (based upon Gauss-Legendre integration points and weights) for the HF molecules to be propagating towards the scattering center.

ii. In parallel to *i.* above, use the angular divergence of the Ar beam to select 4 angles (based upon Gauss-Legendre integration techniques) for the Ar atoms to be propagating towards the scattering center.

iii. Use the most probable velocity and the velocity distribution (obtained from time-of-flight measurements) to select 12 HF velocities (based upon Gauss-Legendre integration techniques).

iv. Only one Ar beam velocity is chosen to construct the Newton diagrams. This one velocity is the most probable velocity obtained from time-of-flight measurements.

Table B.2 displays the beam angles and velocities used to construct all of the Newton diagrams. The relative velocity for each diagram is readily calculated from the angle of intersection (*i.e.*, the difference between the Ar angle and the HF angle) and the selected velocity of each beam. The statistical weight of each particular Newton diagram (not shown) is calculated as a product of the statistical weights of each angle or velocity. This weight is needed when finding the average laboratory-frame DCS from all Newton diagram transformations.

Table B.2 Newton Diagram Setup

HF Angles (deg)	Ar Angles (deg)	v_{HF} (km/s)	v_{Ar} (km/s)		
−1.989	87.839	0.9789	0.5600		
−0.785	89.147	0.9957			
0.785	90.853	1.0248			
1.989	92.161	1.0644			
		1.1120			
		1.1646			
		1.2189			
		1.2715			
		1.3191			
		1.3587			
		1.3879			
		1.4047			
e.g., the two Newton diagrams which give the minimum and maximum relative velocities					
HF Angle (deg)	Ar Angle (deg)	v_{HF} (km/s)	v_{Ar} (km/s)	v_{rel} (km/s)	Prob†
1.989	87.839	0.9789	0.5600	1.0920	0.0091
−1.989	92.161	1.4047	0.5600	1.5494	0.0091

† This probability is divided by the sum of the probabilities of all Newton diagrams when summing over individual laboratory frame DCS's to obtain the average laboratory frame DCS.

Construction of all Newton diagrams before calculating the c.m. DCS establishes the range of relative velocities encompassed by the Newton diagrams. This fact is used to select the relative velocities, which give the relative collision energies, for averaging over the incident kinetic energy distribution. The smallest

and largest relative velocities from the Newton diagrams form the outer limits, and other relative velocities are evenly spaced throughout the range. Four relative velocities (1.092, 1.244, 1.397, and 1.549 km/s), with corresponding collision energies of 82.4, 107.0, 134.8, and 165.8 meV were used to average over the HF+Ar energy distribution.

The decision to calculate the c.m. DCS at only 4 energies, and the use of 4 HF beam angles, 12 HF velocities, 4 Ar beam angles and 1 Ar velocity to construct the Newton diagrams was carefully investigated in the following way: an HF+Ar c.m. DCS was calculated at 24 collision energies. The transformation to the laboratory-frame was then done using the set of parameters (1,12,6,4) for the HF beam angles, HF velocities, Ar beam angles, and Ar velocities. The laboratory-frame DCS obtained with this set of parameters was considered to be properly transformed with no errors due to using a parameter set that required too few Newton diagram transformations. In order to speed up the calculational process, the number of angles and velocities required was decreased in a uniform manner, where after each change in the parameter set the newly calculated laboratory-frame DCS was graphically compared to the properly transformed DCS (from the (1,12,6,4) parameter set). With this trial and error method, it was found that a (1,12,4,1) parameter set would both significantly decrease computational effort and still accurately transform the c.m. DCS to the laboratory-frame. Parameter sets using smaller numbers of beam angles or velocities were found to introduce errors in the transformation process. However, as a measure of safety, the actual parameter set used was (4,12,4,1) so that the HF angular distribution would be properly averaged over when doing the c.m. to laboratory transformation.

The choice of using 4 collision energies was determined in much the same way. Using a larger than necessary number of Newton diagrams (1,12,6,4), the number of collision energies was systematically varied. After each decrease, the

newly calculated laboratory-frame DCS was graphically compared to the properly transformed DCS. This process was continued until choosing a fewer number of collision energies would begin to introduce errors into the transformation process. It is noted that choosing only 3 collision energies would have been sufficient for this system, but 4 collision energies were actually used to introduce a larger margin of safety in the transformation process.

For each collision energy above, the calculation now enters a large loop to determine the c.m. DCS for a given $j \rightarrow j'$ transition. The equations programmed for this part of the calculation are essentially those of Parker and Pack[1], and discussed in Sections 1.3 and 1.4.B. Briefly, the method is as follows: for each angle chosen for the IOS integration (8 angles in all, selected as Gauss-Legendre integration points), the phase shift curve (*i.e.*, η_L^k *vs.* L, L is the total angular momentum quantum number) is determined via a Wentzel-Kramers-Brillion (WKB) integration[4]. Manipulation of Equations 1–49, 1–50, and 1–52, with the conditions of $j''_{max} = 7$ in Equation 1–51 (which is the same as $L_{max}= 7$ in Equation 1–50) and 8 Gauss-Legendre integration points used to find the $\bar{F}_L^k(\theta)$ in Equation 1–50, forms the c.m. DCS for each $0 \rightarrow j''$ transition. Doing the summation over the Clebsh-Gordan terms in Equation 1–51 gives the c.m. DCS for any inelastic or elastic transition specified by j and j'. Recall that this entire sequence is repeated for each of 4 successive collision velocities (*i.e.*, energies).

In the calculation described above, j''_{max} was chosen to be 7 since this would include the first energetically closed channel into the calculation of the $0 \rightarrow j''$ c.m. DCS's. For the IOS integration, 8 angles were chosen since the number of angles (n_{IOS}) must be greater than j''_{max} or else the $0 \rightarrow n_{IOS}$ c.m. DCS is identically zero in the Clebsh-Gordan summation. Greater than 8 IOS angles could be used, but 8 angles was found to be sufficient for a proper IOS integration. The number of Gauss-Legendre integration points for the determination of the $\bar{F}_L^k(\theta)$

was chosen to be the same as the number of IOS integration angles to avoid having to calculate more DCS's (by interpolation) for the Gauss-Legendre integration to calculate $F_L^{\bar{k}}(\theta)$.

It is essential to point out that at this place in the calculation, the IOS equations programmed in this laboratory, and the quantum mechanical based HIBRIDON code each provide the same type of information. Specifically, available to the next step are c.m.-frame DCS's for specified $j \rightarrow j'$ transitions, at the requested c.m. angles, and for the four (or any number) requested energies.

Conversion of the c.m. DCS's (obtained by either IOSA or close-coupled techniques) to the laboratory-frame now follows. Recall that the angles and velocities of each beam composing the Newton diagrams have been established earlier, thus meaning that the collision energy of each Newton diagram is within the range of energies for which the c.m. DCS's have been calculated. With the restriction that the c.m. DCS's do not vary wildly with collision energy,[5] one can use an interpolation routine to find the c.m. DCS at the exact energy of a particular Newton diagram.

With reference to the sample Newton diagrams presented in Figures B.1.A and B.1.B, when taking into account the rotational inelasticity associated with a given DCS, it is first necessary to check whether any tangents to the c.m. circle in the Newton diagram exist. This is necesary to restrict the range of possible laboratory angles, and to prevent the Jacobian factor from tending to infinity at such tangents. Also, for very inelastic DCS's it is possible that for each laboratory angle there can be two corresponding c.m. angles. Figure B.1.A and B.1.B show Newton diagrams with examples of the several different cases that can exist, and that must be accomodated in the transformation.

After establishing all parameters dictating this particular Newton diagram, a loop is entered to convert the c.m. angle and intensity to a laboratory-frame

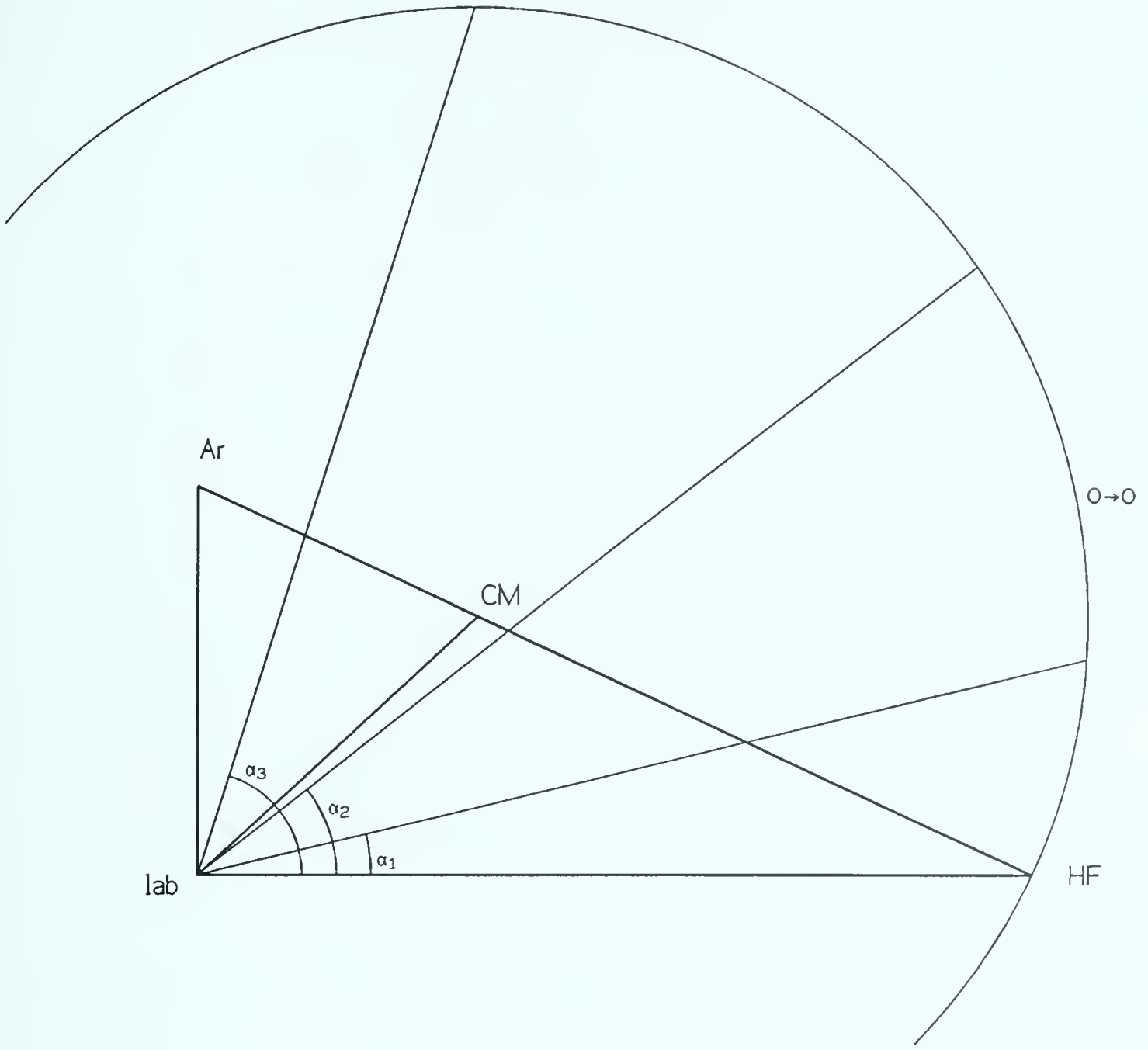

Figure B.1a Newton diagram showing a case where there is a one to one mapping of laboratory angle to c.m. angle such as for laboratory angles α_1, α_2, and α_3. The example here is for the elastic $j = 0 \rightarrow j' = 0$ transition, but could be for any transition with a final HF velocity greater than the velocity of the c.m. (*i.e.*, a Newton circle containing the laboratory origin in its interior).

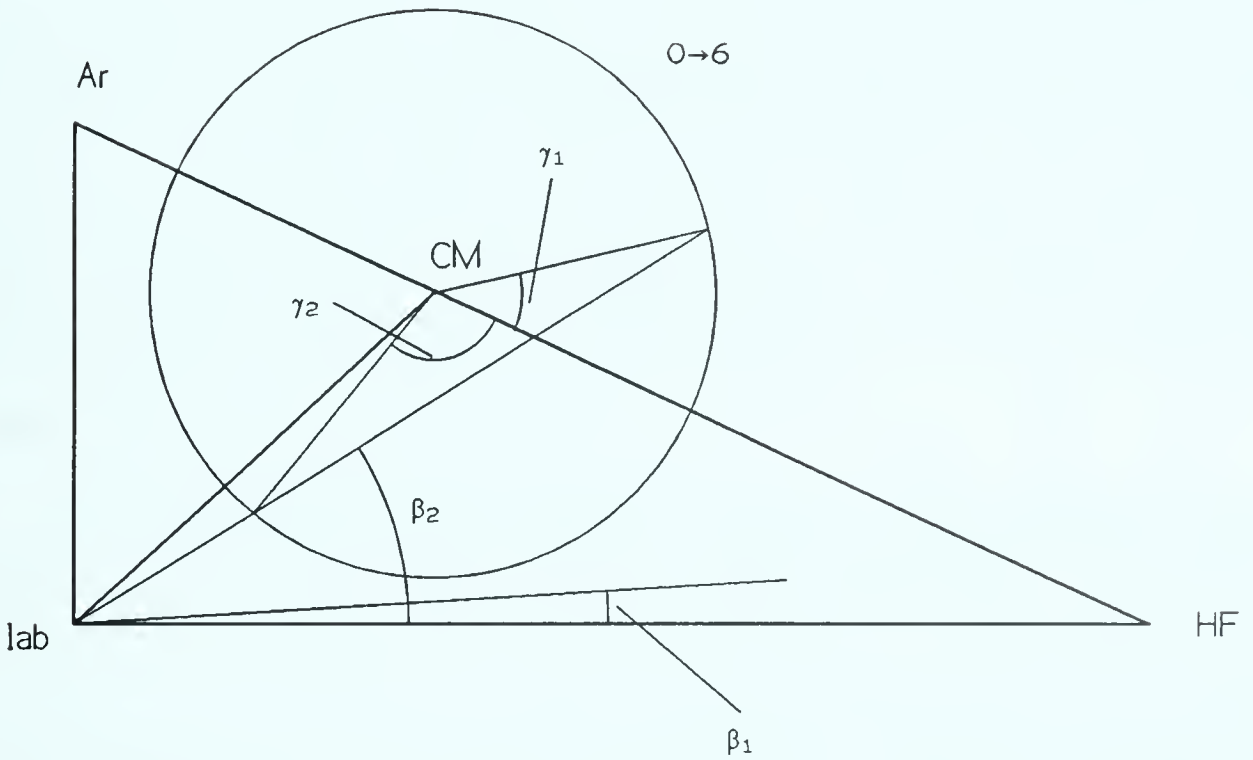

Figure B.1b Newton diagram showing a case where there can be either no corresponding c.m. angle for a given laboratory angle (*i.e.*, β_1), or there can be two c.m. angles (γ_1 and γ_2) for a particular laboratory angle (β_2). This situation can only occur for a highly inelastic transition where the HF c.m. velocity is less than the velocity of the center-of-mass itself.

angle and intensity. The loop is as follows: cycle through the $\theta_{\rm lab}$ grid. For each $\theta_{\rm lab}$, find the corresponding $\theta_{\rm cm}$. (Note that there may be zero, one or two $\theta_{\rm cm}$.) Use interpolation to determine the c.m. DCS at this particular $\theta_{\rm cm}$. Determine the Jacobian factor[6] for this particular $\theta_{\rm lab} \leftrightarrow \theta_{\rm cm}$ combination, and use this Jacobian factor and the energy flux intensity detection factor to convert the c.m. intensity to the laboratory intensity. This loop is continued for all $\theta_{\rm lab}$.

The energy flux intensity detection factor is designed to reflect the change in laboratory frame velocity the primary beam particles experience when scattering through any non-zero angle. It is defined as the ratio of the sum of the incident energy at any angle upon the bolometer (*i.e.,* the sum of the kinetic energy plus the heat of adsorption on the cold bolometer surface) divided by the sum of the incident energy (*i.e.,* kinetic plus adsorption) upon the bolometer at 0°and no rotational inelasticity. By definition, if no scattering event occurs, then the energy flux intensity detection factor is equal to unity.

The calculation now progresses to the next Newton diagram where the checking for tangents and looping over $\theta_{\rm lab}$ is repeated. Each laboratory-frame DCS obtained in this way is multiplied by the weight of each particular Newton diagram. After cylcling through all of the Newton diagrams, the weighted laboratory DCS's are summed together at each desired laboratory angle. The result to this point is a laboratory-frame DCS for a particular $j \rightarrow j'$ transition averaged over the collision energy distribution and the individual beam velocity and angular spreads. A summary of the transformation scheme is outlined in Table B.3.

The experiments conducted did not measure the laboratory-frame DCS for a particular $j \rightarrow j'$ transition, but rather they measured the DCS for transitions from any j to a particular j'. To reflect this, the calculated laboratory DCS's for the transitions from all j to one j' are weighted by the initial rotational state population (*i.e.,* the distribution of j states in the incident beam), and these weighted DCS's

Table B.3 Summary of Center-of-Mass to Laboratory Transformation

Obtained from either IOSA or close-coupling is the center-of-mass DCS for a particular $j \rightarrow j'$ at 4 different collision energies. Represent this by $I(\theta_{cm}(i), E_{rel}(n); j \rightarrow j')$.

Construct an outer loop over the Newton diagrams, and an inner loop over the desired laboratory angles set up via a grid. Using the FORTRAN notation for looping, the scheme is represented as:

```
DO 100   I=1,NND          Loop over the vector of Newton diagrams.
```

(1.) Do an interpolation over the array of $I(\theta_{cm}(i), E_{rel}(n); j \rightarrow j')$ to get a vector of $I(\theta_{cm}(i), E_{ND\#I}; j \rightarrow j')$.

```
DO 200   J=1,NTHLAB       Loop over the vector of lab angles set up by the grid.
```

(1.) Consider the rotational inelasticity represented by the $j \rightarrow j'$ transition. Use geometry on Newton diagram #I to determine θ'_{cm} which corresponds to θ_{lab}(#J). Note that there may be 0, 1, or 2 θ'_{cm} found at this step.

(2.) Interpolate over the vector of $I(\theta_{cm}(i), E_{ND\#I}; j \rightarrow j')$ to get $I(\theta'_{cm}, E_{ND\#I}; j \rightarrow j')$.

(3.) Multiply this scalar by the Jacobian and flux intensity transformation factors to obtain $I(\theta_{lab}, E_{ND\#I}; j \rightarrow j')$.

(4.) Properly weight this quantity $I(\theta_{lab}, E_{ND\#I}; j \rightarrow j')$ by multiplying it by the statistical weight of Newton diagram # I.

```
200   CONTINUE
100   CONTINUE
```

The result obtained thus far is stored as a two dimensional array $I(\theta_{lab}, E_{ND}; j \rightarrow j')$. A summation over the index representing the Newton diagram energies (a third loop) provides the energy averaging needed to give $I(\theta_{lab}, \overline{E}; j \rightarrow j')$.

Weighting each $I(\theta_{lab}, \overline{E}; j \rightarrow j')$ by the population distribution for rotational state j, and doing a summation over j (a fourth loop) gives $I(\theta_{lab}, \overline{E}; j')$. The last type of averaging applied, is over the detector angular resolution to reflect the finite size of detector apertures.

---

are summed together at each laboratory angle to get a laboratory-frame DCS with a specified final rotational state and averaged over all initial rotational states.

The last type of averaging done takes into account the finite angular resolution of the bolometer detector, which is assumed to be a $\cos^2$ function with an angular full width at half maximum (FWHM) of 3.11°.

NOTE: We suspect that an error has been made in the energy flux intensity detection factor mentioned above. This aspect of the calculation is currently under investigation.

REFERENCES:

1. G. A. Parker and R. T Pack, *J. Chem. Phys.* **68**, 1585 (1978).
2. G. Herzberg, *Spectra of Diatomic Molecules* (Van Nostrand Reinhold Company, New York, 1950), pp. 536 - 537.
3. P. F. Vohralik, R. E. Miller, and R. O. Watts, *J. Chem. Phys.* **90**, 2182 (1989).
4. G.C. Maitland, M. Rigby, E.B. Smith, and W.A. Wakeham, *Intermolecular Forces: Their Origin and Determination* (Clarendon, Oxford, 1981).
5. See, for instance, Figure 5.10 for an example of the c.m. DCS varying slowly and smoothly with collision energy.
6. F.A.Morse and R.B.Bernstein, *J. Chem. Phys* **37**, 2019 (1962).

APPENDIX C

UNPUBLISHED EXPERIMENTAL DATA

Chapter 3 reports an HF molecular beam produced by seeding HF in a strong beam of He. The purpose was to produce an HF beam with a higher velocity and narrower velocity distribution than can be obtained under unseeded expansion conditions. As a consequence of the higher HF velocity, the collision energy will also be higher than for unseeded conditions. This allows for a much higher energy of the repulsive part of the interaction potential to be probed.

A series of crossed beam experiments with HF (seeded in He) and scattered by Ar, and pure HF scattered by Ar were performed before the set of experiments resulting in the published data of Chapter 4. This original data was not published when it was discovered that some experimental conditions were not optimized. (In particular, the secondary Ar atomic beam nozzle skimmer distance was too small, resulting in a loss of Ar beam intensity and too a great pressure inside the scattering chamber.) Comparison of low energy (~120 meV) scattering results from before and after the discovery of the incorrect Ar beam conditions show that the incorrect Ar beam conditions produce only a slight difference in DCS shape, along with a degradation in signal to noise quality. Since the unoptimized Ar beam has only resonably small effects upon the DCS shape, it is felt that the high energy (~330 meV) scattering done with the seeded HF beam has qualitatively correct results. These results are presented here for the first time.

Table C.1 presents the seeded and unseeded HF molecular beam conditions along with the unoptimized Ar beam conditions used to generate the high energy DCS's. Table C.2 presents the seeded HF molecular beam rotational distribution (generated from data present in Chapter 3.) Figure C.1 shows the comparision of the low energy DCS's obtained both with and without optimized Ar

conditions to show the qualitative retension of DCS shape. Figure C.2 shows the high energy DCS's obtained for $j' = 0$ and 1, and Table C.3 presents the same data in numerical form.

Table C.1 Molecular Beam Operating Conditions

	HF unseeded	HF seeded	Ar
Nozzle temperature (°K)	500±10	500±10	302
Thermostatic bath temperature (°C)	10±0.5	−50±1	—
Nozzle diameter (mm)	0.10	0.10	0.30
Nozzle pressure (atm)	0.74	4.3	0.64
He seed gas flow (atm-cm^3/min)	—	600	—
Nozzle–skimmer distance (mm)	14	17	15[a]
Skimmer diameter (mm)	0.73	0.73	1.03
Most probable velocity (km/sec)	1.21[b]	2.11[c]	0.56
Velocity FWHM $\left(\frac{\Delta v}{v_{\mathrm{mp}}}\right)$[d]	0.21	0.10	0.079
Collimator diameter (mm)	2.41	2.41	2.56
Dimer/monomer signal ratio[d]	0.06	0.04	0.004

[a] Optimized nozzle-skimmer distance is 18 mm. This incorrect distance resulted in reduced Ar beam intensity (∼ 20% less) and increased scattering chamber pressure (∼9×10^{-6} torr *vs.* ∼3×10^{-6} torr).

[b] The corresponding most probable relative velocity is 1.31 km/sec, with a FWHM spread of 17%. The calculated collision energy is 120 meV.

[c] The corresponding most probable relative velocity is 2.18 km/sec. The calculated collision energy is 330 meV.

[d] For HF, this is the measured $\frac{m}{e} = 21:20$ ratio. Most likely this provides only a lower limit for the true dimer : monomer ratio due to fragmentation in the mass spectrometer.

Table C.2 Seeded HF Beam Rotational Distribution

j	Population (%)[a]
0	46.8
1	39.6
2	9.8
3	2.9
4	0.9

[a] Calculated populations from data presented in Chapter 3.4.B.

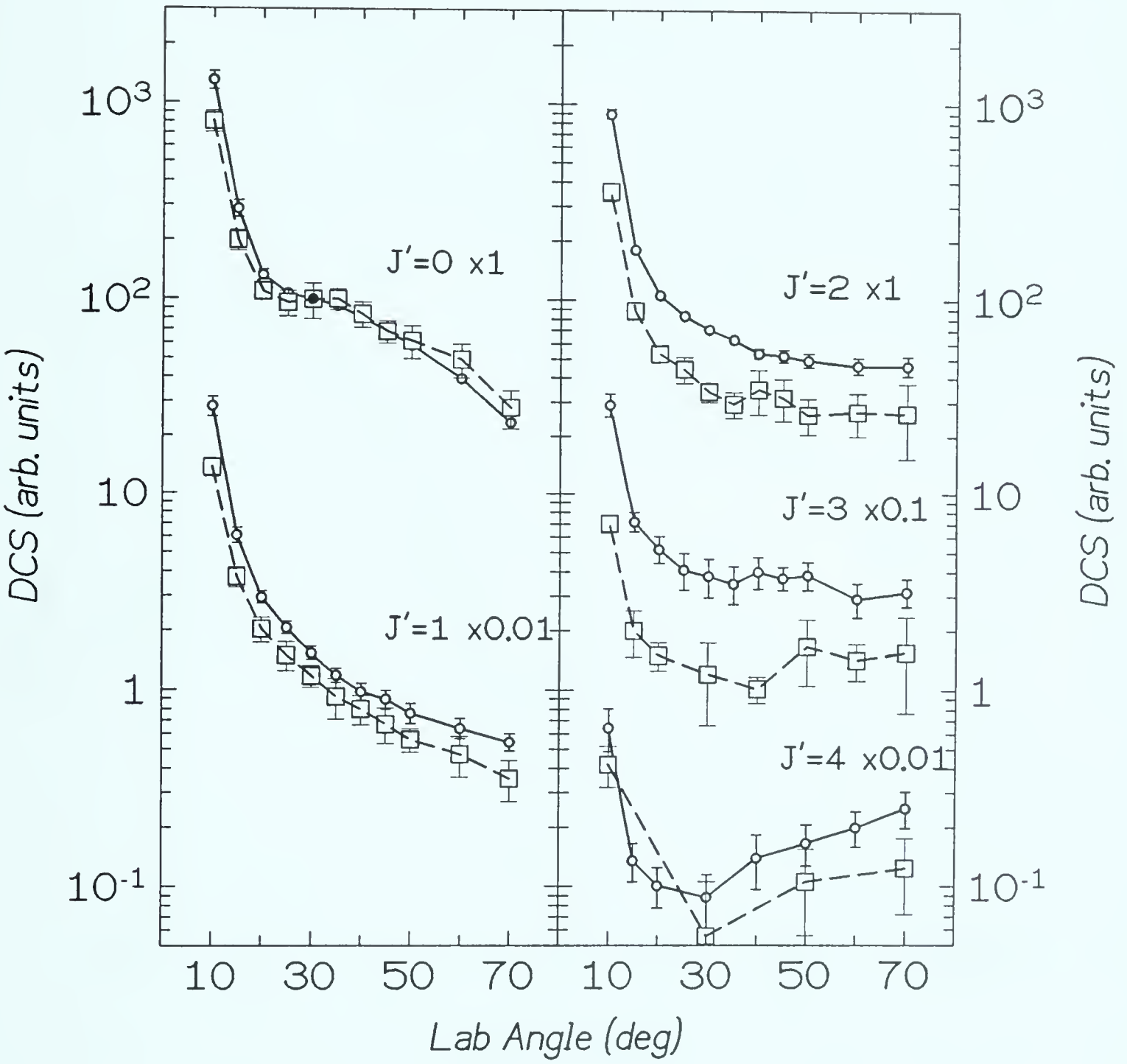

Figure C.1. Published low energy (~120 meV) HF+Ar differential cross sections (circles) *vs.* differential cross sections measured with unoptimized Ar atomic beam (squares). A $j' = 5$ DCS was not measured at the unoptimized conditions because of much poorer signal-to-noise ratios.

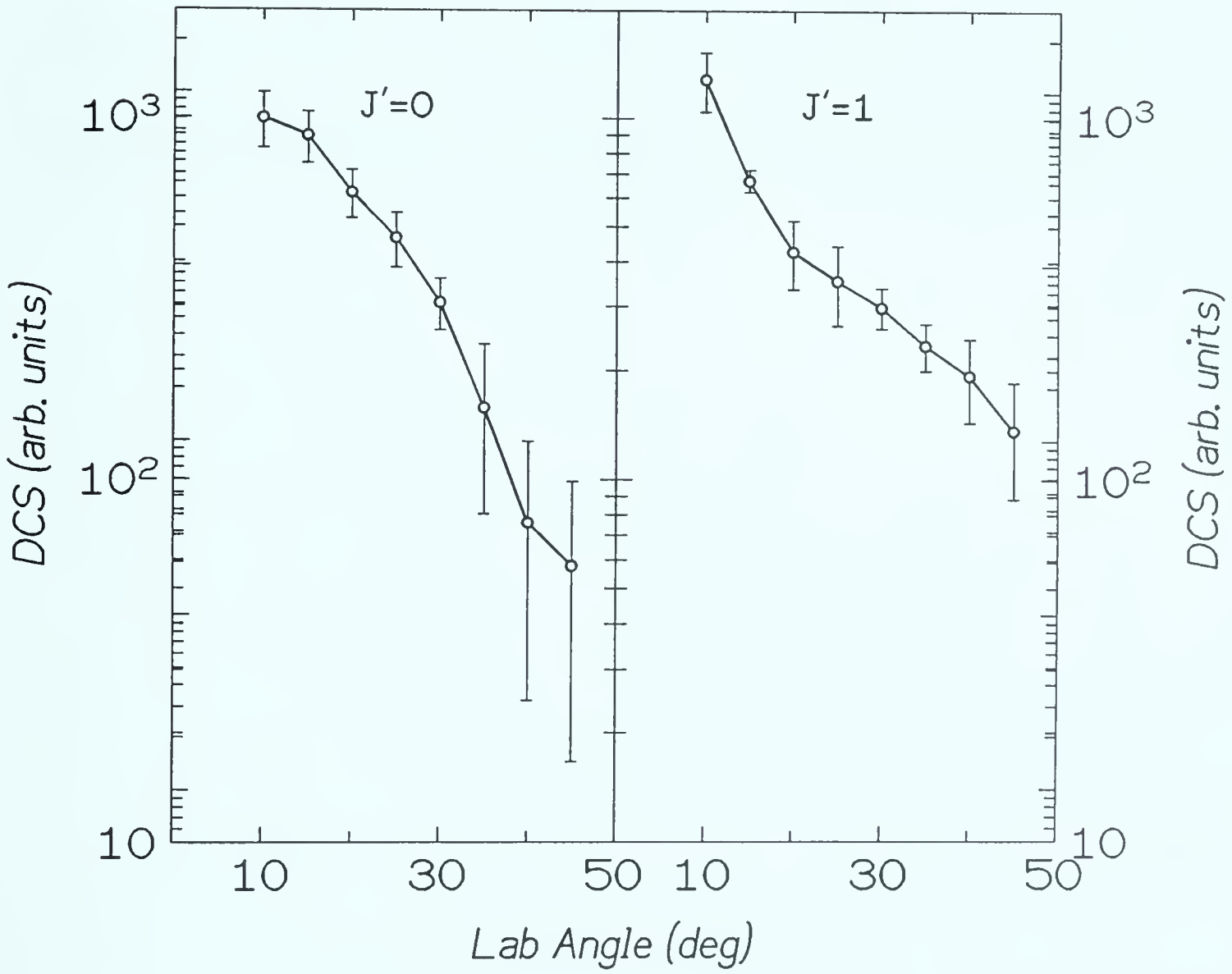

Figure C.2. High energy (∼330 meV) HF+Ar differential cross sections obtained with an unoptimized Ar atomic beam.

Table C.3 High Energy ~330 meV HF+Ar DCS's

Angle (deg)	$j' = 0$ DCS	Error Bar (%)*	$j' = 1$ DCS	Error Bar (%)*
10	1000.0	17.54	1285.6	18.86
15	894.3	16.34	671.7	6.92
20	621.9	15.18	426.7	21.54
25	465.0	17.27	354.3	24.88
30	308.0	16.37	299.5	12.90
35	158.3	49.22	235.0	14.74
40	76.2	67.71	194.1	25.84
45	57.8	71.18	137.1	35.35

* These error bars represent one standard deviation in the measured signal. They have not been smoothed or convoluted with any other source of machine error.

APPENDIX D – ADDITIONAL PUBLICATION

ANISOTROPIC REPULSIVE POTENTIAL ENERGY SURFACES FROM HARTREE–FOCK CALCULATIONS FOR $HeCO_2$ AND HeOCS†

D.1 INTRODUCTION

The *ab initio* construction of reliable potential energy (PE) surfaces remains a daunting task for most systems involving exclusively van der Waals interactions. This has led to the widespread use of semi-empirical models for their characterization.[1] Perhaps the most successful of these, particularly for inter-atomic potentials, have been models that add damped dispersion terms to a Hartree–Fock repulsive core. For the purposes of this paper, such prescriptions will be labeled "HFD", whether the dispersion damping factors are those used by Scoles and co-workers,[2] or those due to Tang and Toennies.[3] An alternative semi-empirical approach, somewhat related to the sum-over-sites parameterization that we adopt here, is provided by the "test–particle" model of Ahlrichs and co-workers.[4]

For interactions between an atom and a molecule, HFD prescriptions have been used primarily for rather weak anisotropies,[5,6] or for those involving diatomic molecules.[7–10] Few attempts have yet been made to apply HFD models to more highly anisotropic systems,[11] and such PE surfaces have been obtained instead by more purely empirical approaches.

Compared to other systems studied in detail,[10,12] the $HeCO_2$ interaction in particular is the most highly anisotropic due to the chain of three heavy atoms. For this system, empirical PE surfaces have been extracted from a wide variety of measurements, ranging from scattering and line-broadening data to thermophysical properties.[13,14] Such a wide variety of studies appears to be necessary, since the

† A version of this chapter has been published.
M. Keil, L. J. Rawluk, and T. W. Dingle *J. Chem. Phys.* **96**, 6621 (1992).

directness and precision of bound-state van der Waals spectroscopy[12] is unavailable for this system. For HeOCS, available evidence[15] substantiates chemical intuition, suggesting clearly that its interaction is even more anisotropic. However, much less is known about HeOCS, with only a handful of experimental results being available.

Implementation of HFD prescriptions require knowledge of the short- and long-range interaction potentials, even if these may be adjusted in subsequent semi-empirical fits to experimental data. For $HeCO_2$, both such components have been generated.[16–18] For HeOCS however, there are no Hartree–Fock calculations available, and only the leading C_6 terms are available for estimating long-range interactions.[15,19]

The purpose of this paper is to present Hartree–Fock calculations for HeOCS. For comparison purposes, we have simultaneously performed calculations for $HeCO_2$. Such a comparison can help establish the particular rôle played by the asymmetry of OCS in its repulsive interaction with He.

Results of the Hartree–Fock calculations are presented in Sec. II of this paper. These are fitted to parametric forms involving sums over atom-atom interactions, yielding PE surfaces that are suitable for dynamical calculations. In Sec. III, we compare pressure-broadening measurements and calculations for infrared and Raman transitions of CO_2 and OCS diluted in He. Alone amongst experimental properties available for these systems, the pressure-broadening results are insensitive to the weak van der Waals attractions,[13] while being caused by rotationally inelastic collisions and therefore sensitive to the anisotropy of the repulsive core. Comparing the experimental results[20–23] to those calculated for the pressure broadening therefore provides a first test for the overall reasonableness of the present repulsive PE surfaces. Further tests for the sensitivity of the pressure-broadening data to the PE surface are also described in Sec. III.

D.2 POTENTIAL ENERGY SURFACES

The co-ordinate system used is depicted in Fig. D.1. For the dynamical calculations to be presented in Sec. III, the molecular centre-of-mass is the most appropriate origin. On the other hand, the PE surface is parameterized in terms of co-ordinates for the He relative to each atomic site of the molecule. The (r_i, γ_i) co-ordinates with respect to each atomic centre i are obtained geometrically from the (r, γ) centre-of-mass co-ordinates as

$$r_i = \left(r^2 + z_i^2 - 2 r z_i \cos\gamma\right)^{1/2} \quad \text{and} \quad \gamma_i = \cos^{-1}\left(\frac{r\cos\gamma - z_i}{r_i}\right), \qquad (D-1)$$

where z_i is the position of each atomic centre $(i = 1, 2, 3)$ relative to the molecular centre-of-mass. These positions are taken from the experimental bond lengths in each molecule.[24]

D.2.A. Hartree–Fock Calculations

Hartree–Fock SCF calculations for the $HeCO_2$ and HeOCS interaction energies were carried out using the GAMESS[25] and SPDFG[26] programs on the AMDAHL 5870 and FPS 164 processors at the University of Alberta. As in our earlier calculations for the HeNe interaction,[27] the basis set for the helium atom was an $(11s)$ basis of Van Duijneveldt[28] contracted to $(7s)$ and supplemented with four p functions to give the basis set (5111111/1111). The energy for the isolated He atom using this basis was $-2.861\,673\,0\,E_h$, compared to $-2.861\,680\,E_h$ from numerical Hartree–Fock calculations.[29]

The basis sets for the carbon and oxygen atoms were $(14s\,10p)$ well-tempered basis sets of Huzinaga and Klobukowski[30] contracted to $(7s\,6p)$ and supplemented with three d functions to give a $(7s\,6p\,3d)$ basis of the form (5671111/511111/111). In all three basis sets, the exponents of the p and d functions were the same as some of the exponents of the s set for faster calculation of the two

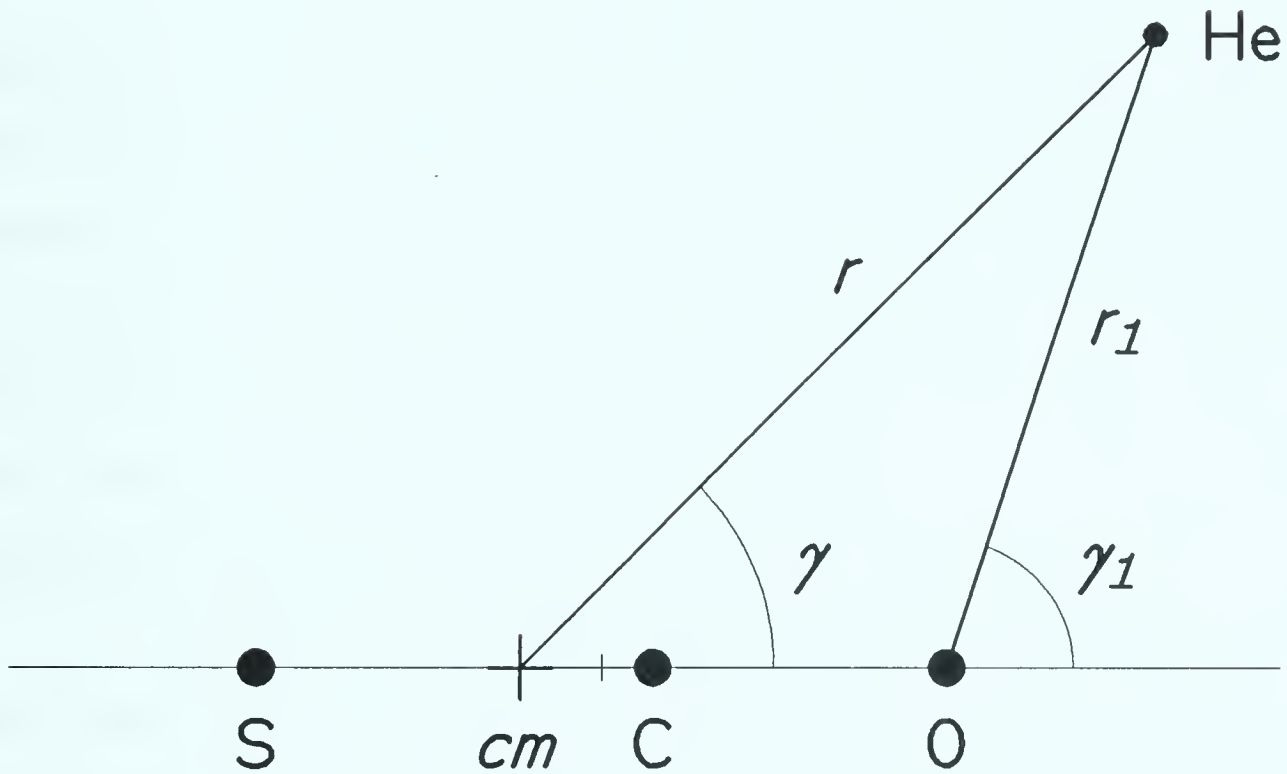

Figure D.1: Co-ordinate system used for the HeOCS sum-over-sites potential parameterization. The geometric centre, used for the $i = 0$ term appearing in Eqn. (D–2), is shown by a small tick to the right of the molecular centre-of-mass (cm).

electron integrals. These basis sets were the same ones tested in extensive calculations reported by Dingle *et al.*[31] on a variety of first row diatomics. For example, the total energy of the CO molecule was calculated to be $\sim 6\,\mathrm{mE_h}$ above the value of obtained from numerical Hartree–Fock calculations.[32] Thus, these $(7s\,6p\,3d)$ sets were close to the Hartree–Fock limit, and they gave values for other properties which were very close to those obtained from larger basis sets.[33]

The Hartree–Fock SCF energy for the isolated CO_2 molecule is calculated to be $-187.717\,13\,\mathrm{E_h}$ with the above basis sets. This is also $\sim 6\,\mathrm{mE_h}$ above the SCF energy of $-187.722\,81\,\mathrm{E_h}$ calculated by McLean and Yoshimine[34] using Slater double zeta basis sets plus $3d$ and $4f$ functions. Similarly, Knowles *et al.*[35] obtained $-187.722\,71\,\mathrm{E_h}$ using basis sets of $(15s\,9p\,4d\,2f)$ contracted to $(11s\,6p\,3d\,1f)$. The latter two calculations are fairly close to the Hartree–Fock limit. Thus, the CO_2 result using the $(7s\,6p\,3d)$ basis is high by about the same amount as for the CO calculation, indicating that the accuracy of these calculations is about the same.

For the S atom in OCS, a basis set of well-tempered functions, $(17s\,13p)$, was contracted to $(9s\,8p)$ and supplemented with $3d$ functions to give a $(9s\,8p\,3d)$ basis with the form (588111111/81111111/111). Exponents of the p and d functions were again made the same as some of those in the s set using guidelines from the work of Dingle *et al.*[31] Although this basis has not been tested as rigorously as that of the C and O atoms, we have used a similar basis for Ar in trial calculations on the HeAr interaction.[36] In this case, the isolated Ar atom had a calculated energy $\sim 5\,\mathrm{mE_h}$ higher than the numerical Hartree–Fock results.[29] For comparison, our earlier calculations for Ne, using a $(7s\ 6p\ 3d)$ basis set similar to the C and O basis sets above, were only $\sim 0.2\,\mathrm{mE_h}$ higher than the corresponding numerical results.[27] This indicates that the $(9s\ 8p\ 3d)$ basis used for S is not quite as close to the Hartree-Fock limit.

The Hartree-Fock energy for an isolated OCS molecule is calculated to be $-510.347\,04\,\mathrm{E_h}$ using the above basis sets. This is lower than the value of

$-510.330\,86\,E_h$ reported by McLean and Yoshimine,[34] who used a very slightly different geometry and Slater double zeta basis sets plus $3d$ and $4f$ functions. Both these values are lower than other SCF calculations using gaussian basis sets,[37,38] but our value is probably still $\sim 10\,mE_h$ or more above the SCF limit.

For the $HeCO_2$ interaction, a total of 21 geometries were chosen for the SCF calculations, while a total of 44 such geometries were chosen for HeOCS. We chose these geometries so that the calculated interaction energies would lie fairly evenly-spaced (on a logarithmic scale) in the range $1\,meV - 2\,eV$. For $HeCO_2$, we used a 45° angular grid from $0° - 90°$ between the He atom and the molecular axis. For HeOCS, this angular range extended from $0° - 180°$. Expecting a more complicated structure of the PE surface to emerge near the carbon atom, we reduced this grid to 15° in the vicinity of the perpendicular orientation. The results of all these calculations are assembled in Tables D.1 and D.2, and are displayed in Figs. D.2 and D.3. Several more calculations for $HeCO_2$, not shown in Table D.1 or Fig. D.2, were performed for interaction energies below 1 meV. At sufficiently large distances, some of these calculations yielded very slightly negative ($-4 \times 10^{-7}\,E_h = -0.01\,meV$) SCF interaction energies. With various uncertainties accumulating in such calculations (as discussed below), it was difficult to say whether any of these negative values were real, and they were not included for any of the fitting calculations conducted in Sec. III.

Also displayed in Fig. D.2 are results from a comparable calculation for $HeCO_2$, as reported by Stroud and Raff.[16] Their He basis set, $(6s)$ contracted to $(1s)$, was one given by Huzinaga,[39] and their C and O basis sets, $(10s\,4p)$ contracted to $(3s\,2p)$, were taken from the GAUSSIAN 70 package.[40] These results are in overall agreement with the present calculations, but they exhibit a steeper repulsive wall. There are also significant disagreements for the larger distances, corresponding to the weakest interactions, where our values are higher except for the 90° approach.

Table D.1 Hartree–Fock Calculations and Fitting Results for $HeCO_2$

		well–tempered basis set (present work)		
γ_C (deg)[a]	r_C (Å)[a]	V^{HF}(meV)	V^{fit}(meV)[b]	ΔV^{HF-fit} (%)[c]
0	2.7497	1355.	1360.	−0.4
0	3.2788	156.2	154.6	1.0
0	3.8080	16.38	16.12	1.6
0	4.3372	1.545	1.542	0.2
45	2.2205	1380.	1387.	−0.5
45	2.7497	215.5	223.6	−3.8
45	3.2788	29.32	30.59	−4.3
45	3.7419	4.730	4.826	−2.0
45	4.0006	1.637	1.655	−1.1
60	1.9050	1454.	1386.	4.7
60	2.8576	52.30	52.42	−0.2
60	3.7042	2.024	1.980	2.2
60	3.8101	1.327	1.289	2.9
75	1.7992	931.3	910.1	2.3
75	2.6459	42.84	41.57	3.0
75	3.4397	1.844	1.795	2.7
90	1.5875	1385.	1406.	−1.5
90	2.1167	205.6	211.0	−2.6
90	2.6459	25.65	25.43	0.9
90	3.1751	2.789	2.785	0.1
90	3.3497	1.288	1.335	−3.6

Table D.1 *Continued*

	6–31G basis set (Ref. 16)	
γ_C (deg)[a]	V^{HF}(meV)	ΔV^{HF-HF} (%)
0	1378.	2
0		
0		
0	1.162	−25
45		
45		
45		
45		
45		
60	1617.	11
60		
60		
60	0.778	−41
75		
75		
75		
90	1654.	19
90		
90		
90		
90	1.193	−7

[a] Angles and distances are measured as in Fig. D.1, with the origin centred on the carbon atom, co-inciding with the molecular centre-of-mass.

[b] Calculated from Eqns. (D–2 and D–3) using the parameters appearing in Table D–3.

[c] Overall standard deviation is 2.4%.

Table D.2 Hartree–Fock Calculations and Fitting Results for HeOCS

γ_C (deg)[a]	r_C (Å)[a]	V^{HF}(meV)	V^{fit}(meV)[b]	ΔV (%)[c]
0	2.7475	1382.	1409.	−2.0
0	3.2767	159.6	159.9	−0.2
0	3.8059	16.77	16.65	0.7
0	4.3351	1.582	1.591	−0.5
45	2.1961	1459.	1394.	4.5
45	2.8046	171.1	170.4	0.4
45	3.4132	16.87	16.70	1.0
45	3.9953	1.651	1.558	5.6
60	1.9050	1462.	1387.	5.1
60	2.5136	178.9	181.1	−1.2
60	2.8576	50.33	51.32	−2.0
60	3.1221	18.39	18.71	−1.7
60	3.8101	1.210	1.201	0.8
75	1.7992	1040.	1052.	−1.2
75	2.6459	48.77	52.83	−8.3
75	3.4397	2.155	2.320	−7.7
90	1.5875	1770.	1739.	1.7
90	1.6892	1297.	1289.	0.6
90	2.2184	232.2	237.8	−2.4
90	2.7475	39.03	38.38	1.7
90	3.2767	6.529	6.116	6.3
90	3.8059	1.102	1.010	8.4
105	1.8521	1334.	1222.	8.4
105	2.2490	450.8	420.1	6.8
105	3.0428	46.13	43.55	5.6
105	3.8365	4.082	3.952	3.2
120	2.2755	1214.	1171.	3.6
120	2.3813	935.8	910.0	2.8
120	3.0692	147.6	151.4	−2.6
120	3.2544	86.38	89.76	−3.9
120	3.8101	16.14	17.15	−6.3
120	4.2070	4.636	4.895	−5.6
120	4.4980	1.823	1.886	−3.4
135	2.5930	1764.	1814.	−2.9
135	3.2544	286.6	297.5	−3.8
135	3.8895	40.12	41.96	−4.6
135	4.5509	4.575	4.611	−0.8
135	4.8155	1.881	1.830	2.7
150	4.8949	3.015	2.725	9.6
180	3.2767	1795.	1893.	−5.4
180	3.8059	291.0	277.8	4.5
180	4.3351	40.11	38.40	4.3
180	4.8642	4.946	5.003	−1.2
180	5.2018	1.228	1.321	−7.6

Continued

[a] Angles and distances are measured as in Fig. D.1, with the origin centred on the carbon atom located 0.523 Å from the molecular centre-of-mass.

[b] Calculated from Eqns. (D–2 and D–3) using the parameters appearing in Table D–4.

[c] Overall standard deviation is 4.5%.

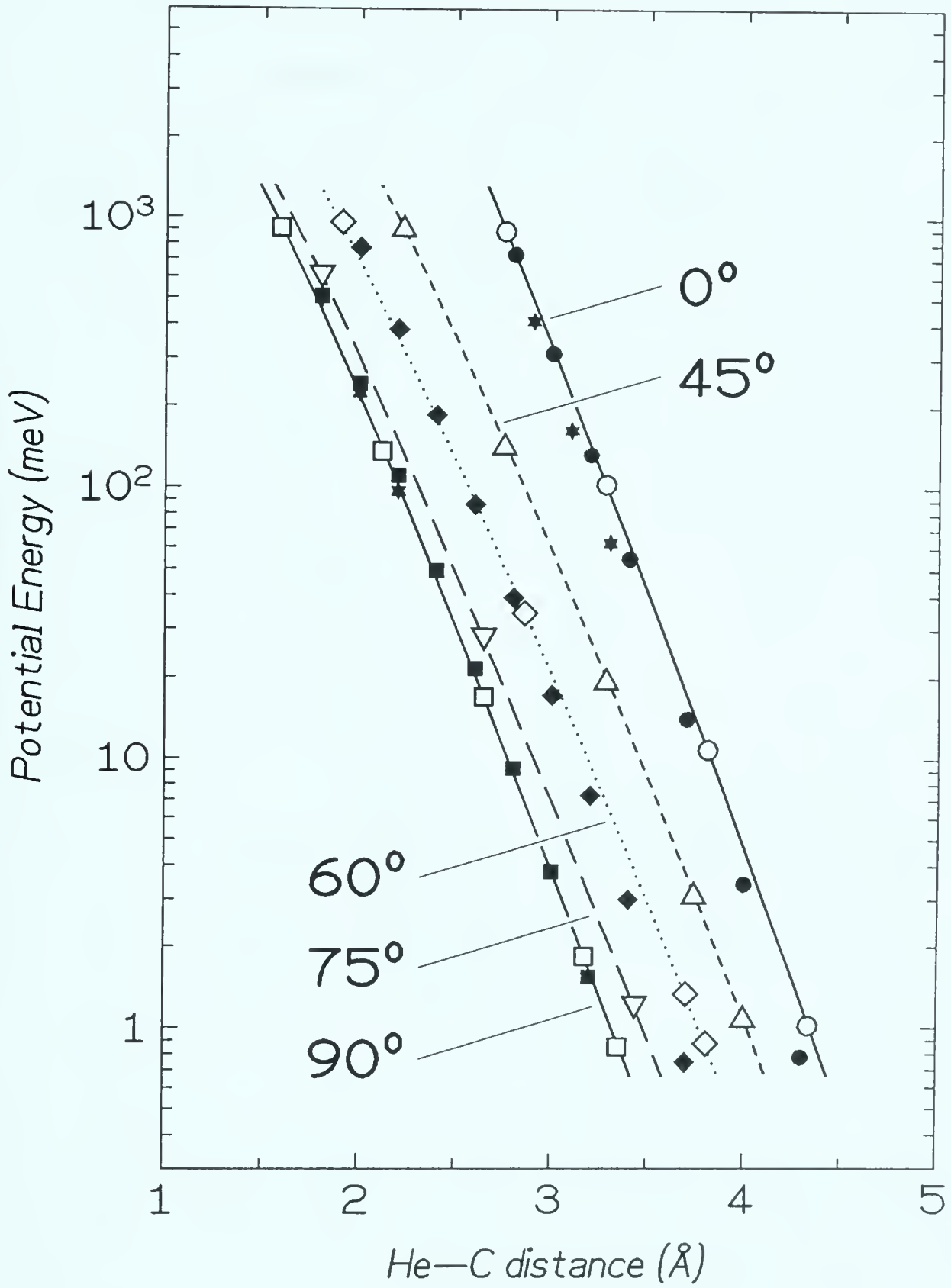

Figure D.2: Results of the present Hartree–Fock calculations for $HeCO_2$ (open symbols) compared to those of Stroud and Raff[16] (closed symbols). Angles and distances are measured as in Table D.1. The curves use the best-fit PE surfaces obtained from the sum-over-sites parameterization described in Sec. D.2.B.

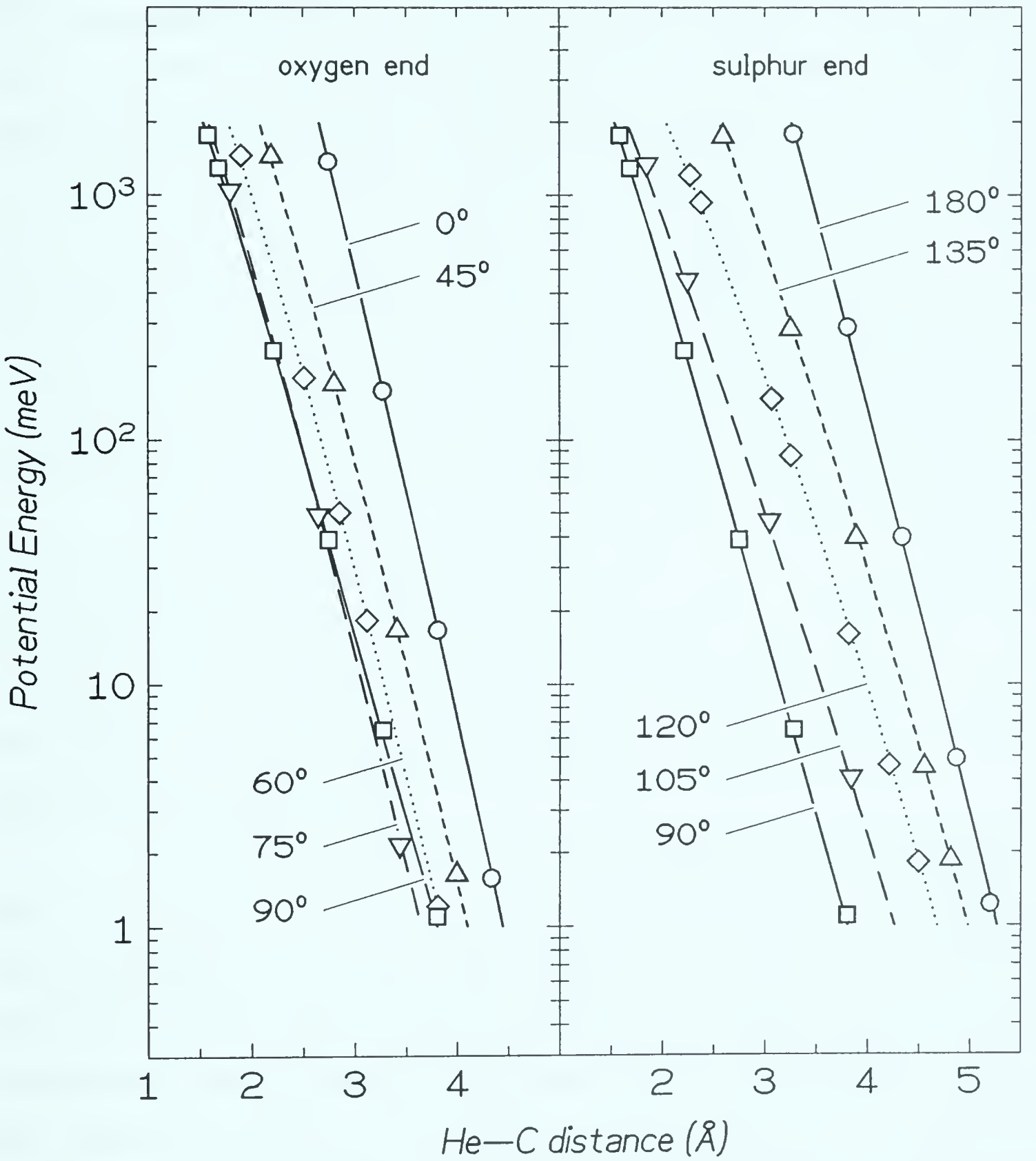

Figure D.3: Results of the Hartree–Fock calculations for HeOCS (open symbols). Angles and distances are measured as in Table D.2; curves as in Fig. D.2.

To clarify the source of the discrepancies with Stroud and Raff's results, we conducted some further calculations. We first applied our programs to several of the geometries they selected, using their basis sets. For example, with $\gamma_C = 60°$ and $r_C = 2.000\,\text{Å}$ we obtained 1172.80 meV for V^{HF} *vs.* the value of 1172.04 meV reported by Stroud and Raff. For a less-repulsive interaction at $\gamma_C = 60°$ and $r_C = 3.700\,\text{Å}$ we obtained 1.11 meV for V^{HF} *vs.* 1.13 meV. Corresponding results of more extensive trial calculations with the Stroud and Raff basis sets at a few of our selected geometries are shown in Table D.1. These show that our programs can reproduce the Stroud and Raff results with a maxiumum error of 2% in V^{HF}. It is therefore evident that most of the discrepancy between the present work and Stroud and Raff's results is due to the basis sets chosen for the two calculations.

A few points high up on the repulsive wall were also calculated by Clary,[17] again using the GAUSSIAN 70 package. For the 90° approach, his results match ours, but for the collinear approach they lie significantly lower, well below even Stroud and Raff's results. In this fairly strongly-repulsive region above 100 meV, we would not normally expect such large discrepancies, and we have no rationalization for them.

Amongst other causes for discrepancies between Hartree–Fock calculations, particularly low down on the repulsive wall, are effects of basis set superposition errors (BSSE). In the present calculations, the BSSE were calculated using the counterpoise method of Boys and Bernardi,[41] where the energy of one molecule is recalculated including the basis set of the other molecule at the appropriate geometry. This energy is used for the isolated molecule. No account was taken for BSSE in either of the other SCF calculations for $HeCO_2$. Again using the Stroud and Raff basis sets, our trial calculations of BSSE corrections raise their results by $\sim 15\%$ for the 60° geometry at large distances. Together with the larger corrections caused by using the well-tempered basis sets, this accounts for the entire discrepancy observed between the two calculations.

We also examined the effect of BSSE corrections for the present calculations. For the helium atom, the effect of the other basis sets is very small ($< 10^{-6}\,E_h$), indicating that the He basis is saturated in the range of our calculations. However, the He basis does contribute to the basis sets for the heavier atoms. The BSSE for the $HeCO_2$ interaction, as a proportion of the calculated interaction potential, range from $\sim 0.1\%$ of the highly repulsive potential at 1 eV, to $\sim 11\%$ for larger distances that correspond to interactions of 1 meV. There is a very slight increase in the proportional BSSE as the He approach angle is changed from broadside to collinear, indicating that the He basis set contributes more to the energy of the CO_2 molecule when it is at the oxygen end. For comparison, the corresponding proportional BSSE for our HeNe results[27] range from $\sim 0.01\%$ to $\sim 5\%$, again suggesting that the $HeCO_2$ calculations are comparable in accuracy to the HeNe calculations. For the HeOCS interaction, the proportional BSSE range from $\sim 0.2\%$ at 1 eV to $10 - 25\%$ at 1 meV, with the greatest BSSE occuring at the oxygen end of the OCS molecule. This suggests the He basis set improves the oxygen end of the molecule more than the sulphur end. Corresponding calculations for the HeAr interaction[36] also suggest that the He basis set does not contribute significantly to the sulphur ($9s\ 8p\ 3d$) basis.

There have been suggestions that the counterpoise procedure for BSSE corrections over-compensates for the effect of the other basis.[42] With good basis sets however, the BSSE is small and the counterpoise correction probably makes it smaller. Various methods have been suggested for making corrections to the counterpoise method, and some of these have been compared in calculations on the ArH_2 system.[42] In Hartree–Fock calculations, the counterpoise BSSE correction reduces the minimum calculated at larger distances using the uncorrected values and in some cases eliminates them. At the SCF level, the other correction methods produce minima of varying depths, but in all cases they are much weaker than

the uncorrected value. Such weak attraction is to be expected from Hartree–Fock calculations, since they do not account for the electron correlation that is responsible for most of the attraction as dispersion terms.

Differences between the various methods for correcting BSSE become greatest at large distances where the interaction is small; hence, the counterpoise method appears to remove the major part of the BSSE. In the present work, we are mostly concerned with the repulsive wall of the PE surface, so the effect of any such differences should be small. Ultimately, our SCF calculations will be merged with a series of attractive dispersion terms, so small errors at large distances in the SCF potential will be absorbed within errors due to the empirical damping functions used for such mergers.[2,3]

D.2.B. Analytical Fitting

The PE surface is parameterized by summing up purely repulsive contributions from the He atom to each of the three atomic sites ($i = 1, 2, 3$) of the molecule:

$$V^{\text{fit}}(r, \gamma) = \sum_{i=0}^{3} V_i(r_i, \gamma_i). \qquad (\text{D} - 2)$$

The $i = 0$ term in the above summation has been added to avoid gaps between the atomic centres, which otherwise become evident for potential energies exceeding a few dozen eV. The term is a strongly repulsive core whose range is so short that it is completely negligible below $\sim 10\,\text{eV}$. It is centred mid-way between the end atoms, making z_0 in Eqn. (D–2) the position of the geometric centre relative to the molecular centre-of-mass. None of the $i = 0$ parameters are fitted.

Each site potential appearing in the summation of Eqn. (D–2) is given as

$$V_i(r_i, \gamma_i) = \frac{A_{0,i}}{r_i^{n_i}} \exp\left[-\alpha_{0,i} r_i - \beta_{0,i} r_i^2 + (A_{2,i} - \alpha_{2,i} r_i) P_2(\cos\gamma_i)\right], \qquad (\text{D} - 3)$$

with the r_i and γ_i atom-centred co-ordinates being obtained from the centre-of-mass r and γ co-ordinates using Eqn. (D–1). Several generalizations to the simple Born–Mayer repulsion ($V = Ae^{-\alpha r}$) are evident in these terms. Firstly, we have added a quadratic dependence in the exponent to allow for the slight curvature evident, even for spherically symmetric potentials, in semi-log plots of the repulsive wall. More importantly for anisotropic PE surfaces, the Born–Mayer parameters are expanded in a Legendre series to P_2, facilitating fits to the π–orbitals on each end atom.[43] The inverse-power repulsive factor r^{-n} is used only for the $i = 0$ core term.

The functional form of Eqn. (D–3) allows up to six parameters for each of the three atomic centres. Such a large number of adjustable parameters cannot

justifiably be fit considering the limited number of Hartree–Fock points computed, so some restrictions are necessary.

For the $HeCO_2$ PE surface, we actually need to consider only two independent atomic centres, eliminating six parameters due to the molecular symmetry. In addition, the carbon atom is somewhat buried between the oxygens and we may, in a first attempt, eliminate the three P_2 terms on the carbon. A standard deviation of 2.3% (between the fitted and the Hartree–Fock potential) is then obtained by fitting the remaining nine parameters to the Hartree–Fock calculations at 21 points.

Several attempts were made to further reduce the number of fitted parameters. Ignoring the curvature in semi-log plots of the repulsive wall, we first fixed $\beta = 0$ for both centres and for both Legendre terms (leaving six free parameters), but this noticeably degrades the fit to 6.7%. If we instead drop the carbon atom's relatively small contribution (still six parameters) the fit is completely unsatisfactory. Fixing $\beta_0 = 0$ just for the carbon (eight parameters) doubles the imprecision. To avoid significant deterioration in the fitting quality, a minimum of three parameters apparently is required for the carbon centre.

Ultimately, we were able to eliminate only the $\beta_2 = 0$ parameter for oxygen, yielding an eight-parameter fit with an insignificant loss of precision (2.4%). The resulting parameters, collected in Table D.3, are used in Table D.1 to compare the fitted PE surface to the Hartree–Fock calculations. All the calculated points are reproduced to better than 5%. The high quality of the present fit is also evident from Fig. D.2.

For HeOCS, all three atomic centres must be included explicitly. Even after eliminating the P_2 terms on the carbon and β_2 parameters on both the oxygen and sulphur, there remain 13 parameters to be fit to the Hartree–Fock calculations at 44 points. This first attempt, even though unwieldy for fitting, yields a standard deviation of 4.5%.

Table D.3 Parameters fitted to the $HeCO_2$ Hartree–Fock calculations[a]

parameter	core	oxygen	carbon
i [Eqn. (D–2)]	0	1,3	2
z_i[b] (Å)	0.000	±1.1621	0.000
$A_{0,i}$ (eV)	10.00	*394.7*	*26.1*
$\alpha_{0,i}$ (Å^{-1})	0.00	*3.280*	*0.985*
$\beta_{0,i}$ (Å^{-2})	0.00	*0.155*	*0.801*
$A_{2,i}$	5.00	*0.324*	0.00
$\alpha_{2,i}$ (Å^{-1})	0.00	*0.252*	0.00
n_i[c]	12.00	0.00	0.00

[a] Potential parameters obtained by fitting to the Hartree–Fock results are shown in italics.

[b] Distance from the molecular centre-of-mass, taken from Herzberg.[24]

[c] Corresponding to r_i in Eqn. (D–3) having units of Å.

Comparing Figs. D.2 and D.3 underscores the chemically reasonable suggestion that the "oxygen-ends" of the $HeCO_2$ and HeOCS Hartree–Fock potentials are almost identical for $\gamma_C \leq 60°$. Such a suggestion is implemented straight-forwardly using the sum-over-sites parameterization of Eqn. (D–2), simply by transfering all the oxygen and carbon parameters obtained from the $HeCO_2$ fitting results. Leaving only the five sulphur-centred parameters, these fits to the HeOCS calculations unfortunately degrade the precision substantially, to 8.2%. It is apparent that site transferrability between molecules, though useful, is imperfect.

A reasonable compromise between high precision and a small parameter set might be obtained by including the oxygen A_0 and A_2 parameters in the fitting. This is justified by noting that A parameters, obtained from purely repulsive Hartree–Fock calculations, are usually adjusted by $10 - 20\%$ in obtaining semi-empirical potentials. It has been suggested that such adjustments are most suitably applied to the A parameter, in that the neglected intra-atomic correlation and inter-intra coupling terms are nearly parallel to the Hartree–Fock calculations (at least for HeH, NeH, and ArH[44]). The additional flexibility allows small adjustments to the repulsive wall position (but not its shape) at the oxygen end. Unfortunately, this seven-parameter fit provides no improvement over fitting just the five sulphur-centred parameters.

The greatest difficulty with these fits occur near the carbon atom ($75° \leq \gamma_C \leq 105°$). Including just one of the carbon parameters in the fitting improves the precision markedly. Repeating the above argument, that additional parameter ought to be the carbon A_0. An even better choice, suggested by the curvature evident in Fig. D.3, is evidently provided by fitting the carbon β_0 parameter instead. This eight-parameter fit yields a precision of 4.5%, just as good as the original 13-parameter fit. The resulting parameters, collected in Table D.4, are used in Table D.2 to compare the fitted PE surface to the Hartree–Fock calculations. All

the calculated points are reproduced to better than 10%. The precision of the present fit can also be judged from Fig. D.3.

Our best-fit Hartree–Fock PE surfaces for $HeCO_2$ and HeOCS are shown as hemispherical contour plots in Figs. D.4 and D.5, respectively.

It is worthwhile comparing the efficiency of the present sum-over-sites model to other parameterizations. The $HeCO_2$ and HeOCS PE surfaces are obviously sufficiently anisotropic that simply expressing the potential in a Legendre expansion would involve far too many terms for meaningful fitting. A popular and productive alternative has been to expand the potential parameters instead.[45] For $HeCO_2$, fitting to a six-parameter $(A_0, A_2, \alpha_0, \alpha_2, \alpha_4, \beta_0)$ expansion potential is quite poor (10.4%) and significantly less precise than the six-parameter sum-over-sites fit obtained above (6.7%). For HeOCS, the parameter expansion algorithm is even less appealing since odd-order Legendre terms must be included. Even with up to eleven parameters, the precision could not be brought below 10%.

Future improvements to the sum-over-sites parameterization may be guided by noticing that, in all cases, the (A, α, β) parameters are highly correlated for a single site and for a single Legendre order. Corresponding correlations between sites, or between Legendre orders on the same site, are quite small.

Finally, we note that using the sum-over-sites parameterization is indispensable to fitting the HeOCS PE surface in a manageable way. Comparing Tables D.3 and D.4 suggests that transfering parameters from one site of a molecule to the same site in a similar molecule can yield reasonably precise results. Of course, our choice of $HeCO_2$ and HeOCS is partially motivated by the clear similarities in the electronic structure and equilibrium geometries of CO_2 and OCS, so our experience with transferability may be somewhat selective. Nevertheless, the present parameterization has obvious appeal for larger molecules. Furthermore, as we will explore seperately,[46] it may also be rather precise for obtaining van der Waals interaction potentials for vibrationally excited molecules, since such PE surfaces can

Table D.4 Parameters fitted to the HeOCS Hartree–Fock calculations[a]

parameter	core	oxygen	carbon	sulphur
i [Eqn. (D–2)]	0	1	2	3
z_i[b] (Å)	+0.323	+1.683	+0.523	−1.037
$A_{0,i}$ (eV)	10.00	*366.6*	26.1	*416.4*
$\alpha_{0,i}$ (Å^{-1})	0.00	3.280	0.985	*2.816*
$\beta_{0,i}$ (Å^{-2})	0.00	0.155	*0.673*	*0.107*
$A_{2,i}$	6.00	*0.429*	0.00	*0.419*
$\alpha_{2,i}$ (Å^{-1})	0.00	0.252	0.00	*0.387*
n_i[c]	12.00	0.00	0.00	0.00

[a] Potential parameters obtained by fitting to the Hartree–Fock results are shown in italics. Parameters transferred from the $HeCO_2$ fitting in Table D.3 are underlined.

[b] Distance from the molecular centre-of-mass, taken from Herzberg.[24]

[c] Corresponding to r_i in Eqn. (D–3) having units of Å.

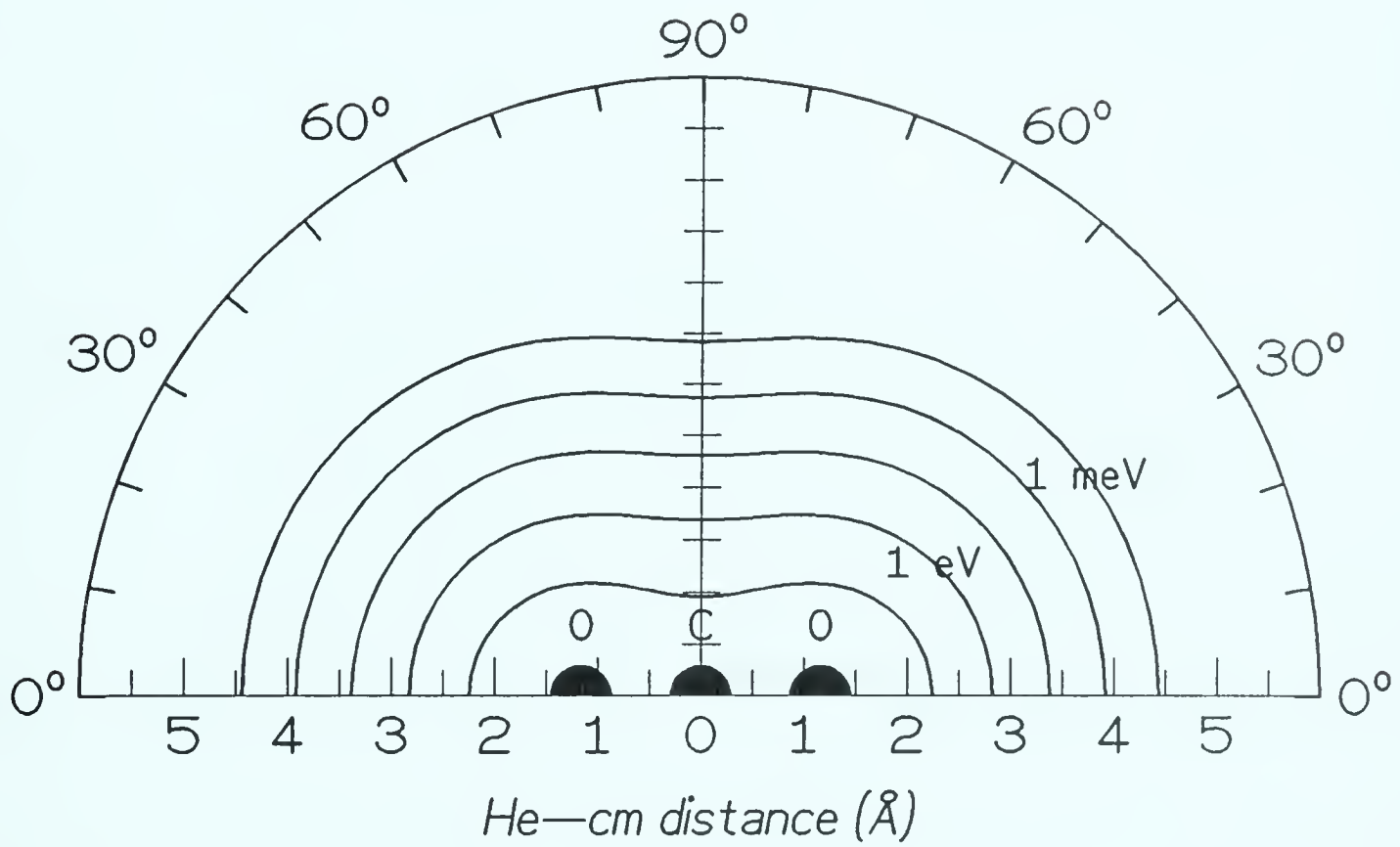

Figure D.4: Contour plot for $HeCO_2$. Contour intervals are from 1 meV, increasing by factors of 10, to 10 eV.

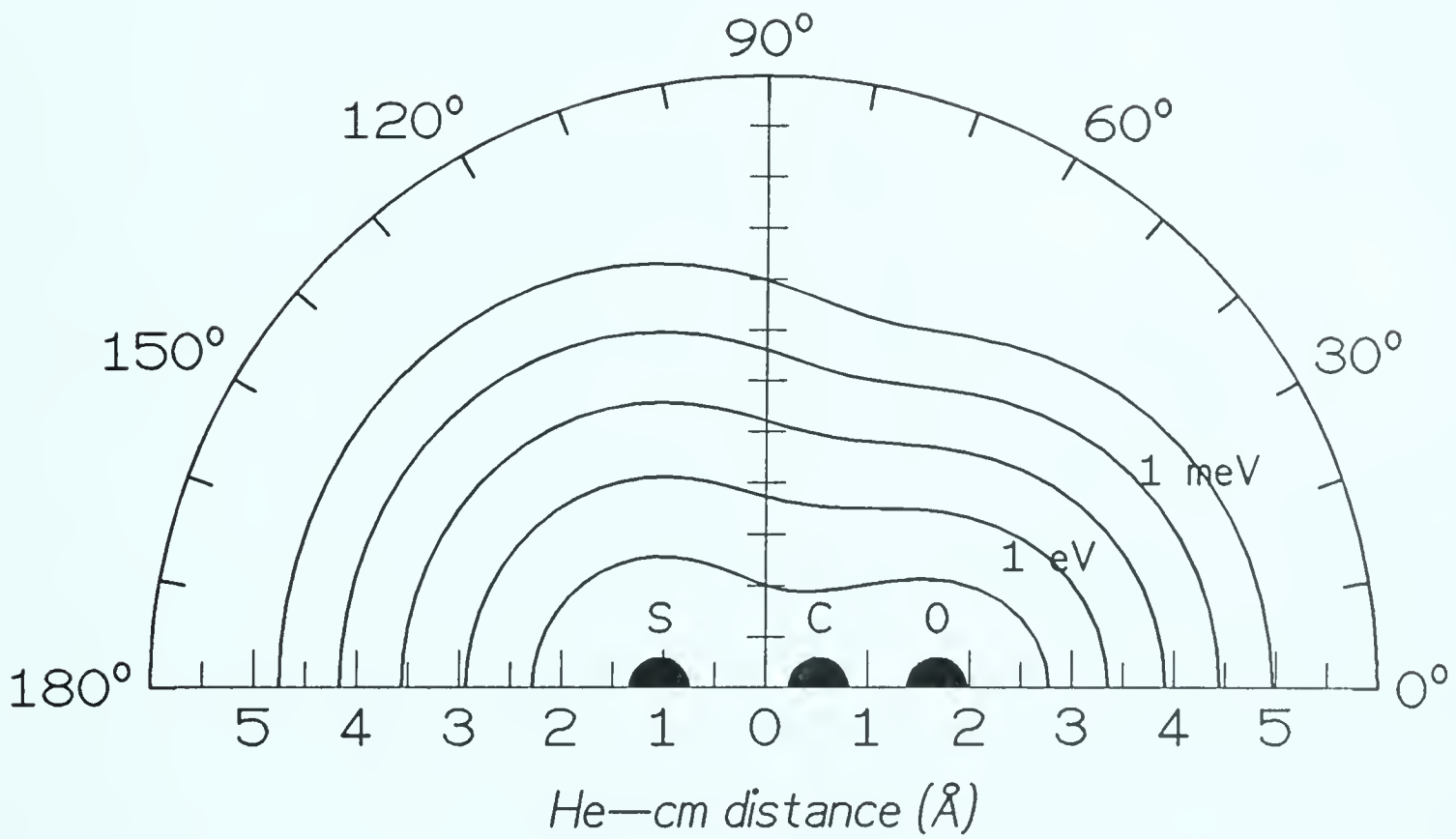

Figure D.5: Contour plot for HeOCS. Note that the origin is placed at the molecular centre-of-mass. Contour intervals as in Fig. D.4.

naturally be expressed by summing over sites that are moving, rather than being fixed at their rigid-rotor positions.[17]

D.3 PRESSURE BROADENING

The pressure broadening of infrared and Raman absorption lines for CO_2 diluted in He have been measured by several authors.[20-22] Infrared measurements for OCS have also been reported and discussed.[23] All these measurements were conducted at room temperature. Since these data are almost entirely independent of attractive contributions to the PE surface,[13] the present sum-over-sites repulsive PE surfaces ought to provide estimates for comparing to the measured pressure-broadening rate coefficients.

We have used the infinite-order sudden[47] approximation (IOSA) for calculating the infrared and Raman pressure broadening rates.[48] The IOSA ought to be reasonably reliable for the two systems considered here, with their low reduced mass, large moment of inertia, and steeply repulsive PE surfaces. We describe the computational details very briefly, using Pack's terminology.[48] All the computations treat the molecules as rigid rotators, though the infrared measurements are for vib-rotational transitions (the Raman measurements are for pure rotational transitions).

The large rotational states involved in the experiments necessitate performing the phase shift calculations at forty atom-molecule orientation angles (twenty for $HeCO_2$) using JWKB phase shifts for computational efficiency. Only four collision energies are needed for Boltzmann averaging over the general relaxation cross sections. Trial calculations for comparison to Pack's results[48] yield calculated relaxation cross sections and pressure-broadening rate coefficients that are identical over the $5-1000\,\mathrm{meV}$ and $200-450\mathrm{K}$ energy and temperature ranges, respectively.

Calculated pressure-broadening rate coefficients for the $HeCO_2$ and HeOCS sum-over-sites PE surfaces are shown in Fig. D.6, and are compared to the available experimental data. The present PE surfaces are reliable enough to provide

predictions to within the experimental accuracy (which unfortunately is not very high), except for falling systematically below the $HeCO_2$ Raman measurements. As discussed on a previous occasion,[13] the Raman and infrared pressure-broadened linewidths depend on the PE surface in very similar ways, so this discrepancy may indicate systematic experimental problems associated with pure rotational Raman linewidth measurements or difficulties with the dynamical assumptions.

We note that the present calculations for $HeCO_2$ give virtually identical results to those obtained from a semi-empirical PE surface.[13] This reflects the similarity between the present Hartree–Fock calculations and those of Stroud and Raff, at least for interaction potentials above $\sim 10\,\mathrm{meV}$ (Fig. D.2). For HeOCS, the only other calculated pressure-broadened linewidths lie a factor of two below the corresponding measurements, and the present results provide clear improvements.

It is evident from Fig. D.6 that the calculated $HeCO_2$ linewidths are considerably smaller than those for HeOCS ($0.115\,\mathrm{cm}^{-1}/atm$ *vs.* $0.159\,\mathrm{cm}^{-1}/atm$ respectively, for large j_a). It is interesting to examine the origin of this difference. In the IOSA, the assumption of degenerate rotational levels renders the moment of inertia irrelevant; in collisions with the light He atom the reduced mass for $HeCO_2$ and HeOCS differ by only 2%. Therefore, the 40% larger linewidths for HeOCS must arise from contributions due to the mass asymmetry (*i.e.,* the displacement between geometric or atomic centres and the molecular centre-of-mass) and to the potential asymmetry (*i.e.,* the difference between the oxygen and sulphur ends of the PE surface).

To distinguish between these contributions, we repeated the line-broadening calculations, replacing the sulphur-centred parameters with the corresponding oxygen-centred values. This "shifted $HeCO_2$" PE surface—symmetric about the $\gamma_C = 90°$ axis but not about the $\gamma = 90°$ axis 0.523 Å away—yields the pressure-broadening linewidths displayed in Fig. D.6. The results show that

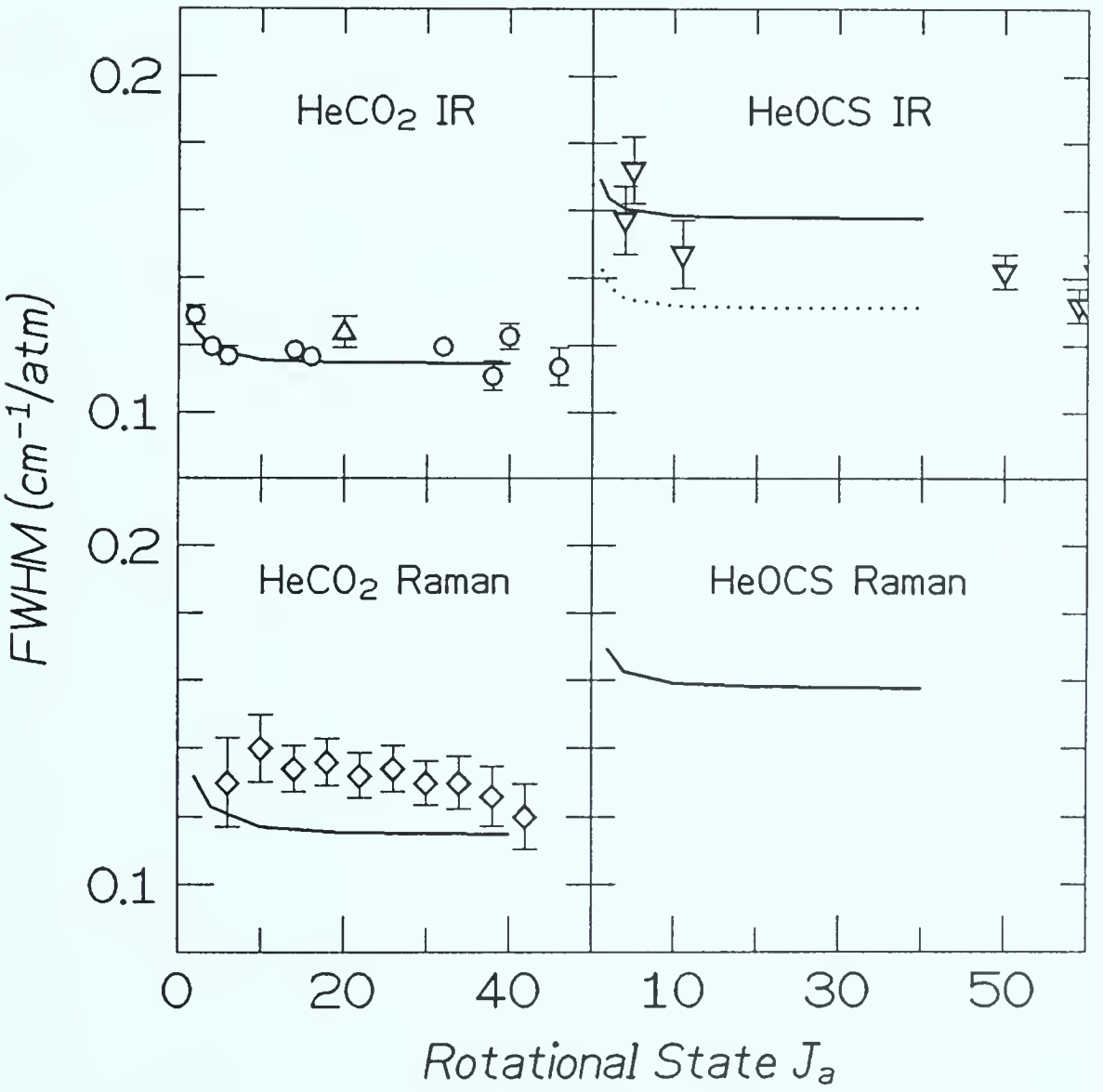

Figure D.6: Pressure-broadening rate coefficients for $HeCO_2$ and HeOCS at room temperature. Available experimental measurements are shown as open symbols, while calculations using the IOSA and the fitted PE surfaces are shown as solid curves. The data are taken from Brimacombe and Reid[22] (◯); Abrams[20] (△); Herpin and Lallemand[21] (◇); and Broquier *et al.*[23] (▽). The dotted curve for HeOCS infrared linewidths is calculated from a "shifted $HeCO_2$" PE surface obtained as described in the text. Note that the linewidths are given as *full*-widths, whereas some authors use half-widths.

only $\sim 35\%$ of the increased linewidth in going from $HeCO_2$ to HeOCS is due to the asymmetric mass distribution. The majority of the increase is due instead to the much larger repulsion at the sulphur end of the molecule. Accurate pressure broadening measurements for HeOCS would therefore provide an important probe for the repulsive potential asymmetry between different ends of the molecule.

D.4 SUMMARY

Accurate Hartree–Fock calculations are performed for purely repulsive interactions of He with CO_2 and OCS. Calculations for both systems are reproduced, to high precision, by eight-parameter fits using analytical expressions for the PE surfaces that sum over interactions between the He atom and each atomic site of the molecule. This sum-over-sites expression requires fewer fitted parameters than other parameterizations that we have tried. This is partially because some parameters may be transferred between atomic sites of different molecules. Chemically reasonable and useful extensions of the sum-over-sites parameterization are discussed.

The repulsive anistropies of the fitted PE surfaces are tested by comparing to experimental pressure-broadening linewidths, with which good agreement is obtained. For van der Waals interaction involving He, very little of the pressure-broadened linewidth is caused by the anisotropy of the weak attractive well.[13] Consequently, reasonably accurate predictions of such linewidths are possible using straight-forward Hartree–Fock quantum chemistry calculations in conjunction with IOSA dynamics on a sum-over-sites PE surface. The difference in linewidths between $HeCO_2$ and HeOCS is separated into contributions due to the asymmetric mass distribution and increased anisotropy at the sulphur end. The latter, more interesting contribution, is responsible for most of the linewidth increase: more accurate line-broadening measurements would likely improve characterizations of the HeOCS potential anisotropy.

REFERENCES:

1. See for example, an extensive review of theoretical methods by A. D. Buckingham, P. W. Fowler, and J. M. Hutson, *Chem. Rev.* **88**, 963 (1988).
2. J. Hepburn, G. Scoles, and R. Penco, *Chem Phys. Lett.* **36**, 451 (1975); R. Ahlrichs, R. Penco, and G. Scoles, *Chem Phys.* **19**, 119 (1977); C. Douketis, G. Scoles, S. Marchetti, M. Zen, and A. J. Thakkar, *J. Chem. Phys.* **76**, 3057 (1982).
3. K. T. Tang and J. P. Toennies, *J. Chem. Phys.* **66**, 1496 (1977); K. T. Tang and J. P. Toennies, *J. Chem. Phys.* **80**, 3726 (1984).
4. H.–J. Bohm and R. Ahlrichs, *J. Chem. Phys.* **77**, 2028 (1982); K. P. Sagarik, R. Ahlrichs and S. Brode, *Mol. Phys.* **57**, 1247 (1986).
5. K. T. Tang and J. P. Toennies, *J. Chem. Phys.* **68**, 5501 (1978).
6. W. R. Rodwell and G. Scoles, *J. Phys. Chem.* **86**, 1053 (1982).
7. M. Faubel, K.–H. Kohl, and J. P. Toennies, *Faraday Disc. Chem. Soc.* **73**, 205 (1982).
8. K. T. Tang and J. P. Toennies, *J. Chem. Phys.* **76**, 2524 (1982).
9. C. Douketis, J. M. Hutson, B. J. Orr, and G. Scoles, *Mol. Phys.* **52**, 763 (1984).
10. R. R. Fuchs, F. R. W. McCourt, A. J. Thakkar, and F. Grein, *J. Phys. Chem.* **88**, 2036 (1984) and references therein.
11. C. Douketis, M. Keil, and G. Scoles, *Faraday Disc. Chem. Soc.* **73**, 286 (1982).
12. J. M. Hutson, *submitted to J. Chem. Phys.* (1991), and references therein.
13. M. Keil and G. A. Parker, *J. Chem. Phys.* **82**, 1947 (1985).
14. L. Beneventi, P. Casavecchia, F. Vecchiocattivi, G. G. Volpi, U. Buck, Ch. Lauenstein, and R. Schinke, *J. Chem. Phys.* **89**, 4671 (1988).
15. L. J. Danielson, K. M. McLeod, and M. Keil, *J. Chem. Phys.* **87**, 239 (1987).
16. C. L. Stroud and L. M. Raff, *J. Chem. Phys.* **72**, 5479 (1980).
17. D. C. Clary, *Chem. Phys.* **65**, 247 (1982).
18. G. A. Parker, R. L. Snow, and R. T Pack, *J. Chem. Phys.* **64**, 1668 (1976).
19. R. E. Johnson, S. T. Epstein, and W. J. Meath, *J. Chem. Phys.* **47**, 1271 (1967); A. Kumar and W. J. Meath, *Chem. Phys.* **91**, 411 (1984).

20. R. L. Abrams, *Appl. Phys. Lett.* **25**, 609 (1974).

21. M. C. Herpin and P. Lallemand, *J. Quant. Spectrosc. Radiat. Transfer* **15**, 779 (1975).

22. R. K. Brimacombe and J. Reid, *IEEE J. Quantum Electron.* **QE19**, 1668 (1983).

23. M. Broquier, A. Picard–Bersellini, B. J. Whitaker, and S. Green, *J. Chem. Phys.* **84**, 2104 (1986).

24. G. Herzberg, *Electronic Spectra and Electronic Structure of Polyatomic Molecules* (Reinhold, Toronto, 1966), pp. 597 – 600.

25. M. W. Schmidt, J. A. Boatz, K. K. Baldridge, S. Koseki, M. S. Gordon, S. T. Elbert and B. Lam, *QCPE Bull.* **7**, 115 (1987).

26. H. King, M. Dupuis, and J. Rys, *Nat. Resour. Comput. Chem. Software Cat., (Lawrence Berkely Laboratory, Berkeley, California, 1980)*, (Program No.QH07, vol. 1.)

27. M. Keil, L. J. Danielson, U. Buck, J. Schleusener, F. Huisken, and T. W. Dingle, *J. Chem. Phys.* **89**, 2866 (1988).

28. F. P. van Duijneveldt, *IBM Research Report* **RJ 945** (IBM, San Jose, 1971).

29. C. Froese-Fischer, *The Hartree–Fock Method for Atoms* (Wiley, New York, 1977).

30. S. Huzinaga and M. Klobukowski, *J. Mol. Struct. (Theochem)* **167**, 1 (1988).

31. T. W. Dingle, S. Huzinaga, and M. Klobukowski, *J. Comput. Chem.* **10**, 753 (1989).

32. D. Sundholm, P. Pyykkö, and L. Laaksonen, *Mol. Phys.* **56**, 1411 (1985); L. Laaksonen, P. Pyykkö and D. Sundholm, *Comput. Phys. Reports* **4**, 313 (1986).

33. M. Klobukowski, T. W. Dingle, and S. Huzinaga, *Theor. Chim. Acta* **77**, 191 (1990).

34. A. D. McLean and M. Yoshimine, *Tables of Linear Molecule Wave Functions* (IBM, San Jose, 1967); M. Yoshimine and A. D. McLean, *Int. J. Quantum Chem.* **1S**, 313 (1967).

35. P. J. Knowles, P. Rosmus, and H.–J. Werner, *Chem. Phys. Lett.* **146**, 230 (1988).

36. T. W. Dingle, *unpublished results.*

37. J. Jokisaari, P. Lazzeretti, and P. Pyykkö, *Chem. Phys.* **123**, 339 (1988).

38. M. T. Carroll and R. F. Bader, *Mol. Phys.* **65**, 695 (1988).

39. S. Huzinaga, *J. Chem. Phys.* **42**, 1293 (1965).

40. W. J. Hehre, R. Ditchfield, and J. A. Pople, *J. Chem. Phys.* **56**, 2257 (1972).

41. S. F. Boys and F. Bernardi, *Mol. Phys.* **19**, 553 (1970).

42. S. Tolosa, J. Espinosa, and F. J. Olivares del Valle, *J. Comput. Chem.* **12**, 611 (1991) and references therein.

43. We wish to thank Prof. Schatz (Northwestern) for the suggestion of adding Legendre terms to the end atoms.

44. A. J. C. Varandas and J. Brandão, *Mol. Phys.* **45**, 857 (1982).

45. R. T Pack, *Chem. Phys. Lett.* **55**, 197 (1978).

46. M. Keil and T. W. Dingle, *manuscript in preparation.*

47. G. A. Parker and R. T Pack, *J. Chem. Phys.* **68**, 1585 (1978).

48. R. T Pack, *J. Chem. Phys.* **70**, 3424 (1979).

University of Alberta Library

0 1620 0239 4896

B44939